

POLITECNICO DI TORINO

Corso di Laurea Magistrale in Ingegneria Meccanica



Tesi di Laurea Magistrale

Design, construction and testing of a highly
efficient arm-powered recumbent trike

Relatrice:

prof.ssa Chiara Gastaldi

Co-relatrice:

prof.ssa Cristiana Delprete

Candidato:

Alessandro Di Gesù, matricola S288704

Anno Accademico 2021/2022

Abstract

For a long time, mankind has heavily depended on animal labour and human-powered work. The advent of industrial machines, and motors in particular, has changed the paradigm: today in developed countries, apart from some exceptions like the Netherlands, the vast majority of people moves with motorized vehicles.

This thesis is about project Cerberus, an arm-powered vehicle developed mainly for use in competitions and designed by students from Team Policumbent at Politecnico di Torino. The aim of the thesis is to lay some general basis for the design of three-wheeled human-powered vehicles, including those for everyday use on public roads.

In this context, the author, in the role of both project manager and head of the mechanical design department for the prototype, decided to write a most complete document incorporating in it both his own, and his teammates work (to whom the credit is explicitly given). The paper not only tells how but also why the vehicle was designed the way it is, so the team's know-how is taken into account, models on the concept design are presented and sometimes alternative designs are discussed too. Not everything though is dealt with in detail, as some teammates have written or are about to write their own thesis with exhaustive information on certain topics concerning the prototype. Furthermore, as there are fields which the author is not too familiar with and can't therefore be discussed thoroughly, for the FEM studies, the electric and electronic parts, a general overview is given without delving too much into detail.

The first part of the thesis is introductory and sets the general information on why the prototype has been developed, as well as what its goals are, and describes the first studies of a concept design. Part two is the core of the document, where the reader delves into the details of the trike's final design. Part three is about the construction and testing of the vehicle and gives some insights of the production phases.

Lastly, in the appendices, it's possible to view the drawings of many of the machined parts and to inspect the prototype's detailed bill of materials.

Contents

I	Introduction, background art & know-how: delta concept design	1
I.1	Introduction	3
I.1.1	Faired bikes	3
I.1.2	Recumbent bikes	4
I.1.3	Recumbent faired bikes	5
I.1.4	IHPVA and WHPVA	6
I.1.5	Handcycles	6
I.1.5.1	Upright vs recumbent	6
I.1.5.2	Delta vs Tadpole	7
I.1.6	Purpose and structure of the thesis	8
I.2	On team Policumbent	9
I.2.1	Birth and history	9
I.2.2	Know-how	9
I.2.2.1	Wheels test bench	13
I.2.2.1.1	Latex vs butile inner tubes	13
I.2.2.1.2	Aerodynamics and bearings' dissipation	13
I.2.2.1.3	Clinchers	14
I.2.2.1.4	Conclusions	14
I.2.2.2	Moving sprocket pack	15
I.2.2.3	Safety	15
I.2.2.3.1	Fairing construction	15
I.2.2.3.2	Dual vision system	16
I.3	Simple stability model of a delta handcycle	17
I.3.1	Overturning condition	17
I.3.1.1	Hypotheses, parameters and equations	17
I.3.1.2	Values and variation ranges of the parameters	20
I.3.1.3	Results and comments	20
I.3.1.4	Additional parameter: camber influence	29
I.3.1.5	Final considerations	30
I.3.2	Self-alignin torque	30
I.3.2.1	Geometric definition in Solidworks	30
I.3.2.2	Forces definition in Solidworks	31
I.3.2.3	Linked designed table and results	33
I.3.2.4	Results and comments	35
I.4	Aerodynamic studies in delta configuration	41

I.4.1	Basis of aerodynamics	41
I.4.1.1	Net drag	41
I.4.1.2	Shear drag	41
I.4.1.3	Separation, vorticity, pressure drag	42
I.4.1.4	Drag coefficient	42
I.4.1.5	Lateral wind	43
I.4.2	Project constraints and geometric parameters	43
I.4.2.1	Length	43
I.4.2.2	Track	43
I.4.2.3	Frontal area, wetted surface	43
I.4.3	Fairings	44
I.4.3.1	ADG_1F_05	45
I.4.3.2	NXS_01 and NXS_01_A	45
I.4.3.3	Comparisons	47
I.4.3.3.1	Wall shear stress	48
I.4.3.3.2	Wake and stream lines	49

II Cerberus’s design: a tadpole handtrike 51

II.1 Aerodynamic design of the fairing in tadpole configuration 53

II.1.1	Detailed CAD modeling process of the shell	53
II.1.1.1	Interferences with the pilot: 3D mannequin	53
II.1.1.2	Preliminary assembly arrangements	54
II.1.1.3	Creation of the fairing part	57
II.1.1.4	Design of fairing ADG_N59	58
II.1.1.4.1	Lower profile	58
II.1.1.4.2	Elbow section	59
II.1.1.4.3	Upper profile	60
II.1.1.4.4	Closing line	62
II.1.1.4.5	Front section	62
II.1.1.4.6	Rear section	64
II.1.1.4.7	Surface loft creation	64
II.1.1.5	Alternative designs: wheel covers	66
II.1.1.6	Alternative designs: lateral spline	66
II.1.1.7	Zebra stripes analysis	67
II.1.1.8	Partition lines	70
II.1.2	CFD simulations with Solidworks	70
II.1.3	CFD simulations with Star CCM+	71
II.1.3.1	Wall shear stress	71
II.1.3.2	Pressure drag and wake visualization	71
II.1.3.3	Pressure coefficient	76
II.1.3.4	C_x and power comparison of the few best fairings	76

II.2 Design of the structural laminated parts 79

II.2.1	Aerodynamic (front) fairing	80
II.2.2	Structural (central) fairing	81
II.2.2.1	Bottom wheel covers	82
II.2.3	Tail (rear) fairing	83

II.2.4	Upper wheel covers	84
II.2.5	Basin	86
II.2.6	Slide	86
II.2.7	Bottom longerons	88
II.2.8	Upper longeron	88
II.2.9	Seat	90
II.3	Additional structural components	91
II.3.1	Components in AlSi10Mg	91
II.3.2	Aluminum plates	92
II.3.3	Carbon fiber tubes	93
II.4	Design of the vision system	97
II.4.1	Plexiglass window	97
II.4.1.1	Requirements	97
II.4.1.2	Design	97
II.4.2	Design of the cameras' supports	98
II.4.2.1	Required functionalities	98
II.4.2.2	Components	100
II.4.2.2.1	Case	101
II.4.2.2.2	Back lid	101
II.4.2.2.3	Vertical translation support	101
II.4.2.2.4	Camera interfaces	101
II.4.2.2.5	Horizontal translation frame	104
II.4.2.2.6	Anti lift guides	104
II.4.2.2.7	Rear lid locking mechanism	104
II.4.2.2.8	Lateral laths	104
II.4.3	Design of the screens' supports	104
II.4.3.1	Required functionalities	104
II.4.3.2	Components	106
II.4.3.2.1	Fairing interface	106
II.4.3.2.2	Screens support	106
II.4.3.2.3	Screens frames	107
II.4.3.2.4	Driver support	107
II.5	Design of the moving cassette system	109
II.5.1	First design: external actuation	109
II.5.2	Second design: actuation internal to the shaft	112
II.5.3	Some important notes	112
II.6	Chain tensioners and carters	117
II.6.1	Fixed branch	117
II.6.2	Sprocket pack branch	118
II.7	Steering mechanism	121
II.7.1	Possible systems	121
II.7.2	Further description of the system and rod-end bearings' dimensioning	121
II.7.3	Final notes	123

II.8	Breaking system	125
II.8.1	Main support	125
II.8.1.1	Caliper	125
II.8.1.2	Caliper mount	125
II.8.1.3	Plate	126
II.8.1.4	Fairing interfaces	126
II.8.2	Brake lever position	129
II.9	Other components	131
II.9.1	Hubs	131
II.9.2	Crankset and handles	132
II.9.3	Wheels	132
II.9.4	Adjustable seat	133
II.9.5	Seatbelt	133
II.9.6	Air filter	135
III	Construction and testing	137
III.1	Fitting tests	139
III.1.1	June 2021 test	139
III.1.2	October 2021 test	140
III.2	Prototype production	143
III.2.1	Molds and models	143
III.2.1.1	From CAD to machining	143
III.2.1.2	Painting	144
III.2.1.3	Sanding	144
III.2.1.4	Surface sealer application	144
III.2.1.5	Detaching agent application	145
III.2.2	Lamination	145
III.2.2.1	Cut of the plies	145
III.2.2.2	Techniques used	146
III.2.2.2.1	Prepreg	146
III.2.2.2.2	Wet-layup	146
III.2.2.2.3	Infusion	147
III.2.2.3	Visual inspections and final refinements	149
III.2.3	Assembly	150
III.2.3.1	Tolerance checks	150
III.2.3.2	Gluing	151
III.2.4	Other parts produced autonomously	151
III.3	Road testing	155
III.3.1	Tests	155
III.3.1.1	Tests in Balocco	155
III.3.1.2	Test in Stupinigi	156
III.3.2	WHPSC	156
III.3.2.1	September 11th	156
III.3.2.2	September 12th	158

III.3.2.3	September 13th	158
III.3.2.4	September 14th	158
III.3.2.5	September 15th	158
III.3.2.6	September 16th	159
III.3.2.7	September 17th	159
III.3.3	Final comments	159

IV	Appendices	I
A	Bill of materials	III
B	Drawings	XIII
	Bibliography	XLIX

Part I

Introduction, background art &
know-how: delta concept design

Chapter I.1

Introduction

The remarkable lack of variety in cycle development over the [past] century is not necessarily a reflection that the existing design is the best possible. Rather, it signifies that the bicycle is enmeshed in a matrix of social, technical and environmental forces which have historically served to close off further development until recent years [1]. As a matter of fact, the Rover Safety Cycle, which was introduced in England in 1884, could easily pass for a modern bicycle; it lacks only a seat brace, which would have formed the modern diamond frame, and a few components such as brakes and multiple gears [2]. The conventional bicycle, as we commonly recognize it, could be dated to the 1890s. So, in a way, we can say that the bicycle, as we familiarly know it, has been the subject of technological closure for most of the past century [1].

For decades the principles of aerodynamics have been applied with great success to improving the speed and efficiency of aircraft, automobiles, motorcycles and even competitive skiers and skaters. Vehicles powered by human energy, however, were virtually ignored until the 1970s, which is strange in view of the fact that air resistance is by far the major retarding force affecting them. With a bicycle, for example, it accounts for more than 80% of the total force acting to slow the vehicle at speeds higher than 30 km/h [2].

I.1.1 Faired bikes

It's not though as over a century (from 1880s to 1980s) there hasn't been any interest in trying to make bicycles more aerodynamic. In fact, already in 1912, Etienne Bunau-Varilla of France patented a *streamlined enclosure for a bicycle and its rider* that was inspired by the shape of the first dirigible balloons [2]; meanwhile German bike manufacturers like Goericke and Brennabor let riders of their teams take part in races with *cloth-faired vehicles*. In the following years various faired bikes competed with each other, like in Berlin, in 1914, in a race between the Dutch world champion Piet Dickentman and the European champion Arthur Stellbrink from Berlin [3, 5].

Marcel Berthet demonstrated, at the age of 47, an upright bicycle with a fairing in 1933. At the time he wanted to be the first cyclist to break the *50 kilometers in one hour* barrier. He almost did it: on November 18, 1933 the measurement at the end of the hour showed 49.992 kilometers. His record was placed in a special category created by the UCI for "sport bicycles" with aerodynamic components. It's not clear though when the UCI banned the fairings from their competitions: some, like [3] seem to suggest that the ban came into effect on 1914 because of a mortal accident to Piet



Figure I.1.1: Faired bicycles in 1914

Dickentman who actually lived until 1950 though [5, 6]. It's possible that such a ban occurred in the mid 1930s like [5] suggests. There's a possibility that the right year is 1938, like written in [2] but in that article there's also written that in the same year also recumbent bicycles were banned, which doesn't clearly to be the case, as described in the next paragraph.

I.1.2 Recumbent bikes

Another important mention goes to Charles Mochet, who used to build small, very light cars before World War I. His wife had decided the common bicycle was far too dangerous for their son George, so Charles built him a pedal-driven four-wheeled vehicle. The 4-wheeler indeed reduced the danger of falling over and *proved to be exceedingly fast too*. This soon led to a demand for the vehicles and Charles Mochet ultimately decided to give up the building of automobiles and devote himself to the construction of HPV's. He built a two-seated, four-wheeled pedal-car for adults that he called "Vélocar". It turned out to be very fast, so much that, *at higher speeds, cornering got very dangerous*. Mochet then experimented and built a vehicle with three wheels, but its tendency towards falling over in curves was even worse than the four-wheeler [3].

Finally, in 1933, he decided to build *a two-wheeled version, in effect a recumbent bicycle* (figure I.1.2). In the same year, on this new prototype, Francis Faure *defeated every first-class track cyclist in Europe, taking advantage of recumbents' clear aerodynamic superiority*. The following year Faure was practically unbeatable in 5000 meter distance events. Even in races against three or four top riders, who would alternate pacing a leader, Faure would leave the Velodrome in the yellow jersey. Beside the successes on the track the Vélocars and their riders won a lot of road races too. Paul Morand, a road racer, won the Paris-Limoges in 1933 on a recumbent bike constructed by Mochet [3].

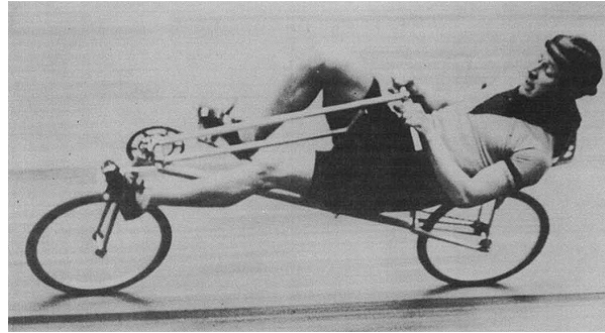


Figure I.1.2: Francis Faure on the Vélocar, in 1933

In the same year, as the UCI had already stated that *"The Vélocar has no add-on aerodynamic components attached so there is no reason to forbid it"*, Faure attempted and was able to establish a new hour record by riding 45,055 km in one hour (beating the 20 years old record of 44,247 km) [3].

Some though didn't welcome the record well and this brought to a hot debate on February 3, 1934, when the UCI designated a task force which would define, or in effect, re-define exactly what was or wasn't a bicycle. After a 58-to-46 vote, the following rules came in effect in UCI sanctioned racing:

- The bottom bracket had to be between 24 and 30 centimeters above the ground.
- The front of the saddle could only be 12 centimeters behind the bottom bracket.
- The distance from the bottom bracket to the axle of the front wheel had to be between 58 and 75 centimeters.

According to these rules, a recumbent wasn't a bicycle, despite having two wheels, a chain, handlebars, a seat, and human propulsion.

Faure's record was then shuffled into a new category called: "Records Set By Human Powered Vehicles (HPV's) without Special Aerodynamic Features". It's likely that this decision led to a decrease in popularity of recumbents; had the UCI decided otherwise, a lot more riders might be riding recumbent bicycles today [3].

I.1.3 Recumbent faired bikes

In 1938 Francis Faure and Georges Mochet (son of Charles) decided to try to better the record of Marcel Berthet in the special class. They produced a faired Vélocar with a modified frame: Faure sat lower and a smaller front wheel was installed to reduce drag (figure I.1.3). On March 5 1938, the eve of WWII, Francis Faure became the first cyclist to travel 50 kilometers in less than one hour without a pace vehicle. He rode 50.537 kilometers on the Vicennes Municipal Cycling Track. The press went wild, both in Europe and the U.S. Pictures of Francis Faure, Georges Mochet and the Vélocar appeared in all the bicycling journals [3].



Figure I.1.3: Francis Faure in the faired Vélocar, in 1938

I.1.4 IHPVA and WHPVA

It seems that after WWII the popularity of both recumbents and faired HPVs declined, until in 1976 the IHPVA (International Human Powered Vehicle Association) was born [7] and HPVs returned to compete. Later the association was reorganized and because of copyright issues today exist the IHPVA (american) and the WHPVA (with national organisations as members).

I.1.5 Handcycles

Handcycles are a type of land HPV that is powered by the arms only or by arms and torso, depending on the configuration. A very appreciated pro of these vehicles is that they can also be used by people who sustained spinal cord injuries or have incurred in the damage of one or both legs (amputation included).

I.1.5.1 Upright vs recumbent

On an handcycle, there are two typical riding positions: the upright, or kneeled, is typical of the competitions in H4-H5 categories while the supine, or recumbent, is used in H1-H2-H3 competitions [8, 9]. For amputated people it's more typical to ride in the knelt configuration (figure I.1.5) while paraplegics and tetraplegics don't have any choice but to ride in the recumbent position (figure I.1.4). As a matter of fact, the latter can't make use of the lower part of the back which is needed for the propulsion in the upright position, in which the cranks are also longer because the the rider can use his torso and not only his arms as a lever; with upright posture, cadences are typically lower though.

From an aerodynamic point of view, it's necessary to consider that the results could be very different depending on the cases. If it's true that, according to [10], an athlete in knelt aero position can achieve a drag coefficient 35% smaller than one in the recumbent, during the propulsive phase, the latter, may have a small advantage. If we consider a full faired vehicle, though, according to the simulations conducted by team Policumbent's aerodynamic division in 2019, the kneeled position is not an option

because it would generate a shape more similar to a bluff body than to a streamliner [11].



Figure I.1.4: Simone Chiarolla, riding in recumbent position



Figure I.1.5: Diego Colombari, riding in kneeling position

I.1.5.2 Delta vs Tadpole

Hancycles are usually 3-wheeled vehicles; hence, even though they are often referred as handbikes, they should be called *handtrikes*. As a matter of fact, since they are powered and handled by the same limbs, stability on a 2-wheeler would be critical. Depending on the position of the wheels, handtrikes are classified as:

- delta: with 1 wheel on the front and 2 one the rear
- tadpole: with 2 wheels on the front and 1 one the rear

The two configurations are very different in terms of mechanical design and realization. The most important difference concerns the fact that a delta handcycle has a single steering wheel, compared to the 2 of tadpoles. Another contrast of the two configurations stands in the driving wheel, which is on the front for deltas and typically on the rear for tadpoles. For the latter, front wheel drive could be possible with the use of a differential, but it's definitely not the standard construction. Concerning aerodynamics, if the vehicle is fully faired, delta loses dramatically, as will be shown later in the thesis (see chapter II.1).

I.1.6 Purpose and structure of the thesis

Student Team Policumbent, from Politecnico di Torino, has participated in both IHPVA and WHPVA since 2010. The purpose of this thesis is to show the design, construction and testing of handtrike prototype Cerberus, that was used in the 2022 WH-PSC (World Human Powered Speed Challenge) competition organized by IHPVA, and to give some advice and material to take into account for Team Policumbent's new projects and for all those who are interested in 3-wheeled HPVs.

In this first part of the thesis, after this brief introduction on land HPVs, Team Policumbent is presented along with its know-how and with some information on hand-cycles; then some stability studies and aerodynamic analysis on a first configuration are analyzed. Part II describes the design of the prototype as of September 2022. Part III shows some insight on the prototype construction, on the testing and on WHPSC 2022 race. Finally, appendix A shows a detailed bill of materials of Cerberus's mechanical components and appendix B contains the drawings of the most important subassemblies' parts.

A final note: this dissertation has been written by the author solely but it incorporates the work of many; some are explicitly cited throughout the thesis in the design procedure as the main designers of certain components or analysis, but many took also part in the design process to a lesser degree or have helped a lot in the assembly phase. Therefore, a huge thanks goes to all the people that contributed to this project and have helped to make it real.

Chapter I.2

On team Policumbent

I.2.1 Birth and history

Founded in 2009 by professor Cristiana Delprete and engineer Paolo Baldissera, Policumbent is a student team from *Politecnico di Torino* which aims to build very efficient land human-powered vehicles (HPV), specifically recumbent HPV. As a matter of fact, the name is a composition of the words *Politecnico*, recalling the name of the team's university, and *recumbent* which is a Latin word with the same meaning it has in English.

From the start, the team has had a dual soul: it was always charmed by the high speeds that recumbents vehicles can reach with little input power but many were also fascinated by the velomobiles and urban mobility. Therefore, as from 2009 to 2012 the team mainly developed recumbents for racing (figures I.2.1, I.2.2 and I.2.3), between 2013 and 2014 built S-Trike, a urban prototype (figure I.2.4). From 2014 onward, though, the main target of the team becomes the speed world record: in 2014-2015 PulaR was built and participated in both the 2015 and 2016 editions of WHPC, reaching a maximum speed of 126,90 km/h. In the meantime, a second 3-wheeler was built and raced in Belgium in 2015 (figure I.2.5). Then prototype Taurus took part in the same race from 2017 to 2019, on which Andrea Gallo reached a maximum speed of 136,49 km/h. Moreover, as the team was becoming bigger and bigger, in 2019 a twin prototype Taurus-X was built and Vittoria Spada rode it to 123,88 km/h the same year. 2020 the team doesn't race due to the virus pandemic but starts to work on two new prototypes: Phoenix and Cerberus, the latter being the first handcycle of the team as well as the object of this thesis. In 2021 Phoenix and Taurus-X take part in the European Speed Battle, an event organized by Team Policumbent itself, and in 2022 the team becomes the first to participate to the WHPSC with 3 prototypes (Taurus-X, Phoenix and Cerberus). The next project of the team might involve urban mobility once more, but it's not sure yet.

I.2.2 Know-how

During the years, in order to build the most efficient prototypes, the team has also delved into the research field, by:

- constructing a test bench for rolling resistance calculation
- developing new transmissions



Figure I.2.1: Team Policumbent's first prototype, C.O.R.A. (Cycling Optimized Recumbent Aeroshape)



Figure I.2.2: Team Policumbent's prototype COR-AL13



Figure I.2.3: Team Policumbent's first streamliner, Pulse



Figure I.2.4: Team Policumbent's velomobile S-Trike



Figure I.2.5: Team Policumbent's prototype LemonTrike



Figure I.2.6: Team Policumbent's prototype PulsarR



Figure I.2.7: Team Policumbent’s prototypes Taurus (left) and Taurus-X (right)

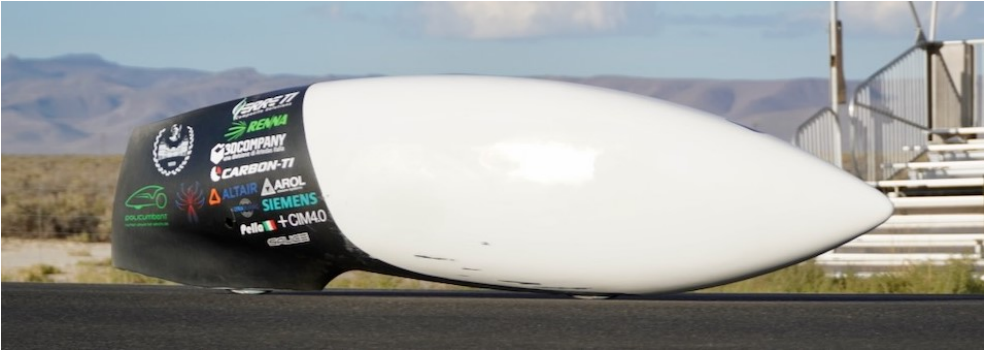


Figure I.2.8: Team Policumbent’s prototype Phoenix [13]



Figure I.2.9: Team Policumbent’s handtrike Cerberus[14]

- computing in-house scripts and methods for the CFD analysis of the prototypes' fairings
- developing codes for simulation and data analyses of the prototypes' runs in various conditions, including weather and altitude

In the following paragraphs, a brief insight on the first two points will be given.

I.2.2.1 Wheels test bench

From March 2019 to October 2020, one of the main activities of the author, in collaboration with teammate Anatolii Zahar has consisted in the experimental analysis of the rolling resistance of various clinchers and overall power absorption of complete wheel sets (each considered as hub, walls, rim, inner tube and clincher altogether) in order to define the best combination among the ones available and use it on newer prototypes.

On March 2019 a first exemplary [15] of the test bench had already been constructed but presented some acquisition problems, with generally high statistical dispersion at low speed.

So, during the following months, further improvement were made:

- the acquisition method was changed from strain gauges on the hub in horizontal direction to a commercial power meter fit in the drum's hub
- a static calibration of the drum was conducted by acquiring the row data generated by the sensors in the power meter over 8 points of the drum's circumference
- the minimum speed for the data acquisition was taken down from 45 km/h to 12 km/h

I.2.2.1.1 Latex vs butile inner tubes

These are the easiest tests to conduct, as it's sufficient to consider a complete wheel set, take measurements, change the tube and retake measurements.

In order to obtain a robust validation of the results, the tests were conducted on different wheels sets.

Latex was found to be faster, in accordance with the tests published on bicyclerollingresistance.com [18, 19, 20].

I.2.2.1.2 Aerodynamics and bearings' dissipation

In order to acquire absolute data in term of dissipation induced by different clinchers, the aerodynamic and internal dissipation of the groups composed by hub and spokes (or disc walls) were measured.

As expected, disc wheels resulted as more aero than the spoked ones. The 3 spoked design came in second place, closer to the disc version than to the 28 and 32 spokes ones.

The data were acquired by connecting the hub to a motor powered by a voltage generator. The power was calculated by reading the values of current and voltage and taking into account the motor's efficiency.

For the determination of the power consumption of the drum, instead, the power meter located inside the hub was used.

I.2.2.1.3 Clinchers

Lastly, tyre compounds were compared by their C_{rr} (rolling resistance coefficient) defined as:

$$C_{rr} = \frac{F_{rr}}{N} \quad (\text{I.2.1})$$

where F_{rr} is the tangential resisting force and N is the normal force, perpendicular to the surface of contact with the wheel[15, 16, 17].

Concerning the test bench, N is known and equal to the load applied on the wheel (i.e. the weight $m \cdot g$), while F_{rr} was calculated as follows.

All the measurements were conducted in a steady-state condition, i.e. at constant angular speed. Therefore, it's safe to assume that the motor's increment in power ΔP_{motor} happens due to:

- aerodynamic dissipation P_{aero}
- bearings friction $P_{bearings}$
- rolling resistance P_{rr}

so it's possible to obtain the last by difference. Hence:

$$P_{rr} = \Delta P_{motor} - P_{aero\&bearings}$$

note that the equation is written with the compact term $P_{aero\&bearings}$ because the two terms were calculated together, as just specified in the last paragraph.

Finally, the rolling resistance force can be expressed as:

$$F_{rr} = \frac{P_{rr}}{\omega \cdot R}$$

and equation I.2.1 can be rewritten as:

$$C_{rr} = \frac{\Delta P_{motor} - P_{aero\&bearings}}{\omega \cdot R \cdot m \cdot g}$$

I.2.2.1.4 Conclusions

Since:

- the data acquired showed that some 20" clinchers perform as good as, if not better than, the best 28" (700x C) clinchers tested
- and because of the measured aerodynamic advantage of a smaller wheels (which also allow to design a smaller fairing)
- latex resulted more efficient than butile
- the team had already produced its own 20" (E.T.R.T.O. 406-20) disc wheels and therefore molds could be reused

E.T.R.T.O. 406-20 disc wheels equipped with latex inner tubes were chosen for this project.



Figure I.2.10: Prototype Taurus's patented gear shifting system

I.2.2.2 Moving sprocket pack

In order to make the drivetrain as efficient as possible, since the design of *Taurus* back in 2017, the team has always constructed prototypes with a moving cassette (figure I.2.10). This ensures that the chain is always aligned with the 2 wheels, hence avoiding the losses of power resulting from the deformations and friction induced by a non aligned chain.

I.2.2.3 Safety

Team Policumbent's first objective is the safety of the riders. Only after this factor is ensured the prototypes are allowed to be tested and to try to go fast.

I.2.2.3.1 Fairing construction

Over the years, high speed crashes have happened both during testing and competitions but, thanks to the studies conducted and to the know-how acquired with time, the Team's vehicles have proven to be quite safe. Amongst the most spectacular incidents stand out:

- Battle Mountain on September 2019: due to a pinch flat that occurred at over 100 km/h, Taurus-X overturned a few time then turned on a side of the fairing and continued to slide for a few meters before finally coming to a stop. Vittoria came out of from the prototype with a burnt elbow, which had scratched on the inside of the fairing, and a bruise on an shoulder, which had hit the roll cage.
- Balocco, during the European Speed Battle on October 24th, 2021: due to a screw of the rear fork that had loosened a bit over time, probably a bump (or a gust of lateral wind, it was not clear) caused the rear wheel to move of a few



Figure I.2.11: Vittoria Spada, rider of Taurus X, standing unharmed with the prototype's fairing in her hand after a crash at 70 km/h

millimeters and take its clincher in contact with the wheel cover, causing an unexpected brake and pulling the vehicle into an unstable condition. Taurus-X therefore crashed at about 70 km/h over the cement jersey barrier and slid on the asphalt. While the fairing was scratched and partially delaminated on a few areas, Vittoria was safely extracted from the prototype with nothing but a scratch on a hand (figure I.2.11).

I.2.2.3.2 Dual vision system

Since 2016, all the running prototypes of Team Policumbent have had a double vision system. This ensures that the pilot is able to see the road, even if a damage occurs to one circuit. Specifically:

- Pulsar mounted a single camera and a monitor while it was possible to see directly through the front fairing in plexiglass too. Later a double system of digital cameras and monitors on independent circuits was introduced
- Taurus used a double digital cameras vision system
- Taurus-X started with a double digital camera vision system and at the moment uses a digital camera on the main circuit and an analog one on the backup circuit
- Phoenix started with a double analog camera vision system and at the moment uses the same system mounted on Taurus-X

Chapter I.3

Simple stability model of a delta handcycle

I.3.1 Overturning condition

Overturning condition is a dramatic event that has to be avoided at any cost. Even though the team's vehicles are fairly safe, as reported in section I.2.2.3, an overturn could damage pretty badly the fairing and other components of the prototype.

As Team Policumbent's vehicles run on straight or at most over parabolic roads, the overturning condition should be a rare event and as a matter of fact, as shown further in the chapter, there is a huge safety margin with the considered geometry.

I.3.1.1 Hypotheses, parameters and equations

Figure I.3.1 shows the free body diagram of a balanced trike (i.e. the centre of gravity CG of the suspended mass is located on the symmetry axis of the fairing) traveling on a corner in a steady state condition (i.e. it moves with a constant angular speed) and is therefore solely subject to:

- weight
- centrifugal force
- vincular reactions

In our case, there are no suspensions so $\phi \simeq 0$ therefore the centre of gravity is always located at $y = 0$.

The critical condition of overturning, shown in figure I.3.2 for a left turn, happens when only the external rear wheel and the front one support the weight; therefore the overturning axis is the one that virtually connects those two wheels through the ground.

Writing the torque equilibrium around the overturning axis, one has:

$$mg \cdot b = ma_{y_{max}} \cdot h_{cg}$$

which means that the maximum lateral acceleration is:

$$a_{y_{max}} = g \cdot \frac{b}{h_{cg}} \tag{I.3.1}$$

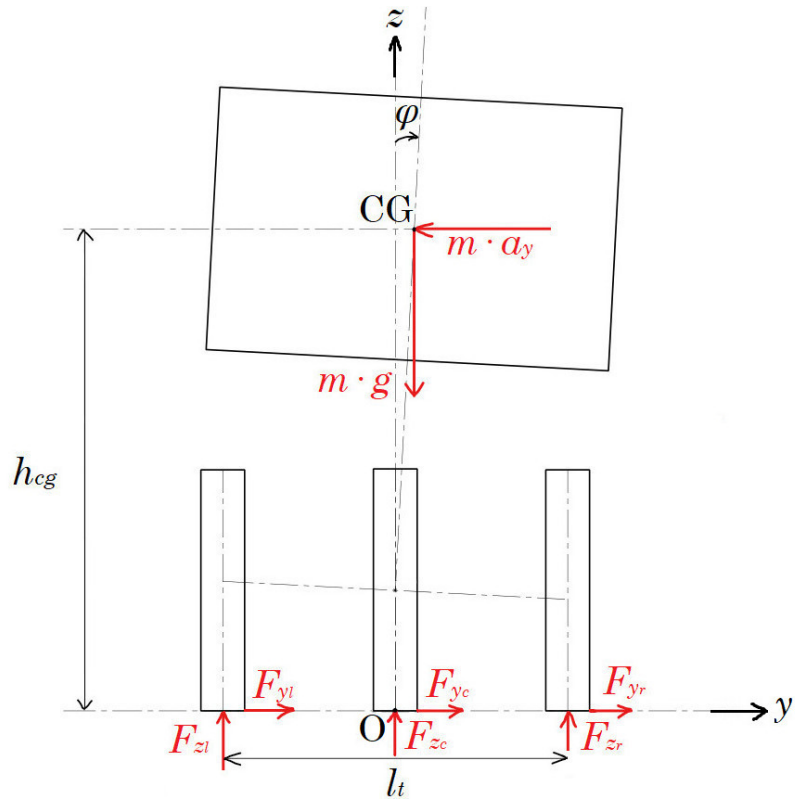


Figure I.3.1: Free body diagram (front view) of a cornering trike

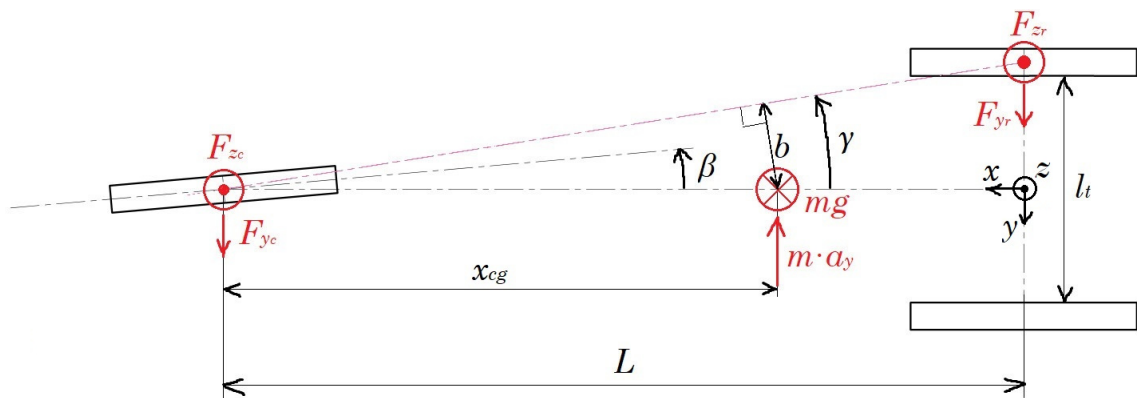


Figure I.3.2: Free body diagram (top view) of an overturning trike

where the parameter b is the lever arm of the weight and depends on the centre of gravity longitudinal position x_{cg} in figure I.3.2 (i.e. depends on the weight distribution) and can be geometrically deduced as follows:

$$\begin{cases} b = x_{cg} \cdot \sin(\gamma) \\ \gamma = \arctan\left(\frac{l_t}{2L}\right) \end{cases}$$

therefore, one has:

$$b = x_{cg} \cdot \sin\left(\arctan\left(\frac{l_t}{2L}\right)\right)$$

Now, substituting b in equation (I.3.1), the maximum lateral acceleration can be expressed as a function of 2 important geometrical parameters of the frame and the position of the centre of gravity:

$$a_{y_{max}} = g \cdot \frac{x_{cg}}{h_{cg}} \cdot \sin\left(\arctan\left(\frac{l_t}{2L}\right)\right)$$

In pure kinematic condition, though a_y coincides with the centripetal acceleration, which is a function of the curvature radius R as:

$$a_{y_{max}} = \frac{v_{max}^2}{R}$$

Therefore, under these assumptions, the vehicle doesn't overturn over a flat turn of radius R if the speed is at most:

$$v_{max} = \sqrt{a_{y_{max}} \cdot R} = \sqrt{g \cdot \frac{x_{cg}}{h_{cg}} \cdot \sin\left(\arctan\left(\frac{l_t}{2L}\right)\right) \cdot R}$$

Given that the curvature radius is way bigger than the length of the vehicle, it's possible to define

$$R \simeq \frac{L}{\sin(\beta)}$$

hence:

$$v_{max} = \sqrt{g \cdot \frac{x_{cg}}{h_{cg}} \cdot \sin\left(\arctan\left(\frac{l_t}{2L}\right)\right) \cdot \frac{L}{\sin(\beta)}} \quad (\text{I.3.2})$$

where β is the steering angle projected to the ground (see figure I.3.2).

Rearranging and separating the various terms, equation (I.3.2) can be rewritten as:

$$v_{max} = \sqrt{g} \cdot \sqrt{\frac{x_{cg}}{h_{cg}}} \cdot \sqrt{L \cdot \sin\left(\arctan\left(\frac{l_t}{2L}\right)\right)} \cdot \sqrt{\frac{1}{\sin(\beta)}} \quad (\text{I.3.3})$$

This last rearrangement of the formula highlights the dependence of the maximum speed from:

- the constant \sqrt{g}
- the weight distribution $\sqrt{\frac{x_{cg}}{h_{cg}}}$
- the frame geometry $\sqrt{L \cdot \sin\left(\arctan\left(\frac{l_t}{2L}\right)\right)}$
- the steering angle $\sqrt{\frac{1}{\sin(\beta)}}$

I.3.1.2 Values and variation ranges of the parameters

Now that the equations are finally rewritten in a way that takes into account the intended parameters, it's necessary to impose the variability ranges in order to study their influence over the stability of the vehicle.

Concerning the weight distribution, the h_{cg} parameter was set at a fixed value of 0,4 m which is higher than the final expected value of the centre of gravity of the prototype. As a matter of fact, the height of the handcycle was thought to fall in a range of 750 mm to 850 mm but the bottom part of the fairing was expected to be heavier and the pilot was anticipated to stay above 400 mm from the ground with only the head and, depending on the phase of propulsion, the upper limbs. The overestimation of the h_{cg} gives us a certain safety factor on the rollover condition.

The x_{cg} was the most difficult parameter to define, as no part of the prototype existed yet. It was therefore decided that a new parameter k_{cg} , inversely proportional to L , be introduced. This way, it's possible to express the position x_{cg} as a fraction of the wheelbase:

$$x_{cg} = k_{cg} \cdot L$$

The value given to x_{cg} was 0,5; i.e. the centre of mass was set at the centre of the wheelbase since it wasn't possible to define an accurate location.

Regarding the frame geometry, in order to have the possibility to make an aerodynamic fairing, the study was conducted with a track that varied from as little as 300 mm up to 400 mm * **which are certainly small values in comparison with those of regular handcycles, [add source]** * whilst the wheelbase was analyzed over the broad that goes from 1100 mm to 1700 mm range.

Lastly, the steering angle β was initially set between $0,1^\circ$ and 7° in order to observe an ample range of curvature radii, but what really interests us in this analysis are steering angles up to $0,7^\circ$ as the prototype never runs in places with turns of less than 150 m in radius. For the design of vehicles that should run on public roads, though, an accurate analysis on sharper turns should be conducted.

I.3.1.3 Results and comments

The results of the study are displayed hereafter. Note that the following tables also include the control parameter of the critical lateral acceleration $a_{y_{max}}$, which we don't want to be bigger than $4,5 \text{ m/s}^2$ (less than $1/2 g$) as not to bother the rider too much.

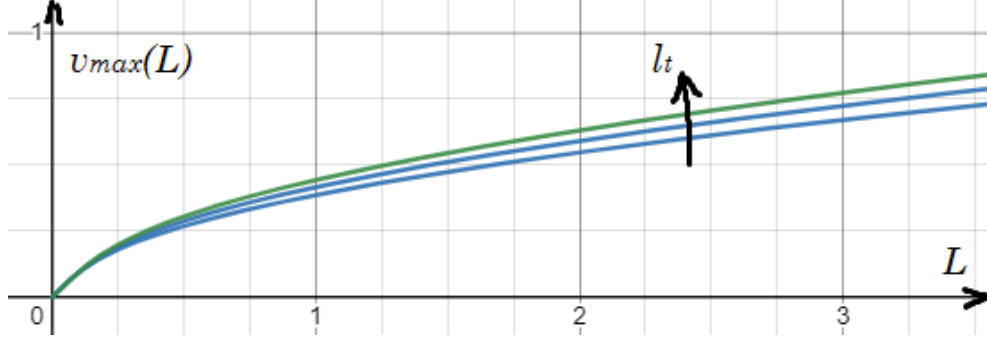


Figure I.3.3: Shape of the function $v_{max}(L)$. Graph drawn with the constant value set at 1 and $l_t = \{0, 3; 0, 35; 0, 4\}$

As shown in all the tables from I.3.1 to I.3.21, the maximum acceleration is always acceptable (highest value is $2,436 \text{ m/s}^2$ for $l_t = 0, 4$ and $L = 1, 7 \text{ m}$).

By looking at these table, it's possible to extract some interesting information:

- first of all, it's clear that both an increase in L and l_t makes the trike more stable. If the second was to be expected and is more intuitive for many people since it make the overturning axis more tilted, the former has a simple explanation if we take into account the fact that k_{cg} was set at a constant value of 0,5. This means that, as we make the wheelbase longer, we are assuming that the centre of mass moves from the front wheel and increases the lever arm b . Mathematically, this is visible by taking into account equation (I.3.3). By writing k_{cg} in function of L , it becomes:

$$\begin{aligned} v_{max} &= \sqrt{g} \cdot \sqrt{\frac{k_{cg}}{h_{cg}}} \cdot L \sqrt{\sin\left(\arctan\left(\frac{l_t}{2L}\right)\right)} \cdot \sqrt{\frac{1}{\sin(\beta)}} = \\ &= \text{const} \cdot L \sqrt{\sin\left(\arctan\left(\frac{l_t}{2L}\right)\right)} \cdot \sqrt{\frac{1}{\sin(\beta)}} \end{aligned}$$

and, for a fixed angle β , is simply

$$v_{max} = \text{const} \cdot L \sqrt{\sin\left(\arctan\left(\frac{l_t}{2L}\right)\right)} \quad (\text{I.3.4})$$

hence we have a function that, looking at the parameter L , has a predominant linear characteristic that is disturbed by the square root of an inversely proportional function embedded in 2 limited functions; hence, for positive values of l_t (which is our case) increasing L results in an increase of v_{max} . Figure I.3.3 shows the shape of the function $v_{max}(L)$ at eq. (I.3.4).

- An interesting discovery that comes from the analysis of these tables is that the wider the track is, the higher is the lateral acceleration that has to be generated to fall into a critical condition at the same speed (compare tab. I.3.3 with tab. I.3.8, tab. I.3.4 with tab. I.3.9, tab. I.3.5 with tab. I.3.10, tab. I.3.6 with tab. I.3.11 and tab. I.3.16, tab. I.3.7 with tab. I.3.12 for instance); conversely this means that it's possible to ride over sharper turn without overturning.

Constants		Sets			Results			Control parameter
$\frac{h_{cg}}{m}$	k_{cg}	$\frac{l_t}{m}$	$\frac{L}{m}$	$\frac{\beta}{deg}$	$\frac{R}{m}$	$\frac{v_{max}}{m/s}$	$\frac{v_{max}}{km/h}$	$\frac{a_{y_{max}}}{m/s^2}$
0,4	0,5	0,3	1,1	0,1	630,25	33,89	122,01	1,823
				0,2	315,13	23,97	86,27	
				0,3	210,09	19,57	70,44	
				0,4	157,56	16,95	61,01	
				0,5	126,05	15,16	54,56	
				0,6	105,04	13,84	49,81	
				0,7	90,04	12,81	46,12	

Table I.3.1: Overtuning condition analysis with a track of 300 mm and a wheelbase of 1,1 m; centre of mass located at half the wheelbase and height of 400 mm from the ground

Constants		Sets			Results			Control parameter
$\frac{h_{cg}}{m}$	k_{cg}	$\frac{l_t}{m}$	$\frac{L}{m}$	$\frac{\beta}{deg}$	$\frac{R}{m}$	$\frac{v_{max}}{m/s}$	$\frac{v_{max}}{km/h}$	$\frac{a_{y_{max}}}{m/s^2}$
0,4	0,5	0,3	1,2	0,1	687,55	35,42	127,53	1,825
				0,2	343,78	25,05	90,18	
				0,3	229,18	20,45	73,63	
				0,4	171,89	17,71	63,76	
				0,5	137,51	15,84	57,03	
				0,6	114,59	14,46	52,06	
				0,7	98,22	13,39	48,20	

Table I.3.2: Overtuning condition analysis with a track of 300 mm and a wheelbase of 1,2 m; centre of mass located at half the wheelbase and height of 400 mm from the ground

- Now, concerning the cornering radius, since R was calculated as a function inversely proportional to the wheelbase length, it's clear that the radiuses calculated in table I.3.1 are the same that are shown in tab. I.3.8 and tab. I.3.15 (and likewise for the other 6 table triplets). Thanks to this it's possible to take a better look at the last relation discussed (i.e. the same turn can be tackled at a higher speed with a larger track).

Constants		Sets			Results			Control parameter
$\frac{h_{cg}}{m}$	k_{cg}	$\frac{l_t}{m}$	$\frac{L}{m}$	$\frac{\beta}{deg}$	$\frac{R}{m}$	$\frac{v_{max}}{m/s}$	$\frac{v_{max}}{km/h}$	$\frac{a_{y_{max}}}{m/s^2}$
0,4	0,5	0,3	1,3	0,1	744,85	36,89	132,81	1,827
				0,2	372,42	26,09	93,91	
				0,3	248,28	21,30	76,68	
				0,4	186,21	18,45	66,41	
				0,5	148,97	16,50	59,40	
				0,6	124,14	15,06	54,22	
				0,7	106,41	13,94	50,20	

Table I.3.3: Overturning condition analysis with a track of 300 mm and a wheelbase of 1,3 m; centre of mass located at half the wheelbase and height of 400 mm from the ground

Constants		Sets			Results			Control parameter
$\frac{h_{cg}}{m}$	k_{cg}	$\frac{l_t}{m}$	$\frac{L}{m}$	$\frac{\beta}{deg}$	$\frac{R}{m}$	$\frac{v_{max}}{m/s}$	$\frac{v_{max}}{km/h}$	$\frac{a_{y_{max}}}{m/s^2}$
0,4	0,5	0,3	1,4	0,1	802,14	38,30	137,89	1,829
				0,2	401,07	27,08	97,50	
				0,3	267,38	22,11	79,61	
				0,4	200,54	19,15	68,94	
				0,5	160,43	17,13	61,67	
				0,6	133,69	15,64	56,29	
				0,7	114,59	14,48	52,12	

Table I.3.4: Overturning condition analysis with a track of 300 mm and a wheelbase of 1,4 m; centre of mass located at half the wheelbase and height of 400 mm from the ground

Constants		Sets			Results			Control parameter
$\frac{h_{cg}}{m}$	k_{cg}	$\frac{l_t}{m}$	$\frac{L}{m}$	$\frac{\beta}{deg}$	$\frac{R}{m}$	$\frac{v_{max}}{m/s}$	$\frac{v_{max}}{km/h}$	$\frac{a_{y_{max}}}{m/s^2}$
0,4	0,5	0,3	1,5	0,1	859,44	39,66	142,78	1,830
				0,2	429,72	28,04	100,96	
				0,3	286,48	22,90	82,43	
				0,4	214,86	19,83	71,39	
				0,5	171,89	17,74	63,85	
				0,6	143,24	16,19	58,29	
				0,7	122,78	14,99	53,97	

Table I.3.5: Overturning condition analysis with a track of 300 mm and a wheelbase of 1,5 m; centre of mass located at half the wheelbase and height of 400 mm from the ground

Constants		Sets			Results			Control parameter
$\frac{h_{cg}}{m}$	k_{cg}	$\frac{l_t}{m}$	$\frac{L}{m}$	$\frac{\beta}{deg}$	$\frac{R}{m}$	$\frac{v_{max}}{m/s}$	$\frac{v_{max}}{km/h}$	$\frac{a_{y_{max}}}{m/s^2}$
0,4	0,5	0,3	1,6	0,1	916,73	40,97	147,51	1,831
				0,2	458,37	28,97	104,30	
				0,3	305,58	23,66	85,16	
				0,4	229,18	20,49	73,75	
				0,5	183,35	18,32	65,97	
				0,6	152,79	16,73	60,22	
				0,7	130,97	15,49	55,75	

Table I.3.6: Overtuning condition analysis with a track of 300 mm and a wheelbase of 1,6 m; centre of mass located at half the wheelbase and height of 400 mm from the ground

Constants		Sets			Results			Control parameter
$\frac{h_{cg}}{m}$	k_{cg}	$\frac{l_t}{m}$	$\frac{L}{m}$	$\frac{\beta}{deg}$	$\frac{R}{m}$	$\frac{v_{max}}{m/s}$	$\frac{v_{max}}{km/h}$	$\frac{a_{y_{max}}}{m/s^2}$
0,4	0,5	0,3	1,7	0,1	974,03	42,25	152,08	1,832
				0,2	487,02	29,87	107,54	
				0,3	324,68	24,39	87,81	
				0,4	243,51	21,12	76,04	
				0,5	194,81	18,89	68,01	
				0,6	162,34	17,25	62,09	
				0,7	139,15	15,97	57,48	

Table I.3.7: Overtuning condition analysis with a track of 300 mm and a wheelbase of 1,7 m; centre of mass located at half the wheelbase and height of 400 mm from the ground

Constants		Sets			Results			Control parameter
$\frac{h_{cg}}{m}$	k_{cg}	$\frac{l_t}{m}$	$\frac{L}{m}$	$\frac{\beta}{deg}$	$\frac{R}{m}$	$\frac{v_{max}}{m/s}$	$\frac{v_{max}}{km/h}$	$\frac{a_{y_{max}}}{m/s^2}$
0,4	0,5	0,35	1,1	0,1	630,25	36,55	131,57	2,119
				0,2	315,13	25,84	93,03	
				0,3	210,09	21,10	75,96	
				0,4	157,56	18,27	65,78	
				0,5	126,05	16,34	58,84	
				0,6	105,04	14,92	53,71	
				0,7	90,04	13,81	49,73	

Table I.3.8: Overtuning condition analysis with a track of 350 mm and a wheelbase of 1,1 m; centre of mass located at half the wheelbase and height of 400 mm from the ground

Constants		Sets			Results			Control parameter
$\frac{h_{cg}}{m}$	k_{cg}	$\frac{l_t}{m}$	$\frac{L}{m}$	$\frac{\beta}{deg}$	$\frac{R}{m}$	$\frac{v_{max}}{m/s}$	$\frac{v_{max}}{km/h}$	$\frac{a_{y_{max}}}{m/s^2}$
0,4	0,5	0,35	1,2	0,1	687,55	38,21	137,56	2,12
				0,2	343,78	27,02	97,27	
				0,3	229,18	22,06	79,42	
				0,4	171,89	19,11	68,78	
				0,5	137,51	17,09	61,52	
				0,6	114,59	15,60	56,16	
				0,7	98,22	14,44	51,99	

Table I.3.9: Overturning condition analysis with a track of 350 mm and a wheelbase of 1,2 m; centre of mass located at half the wheelbase and height of 400 mm from the ground

Constants		Sets			Results			Control parameter
$\frac{h_{cg}}{m}$	k_{cg}	$\frac{l_t}{m}$	$\frac{L}{m}$	$\frac{\beta}{deg}$	$\frac{R}{m}$	$\frac{v_{max}}{m/s}$	$\frac{v_{max}}{km/h}$	$\frac{a_{y_{max}}}{m/s^2}$
0,4	0,5	0,35	1,3	0,1	744,85	39,80	143,28	2,127
				0,2	372,42	28,14	101,32	
				0,3	248,28	22,98	82,72	
				0,4	186,21	19,90	71,64	
				0,5	148,97	17,80	64,08	
				0,6	124,14	16,25	58,50	
				0,7	106,41	15,04	54,16	

Table I.3.10: Overturning condition analysis with a track of 350 mm and a wheelbase of 1,3 m; centre of mass located at half the wheelbase and height of 400 mm from the ground

Constants		Sets			Results			Control parameter
$\frac{h_{cg}}{m}$	k_{cg}	$\frac{l_t}{m}$	$\frac{L}{m}$	$\frac{\beta}{deg}$	$\frac{R}{m}$	$\frac{v_{max}}{m/s}$	$\frac{v_{max}}{km/h}$	$\frac{a_{y_{max}}}{m/s^2}$
0,4	0,5	0,35	1,4	0,1	802,14	41,33	148,78	2,129
				0,2	401,07	29,22	105,21	
				0,3	267,38	23,86	85,90	
				0,4	200,54	20,66	74,39	
				0,5	160,43	18,48	66,54	
				0,6	133,69	16,87	60,74	
				0,7	114,59	15,62	56,24	

Table I.3.11: Overturning condition analysis with a track of 350 mm and a wheelbase of 1,4 m; centre of mass located at half the wheelbase and height of 400 mm from the ground

Constants		Sets			Results			Control parameter
$\frac{h_{cg}}{m}$	k_{cg}	$\frac{l_t}{m}$	$\frac{L}{m}$	$\frac{\beta}{deg}$	$\frac{R}{m}$	$\frac{v_{max}}{m/s}$	$\frac{v_{max}}{km/h}$	$\frac{a_{y_{max}}}{m/s^2}$
0,4	0,5	0,35	1,5	0,1	859,44	42,80	154,08	2,131
				0,2	429,72	30,26	108,95	
				0,3	286,48	24,71	88,96	
				0,4	214,86	21,40	77,04	
				0,5	171,89	19,14	68,91	
				0,6	143,24	17,47	62,90	
				0,7	122,78	16,18	58,24	

Table I.3.12: Overtuning condition analysis with a track of 350 mm and a wheelbase of 1,5 m; centre of mass located at half the wheelbase and height of 400 mm from the ground

Constants		Sets			Results			Control parameter
$\frac{h_{cg}}{m}$	k_{cg}	$\frac{l_t}{m}$	$\frac{L}{m}$	$\frac{\beta}{deg}$	$\frac{R}{m}$	$\frac{v_{max}}{m/s}$	$\frac{v_{max}}{km/h}$	$\frac{a_{y_{max}}}{m/s^2}$
0,4	0,5	0,35	1,6	0,1	916,73	44,22	159,20	2,133
				0,2	458,37	31,27	112,57	
				0,3	305,58	25,53	91,91	
				0,4	229,18	22,11	79,60	
				0,5	183,35	19,78	71,20	
				0,6	152,79	18,05	64,99	
				0,7	130,97	16,71	60,17	

Table I.3.13: Overtuning condition analysis with a track of 350 mm and a wheelbase of 1,6 m; centre of mass located at half the wheelbase and height of 400 mm from the ground

Constants		Sets			Results			Control parameter
$\frac{h_{cg}}{m}$	k_{cg}	$\frac{l_t}{m}$	$\frac{L}{m}$	$\frac{\beta}{deg}$	$\frac{R}{m}$	$\frac{v_{max}}{m/s}$	$\frac{v_{max}}{km/h}$	$\frac{a_{y_{max}}}{m/s^2}$
0,4	0,5	0,35	1,7	0,1	974,03	45,60	164,15	2,135
				0,2	487,02	32,24	116,07	
				0,3	324,68	26,33	94,77	
				0,4	243,51	22,80	82,08	
				0,5	194,81	20,39	73,41	
				0,6	162,34	18,62	67,02	
				0,7	139,15	17,23	62,05	

Table I.3.14: Overtuning condition analysis with a track of 350 mm and a wheelbase of 1,7 m; centre of mass located at half the wheelbase and height of 400 mm from the ground

Constants		Sets			Results			Control parameter
$\frac{h_{cg}}{m}$	k_{cg}	$\frac{l_t}{m}$	$\frac{L}{m}$	$\frac{\beta}{deg}$	$\frac{R}{m}$	$\frac{v_{max}}{m/s}$	$\frac{v_{max}}{km/h}$	$\frac{a_{y_{max}}}{m/s^2}$
0,4	0,5	0,4	1,1	0,1	630,25	39,00	140,39	2,413
				0,2	315,13	27,58	99,27	
				0,3	210,09	22,51	81,05	
				0,4	157,56	19,50	70,19	
				0,5	126,05	17,44	62,78	
				0,6	105,04	15,92	57,31	
				0,7	90,04	14,74	53,06	

Table I.3.15: Overturning condition analysis with a track of 400 mm and a wheelbase of 1,1 m; centre of mass located at half the wheelbase and height of 400 mm from the ground

Constants		Sets			Results			Control parameter
$\frac{h_{cg}}{m}$	k_{cg}	$\frac{l_t}{m}$	$\frac{L}{m}$	$\frac{\beta}{deg}$	$\frac{R}{m}$	$\frac{v_{max}}{m/s}$	$\frac{v_{max}}{km/h}$	$\frac{a_{y_{max}}}{m/s^2}$
0,4	0,5	0,4	1,2	0,1	687,55	40,78	146,82	2,419
				0,2	343,78	28,84	103,82	
				0,3	229,18	23,55	84,77	
				0,4	171,89	20,39	73,41	
				0,5	137,51	18,24	65,66	
				0,6	114,59	16,65	59,94	
				0,7	98,22	15,41	55,49	

Table I.3.16: Overturning condition analysis with a track of 400 mm and a wheelbase of 1,2 m; centre of mass located at half the wheelbase and height of 400 mm from the ground

Constants		Sets			Results			Control parameter
$\frac{h_{cg}}{m}$	k_{cg}	$\frac{l_t}{m}$	$\frac{L}{m}$	$\frac{\beta}{deg}$	$\frac{R}{m}$	$\frac{v_{max}}{m/s}$	$\frac{v_{max}}{km/h}$	$\frac{a_{y_{max}}}{m/s^2}$
0,4	0,5	0,4	1,3	0,1	744,85	42,49	152,97	2,424
				0,2	372,42	30,05	108,16	
				0,3	248,28	24,53	88,32	
				0,4	186,21	21,25	76,48	
				0,5	148,97	19,00	68,41	
				0,6	124,14	17,35	62,45	
				0,7	106,41	16,06	57,82	

Table I.3.17: Overturning condition analysis with a track of 400 mm and a wheelbase of 1,3 m; centre of mass located at half the wheelbase and height of 400 mm from the ground

Constants		Sets			Results			Control parameter
$\frac{h_{cg}}{m}$	k_{cg}	$\frac{l_t}{m}$	$\frac{L}{m}$	$\frac{\beta}{deg}$	$\frac{R}{m}$	$\frac{v_{max}}{m/s}$	$\frac{v_{max}}{km/h}$	$\frac{a_{y_{max}}}{m/s^2}$
0,4	0,5	0,4	1,4	0,1	802,14	44,13	158,87	2,428
				0,2	401,07	31,20	112,34	
				0,3	267,38	25,48	91,72	
				0,4	200,54	22,07	79,43	
				0,5	160,43	19,74	71,05	
				0,6	133,69	18,02	64,86	
				0,7	114,59	16,68	60,05	

Table I.3.18: Overtuning condition analysis with a track of 400 mm and a wheelbase of 1,4 m; centre of mass located at half the wheelbase and height of 400 mm from the ground

Constants		Sets			Results			Control parameter
$\frac{h_{cg}}{m}$	k_{cg}	$\frac{l_t}{m}$	$\frac{L}{m}$	$\frac{\beta}{deg}$	$\frac{R}{m}$	$\frac{v_{max}}{m/s}$	$\frac{v_{max}}{km/h}$	$\frac{a_{y_{max}}}{m/s^2}$
0,4	0,5	0,4	1,5	0,1	859,44	45,71	164,55	2,431
				0,2	429,72	32,32	116,36	
				0,3	286,48	26,39	95,00	
				0,4	214,86	22,85	82,28	
				0,5	171,89	20,44	73,59	
				0,6	143,24	18,66	67,18	
				0,7	122,78	17,28	62,20	

Table I.3.19: Overtuning condition analysis with a track of 400 mm and a wheelbase of 1,5 m; centre of mass located at half the wheelbase and height of 400 mm from the ground

Constants		Sets			Results			Control parameter
$\frac{h_{cg}}{m}$	k_{cg}	$\frac{l_t}{m}$	$\frac{L}{m}$	$\frac{\beta}{deg}$	$\frac{R}{m}$	$\frac{v_{max}}{m/s}$	$\frac{v_{max}}{km/h}$	$\frac{a_{y_{max}}}{m/s^2}$
0,4	0,5	0,4	1,6	0,1	916,73	47,23	170,04	2,434
				0,2	458,37	33,40	120,23	
				0,3	305,58	27,27	98,17	
				0,4	229,18	23,62	85,02	
				0,5	183,35	21,12	76,04	
				0,6	152,79	19,28	69,42	
				0,7	130,97	17,85	64,27	

Table I.3.20: Overtuning condition analysis with a track of 400 mm and a wheelbase of 1,6 m; centre of mass located at half the wheelbase and height of 400 mm from the ground

Constants		Sets			Results			Control parameter
$\frac{h_{cg}}{m}$	k_{cg}	$\frac{l_t}{m}$	$\frac{L}{m}$	$\frac{\beta}{deg}$	$\frac{R}{m}$	$\frac{v_{max}}{m/s}$	$\frac{v_{max}}{km/h}$	$\frac{a_{y_{max}}}{m/s^2}$
0,4	0,5	0,4	1,7	0,1	974,03	48,71	175,35	2,436
				0,2	487,02	34,44	123,99	
				0,3	324,68	28,12	101,24	
				0,4	243,51	24,35	87,67	
				0,5	194,81	21,78	78,42	
				0,6	162,34	19,89	71,59	
				0,7	139,15	18,41	66,28	

Table I.3.21: Overturning condition analysis with a track of 400 mm and a wheelbase of 1,7 m; centre of mass located at half the wheelbase and height of 400 mm from the ground

I.3.1.4 Additional parameter: camber influence

After this general analysis was finished, it was decided that an analysis on how much the camber angle presence (figure I.3.4) would influence the vehicle's stability be conducted as well. The aforementioned model is very simply adaptable to this new parameter by modifying the definition of lever arm b . As a matter of fact, the effect of a negative camber δ is that of a virtual widening of the track projection on the ground, resulting in a more stable vehicle while cornering.

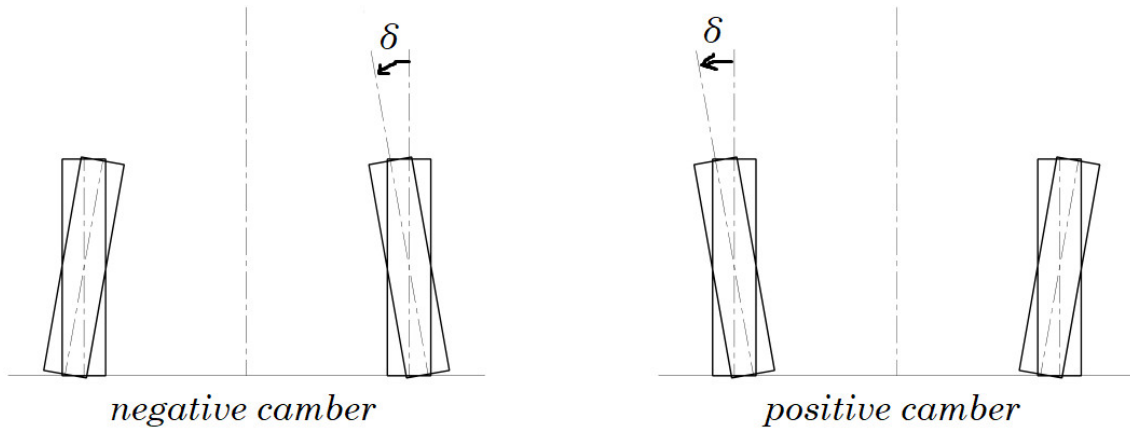


Figure I.3.4: Definition of positive and negative camber

So, with the addition of this new parameter, the lever arm definition becomes:

$$b = x_{cg} \cdot \sin(\gamma) - \frac{D_{wheel}}{2} \cdot \sin(\delta)$$

As shown in table I.3.22, in a pure kinematic condition, a -5° camber would allow to tackle a flat turn with a 9,9% increment in speed (from 71,05 km/h to 78,05 km/h) with a 20,7% increment in lateral acceleration (from 2,428 m/s² to 2,930 m/s²).

The application of a camber angle to a wheel that is advancing in a longitudinal direction, though, determines the birth of tangential shear reactions with non null resultant [16].

Constants		Sets				Results			Control parameter
$\frac{h_{cg}}{m}$	k_{cg}	$\frac{l_t}{m}$	$\frac{L}{m}$	$\frac{\beta}{deg}$	$\frac{\delta}{deg}$	$\frac{R}{m}$	$\frac{v_{max}}{m/s}$	$\frac{v_{max}}{km/h}$	$\frac{a_{y_{max}}}{m/s^2}$
0,4	0,5	0,4	1,4	0,5	0	160,43	19,74	71,05	2,428
					-1	160,43	20,14	72,51	2,528
					-2	160,43	20,54	73,93	2,629
					-3	160,43	20,93	75,33	2,729
					-4	160,43	21,31	76,71	2,830
					-5	160,43	21,68	78,05	2,930

Table I.3.22: Camber angle influence on the overturning condition. Track of 400 mm and a wheelbase of 1,4 m; centre of mass located at half the wheelbase and height of 400 mm from the ground

Therefore, since this prototype has to ride mostly on straight roads, it was decided that no camber be used on the vehicle.

I.3.1.5 Final considerations

After all these considerations, taking into account that the sharpest turn on a track that was intended to be used for the testing of the prototype has a radius of about 145 m, that the height of the centre of mass was probably set way higher than the real one and due to the fact that the lateral slope of those sharp curves wasn't taken into account (making the analysis more conservative), it seems safe to assume that overturning should not be an issue for the handcycle (turns of about 145 m of radius are critical in a range of about 60 to 70 km/h under these conservative conditions but most of the time the prototype runs on road with no less than 800 m in radius).

Note that the model presented is also applicable for an handcycle in tadpole configuration.

I.3.2 Self-alignin torque

The aim of this analysis was to come up with a geometry of the frame that would give a nice feedback to the rider during the steering process. Handling is a complicated matter that is influenced by many parameters, so, in order to have a first approximation of the behaviour of the vehicle when cornering, only geometric parameters were taken into account (the vehicle dynamic was not taken into account).

For the purpose of studying the influence of the frame geometry over the handling of the vehicle, a parametric CAD (figure I.3.5) was implemented in *Solidworks* and the study was conducted with the help of a *design table* directly linked to the CAD, that would allow for a flexible generation of many different configurations.

I.3.2.1 Geometric definition in Solidworks

The construction was very straightforward: as shown in the design tree of figure I.3.5, the first step was to define the track width and the dimension of the wheels (figure I.3.7); then after defining a plane parallel to the top one and tangent to the wheels,

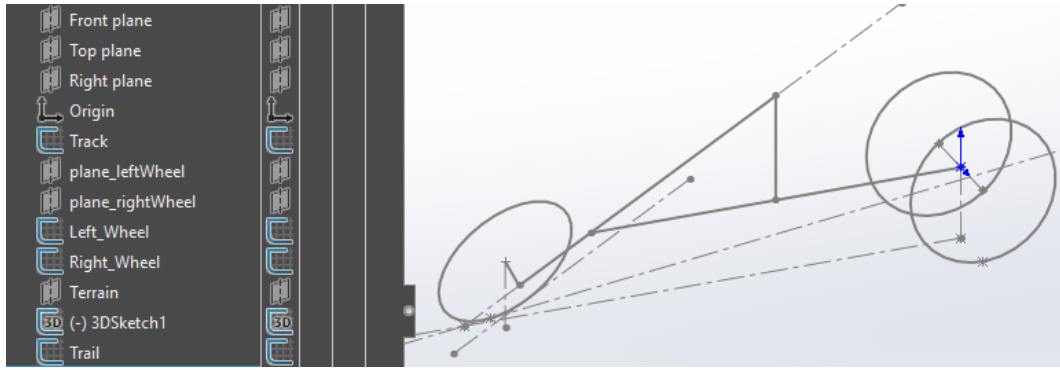


Figure I.3.5: Overall frame geometry of the delta trike and its design tree

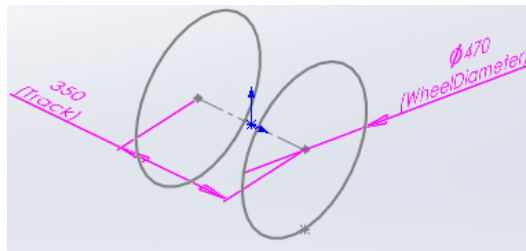


Figure I.3.6: Frame geometry of a trike in delta configuration: track and wheels diameter

the main geometry was drawn by defining the frame's length, the rake and the steering angles (figure I.3.7). In order to complete all the geometric parameters necessary for the study later on, the sketches shown in figures I.3.8 and I.3.9 were drawn too.

Particular attention was taken in the design of the steering mechanism: as a matter of fact, as it's clearly visible in figures I.3.5, I.3.7 and I.3.9, the front wheel turns around the steering column axis, therefore the hub is not a fixed point but it itself revolves around the steering axis, with a radius that take the name *rake* and it's a very important parameter. The other derived parameter of interest is the *trail* which is the distance between the contact point of the wheel and the projection of the steering axis on the ground in the non-steered configuration. The trail is positive if the projection of the steering axis stands in front of the contact point of the wheel and negative otherwise. Ultimately, as we'll see later in the chapter, the trail is the most relevant parameter when taking into account kinematic the self-aligning torque.

I.3.2.2 Forces definition in Solidworks

The forces taken into account for this study are only 2: the trike is considered as a whole body on which act the static weight and the centrifugal force under the assumption that the vehicle is moving with a uniform circular motion. On a first attempt, also the friction forces on the wheels were taken into account but after some calculations it was clear that the friction influence was negligible for our purposes. Therefore, in order to simplify the process without having to calculate the required angles on 3 different direction, the CAD was used to project all the forces on the wanted direction. The length of the forces was calculated in an *Excel* table linked to the CAD which is going to be discussed in a little bit.

Figure I.3.10 shows the forces applied to the wheel: one is the vertical force N_y ,

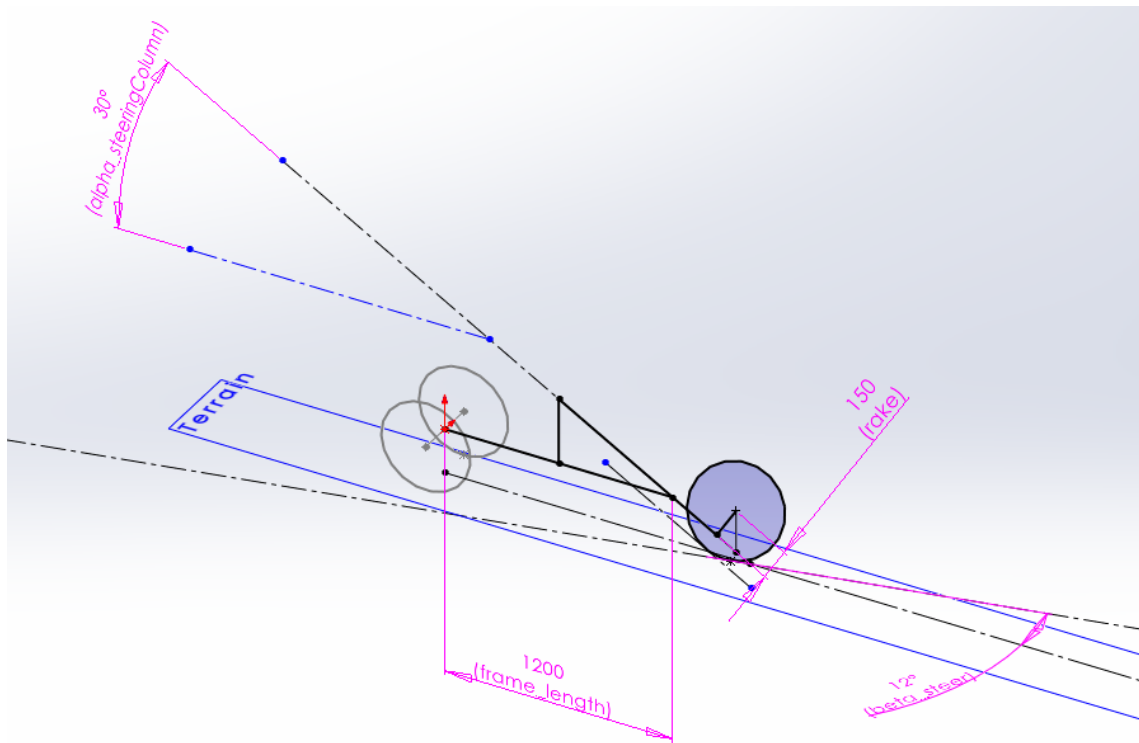


Figure I.3.7: Frame geometry of a trike in delta configuration: frame length, rake and steering angles definitions

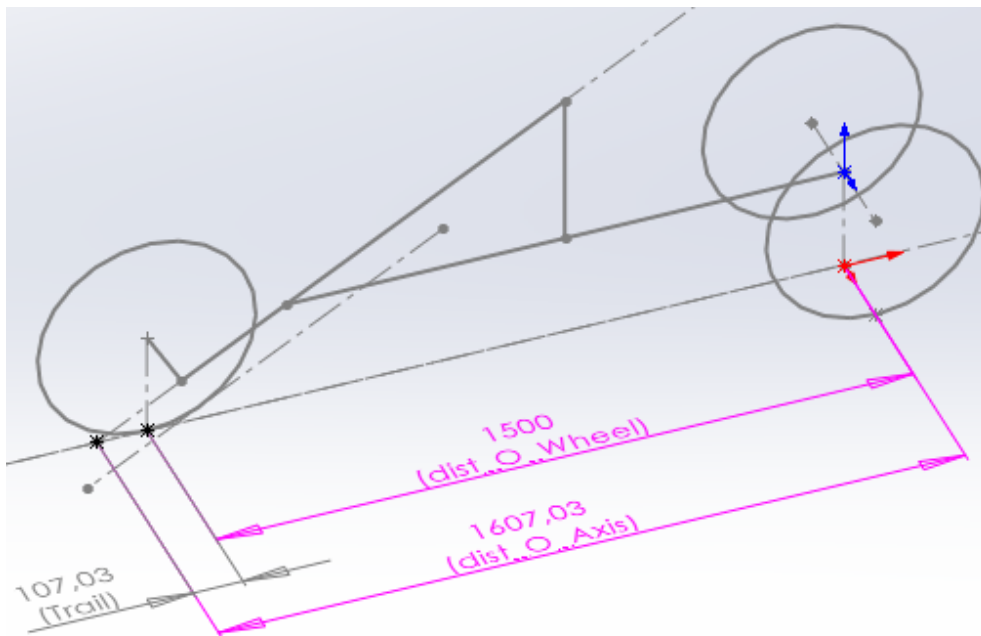


Figure I.3.8: Frame geometry of a trike in delta configuration: trail length later to be used in the stability analysis

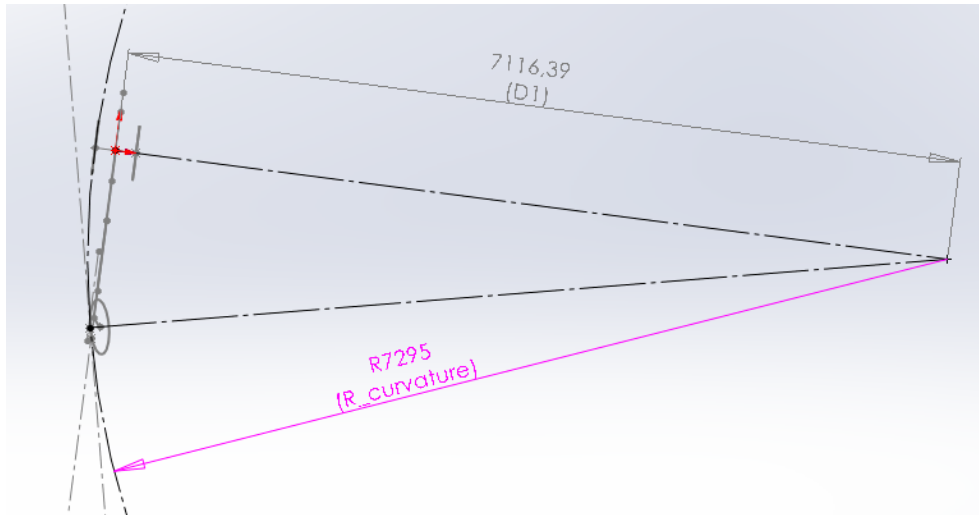


Figure I.3.9: Frame geometry of a trike in delta configuration: curvature radius approximation later to be used in the stability analysis

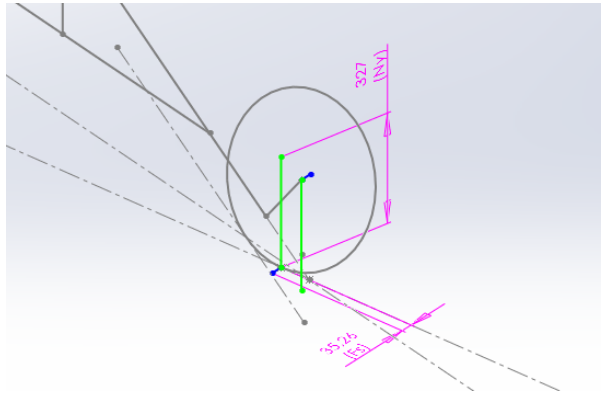


Figure I.3.10: Forces applied to the isolated front wheel

which represents the vincular reaction of the share of the weight discharged to the ground through the front wheel; the second is the lateral reaction F_s . Being the wheel attached to the frame through the hub, it's clear that equal and opposite forces are born on it.

If we take into account a cut of the entire group of the wheel and the steering column, we get the internal reactions on the axle of rotation of the steering mechanism, as shown in figure I.3.11. Due to this fact, the only forces that generate a torque, which has to be compensated by the rider, are the 2 forces on the ground; therefore, only those 2 where projected on a plane perpendicular to the steering axle (figures I.3.12 and I.3.13) to define the wanted torque.

I.3.2.3 Linked designed table and results

The design table is an useful tool that allows to build multiple configurations of parts or assemblies by specifying parameters in an embedded Microsoft Excel worksheet. The design table is saved in the model document and it's possible to link the model document to the Excel file in order to obtain a large quantity of data at once for the analysis.

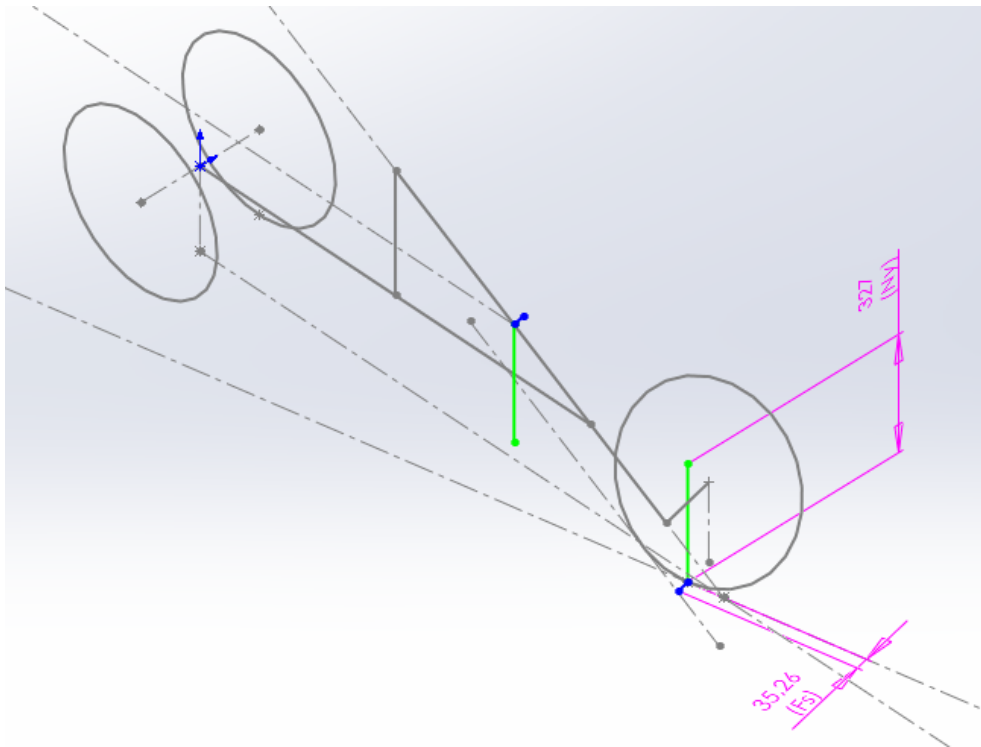


Figure I.3.11: Forces applied to the front wheel and steering column group

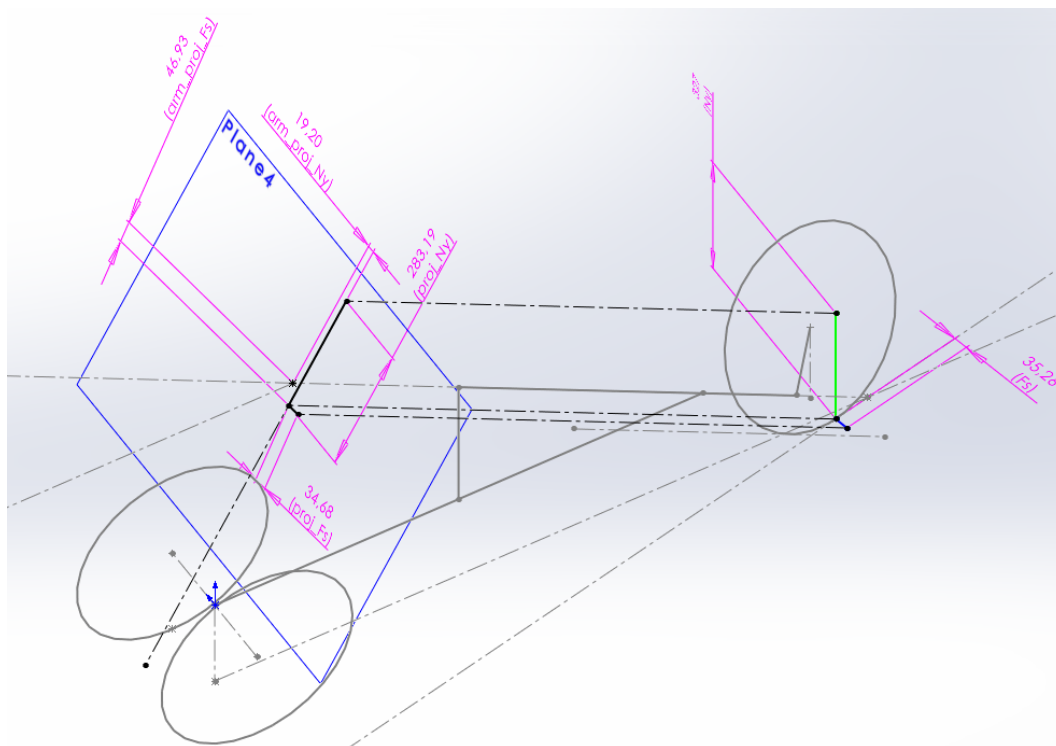


Figure I.3.12: Projection of the forces with non-null lever arms

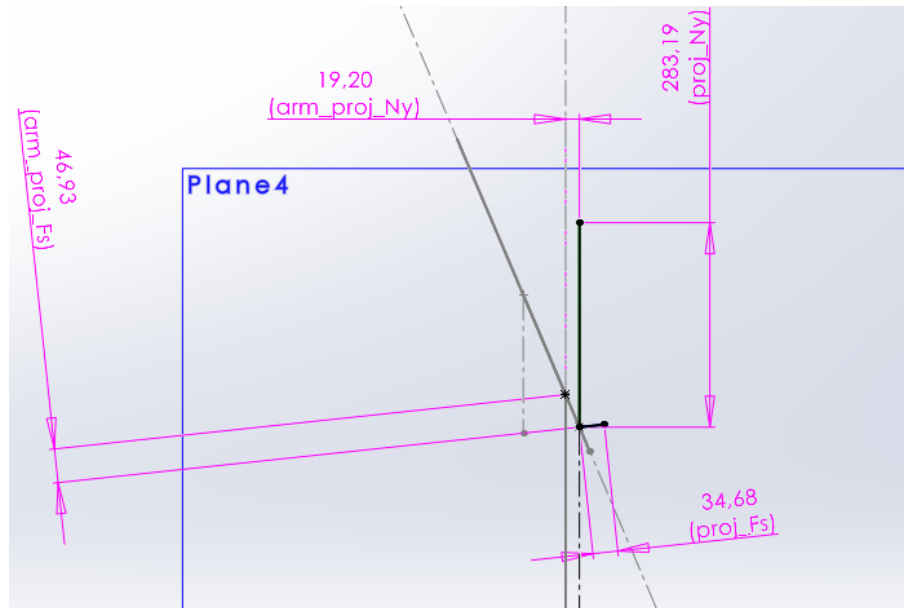


Figure I.3.13: Normal view of the projected of the forces with non-null lever arms

Figure I.3.14 shows the first rows of the design table, which was used to produce 107 configurations at a time.

The input parameters are to be set in row 3 (Default configuration) from column B to G. The first 2 parameters (in white) are considered constant and the third was defined beforehand (column C) in relation to the speed. So the user can see how the frame geometry impacts on the handling by modifying the 3 parameters in blue.

Proceeding alphabetically, column H is read from the CAD and automatically ad-journed while column I and J are calculated inside the spreadsheet on the basis of the user input (mass and its distribution and speed) and of the value of the radius from column H. In particular, the mass was set at 100 kg and the distribution on the front wheel was set at 1/3 and 2/3 on the rear (defined by the k parameter set to 3 and visible in figure I.3.15). These parameters where set in the second page of the file.

Columns from K to N are automatically overwritten each time that the CAD is modified on the basis of the values imposed by columns I and J. Finally columns O and P are used to define the sign of the torque, as well as the dimensions of the wheelbase and of the trail.

The third page of the file calculates the torque for every configuration (figure I.3.16) and generates the wanted graphs, such as those illustrated in figures I.3.17 and I.3.18.

I.3.2.4 Results and comments

As said earlier, the synthesis parameter for this analysis is the trail, as its sign determines whether the reaction torque generated by the ground is balancing (tends to straighten the steering column) or unbalancing (enhances the steering action and might cause oversteering). The modulus of the trail is important too, as it's related to the lever arms of the forces acting on the wheel: it's, for instance, possible to compare figures I.3.17 and I.3.19 (or figures I.3.18 and I.3.20) to see that the torques can be of different order of magnitude. Lastly, figures I.3.21 and I.3.22 show that the unbalancing torque assumes a positive sign for negative trail values.

So the key point that comes from this analysis is that the frame geometry has to be defined so that a positive trail is generated.

1	A	B	C	D	E	F	G	H	I	J	K	L	M	N	O	P
2	Design Table for: Telaio	Track@Track	WheelDiameter@Left_Wheel	beta_steer@3DSketch1	alpha_steeringColumn@3DSketch1	rake@3DSketch1	Frame_length@3DSketch1	R_curvature@CurvatureRadius	Ny@Ny	Fs@Fs	proj_Ny@projections	proj_Fs@projections	rim_proj_Ny@projections	rim_proj_Fs@projections	Dist_O_Axis@Trail	Dist_O_Wheel@Trail
3	Default	350	470	12	30	150	1200	7295,004944	327	35,25722711	283,190307	34,68099052	19,19707293	46,93348128	1607,03194	1516,716812
4	Trail	350	470	0	30	150	1200	7295,004944	327	35,25722711	283,190307	35,25722711	0	53,51596989	1607,03194	1500
5	v010-beta0,05	350	470	0,1	30	150	1200	859437,8578	327	0,299267299	283,190307	0,299267213	0,093402734	53,51584655	1607,03194	1500,000318
6	v010-beta0,2	350	470	0,2	30	150	1200	429720,6766	327	0,598532163	283,190307	0,598529428	0,373595708	53,51399646	1607,03194	1500,005088
7	v010-beta0,4	350	470	0,4	30	150	1200	214863,8335	327	1,197044854	283,190307	1,197022975	0,747093968	53,50807671	1607,03194	1500,02035
8	v010-beta0,6	350	470	0,6	30	150	1200	143246,4387	327	1,795518607	283,190307	1,79544477	1,120397383	53,49821227	1607,03194	1500,045782
9	v010-beta0,8	350	470	0,8	30	150	1200	107438,9055	327	2,393933974	283,190307	2,393758963	1,493408655	53,48440586	1607,03194	1500,081374
10	v010-beta01	350	470	1	30	150	1200	85955,31635	327	2,992271531	283,190307	2,991929735	1,866030632	53,46666126	1607,03194	1500,127116
11	v010-beta02	350	470	2	30	150	1200	42995,1026	327	5,982114951	283,190307	5,979382052	3,719917447	53,31907335	1607,03194	1500,507442
12	v010-beta03	350	470	3	30	150	1200	28682,72663	327	8,967126779	283,190307	8,957911508	5,549670104	53,07421144	1607,03194	1501,137926
13	v010-beta04	350	470	4	30	150	1200	21532,24618	327	11,94495196	283,190307	11,92313564	7,343600141	52,73372259	1607,03194	1502,013565
14	v010-beta05	350	470	5	30	150	1200	17246,45404	327	14,91330598	283,190307	14,87076406	9,090459559	52,29985448	1607,03194	1503,127512
15	v010-beta06	350	470	6	30	150	1200	14392,93355	327	17,86999469	283,190307	17,7966249	10,7795654	51,77540049	1607,03194	1504,471226
16	v010-beta07	350	470	7	30	150	1200	12357,78101	327	20,81293121	283,190307	20,69668791	12,40090694	51,16363353	1607,03194	1506,034658

Figure I.3.14: Upper part of the first page of the design table

	A	B	C
1	m/kg	k	v/(km/h)
2	100	3	10
3			20
4			30
5			40
6			50
7			60
8			70
9			80
10			90
11			100
12			110
13			120

Figure I.3.15: Second page of the design table with the definition of mass distribution and speeds to be used

Torque/(N m)	Trail	Flag	Wheelbase
-2,0845585	-43 mm	-1	1650 mm
$= \$F\$2 * (\$geometry.K4 * \$geometry.M4 - \$geometry.L4 * \$geometry.N4) / 1000$			

Figure I.3.16: Third page of the design table used to elaborate all the acquired data

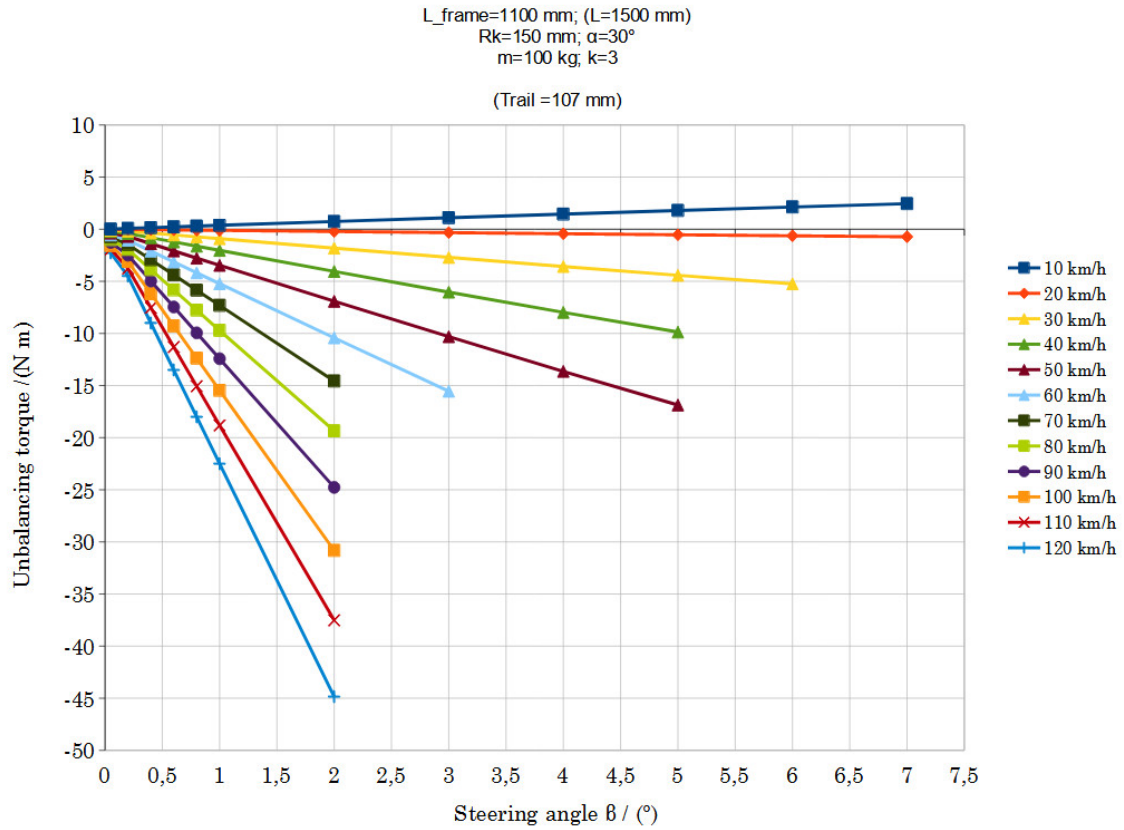


Figure I.3.17: Graph of the balancing torque for a positive trail configuration

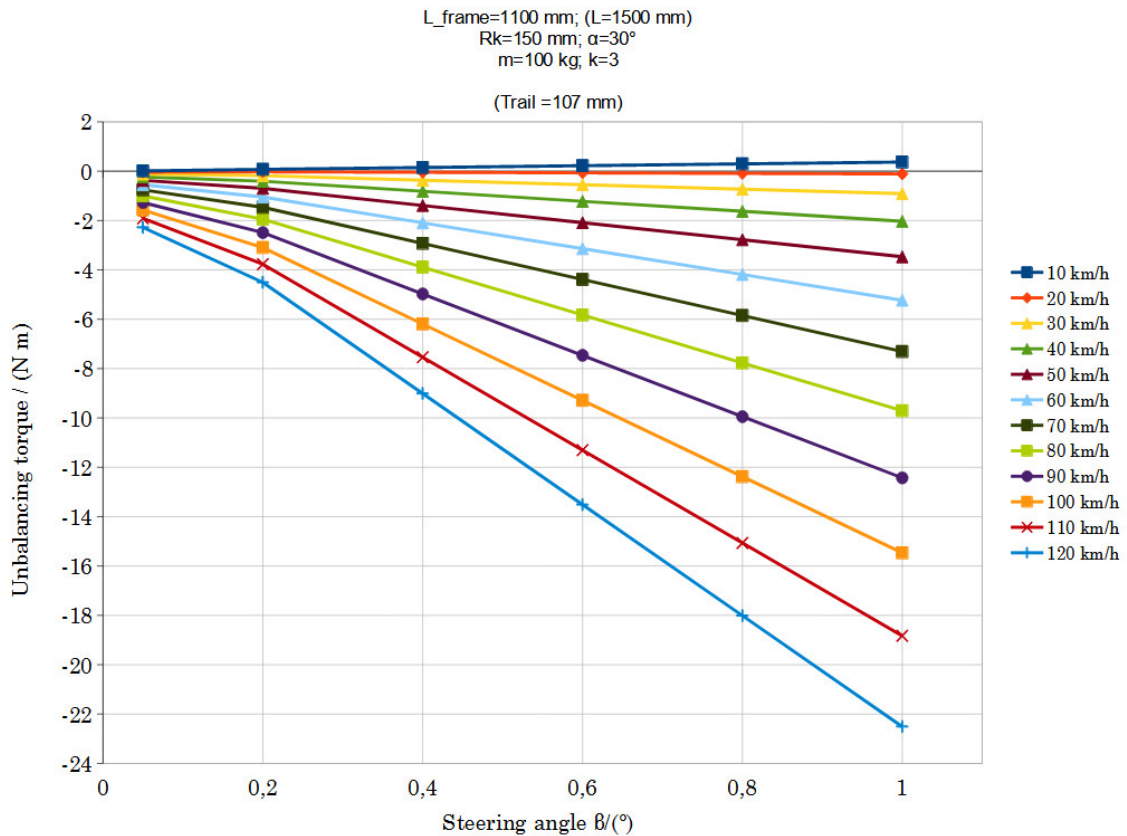


Figure I.3.18: Zoom of graph in figure I.3.17

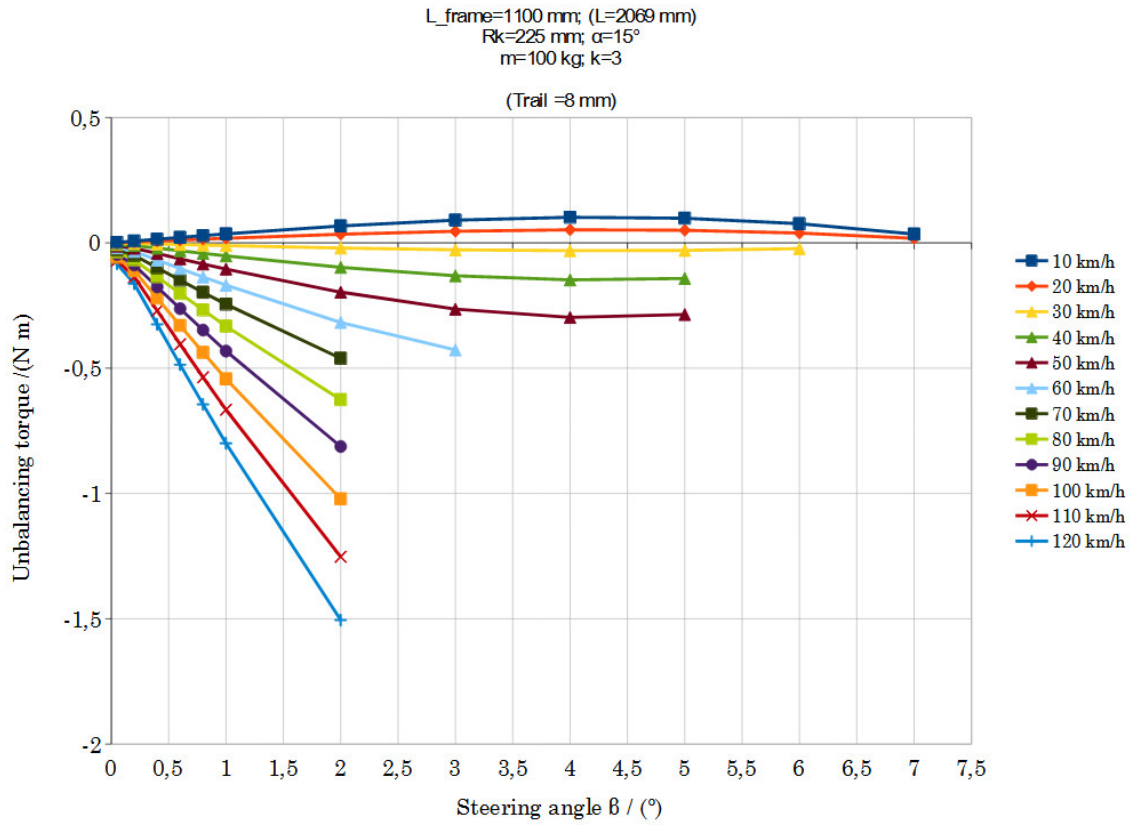


Figure I.3.19: Graph of the balancing torque for an almost null trail configuration

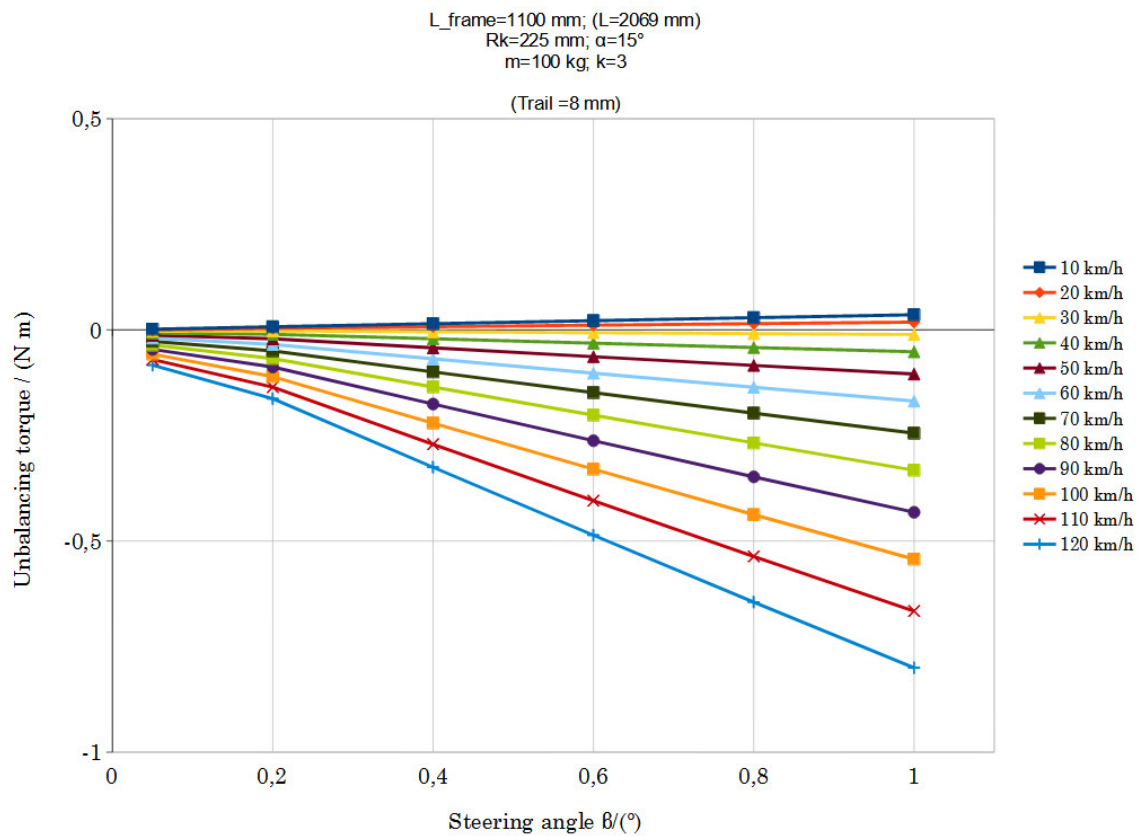


Figure I.3.20: Zoom of graph in figure I.3.19

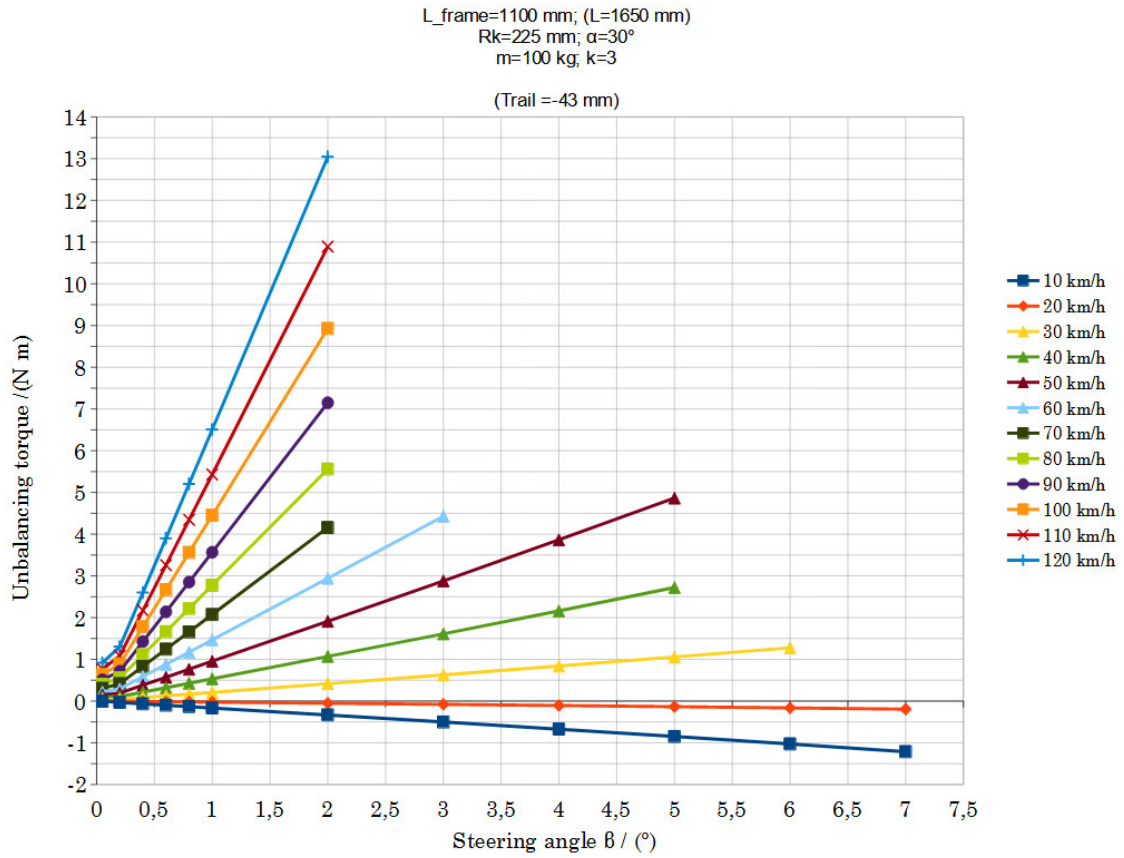


Figure I.3.21: Graph of the balancing torque for a negative trail configuration

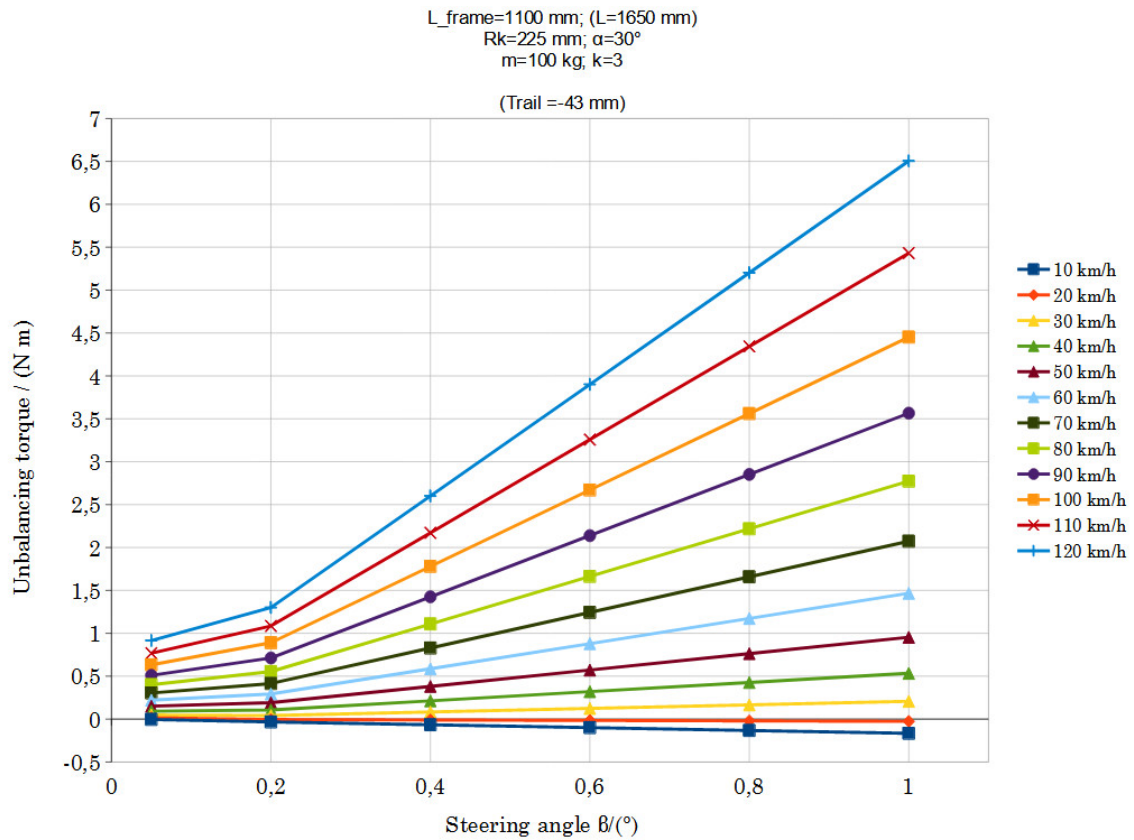


Figure I.3.22: Zoom of graph in figure I.3.21

Chapter I.4

Aerodynamic studies in delta configuration

As described in Nicola Dan Maries's thesis, *Design of speed record handcycle* [11], the preliminary CFD simulations conducted by the team's aerodynamics department and some studies cited in literature, led to the conclusion that a fairing in recumbent position was to be produced.

Within this framework, the first part of the following chapter is dedicated to a general introduction on the aerodynamic dissipation phenomena; then the most important geometric parameters are presented and, lastly, some fairings in delta configuration are presented and compared with one another.

I.4.1 Basis of aerodynamics

I.4.1.1 Net drag

Net drag F_{drag} is the overall resistant force that acts on a body immersed in a fluid. Usually, the phenomenon is described as the superposition of 2 different attributes: shear and pressure drag.

I.4.1.2 Shear drag

In fluid dynamics, the no-slip condition for viscous fluids assumes that at a solid boundary, the fluid will have zero velocity relative to the boundary.

The fluid velocity at all fluid–solid boundaries is equal to that of the solid boundary. Conceptually, one can think of the outermost molecules of fluid as stuck to the surfaces past which it flows. [22]

Because of this reason, in proximity of the body's surface, there's a thin layer that presents a velocity gradient which takes the speed of the fluid from null to free-flow's.

This zone, called boundary-layer, is characterized by shear stress between the fluid particles that are accelerated. This phenomenon, integrated on the all the boundary surface (also referred as *wetted area*) gives birth to a resisting force, called *shear drag*, on the body.

I.4.1.3 Separation, vorticity, pressure drag

Since this paragraph is intended as a brief overview of a topic that could be discussed at length, only the behaviour of 2D symmetric shapes immersed in a steady-state and incompressible flow directed parallel to the symmetry axis of the body itself, is taken into account.

Due to the aforementioned no-slip condition, the flow trajectories are deformed by the passage of the body but, for low Re values, the stream lines are still able to almost completely follow the body's shape. By increasing the Re value, though, the fluid particles, which slide along the body, are initially slowed down in the front part of the body, with a consequential increase in pressure. They're then accelerated, with a fall in pressure, just to be decelerated once again in the rear part of the body. The drop in kinetic energy compensates for the pressure recovery; however, part of the kinetic energy gained during the acceleration phase is dissipated in heat by friction; hence, not all the pressure is recovered, and this phenomenon intensifies as speed increases. Consequently, the stream lines tend to spread in the rear zone and create an enclosed area called *separation bubble* in which swirls are born. This zone is confined by the *separation lines* that origin on the body in the *separation points*, where the flow detaches from the wall and gets into the external flow [21].

As a result, because of the low pressure zone located behind the separation points, the body is subject to a force acting in the opposite direction of the relative motion. *Pressure drag* takes into account this phenomenon as well as the wake turbulent dissipation.

During CFD (computational fluid dynamics) analyses, this phenomenon is evaluated by looking at velocity and pressure fields as well as by the vorticity, turbulent viscosity ratio and other parameters.

I.4.1.4 Drag coefficient

The drag coefficient, C_d or C_x , is a dimensionless quantity that is used to quantify the resistance of an object in a fluid environment. The drag coefficient is always associated with a particular surface area A ; for road vehicles the reference is the frontal area, i.e. the projection of the vehicle's silhouette on a plane normal to the longitudinal direction, while for airfoils it's more usual to consider the nominal wing area.

The mathematical definition is:

$$C_d = \frac{F_{drag}}{\frac{1}{2}\rho_{\infty}u_{\infty}^2 A}$$

where ρ_{∞} and u_{∞} represent the density and relative speed of the undisturbed flow[23, 21].

Given the definition, is clear that, for fixed fluid conditions, a smaller C_x stands for a more aerodynamic shape. In general, C_d is not an absolute constant for a given body shape. It varies with the speed of airflow (or more generally with Reynolds number Re). A smooth sphere, for example, has a C_d that varies from high values for laminar flow to 0,47 for turbulent flow. Although the drag coefficient decreases with increasing Re , the drag force increases[23].

Sometimes, for absolute comparison of different bodies, the $C_d A$ parameter, expressed in m^2 is analyzed.

I.4.1.5 Lateral wind

In case of:

- 3 dimensional shapes (spherical excluded)
- 2D asymmetric bodies
- 2D symmetric structures immersed in a flow incident to the symmetry axis

stream lines are dispatched unevenly and a transverse component is born too: on road vehicles, this impacts the stability (both the handling and the overturning condition). Due to lack of time, the design of the fairing didn't take into account how the presence of lateral wind could affect the overall drag and stability of the prototype. This is actually something that has not been done for the two-wheeled vehicles of Team Policumbent either (since they typically don't ride in windy weather) but it's definitely a topic to keep in mind for the next projects, all the more if the bike is to be ridden on public roads.

I.4.2 Project constraints and geometric parameters

The design of a fairing has to take into account many factors. First of all it's utmost important to define the vehicle application, i.e. where the vehicle is going to be used (on land, on the water, in water, in air), and the final purpose for its construction, since this highly influences the starting point for the whole design. As an example, since Cerberus was not developed for high speed cornering, no flaps or other kinds of stabilizers were ever designed because they'd be useless. In fact, they'd have the unwanted effect of enhancing the overall drag on a vehicle that's produced to aim for the highest possible speed on a straight road.

I.4.2.1 Length

For shipping costs, it was decided that the maximum allowable length would be 2800 mm. It's also very important since it affects the wetted area and a variation on it can change the mass distribution, depending on the position and length of the wheelbase.

I.4.2.2 Track

It should be large enough to avoid the overturning condition, described in chapter I.3, and to allow a clean steering without any risk of interference between both: the wheels and the pilot, and between the wheels and the structural fairing.

I.4.2.3 Frontal area, wetted surface

As explained above, the C_x definition comprises the frontal area. This is a parameter that's highly dependent on the shape of the rider's body and on the movements that must be permitted inside the vehicle.

As said, the shear drag is proportional to the boundary surface (i.e. the wetted area), so it's important to consider that sometimes, if the shape is already sufficiently streamlined, it's better to have a slightly larger (i.e. with a bigger frontal area) and

ID	NXS_01	NXS_01_A	ADG_1F_05
<i>Speed</i> /(km/h)	100	100	100
<i>Speed</i> /(m/s)	27,78	27,78	27,78
A_{front} /(m ²)	0,3867	0,4488	0,4844
A_{wetted} /(m ²)	5,163526	5,228102	5,363526
<i>Shear Drag</i> /N	5,291	4,043	3,757
<i>Pressure Drag</i> /N	3,916	3,163	4,711
<i>% Shear</i>	57,47%	56,11%	44,36%
<i>Lift</i> /N	-61,6	-76,3	-76,2
<i>Drag</i> /N	9,207	7,205	8,468
C_x	0,06066	0,04091	0,04454
$C_x \cdot A$ /(m ²)	0,02346	0,01836	0,02157
P_{aero} /W	255,77	200,17	235,24
<i>Length</i> /mm	2800	2800	2780

Table I.4.1: Comparison of fairings NXS_01, NXS_01_A and ADG_1F_05

shorter vehicle, since lengthening the shape could enhance the shear drag component without any important decrement on the pressure's one. A rather intuitive example could be that of considering a 2D plate: since it doesn't have a 3rd dimension, it's front and lateral views are simple segments with null area but such body would still produce shear drag on its top and bottom surfaces (i.e. its wetted area).

I.4.3 Fairings

Many fairings were designed during 2020 by the aerodynamics division but all of them were actually way too small. After the full definition of the mannequin to be used (see section II.1.1.1), a new set of fairings was drawn amongst which NXS_01 was the best. In the meanwhile, the author began to design his own fairings and ADG_1F_05 (figure I.4.1), which was his only shell in delta configuration to be simulated on STAR CCM+, resulted to perform better. After some design iterations, Lucas Fernandes (former head of the aerodynamics division) upgraded his best fairing to NXS_01_A (figure I.4.2). Table I.4.1 below shows the comparison between this 3 hulls. Following, some screenshots are presented and are analyzed in short.

I.4.3.1 ADG_1F_05

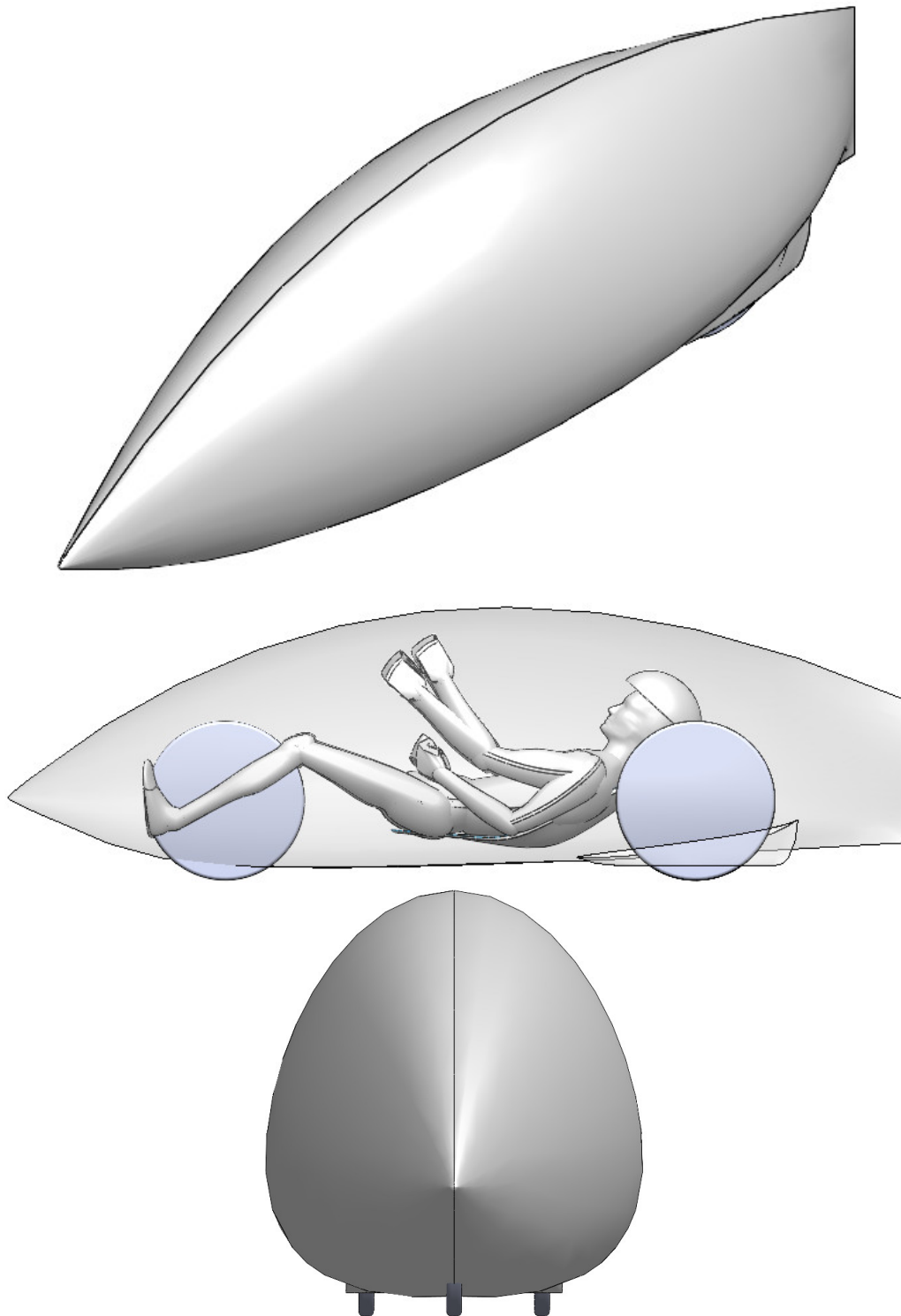


Figure I.4.1: Fairing ADG_1F_05

I.4.3.2 NXS_01 and NXS_01_A

Drawn by Lucas Fernandes, head of the aerodynamics department at the time.

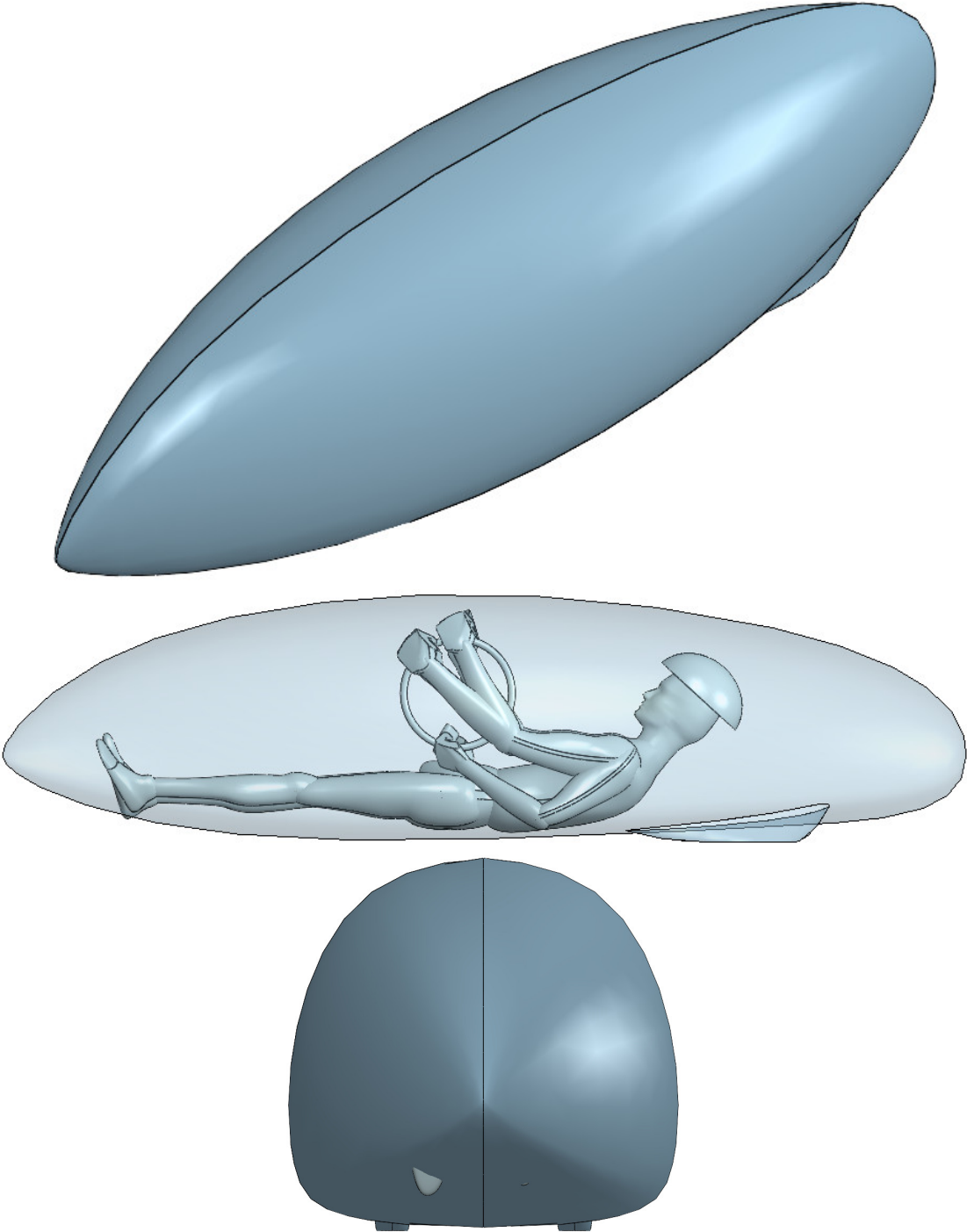


Figure I.4.2: Fairing NXS_01_A. CAD by Lucas Fernandes

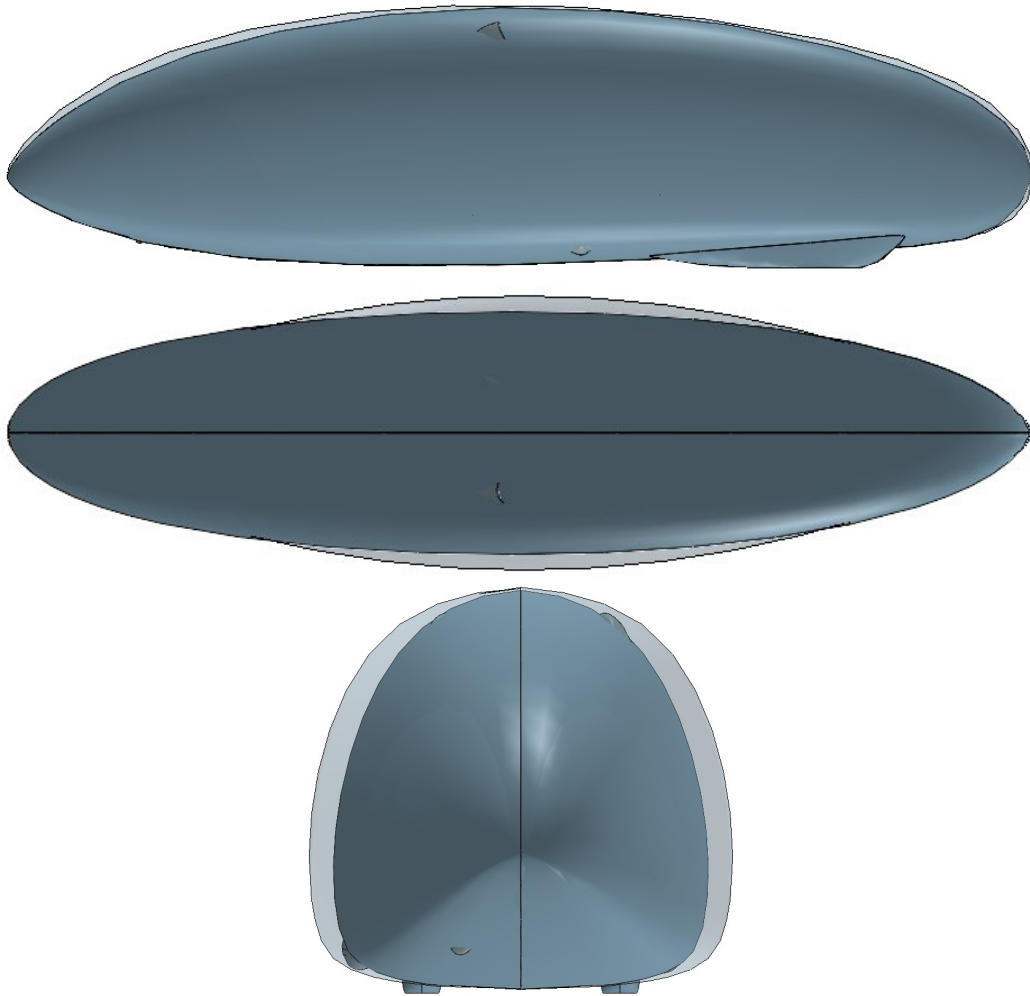


Figure I.4.3: Overlap of fairings NXS_01 and NXS_01_A in lateral, top and front views

I.4.3.3 Comparisons

As shown below in figure (I.4.3), NXS_01_A has a very similar lateral profile but it's pointier and closes more gently on the rear. This improved greatly the shear stress as shown by both the visualization in STAR (figure I.4.4) and the aforeshown table (I.4.1). This is one of those examples, where increasing the frontal area actually reduces dramatically the drag.

ADG_1F_05 outperformed both NXS_01 and NXS_01_A in shear stress but lost to the latter in terms of pressure and net drags (and therefore in terms of C_d). As a matter of fact, it seems to separate a little earlier on the tail (figure I.4.4) and to generate a larger and less uniform wake (figure I.4.5). Lastly, a view of the stream lines (figure I.4.6) suggest a more homogeneous distribution in the rear zone (figure I.4.6)

I.4.3.3.1 Wall shear stress

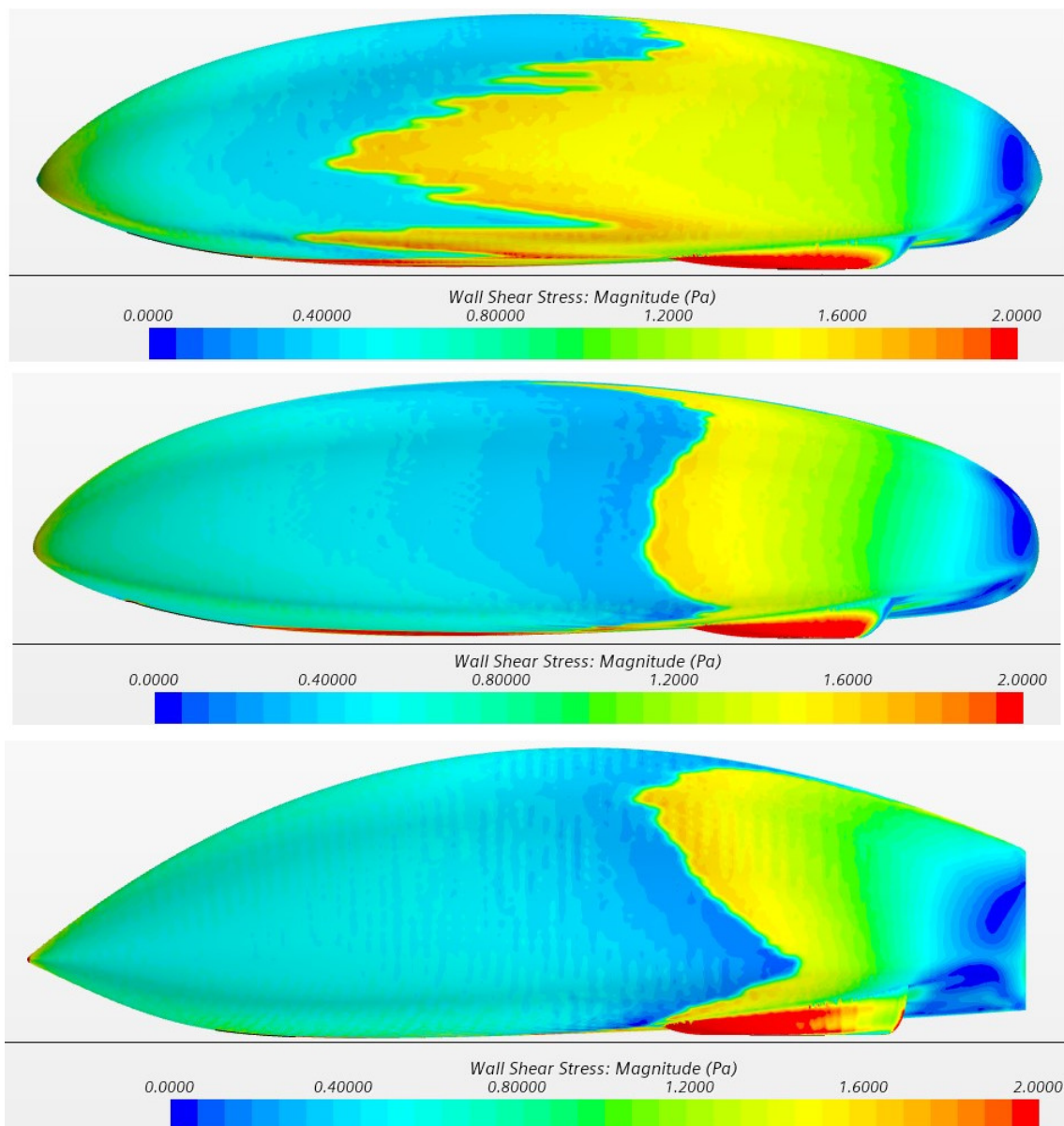


Figure I.4.4: Wall shear stress comparison of fairing (from top to bottom) NXS_01, NXS_01_A and ADG_1F_05 at 100 km/h

I.4.3.3.2 Wake and stream lines

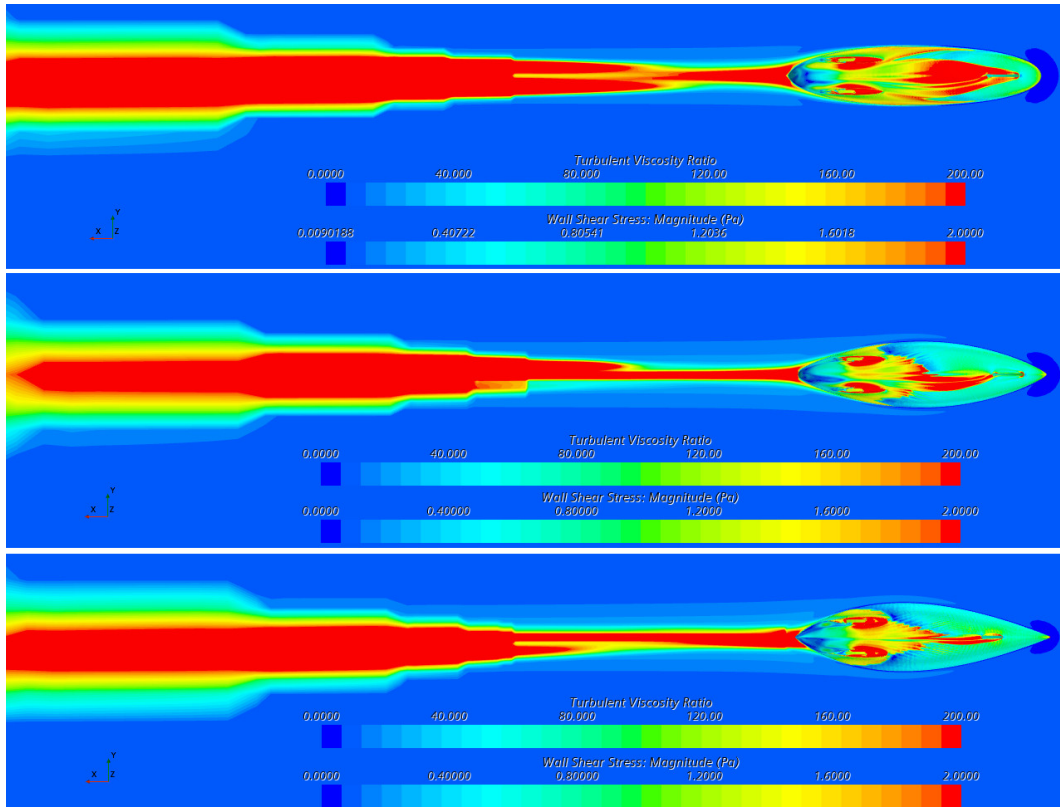


Figure I.4.5: Wake comparison of fairing (from top to bottom) NXS_01, NXS_01_A and ADG_1F_05 at 100 km/h

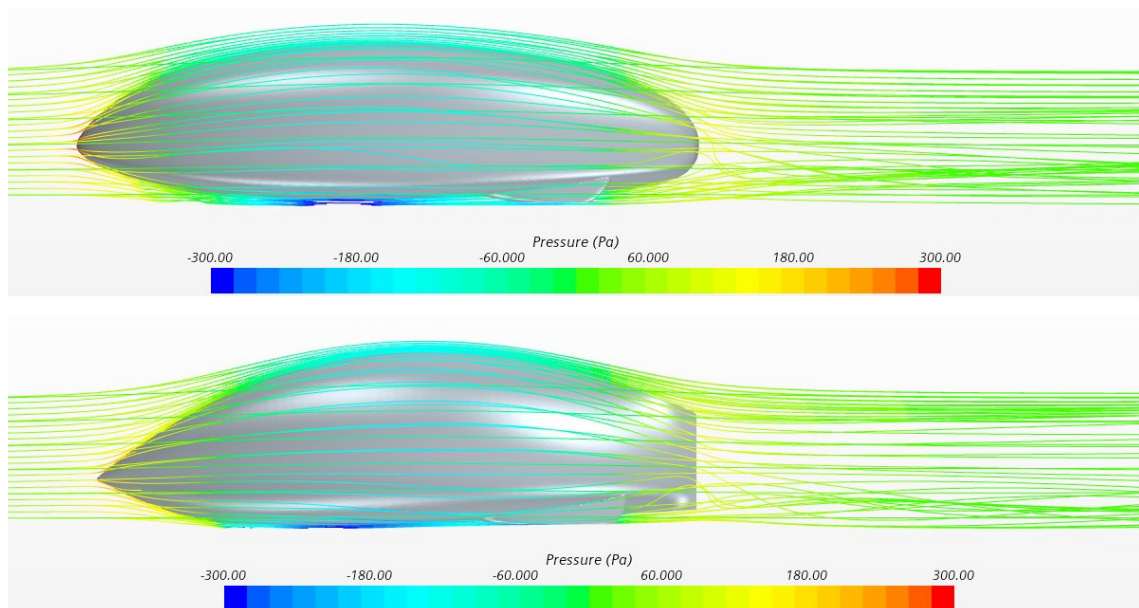


Figure I.4.6: Streamlines comparison of fairing NXS_01_A (top) and ADG_1F_05 (bottom) at 100 km/h.

Part II

Cerberus's design: a tadpole handtrike

Chapter II.1

Aerodynamic design of the fairing in tadpole configuration

In april 2021, former head of the aerodynamic department Giorgio Nicola (who had designed both Taurus's and Phoenix's hulls) tried to draw a fairing in tadpole configuration (figure II.1.1). Even though the hull looked a bit too tight on the mannequin, a the simulation on STAR CCM+ was performed anyway. The result was unexpectedly encouraging, with a overall drag force of just 6,356 N. At the time

- (-31% compared to 9,207 N of NXS_01)
- (-25% compared to 8,468 N of ADG_1F_05)
- (-12% compared to 7,205 N of NXS_01_A).

II.1.1 Detailed CAD modeling process of the shell

The prototype's fairing was designed in *Solidworks*, software that is available for free to all the students at *Politecnico di Torino*.

This section introduces to some design methods that the author came up with by watching surface modeling tutorials on the web and by acquiring some trial and error experience during various attempts over the months.

For those who read this and are interested in trying to design a fairing, the suggestion is to start with a solid basis, maybe using the following procedures as a reference, but then to move on and try different approaches, in order to find the one that suits oneself the best.

II.1.1.1 Interferences with the pilot: 3D mannequin

Since, as shown above (paragraph I.4.2.3), frontal area is an important parameter, it was critical to design a small vehicle which though had to be big enough to avoid interferences with the rider during the run. In order to do so, 3D scans of the Team's pilots seat in position on a handcycle where performed (example shown in figure II.1.2). Since the build of the 2 pilots were different, the 2 scans where compared to one another and later the result was overlapped on a simplified 3D dummy which was then rescaled to the correct dimensions. This process was made with the purpose to obtain a lighter CAD of the mannequin. Lastly, the mannequin was updated to have 4 arms, and 2 toroids were added in order to visually take into account the various positions of the

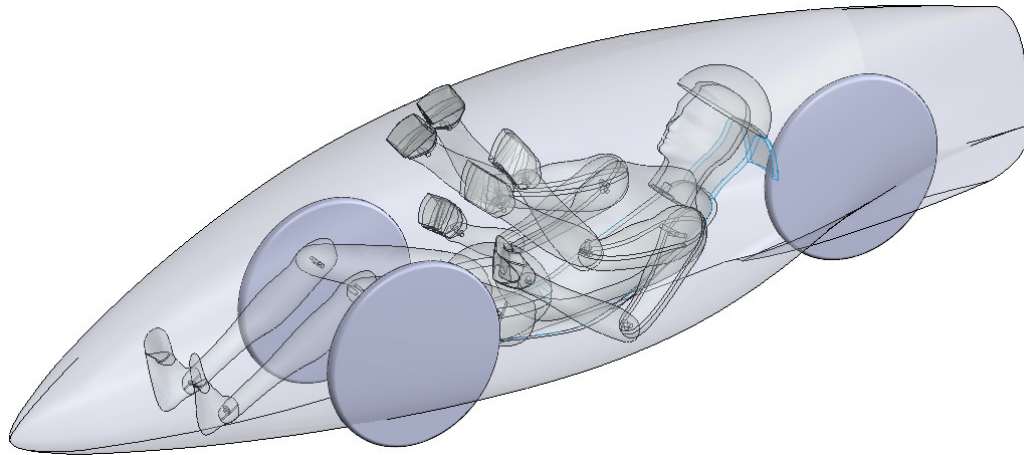


Figure II.1.1: First attempt to draw the handcycle in tadpole configuration. CAD by Giorgio Nicola



Figure II.1.2: 3D scan of Simone Chiarolla on his handcycle

hands during the propulsion movement (figure II.1.3). Later, the dummy obtained from this process, was used as a reference for the design of the fairing and other components.

This process was not the author's work. It was done by some other teammates.

II.1.1.2 Preliminary assembly arrangements

The essential parts that have to be inserted into the assembly beforehand are the mannequin and the wheels. The more logical procedure is to start by adding the wheels first. They can be set in place in various ways; hereafter 3 methods are presented:

- using a fully defined 3D sketch as reference and mating the wheels with the drawn points/circumferences (figure II.1.4)
- using a 3D sketch as a partial reference and mating the wheels with the drawn points/circumferences (figure II.1.5)
- directly using the “mate” tool and setting distances (figure II.1.6).

The first method is generally the best option, as it gives a visual feedback of the distances: it is therefore simple to change the positions of the wheels by double clicking

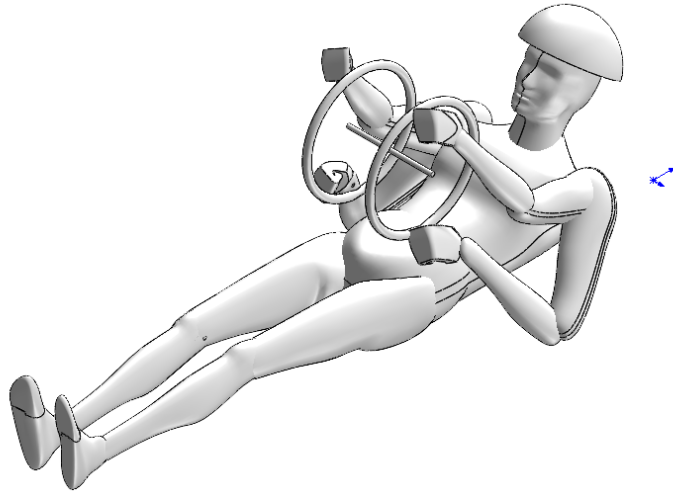


Figure II.1.3: Re-elaborated and simplified CAD of the mannequin

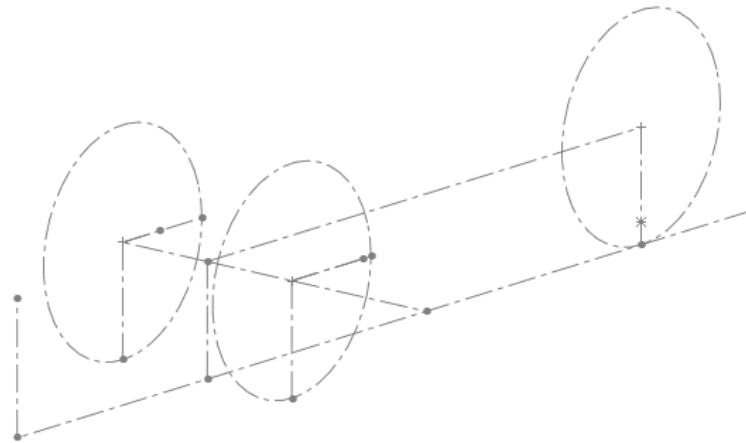


Figure II.1.4: Fully setting the wheels location with a 3D sketch

the sketch and editing the dimensions. It is moreover possible to generate different configurations of the frame geometry and use a parametric approach, which may be useful during preliminary studies, as shown in Chapter I.3.

The major disadvantage, though, is that by doing so directly in the assembly, editing the position of the wheels might become a bit slow and tedious. A good method, if the relative position of the wheels has already been defined, would be to create a subassembly that contains the 3 wheels and to later set in position by mating only 2 plans. This allows for a fast translation of the 3 bodies relatively to the, later to be designed, fairing.

The final dimensions of track and wheelbase for project Cerberus are 458 mm and 1370 mm respectively.

After placing the wheels, is then possible to insert the mannequin. For its positioning, the only initial constraint set was the coincidence between the dummy and the assembly's right planes. The distance of the mannequin's buttocks was set at about 75 mm from the ground while the longitudinal position was set approximately but left unconstrained. Figure II.1.7 shows the initial configuration of the assembly, now

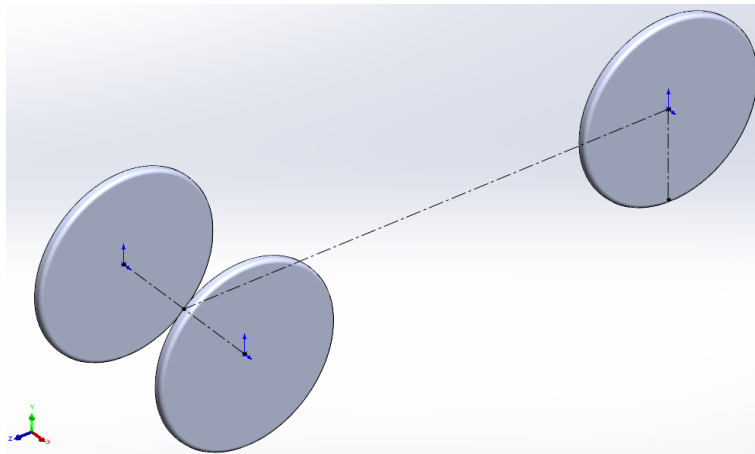


Figure II.1.5: Partly setting the wheels location with a 3D sketch

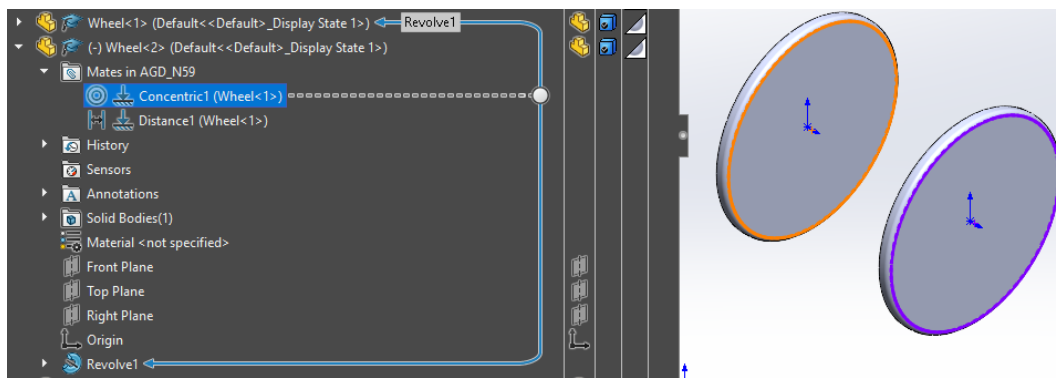


Figure II.1.6: Setting the wheels location with the “Mates” tool only.

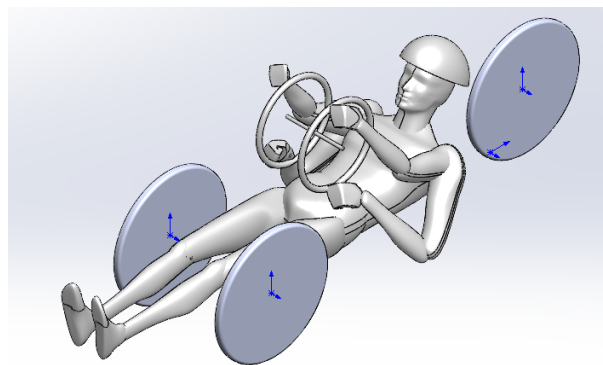


Figure II.1.7: Dummy and wheels set in place in the assembly

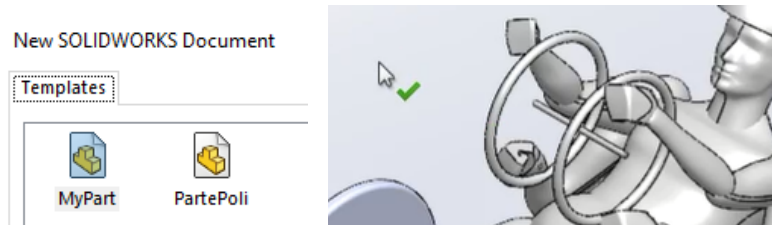
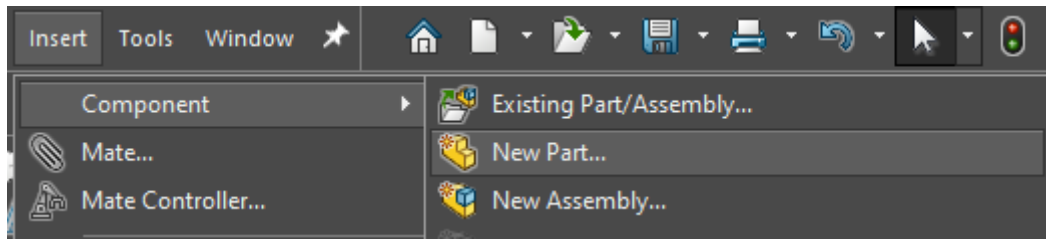


Figure II.1.8: Procedure to insert a part directly from the assembly



Figure II.1.9: Edit a part from an assembly

sufficiently set up for the fairing's design.

II.1.1.3 Creation of the fairing part

Since there are many volume constraints to keep in mind in order to avoid interferences with both the internal parts of the trike and the pilot, a design of the part directly in the assembly was chosen. In order to do so (figure II.1.8), from the assembly file click on: **Insert** --> **Component** --> **New Part**. You will then be asked for the template to use to create the part and lastly, a green check mark will appear near the mouse pointer. The suggestion is to click on a blank point of the assembly: this way, the origin of the new part, will coincide with the assembly's one. After saving the part, depending on the document settings, the component could either result as *virtual* or *independent*. Note that, while the latter is a standard part, the former is a component directly created in the assembly and will therefore not be visible in the PC's directory. This also means that a variation in the design of a virtual part won't affect other assemblies that have been created as a copy and that have same part in them. It's possible to switch between virtual and independent parts by right clicking their name in the Solidworks feature manager and then checking **make virtual** or **make independent**. In this project, a virtual part was always used in the process.

Now that the part has been created, it's possible to modify it by clicking on its name from the feature manager and selecting the 4th icon, called **edit part** (figure II.1.9).

Before getting into further details, let's take a look at the full feature manager of fairing ADG_N59 (figure II.1.10), which is the one that was later used for the construction of the prototype, to see the advantages of creating and editing a part from inside an assembly rather than doing it in a more traditional way: note how the

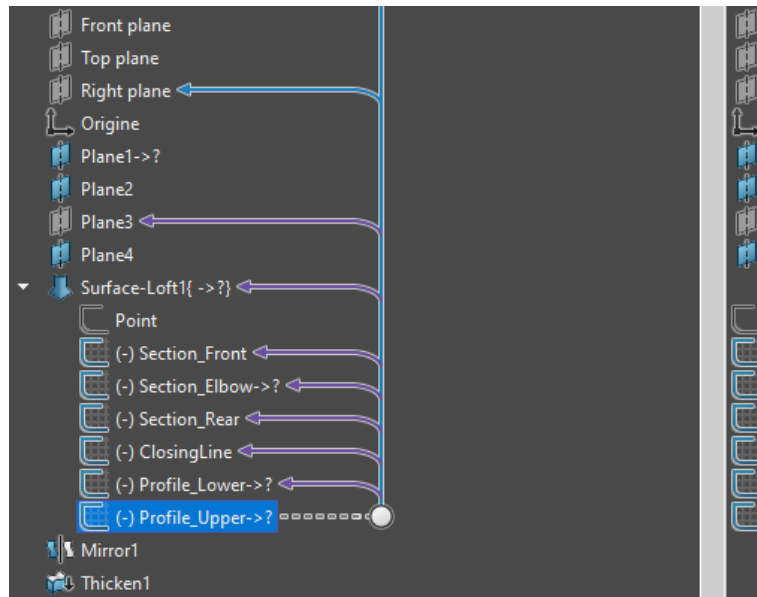


Figure II.1.10: Feature manager design tree of ADG_N59. The symbol ->? refers to relations linked to external references

symbol ->? , which refers to external references, is placed near many elements.

II.1.1.4 Design of fairing ADG_N59

In the aforementioned figure II.1.10, we can see the final structure of the fairing's design tree. Now, starting from scratch, we're going to delve in the details of the sketches drawn and the features used.

Since a loft was to be used, the first sketches to be drawn were the lower and upper profiles along with a middle section that will serve as a guide for the curvature of the fairing.

II.1.1.4.1 Lower profile

Concerning the lower profile, in figure II.1.11 we can see that the maximum allowed length (as specified in I.4.2.1) was set to 2800 mm. Other interesting constraints are:

- the height from the ground, which was set to be quite low in order to keep at a minimum the interaction between the air and the rotating wheels
- and that, on the tip, a restriction over the minimum radius was set (in this case 15 mm) both for production and safety purposes: it could indeed be dangerous to have a pointy tip and having it would anyway result in a difficult piece to properly laminate.

In figure II.1.12 is shown the way the tip was drawn, with a reference geometry circumference over which an arc of unconstrained length was placed. A construction segment was then constrained with an extremity on the centre of the aforementioned circle and forced to pass through the ending point of the unconstrained arc. This way, it's possible to change the form of the tip by clicking on the construction segment and changing its orientation. Solutions of this kind come with both pros and cons: if a fully parametric

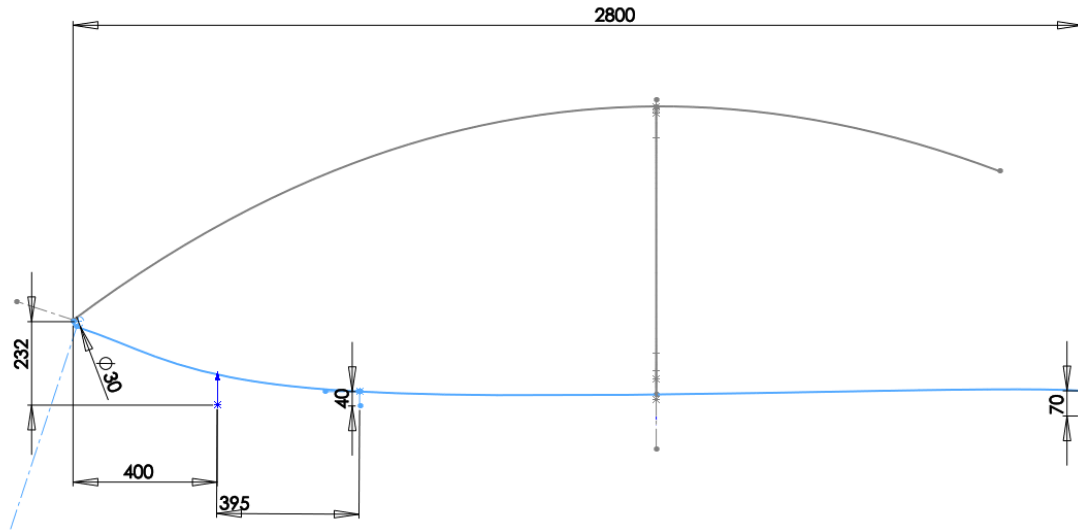


Figure II.1.11: Dimensions set in the lower profile sketch

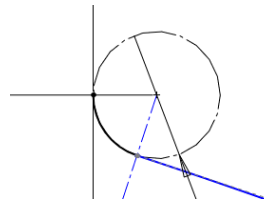


Figure II.1.12: Zoom on the curvature tip control in the lower profile sketch

construction has the benefit of being easily editable without opening the sketch and to even be manageable through a parametric table, it's also true that such approach could result in corrupted geometries with unwanted intersections and/or cusps. So, it's sometimes wiser, especially when working with splines, to do some things entirely by hand, at least in the beginning, and observe how minor changes can result in major variations of the entire geometry.

II.1.1.4.2 Elbow section

This section was necessary to make room for hands and elbows and guarantee that they wouldn't intersect the fairing.

The first step to draw the wanted sketch was to define the drawing plane: as shown in figure II.1.13, this action was performed from the assembly, taking as references the front plane and a point on the mannequin's elbow.

Figure II.1.14 shows the dimensioning of this section: the height is set relatively low even compared to racing cars **[add source]**. The curvatures of the complete profile were adjusted after viewing the CFD results (discussed further on in this thesis) in order to provide what seemed to be a nice overall profile of the fairing.

Figure II.1.15 is a zoom on the elbow, showing that one of the 2 circles was concentric to the same point used for the plane construction while in figure II.1.16 it's shown how the assembly was used as a visual reference only and the centres of the circles were set as fixed (the **Fixed** constraint is denoted by the anchor symbol): the one on the hand is slightly larger, as the hand itself doesn't intersect the plane of that sketch so it has to be big enough not to produce intersection between the hands and the fairing

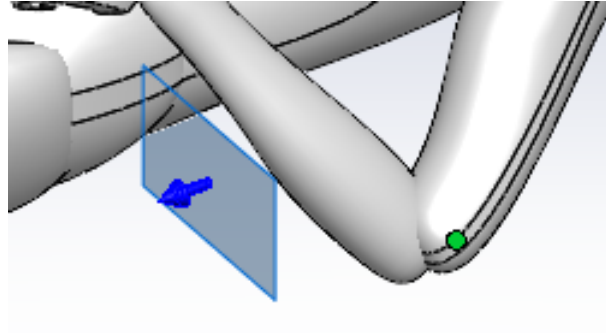


Figure II.1.13: Reference for the elbow plane construction

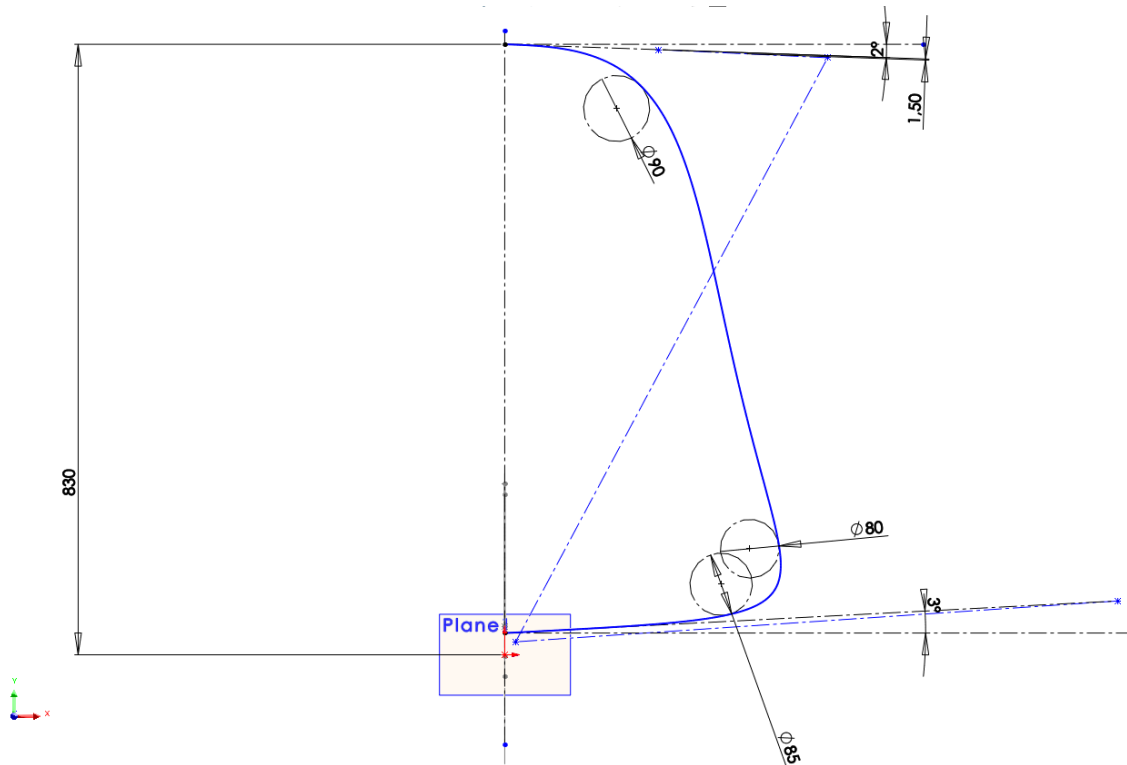


Figure II.1.14: Elbow section general dimensions

itself.

It's additionally important to remind that, in this phase, the safety margin over intersection with the fairing has to be quite large as the hull itself is going to have its own thickness, which will offset internally the just drawn surface.

II.1.1.4.3 Upper profile

Similarly to the approach used for the lower profile, the upper one was designed with a constraint on the tip curvature using the same circumference shown in figure II.1.12 and the length and height of the tail was set (figure II.1.17). Furthermore, the line was constrained to pass through the Elbow section with the **Pierce** command (figure II.1.18). This last step is absolutely necessary in order to avoid unwanted errors during the, later to be lofted, surface creation as the **Pierce** command ensures that a point and a curve intersect in 3 dimensions. If the point is also part of a second line, this ensures

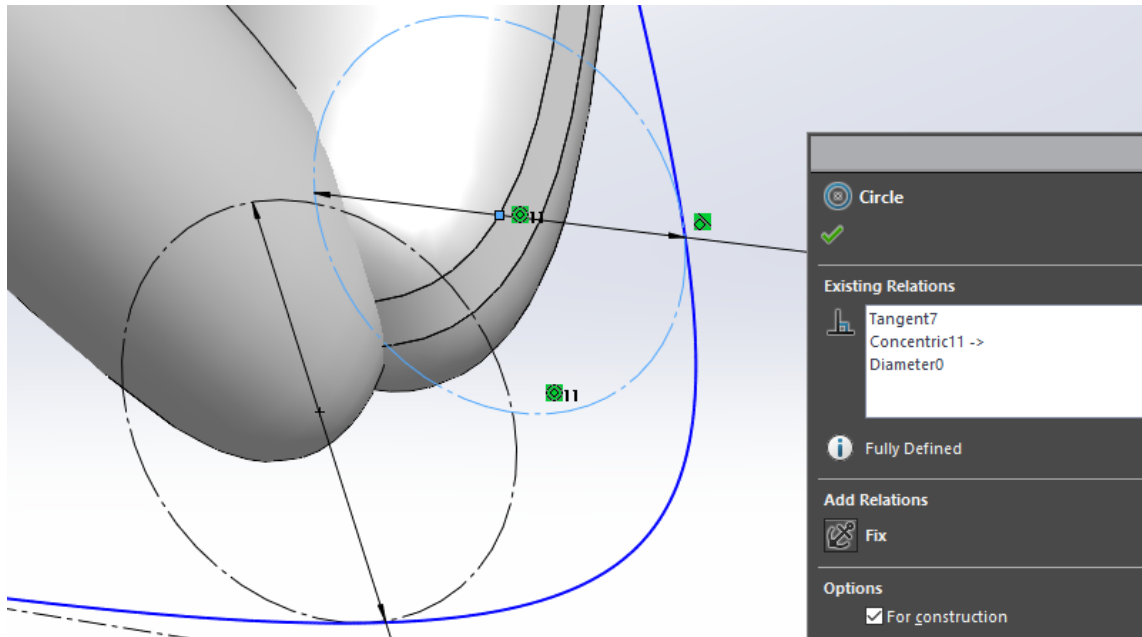


Figure II.1.15: Elbow section zoom: making room for hands and elbows

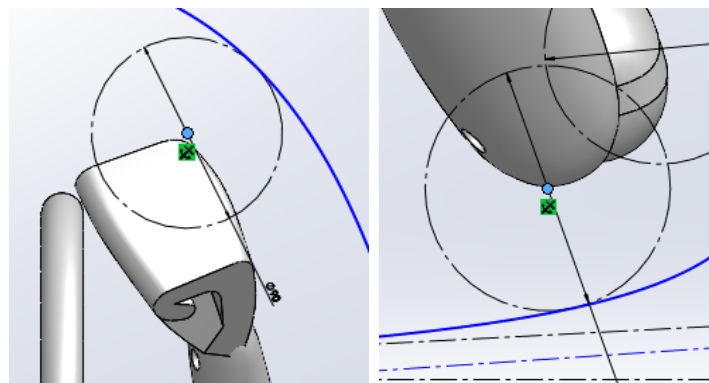


Figure II.1.16: Elbow section zoom: fixed centered circles

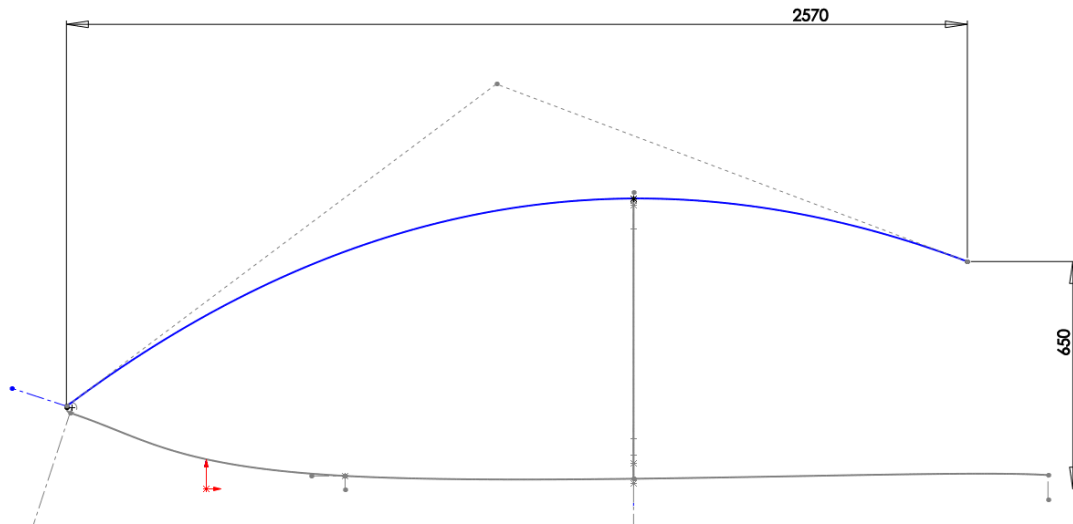


Figure II.1.17: Dimensions set in the upper profile sketch

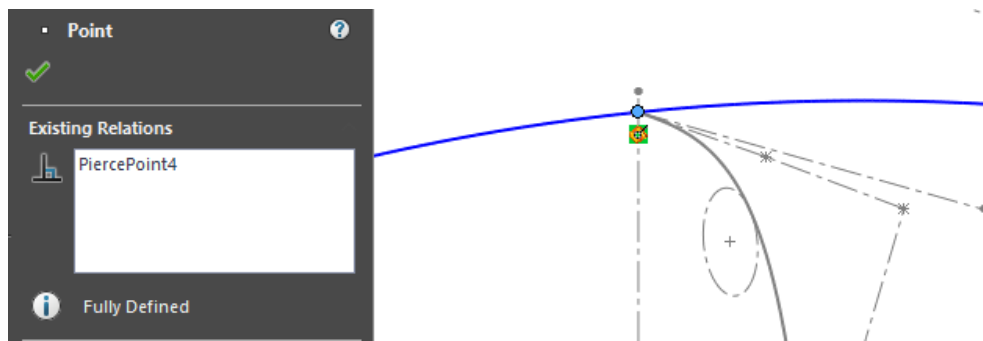


Figure II.1.18: Piercing the upper profile sketch with the elbow profile sketch

that the 2 lines intersect in that point. Coincidence is instead a minor constraint which consists in the intersection of a sketch entity and the projection of a different entity: therefore, in our example of a point and a curve, coincidence and piercing are equivalent only if the old curve which we want the new curve to intersect with ends with a point coincident to the sketch plane. The `Pierce` command is extremely useful while using 3D sketches and when used on a 2D sketch ensures that we're not making errors in creating a continuously linked geometry.

II.1.1.4.4 Closing line

This is the last of the minimum elements required to define a complete spline for the fairing. It's a simple sketch that connects the upper and lower profiles. The curvature was set as in figure II.1.19 after the CFD analyses.

II.1.1.4.5 Front section

In ADG_N59 fairing, a front section was introduced in order to force the profile of the shell away from the wheels. As the fairing is supposed to be as continuous as possible, the front section was drawn with the elbow section in background (figure II.1.20) as reference. The perfecting of the various sketch was iterative and implied the use of both CFD analyses and zebra stripes analyses, as shown in paragraph II.1.1.7.

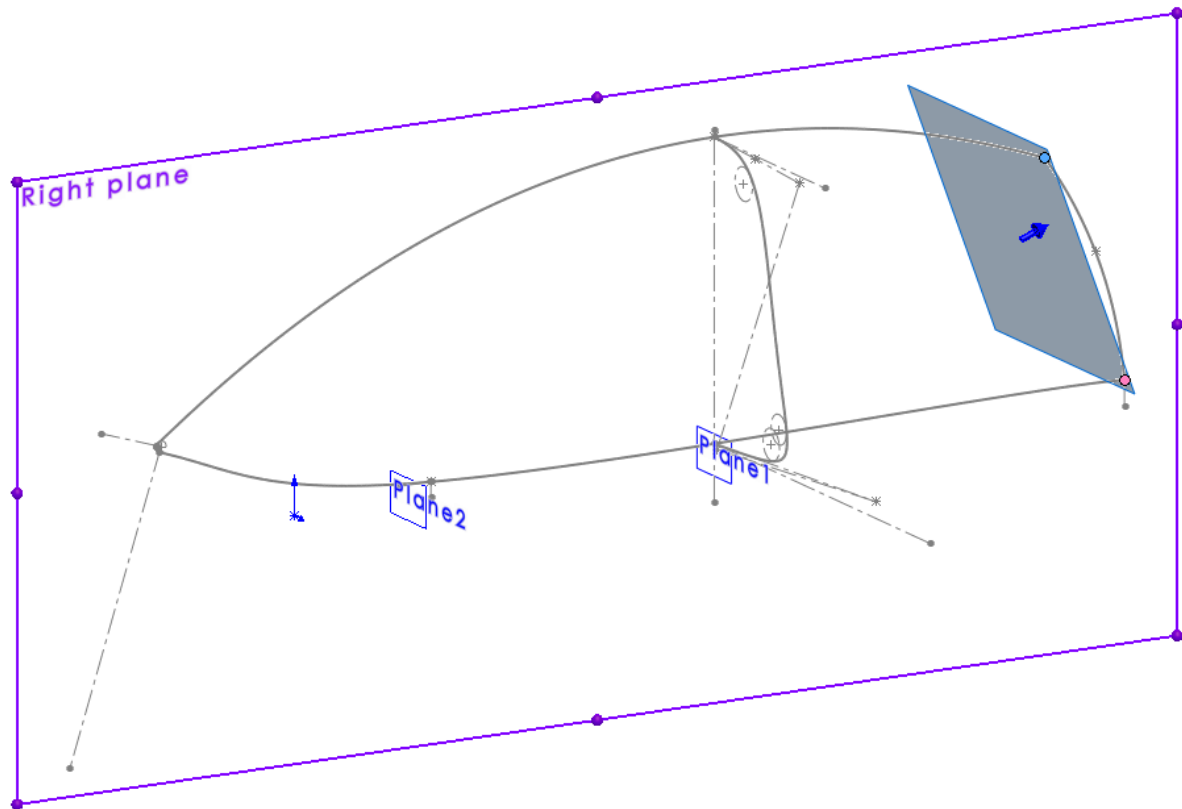


Figure II.1.21: Definition of Plane 3

II.1.1.4.6 Rear section

During many of the first attempts, the rear section was absent as the references for the curvature were given with a lateral spline (detailed explanation in paragraph II.1.1.6). Trying to change the approach, in the first attempts with a rear section, the sketch was drawn on a plane parallel to the front one but the results weren't as satisfying as a rear section drawn on an inclined plane. As the width of the upper and lower parts of the elbow sketch are indeed quite different, drawing a sketch for the rear section on an inclined plane allows the curvature gradient to be more similar over the entire section.

The plane at issue (Plane 4 in figure II.1.22) was defined with the support of a reference plane (Plane 3 in figure II.1.21) which passes through the vertices of the closing line and is perpendicular to the right plane.

II.1.1.4.7 Surface loft creation

With all the sections and profiles needed, it is now possible to take a look (figure II.1.23) at how the external surface of the fairing was drawn.

Note that, when defining a loft, be it a solid or a surface, it's mandatory to take into account the order in which the profiles are placed. As a matter of fact, Solidworks tries to connect the various profiles in the given order so, taking figure II.1.24 as an example, placing *Section_Rear* before *Section_Elbow* would generate an error.

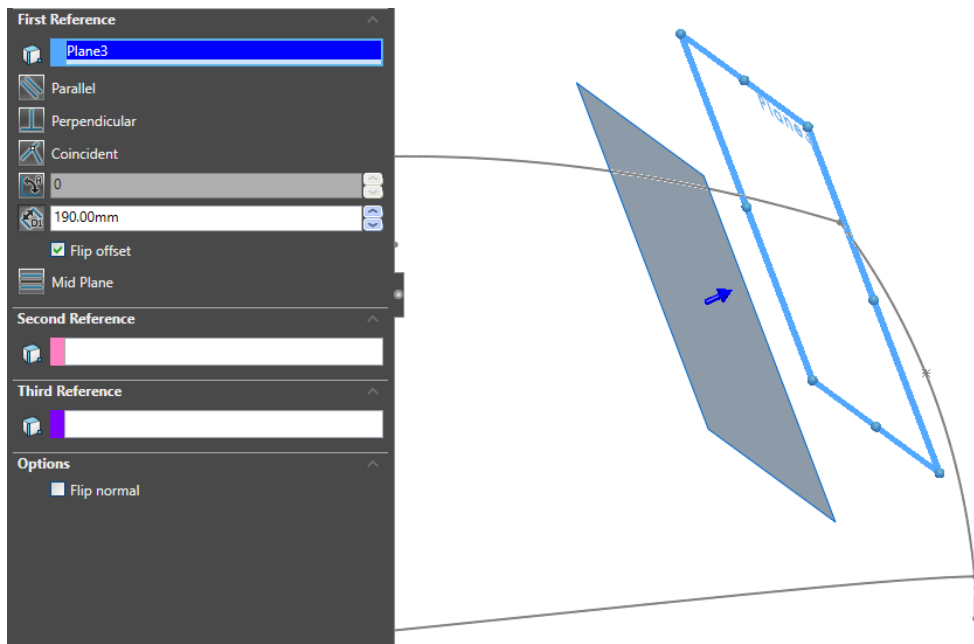


Figure II.1.22: Definition of Plane 4 for the sketch of the rear section

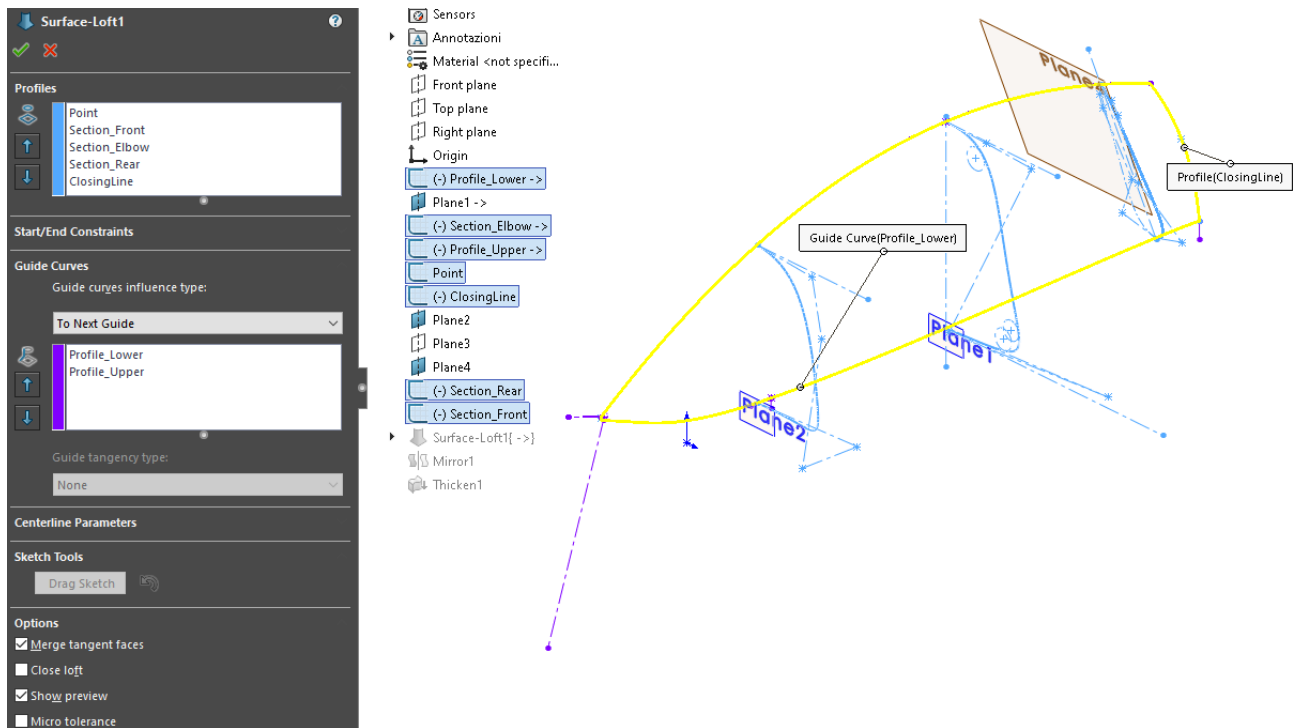


Figure II.1.23: Loft definition of fairing ADG_N59

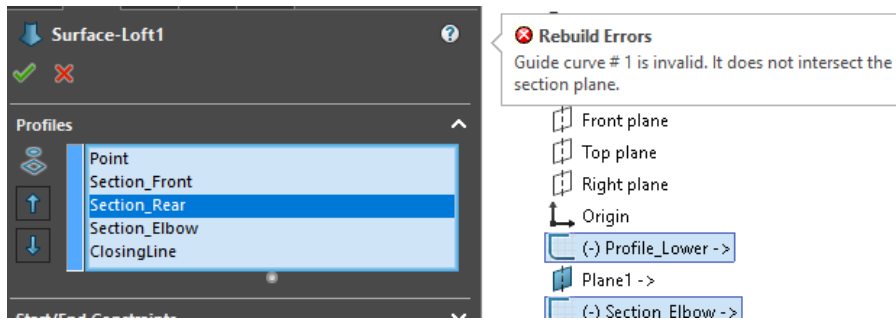


Figure II.1.24: Keep in mind the order in which the profiles should be placed in order to avoid errors during the loft generation

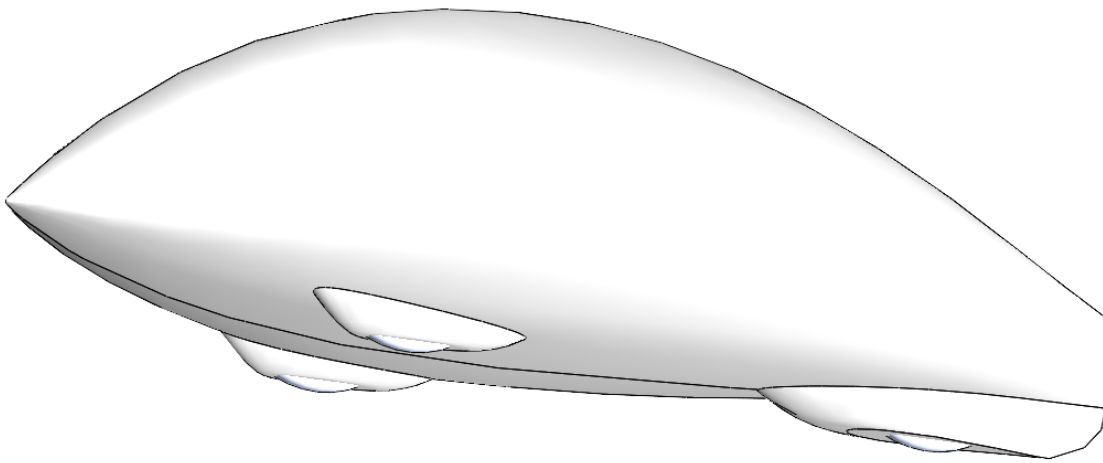


Figure II.1.25: Fairing ADG_2F_35 showing an attempt to design external wheel covers

II.1.1.5 Alternative designs: wheel covers

In a few cases, as for fairing ADG_2F_35 shown in figure II.1.25, an attempt to introduce dedicated wheel covers on the front wheels was made.

Furthermore, inspired by the Team’s bicycles Taurus and Phoenix, the possibility to have a dedicated rear wheel cover was taken into account.

In the end, though, over the various attempts conducted, the covers directly integrated in the main fairing seemed to be the best solutions.

II.1.1.6 Alternative designs: lateral spline

In some cases, rather than defining one or more sections (in ADG_N59 are front, elbow and rear) the fairing was drawn with the assistance of a lateral spline, which was constructed on the same direction of the upper and lower (i.e. from front to rear).

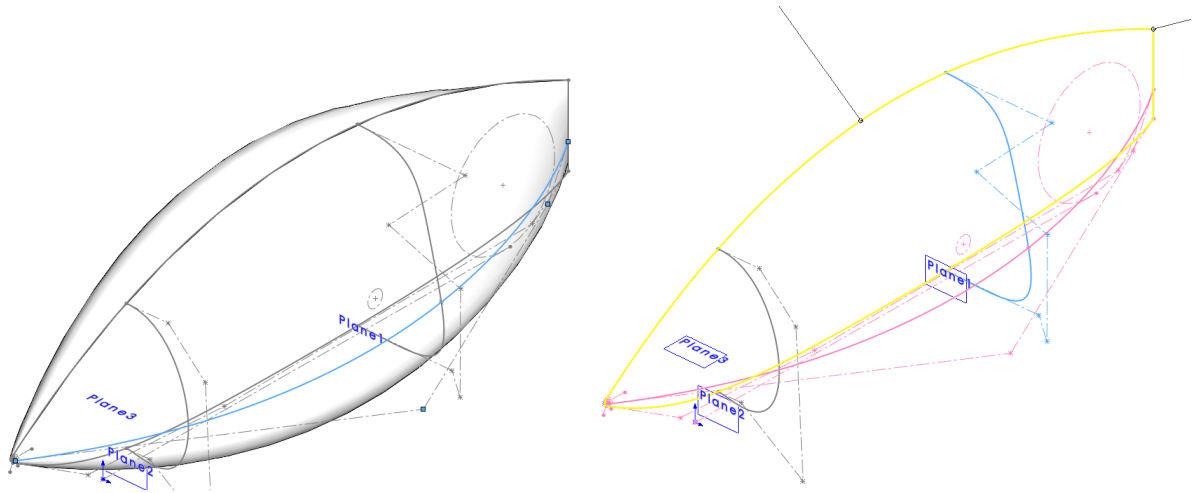


Figure II.1.26: Fairing ADG_N_6 showing a lateral spline as guide curve for the loft

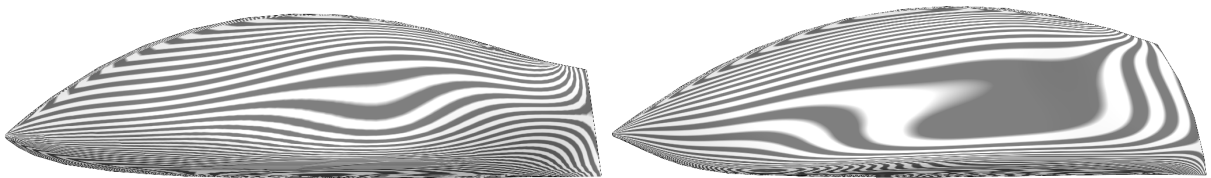


Figure II.1.27: Lateral view: zebra stripes analyses, with horizontal lines, of fairing ADG_N24 (on the left) and ADG_N59 (on the right).

II.1.1.7 Zebra stripes analysis

In Solidworks as in many other software (e.g. CATIA, NX, OnShape and Fusion 360) it's possible to conduct the **Zebra stripes analysis** which consists in a visual check of the form of a surface. The more the lines are well distributed, the smoother and more continuous the geometry is.

Note though, how the drag coefficient is not directly related to continuity: i.e., if not too big, a more pronounced variation of the shape could release both shear and pressure drag. As a matter of fact, if at first sight someone could indeed say that fairing ADG_N24 has a better shape than ADG_N59 by looking at figure II.1.27, the latter is actually far better: at 100 km/h it's got a 10% decrease in C_x as well as a 14% of total drag force reduction (C_x and total drag are slightly different as the frontal and wetted areas are different in the 2 fairing), with a massive reduction (20%) in pressure drag. This fact can be partially justified by looking at the vertical stripes (figure II.1.28), that highlights a more continuous curvature on the tail. The fact is also clearer by looking at figure II.1.31 and even more by figure II.1.32. Lastly, for completeness reasons, figure II.1.29 and II.1.30 show the front zebra stripes analyses of the two fairing discussed.

So, in the end, zebra stripes are a very useful tool to check whether or not the geometry is continuous enough but a solid background on aerodynamic studies is needed in order to generate a very efficient fairing.

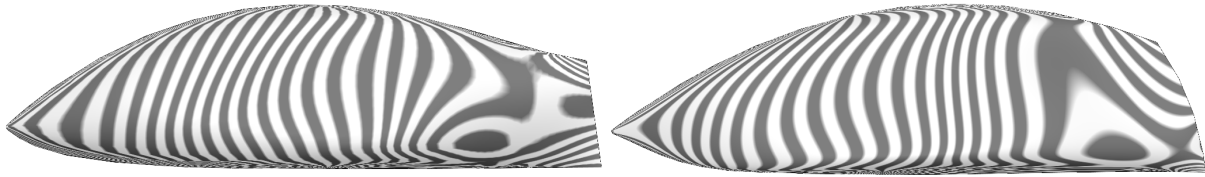


Figure II.1.28: Lateral view: zebra stripes analyses, with vertical lines, of fairing ADG_N24 (on the left) and ADG_N59 (on the right).

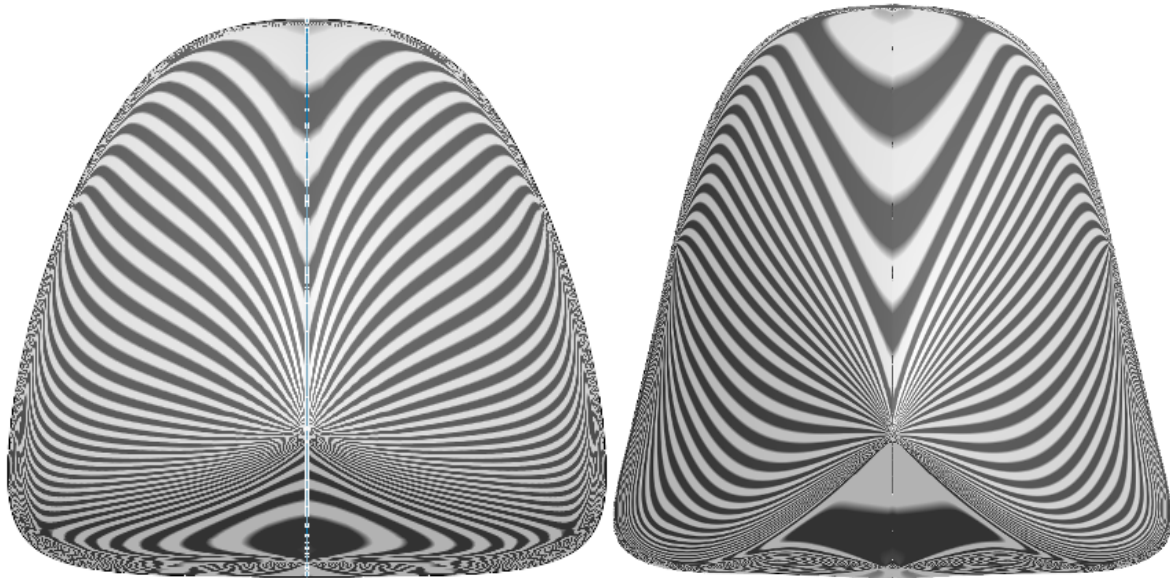


Figure II.1.29: Frontal view: zebra stripes analyses, with horizontal lines, of fairing ADG_N24 (on the left) and ADG_N59 (on the right).

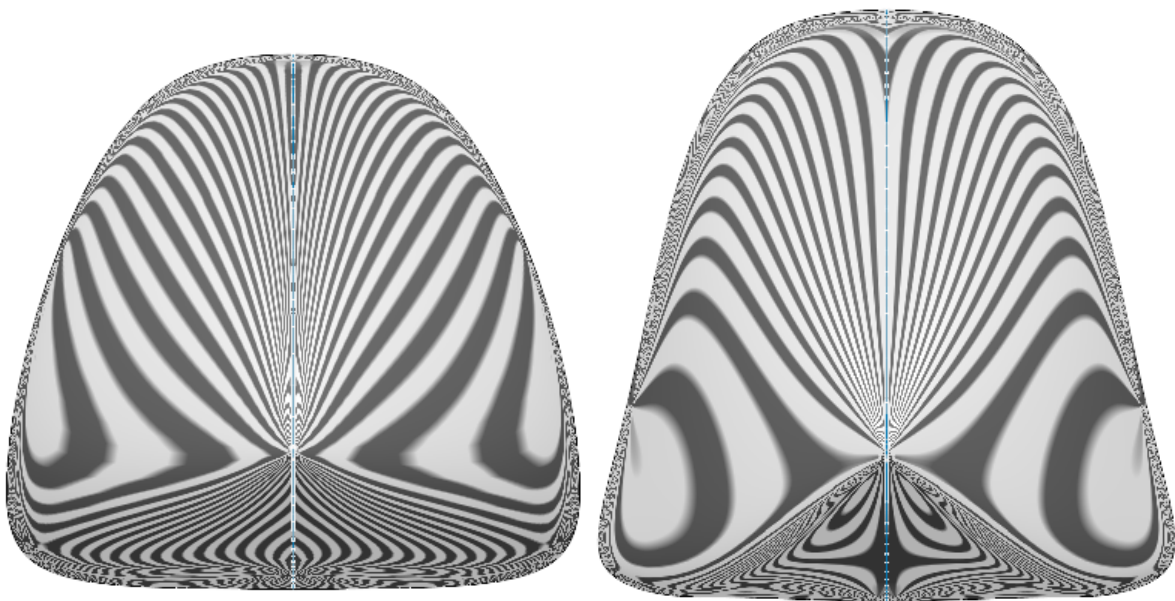


Figure II.1.30: Frontal view: zebra stripes analyses, with vertical lines, of fairing ADG_N24 (on the left) and ADG_N59 (on the right).

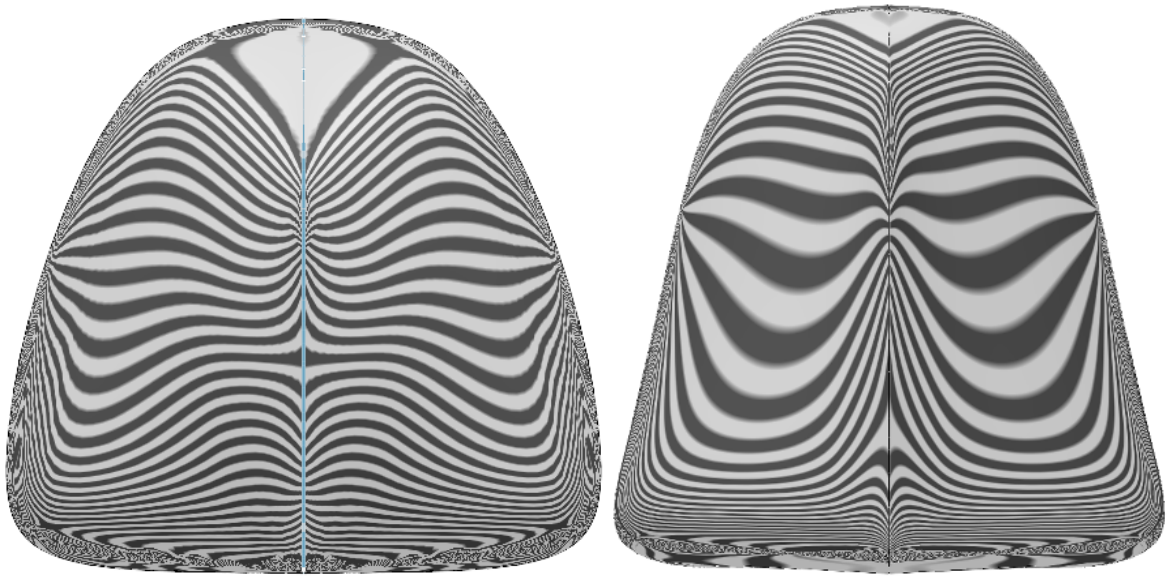


Figure II.1.31: Rear view: zebra stripes analyses, with horizontal lines, of fairing ADG_N24 (on the left) and ADG_N59 (on the right).

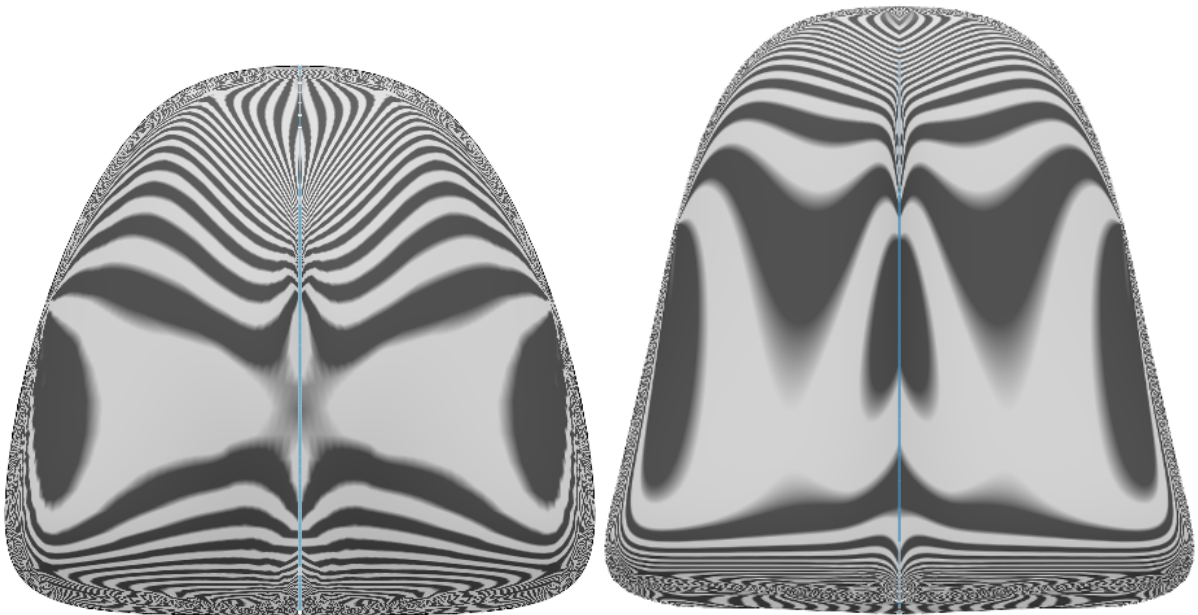


Figure II.1.32: Rear view: zebra stripes analyses, with vertical lines, of fairing ADG_N24 (on the left) and ADG_N59 (on the right).

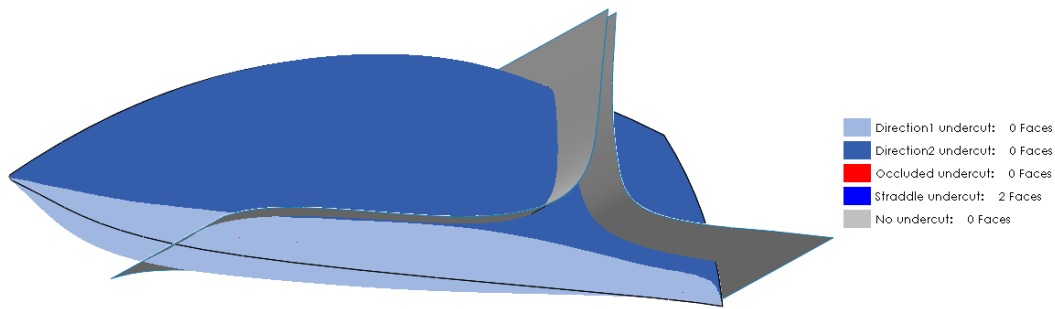


Figure II.1.33: Definition of the cuts and undercuts analysis of fairing ADG_N59

II.1.1.8 Partition lines

After the final geometry of the fairing was decided, it was necessary to define where to divide it in order to guarantee the accessibility to the vehicle. The 2 technical constraints that guided to the decision of where to put those discontinuities, where:

- undercuts, which were studied with the **Undercut Analysis** command from inside Solidworks (figure II.1.33)
- shear stress, discussed more in depth in the next few pages (because we want to place the cuts behind the partition points)
- safety reasons (the cuts should create a roll cage and completely enclose the pilot)

Undercuts in production were set to be later bypassed by making decomposable molds but were still quite important in terms of assembling the fairing altogether. As a matter of fact, thanks to the deformability of the shells, it's possible to overcome small undercuts without any problems. So, the idea was to stay as close as possible to the undercut line at least for the front fairing, which is a lot stiffer than the rear one. The final cuts surfaces are shown in figure

II.1.2 CFD simulations with Solidworks

For a fast preliminary analysis, the Solidworks Flow Simulation add-in was used.

In order to perform the analysis, it's necessary to access the wizard. There, the user is asked to:

- name the new project, in the first page
- choose the unity system in the second
- decide whether the simulation should be internal or external (we choose internal)
- define the fluid to use (in our case air with both laminar and turbulent conditions permitted)
- give custom border conditions (the default adiabatic and no rough walls were chosen)
- input the values for the intended control parameters (pressure, temperature and speed)

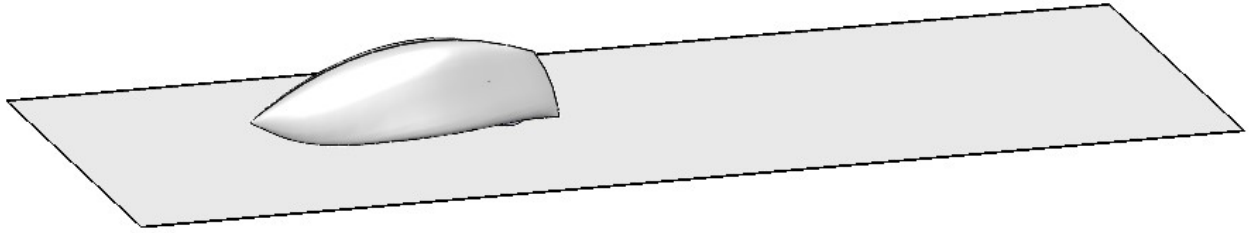


Figure II.1.34: Addition of the terrain in the assembly for the analysis

After the creation of the project, it's necessary to set the goal parameters (in our case just the Drag Force along Z was selected) and to refine the computational domain.

Note that for these analyses, a terrain was added (figure II.1.34).

II.1.3 CFD simulations with Star CCM+

The aerodynamics department of the team has used the software *Star CCM+* by *Siemens*, to conduct CFD analyses.

The full set up procedure has been done by the members of the aerodynamics section. The author has only analysed the results in order to draw better fairings over time; therefore that's what is going to be shown hereafter.

As, mentioned at the beginning in chapter I.4, some CFD parameters, like C_d and net drag force, can be synthesized as overall coefficients, while for others it's important to see the punctual value on the surface. For this reason, pressure, velocity and vorticity must be viewed in various sections and orientations. In the next pages just a few representative screenshots of Star CCM+ scenes are displayed in order to show some the characteristics of ADG_N59 (the final fairing) and some improvements on the design in comparison to a few other shells.

II.1.3.1 Wall shear stress

Figure II.1.36 shows the wall shear stress distribution of fairing ADG_N50 at 90 km/h. By comparing it with fairing ADG_N13 at the same speed (figure II.1.35), it's visible the great improvement in the position of the separation area (deep blue colour) that is clearly moved back (as a result C_d was reduced by 14%). A less pronounced, but still relevant, betterment is visible by comparing ADG_N50 with ADG_N59 shown in figure II.1.37. Note that a relatively slight adjustment in the CAD (figure II.1.38) managed to improve the shear drag force of about 4% (from 2,108 N to 2,027 N) without increasing the frontal area or the pressure drag.

II.1.3.2 Pressure drag and wake visualization

Since all these factors are related to one another, it's interesting to see how the wake changes after some improvements in the fairing's shape: note the drastic change in position of the separation points and how alterations of the bottom surface can ameliorate the containment of the wheels' wake (figures II.1.39 and II.1.40). From ADG_N13 to ADG_N59, at 90 km/h, pressure drag fell from 3,112 N to 2,027 N which is a 35% improvement.

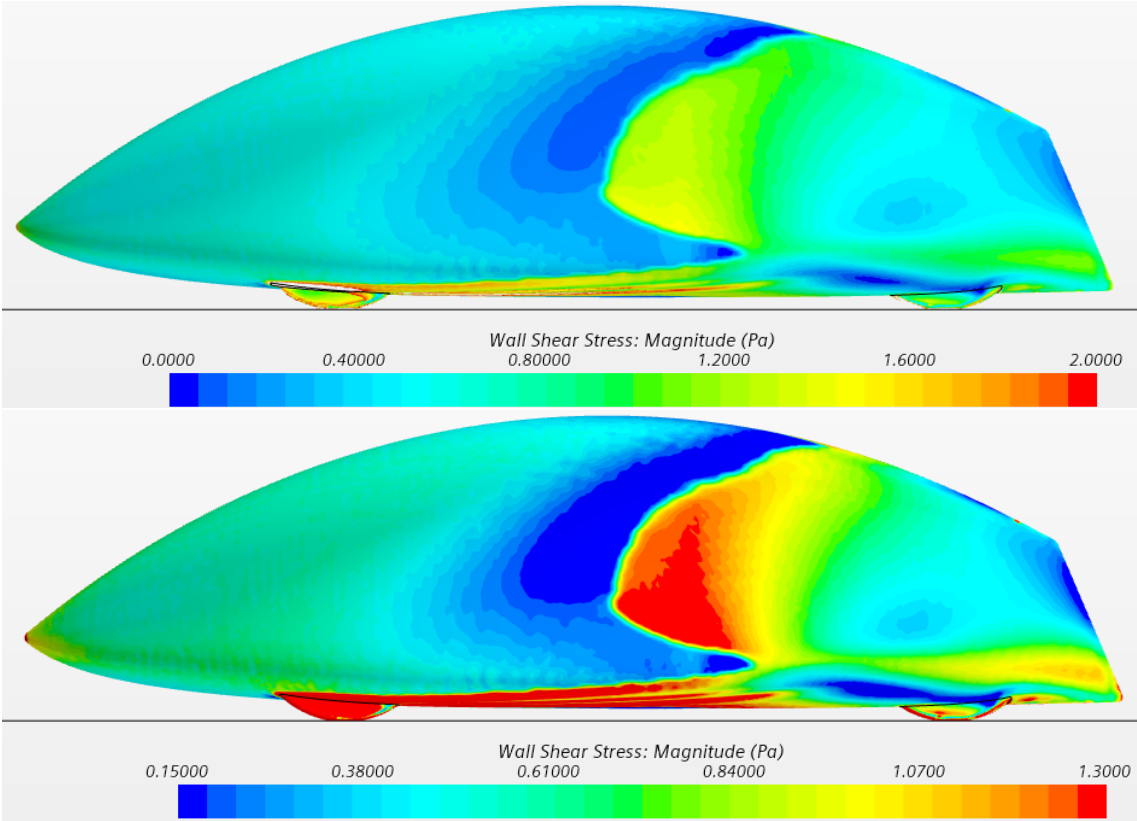


Figure II.1.35: Wall shear stress of fairing ADG_N13 at 90 km/h

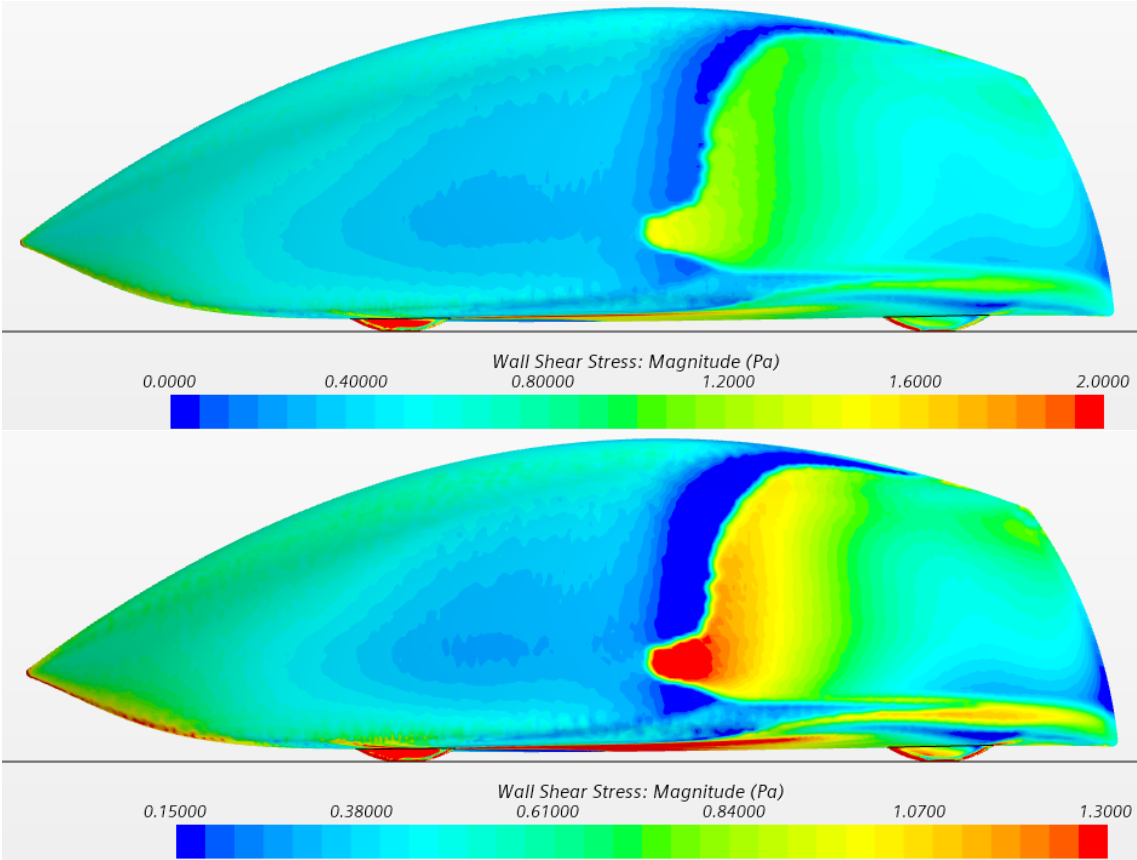


Figure II.1.36: Wall shear stress of fairing ADG_N50 at 90 km/h

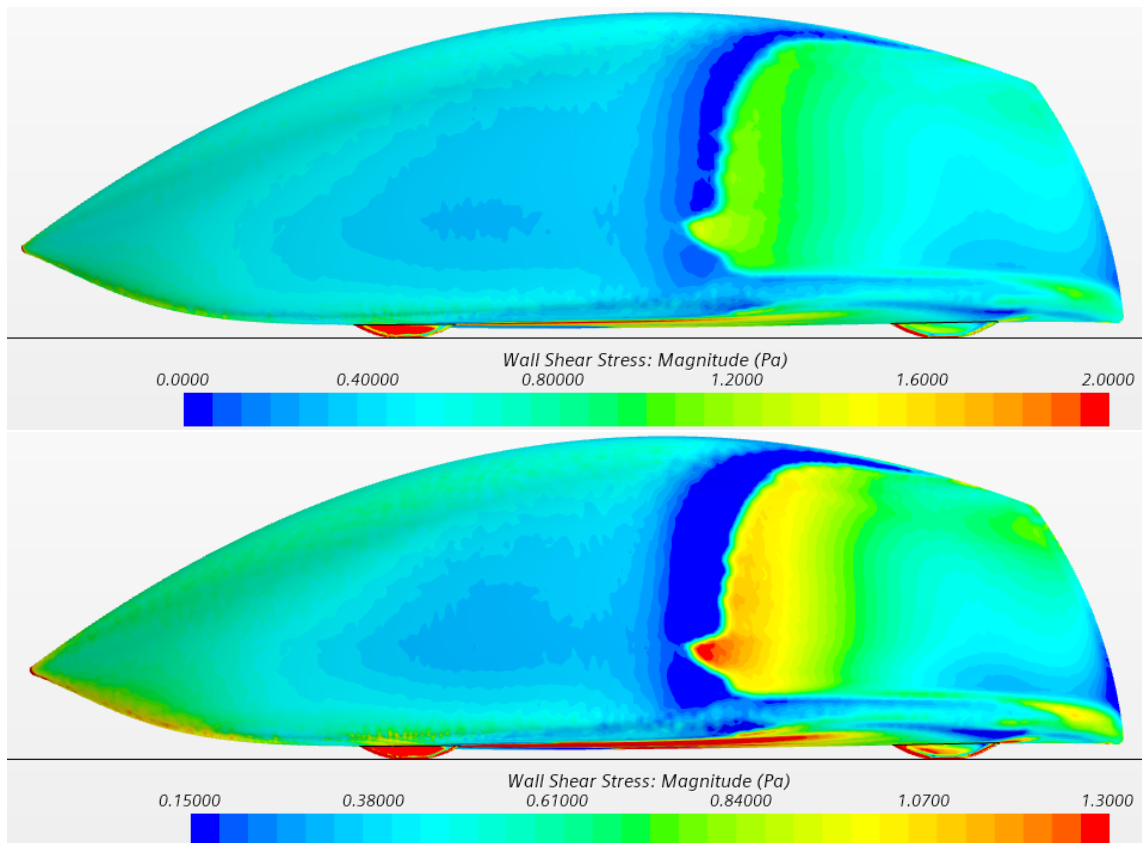


Figure II.1.37: Wall shear stress of fairing ADG_N59 at 90 km/h

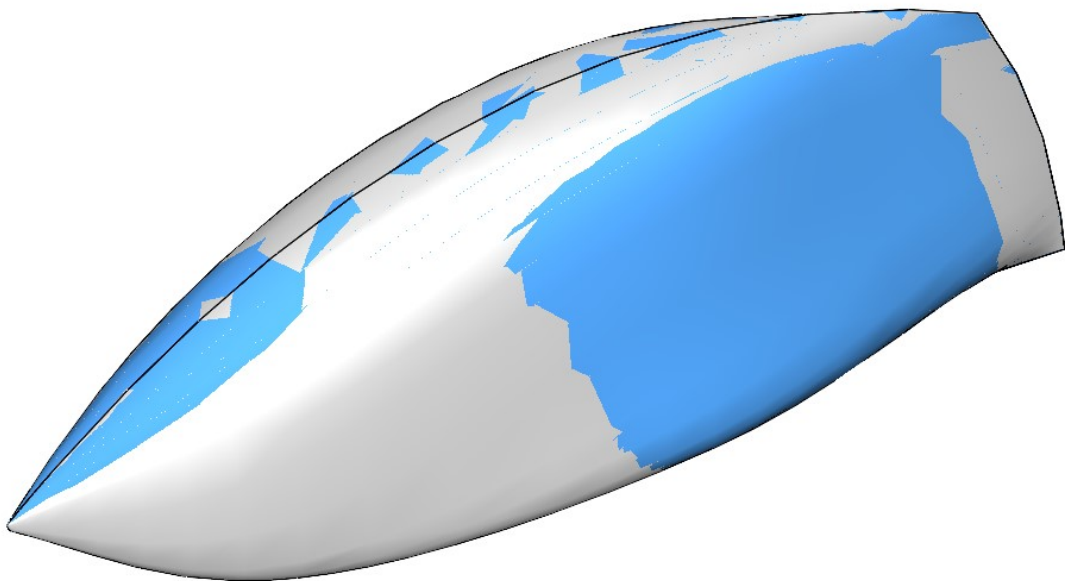


Figure II.1.38: Overlapping CADs of ADG_N50 (in grey) and ADG_N59 (in blue)

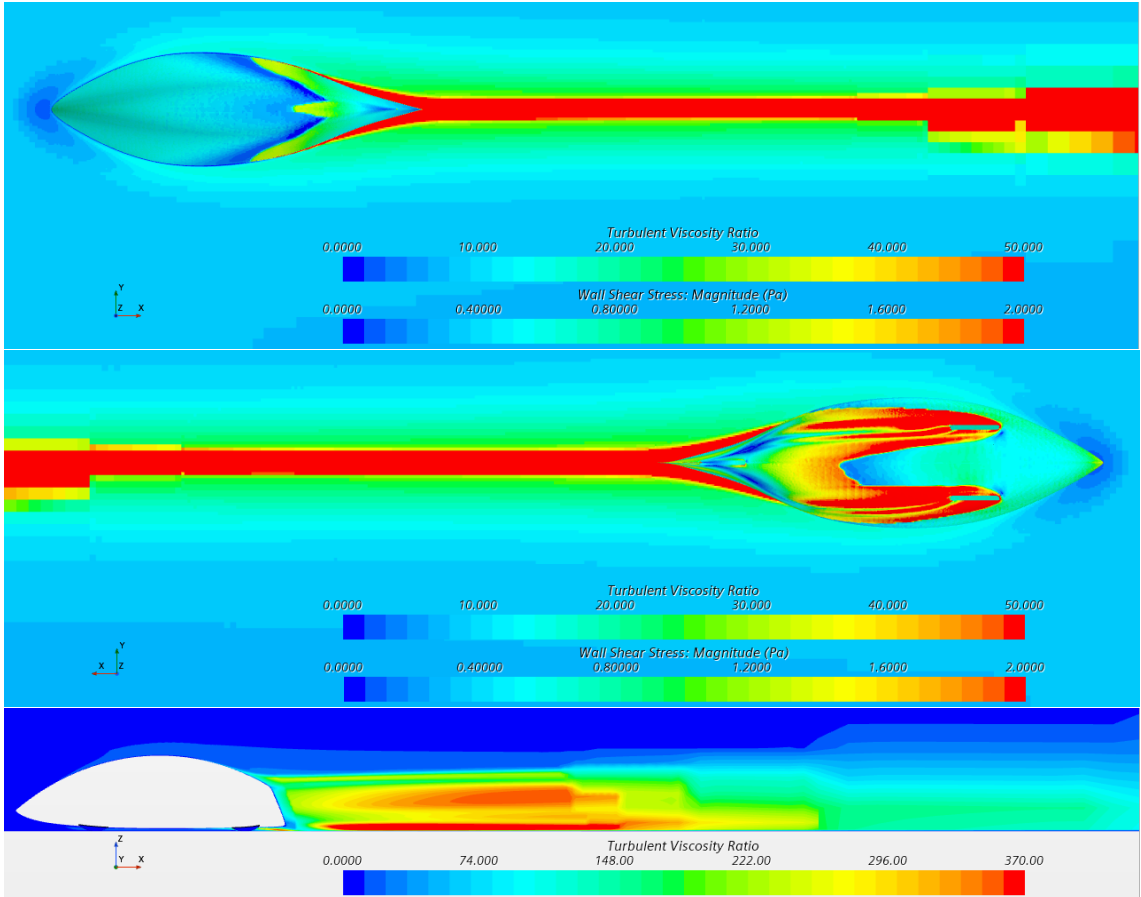


Figure II.1.39: Wake of fairing ADG_N13 at 90 km/h

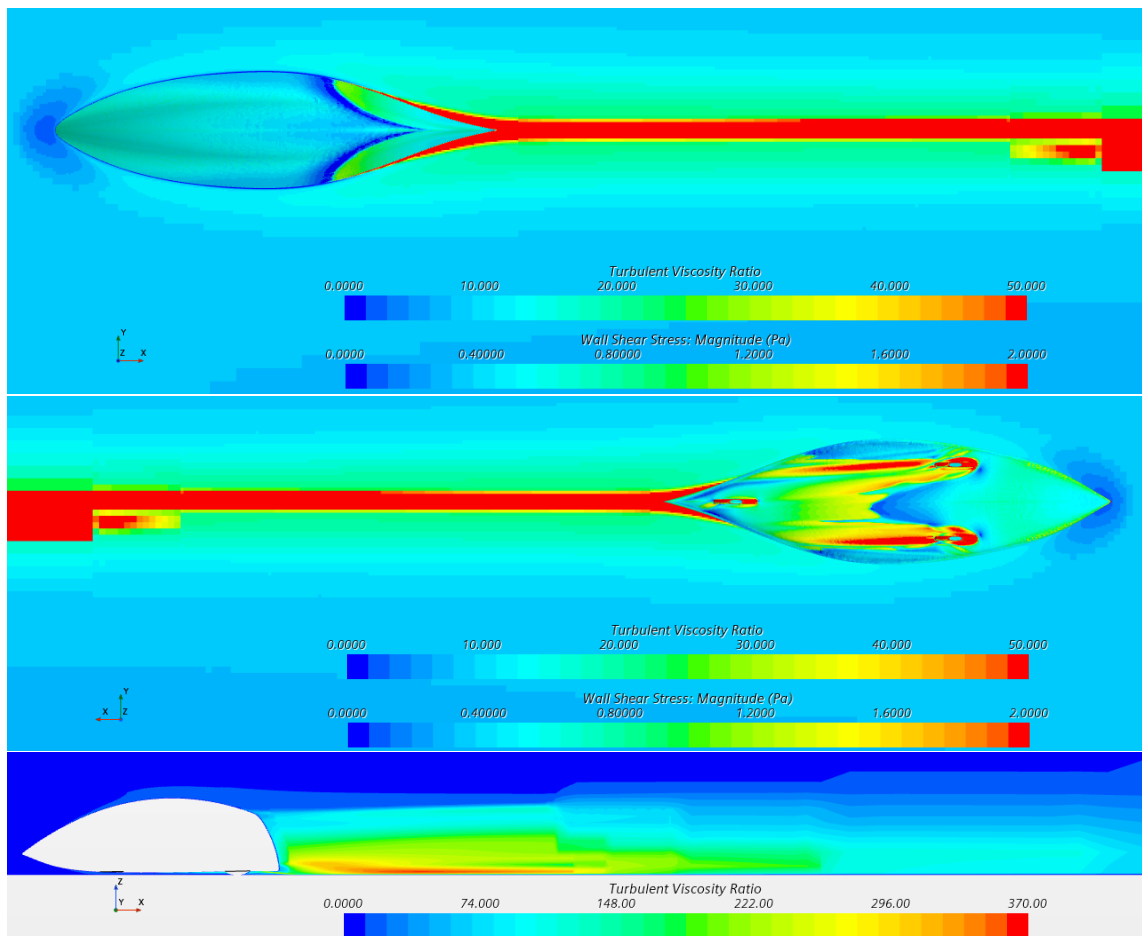


Figure II.1.40: Wake of fairing ADG_N59 at 90 km/h

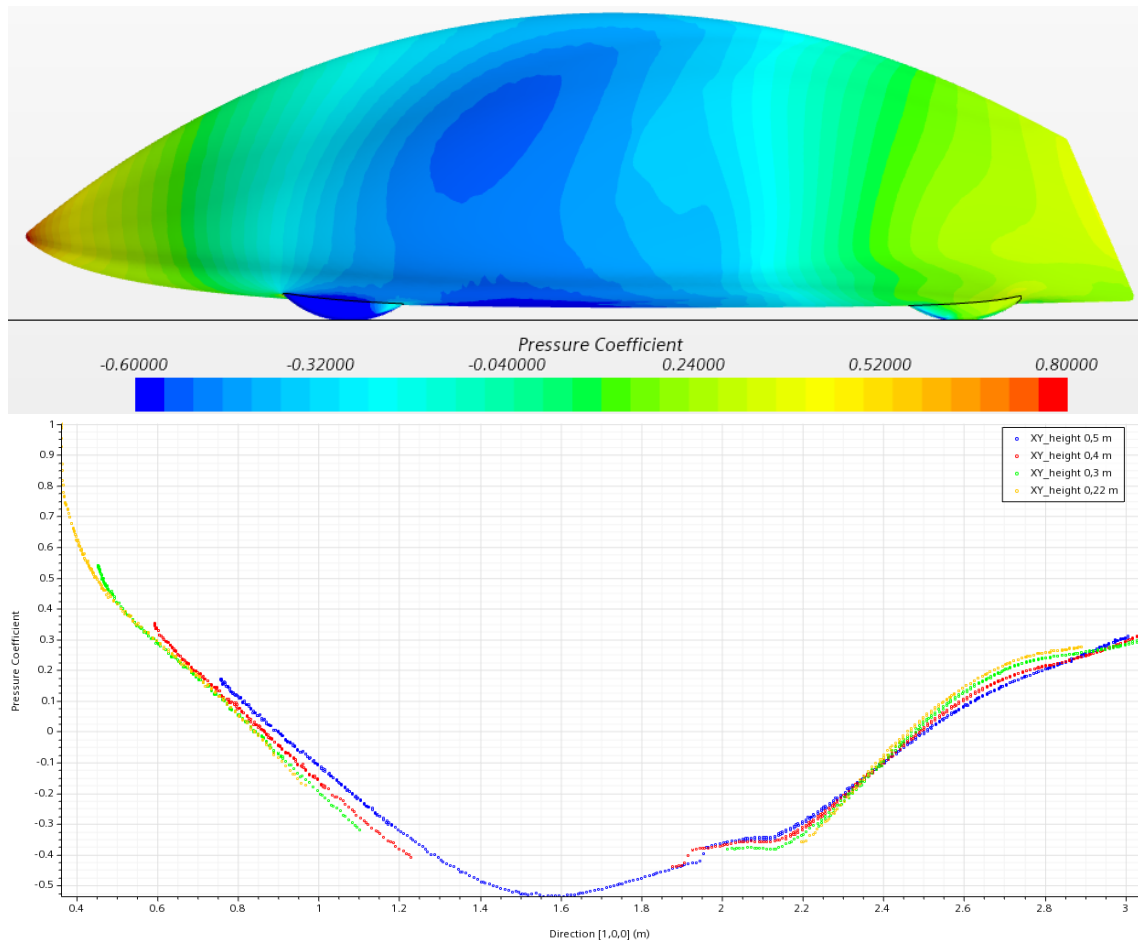


Figure II.1.41: C_p of fairing ADG_N13 at 90 km/h

II.1.3.3 Pressure coefficient

Another interesting factor too take into consideration is the C_p : looking at figures II.1.41 and II.1.42, one may think that, thanks to the higher pressure recovery, ADG_N13 could be the better fairing; though, due to the massive aforementioned wake, pressure drag had actually taken an impressive fall. So, once again, it's important to always look at many parameters before taking a final decision.

II.1.3.4 C_x and power comparison of the few best fairings

In Star CCM+ it's also possible to compute the C_d of the fairings. Multiple analyses conducted at different speeds where done on a few of the best fairings, in order to extract the trend of this parameter over velocity (figure II.1.43). The "best" were earlier deduced by simulations at 100 km/h and, in some cases, at 90 km/h too.

Finally, the total aerodynamic power dissipated was calculated by the definition:

$$P_{aero} = v \cdot F_{drag}$$

The lack of improvement led to stop trying to find a better shape (keep in mind that we were running late, too). In the end, ADG_N57 was maybe slightly better but, since it could have given some problems in terms of fitting the riders into the prototype, eventually fairing ADG_N59 was chosen.

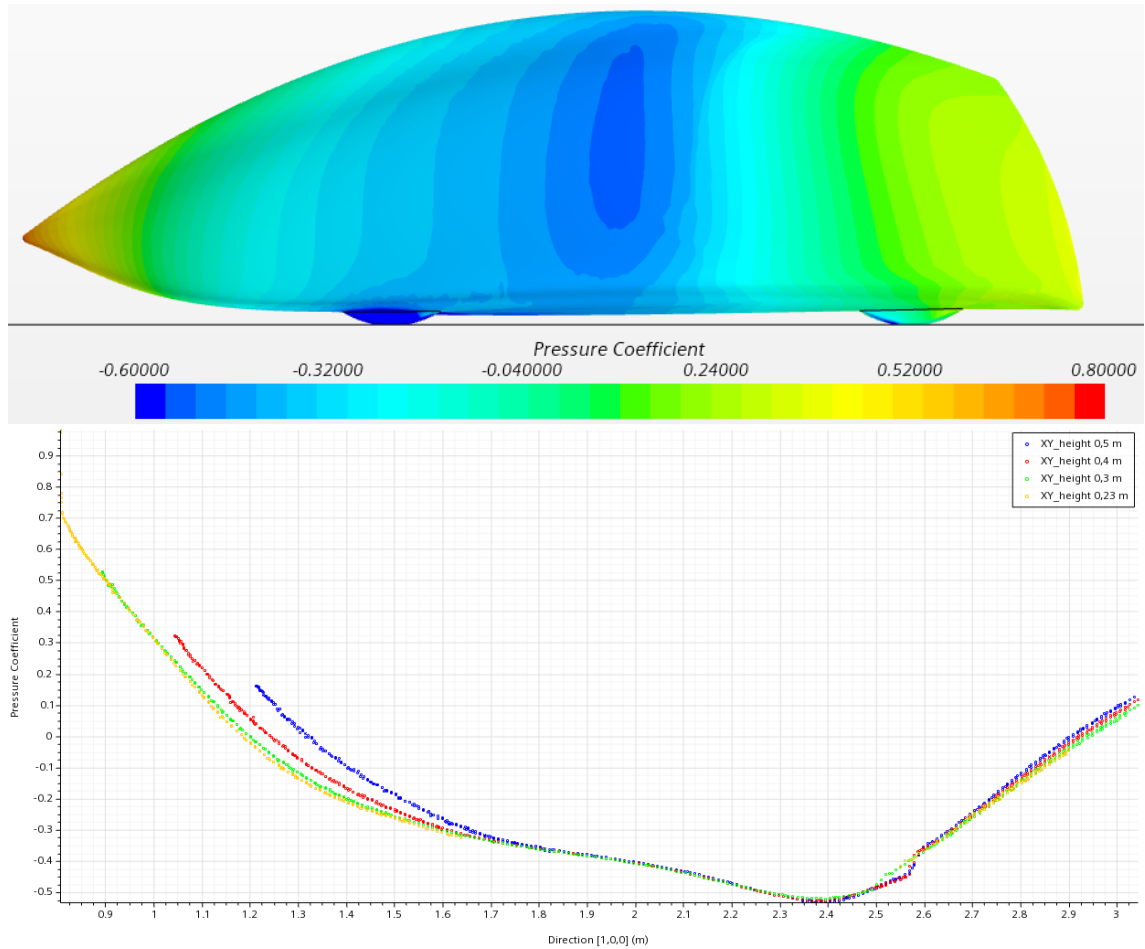


Figure II.1.42: C_p of fairing ADG_N59 at 90 km/h

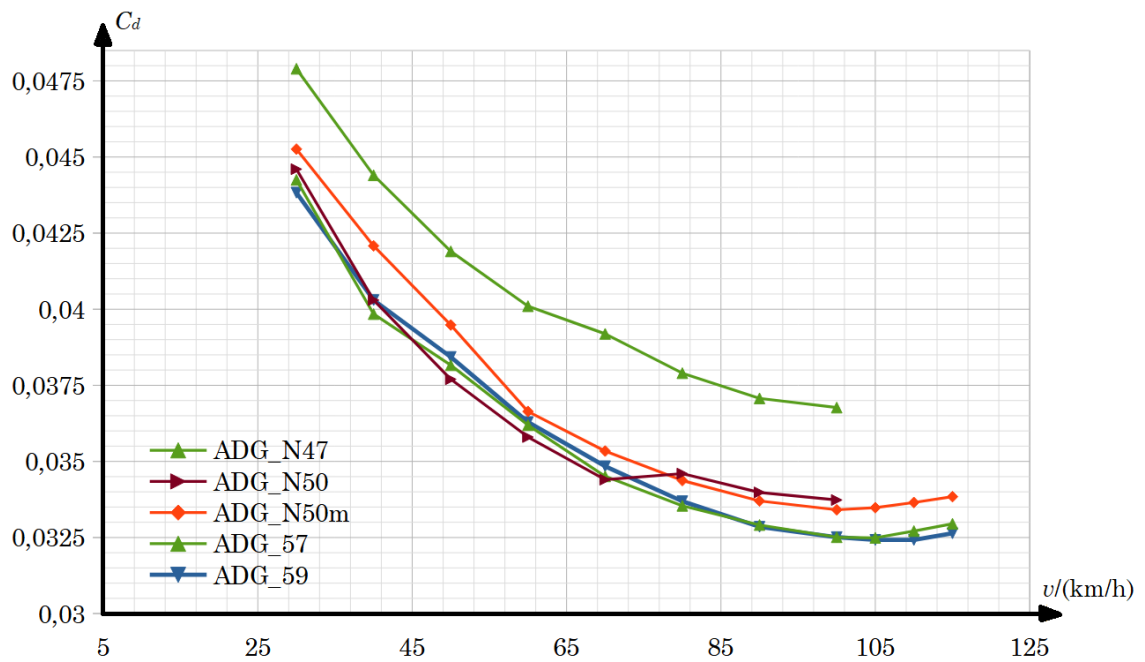


Figure II.1.43: Comparison by C_d of the best 3 fairings

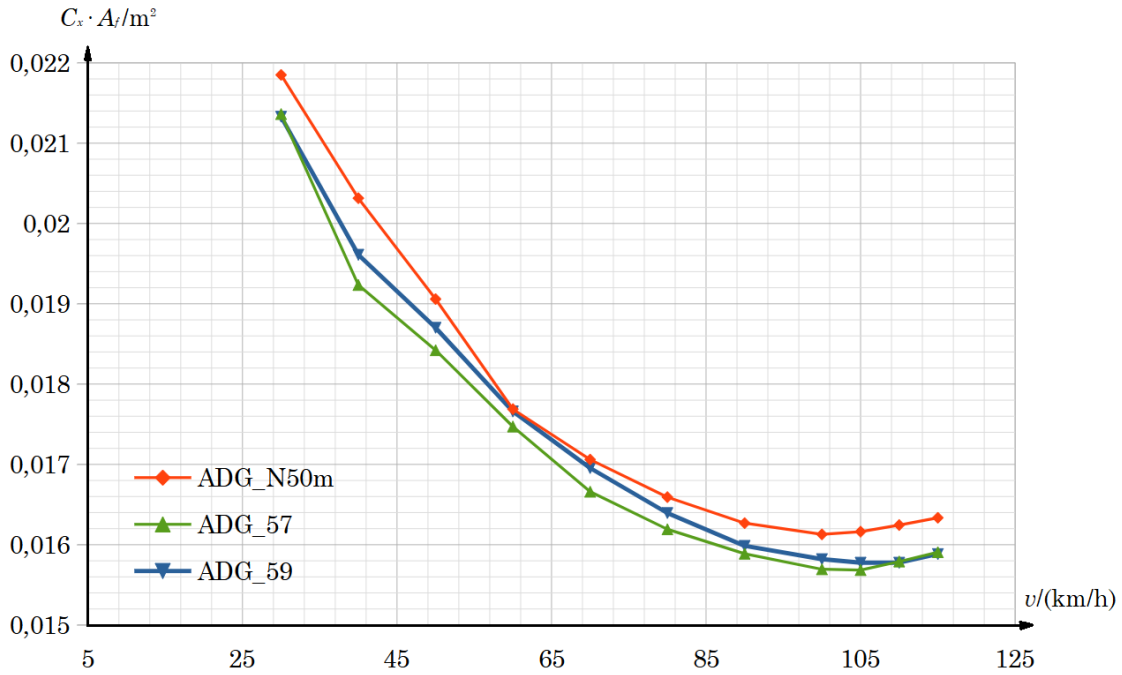


Figure II.1.44: Comparison by $C_x \cdot A_f$ of the best 3 fairings

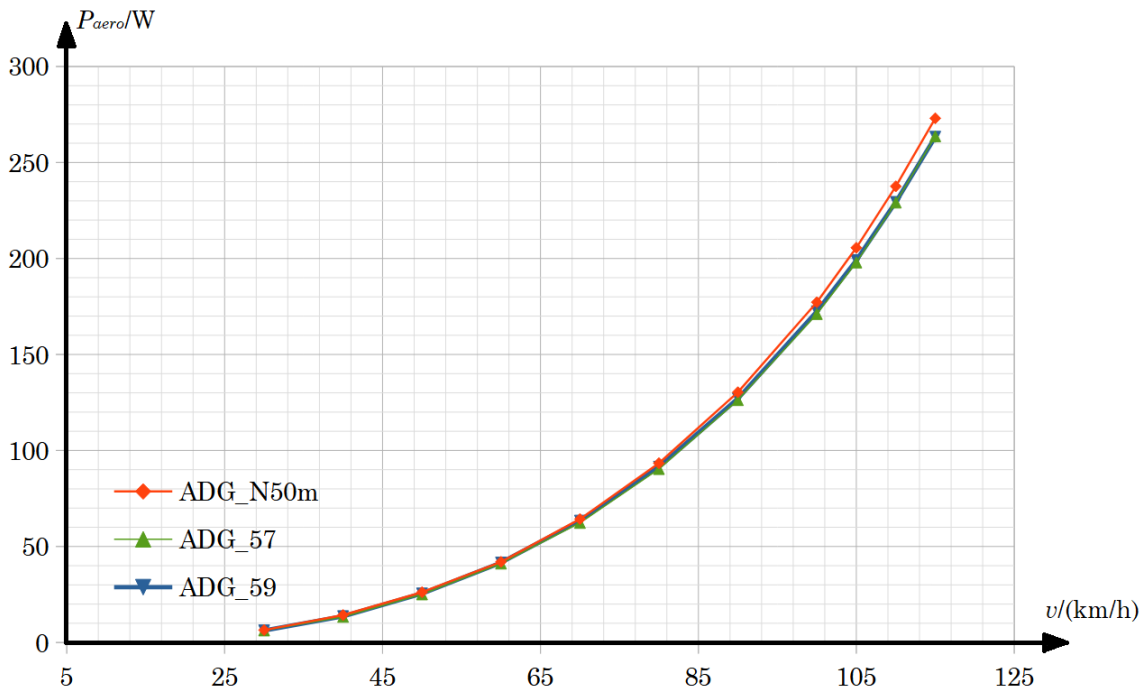


Figure II.1.45: Comparison of the best 3 fairings by power lost in aerodynamic dissipation

Chapter II.2

Design of the structural laminated parts

All composites parts of the trike that required professional molds in production were accurately studied with structural analyses, mainly conducted by Riccardo Grossi, head of the FEM department at the time. Therefore, even though the author drew all the components presented in this chapter, the paternity of the simulations shouldn't be entitled to him.

The layouts hereafter presented are the result of the simulations conducted with HyperWorks environment, based on the pre-processor HyperMesh and making use of OptiStruct solver by Altair (figures II.2.1-II.2.2).

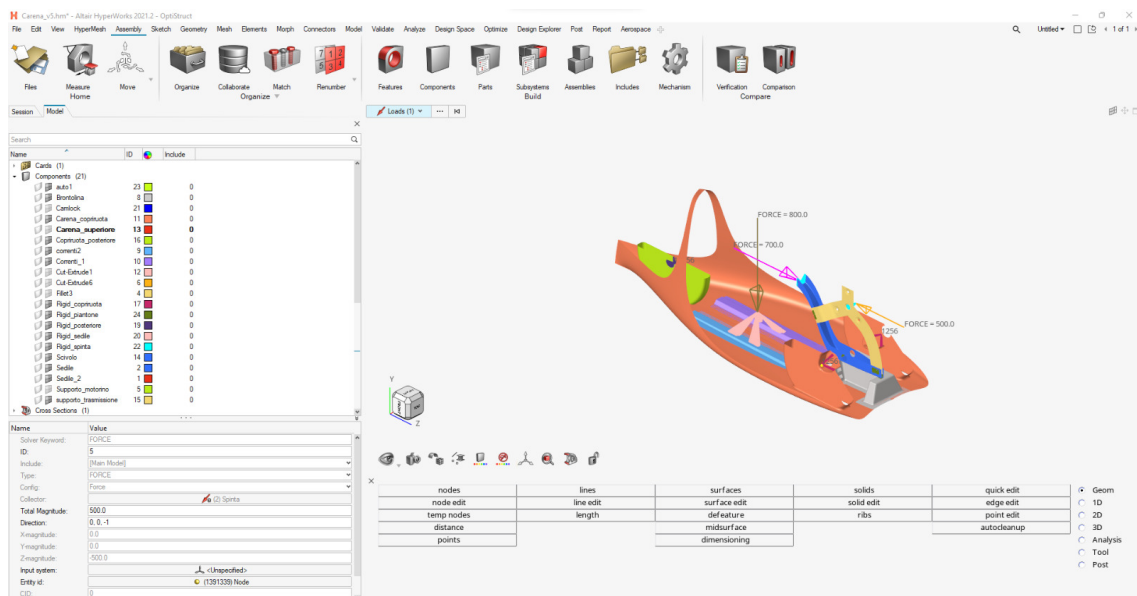


Figure II.2.1: Setting up a FEM in Hyperworks environment

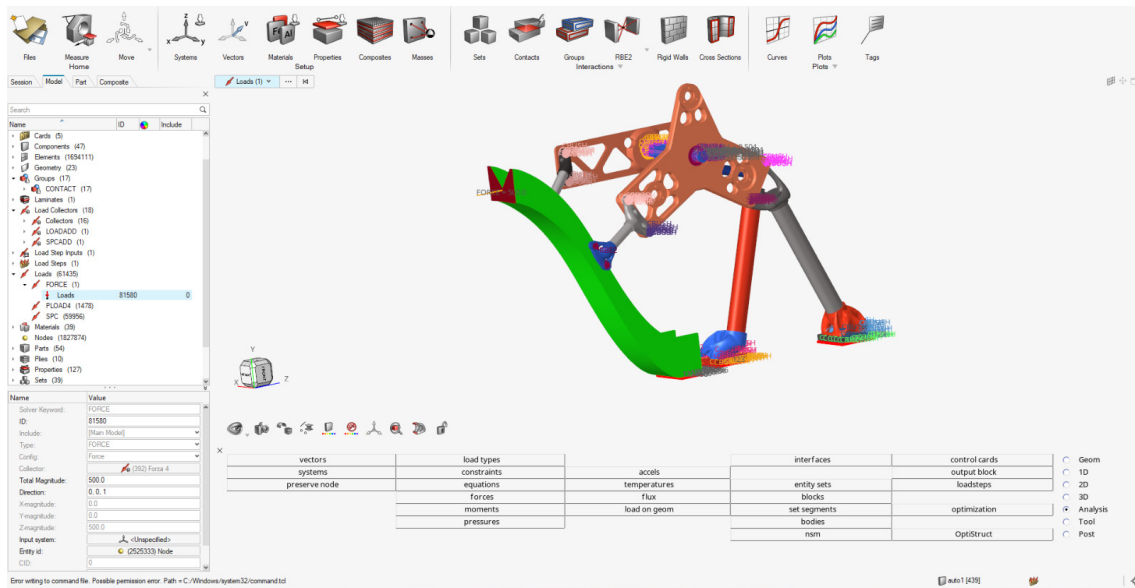


Figure II.2.2: Detail of the set up of a subsystem's FEM analysis

II.2.1 Aerodynamic (front) fairing

The stratification (table II.2.1) of the front fairing (figure II.2.3) was made thanks to the know-how acquired by the team over the years. As a matter of fact, with these materials and similar stratification, some of the Team's prototypes have sustained crashes at high speed with very light injuries for the rider and (as reported in section I.2.2.3) not irreparable damages to the fairing. Moreover, the fairing itself showed to be structurally good when after a roll over (see chapter III.3) didn't get damaged.

Reinforcement of 0,4 mm thick glass fiber, were placed on the borders in order to create an interface for the mating with the structural fairing.

Material	Orientation/deg	Thickness/mm
Carbon, T300	0	0,2
PVC		3
Carbon, T300	0	0,2
Kevlar	0	0,2

Table II.2.1: Stratification of Cerberus's aero fairing



Figure II.2.3: CAD image of the surface used for the front fairing's molds generation

II.2.2 Structural (central) fairing

Table II.2.2 shows the stratification of the structural fairing (figure II.2.4). In the relatively narrow zone set between the front and rear fairing connections, though, some scrap layers were added in order to make a more robust roll cage in case of impact.

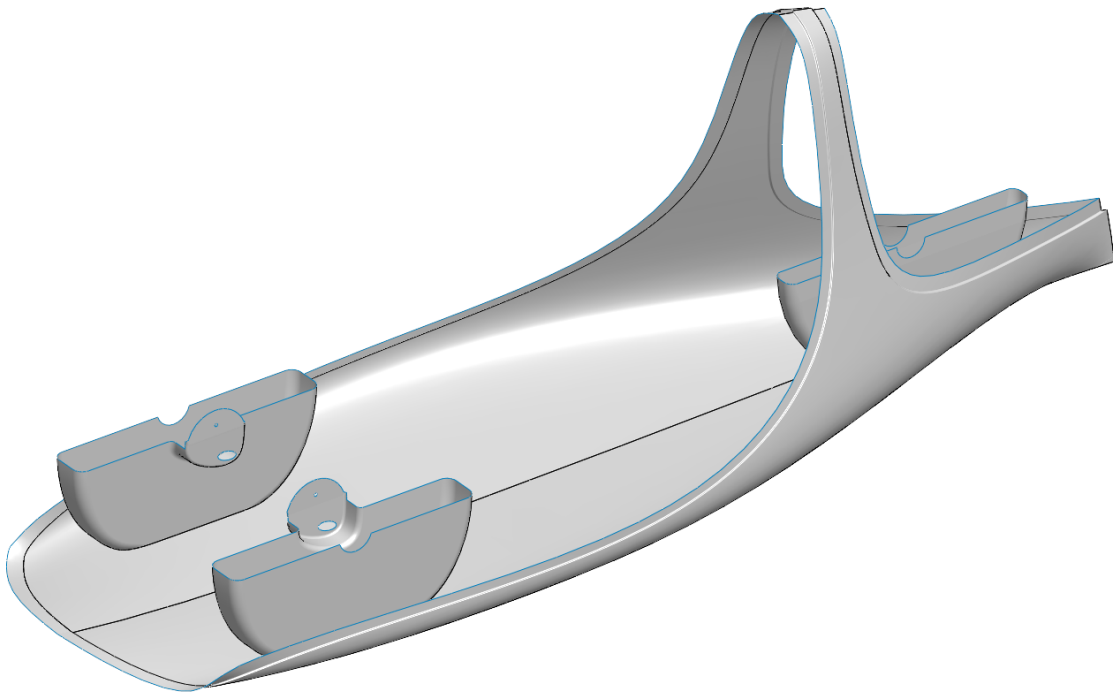


Figure II.2.4: CAD image of the surface used for the structural fairing's molds generation

Material	Orientation/deg	Thickness/mm
Carbon, T300	0	0,2
Carbon, UD	0	0,15
Carbon, T300	0	0,2
Carbon, UD	0	0,15
Carbon, T300	0	0,2
Carbon, T300	45	0,2
Carbon, T300	0	0,2
Carbon, T300	45	0,2
Carbon, T300	0	0,2
PVC		10
Carbon, T300	0	0,2
Carbon, T300	45	0,2
Carbon, T300	0	0,2
Carbon, T300	45	0,2
Carbon, T300	0	0,2
Carbon, UD	0	0,15
Carbon, T300	0	0,2
Carbon, UD	0	0,15
Carbon, T300	0	0,2

Table II.2.2: Stratification of Cerberus's structural fairing

II.2.2.1 Bottom wheel covers

The bottom wheel (figure II.2.5) covers have a different layup than that of the rest of the structural fairing (table II.2.3).

Material	Orientation/deg	Thickness/mm
T300	0	0,2
T300	45	0,2
T300	0	0,2
PVC	-	10
T300	0	0,2
T300	45	0,2
T300	0	0,2

Table II.2.3: Stratification of Cerberus's structural fairing

On the borders, PVC is replaced with double carbon layers (table II.2.4). Aluminum plates are colaminated on the vertical face that is to be connected to the uprigths with the rod-end bearings.

Material	Orientation/deg	Thickness/mm
T300	0	0,2
T300	45	0,2
T300	0	0,2
T300	0	0,2
T300	45	0,2
T300	0	0,2
T300	0	0,2
T300	45	0,2
T300	0	0,2
T300	0	0,2
T300	45	0,2
T300	0	0,2

Table II.2.4: Stratification of Cerberus's structural fairing



Figure II.2.5: Structural fairing - bottom wheel covers

II.2.3 Tail (rear) fairing

Table II.2.5 shows the layup of the rear fairing (figure II.2.6). Glass fibre was chosen for this component in order to allow a good data transmission of the various sensors and of the radio signals, because glass is not a conductor, in contrast to C which is a semi-conductor.

Reinforcement of 0,4 mm thick glass fiber, were placed on the borders in order to create an interface for the mating with the structural fairing and on the junction of the 2 halves of the mold .

Material	Orientation/deg	Thickness/mm
Glass	0	0,2
Glass	45	0,2
Glass	0	0,2
Glass	45	0,2
Glass	0	0,2

Table II.2.5: Stratification of Cerberus's rear fairing

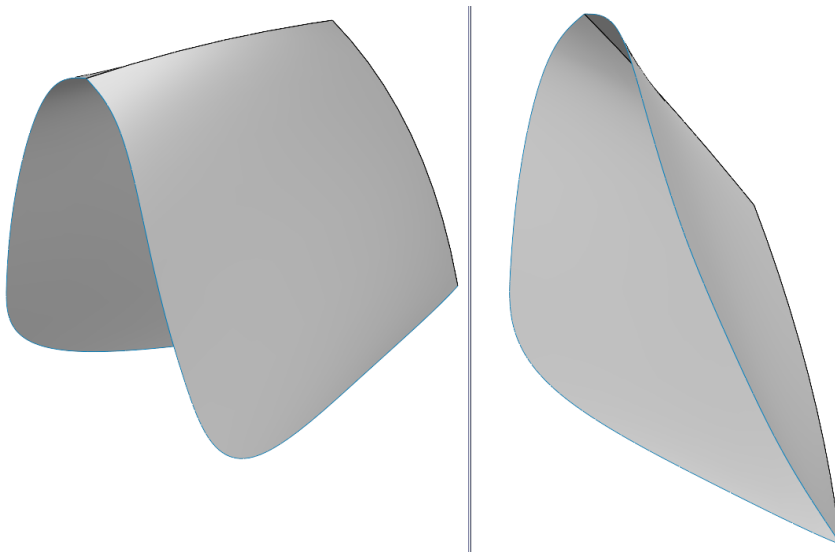


Figure II.2.6: CAD image of the surface used for the rear fairing's molds generation

II.2.4 Upper wheel covers

Note that the left wheel cover (figure II.2.8) couldn't be produced from the same mold of the right (figure II.2.7) one since the surface is not symmetric in a lateral view. The stratification (table II.2.6), though, is the same for both as well as for the rear one (figure II.2.9). Only 3 layers were used since the front ones shouldn't be loaded with anything but the air pressure and on the rear the external load is really light (there's the air filter attached on top of the hole).

Material	Orientation/deg	Thickness/mm
Carbon, T300	0	0,2
Carbon, T300	0	0,2
Carbon, T300	0	0,2

Table II.2.6: Stratification of Cerberus's upper wheel covers (for both of the front and the rear)

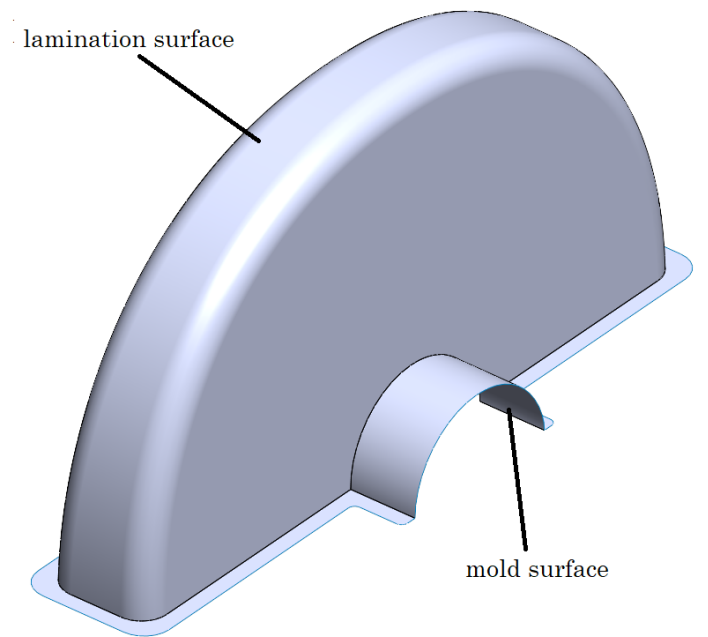


Figure II.2.7: CAD image of the surface used for the front right wheel cover's mold generation

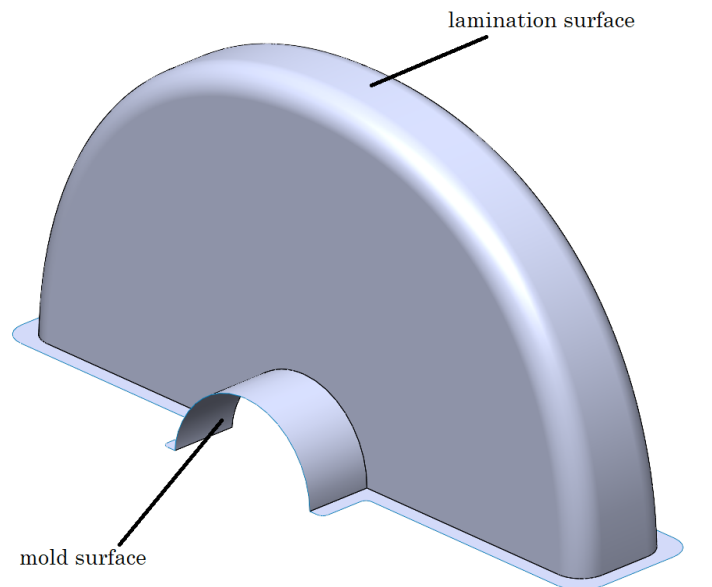


Figure II.2.8: CAD image of the surface used for the front left wheel cover's mold generation

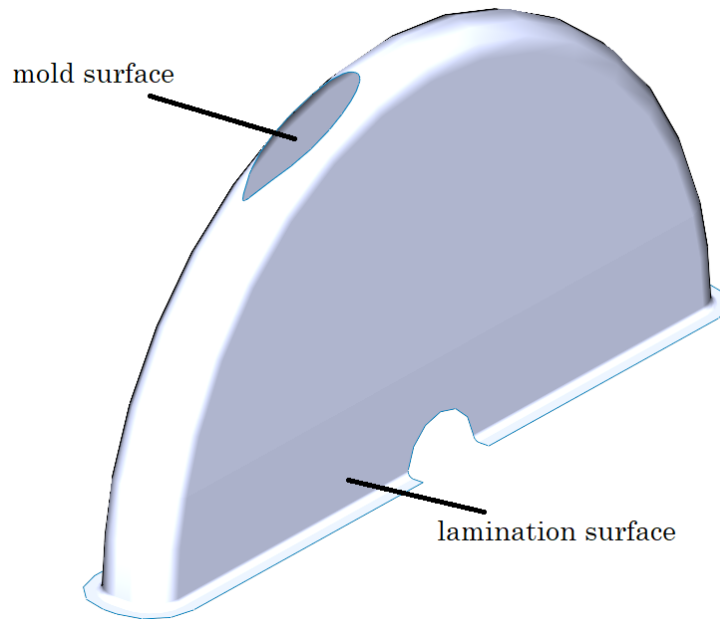


Figure II.2.9: CAD image of the surface used for the rear wheel cover's mold generation

Material	Orientation/deg	Thickness/mm
Carbon, T300	0	0,2
Carbon, T300	0	0,2
Carbon, T300	45	0,2
Carbon, T300	45	0,2
Carbon, T300	0	0,2
Carbon, T300	0	0,2
Carbon, T300	45	0,2
Carbon, T300	45	0,2
Carbon, T300	0	0,2
Carbon, T300	0	0,2

Table II.2.7: Stratification of Cerberus's basin

II.2.5 Basin

The basin's layup is shown in table II.2.7. The basin (figure II.2.10) is an important component that has the double function of stiffening the structure and of supporting the Slide and other structural interfaces presented in the next chapter.

II.2.6 Slide

The slide (figure II.2.11) is a very stiff component (layup in table II.2.8) which was probably overdimensioned because initially there were some doubts on the FEM analysis conducted in terms of displacements. It also presents some aluminum plates colaminated in the areas that were later bolted to the AlSi10Mg parts discussed in section II.3.1.

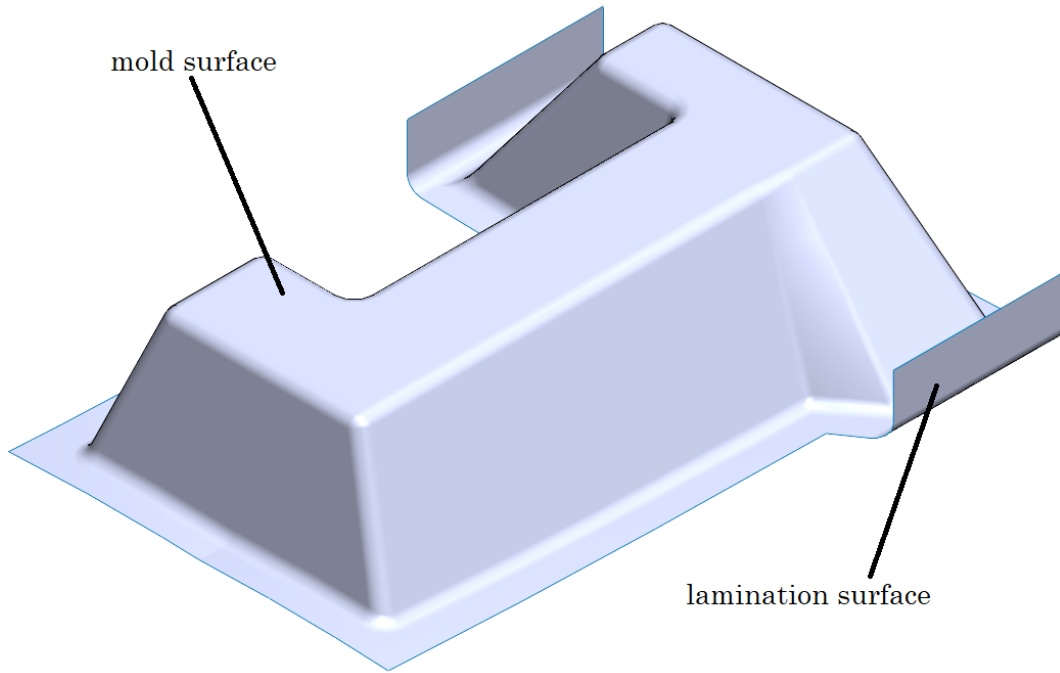


Figure II.2.10: CAD image of the surface used for the basin's mold generation

Material	Orientation/deg	Thickness/mm
Carbon, T300	0	0,2
Carbon, T300	0	0,2
Carbon, T300	45	0,2
Carbon, T300	45	0,2
Carbon, T300	0	0,2
Carbon, T300	0	0,2
Carbon, T300	45	0,2
Carbon, T300	45	0,2
Carbon, T300	0	0,2
Carbon, T300	0	0,2
PVC		6
Carbon, T300	0	0,2
Carbon, T300	0	0,2
Carbon, T300	45	0,2
Carbon, T300	45	0,2
Carbon, T300	0	0,2
Carbon, T300	0	0,2
Carbon, T300	45	0,2
Carbon, T300	45	0,2
Carbon, T300	0	0,2

Table II.2.8: Stratification of Cerberus's slide

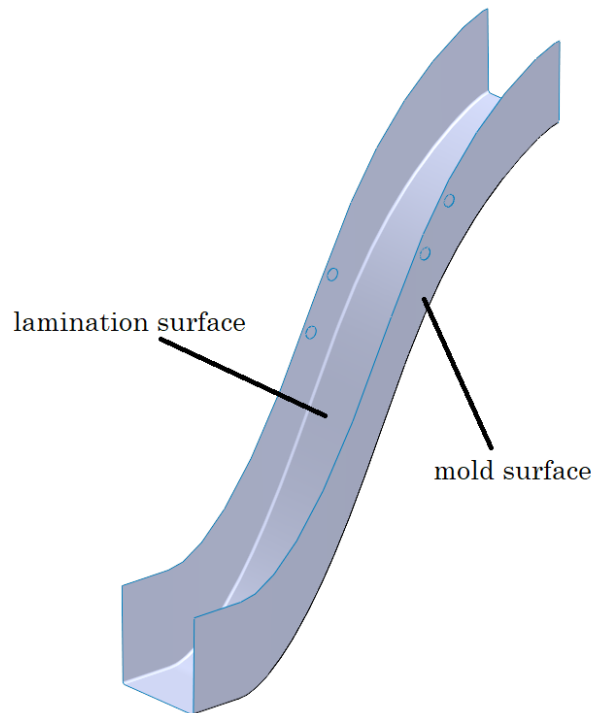


Figure II.2.11: CAD image of the surface used for the slide's mold generation

II.2.7 Bottom longerons

The first function of the bottom longerons (figure II.2.12) is to act as a reinforcement that contrasts the flexion generated by the weight; therefore the stratification (table II.2.9) is mainly composed of unidirectional fibres. The second function is to support the seat: in the 4 areas of interface with the seat there are both aluminum and wood reinforcement (see part III).

Material	Orientation/deg	Thickness/mm
Carbon, T300	0	0,2
Carbon, UD	0	0,15
Carbon, T300	0	0,2

Table II.2.9: Stratification of Cerberus's bottom longerons

II.2.8 Upper longeron

The upper longeron (figure II.2.13) acts both as a reinforcement of the aero fairing and as a cable duct for the connection between the cameras and the screens. The last ply

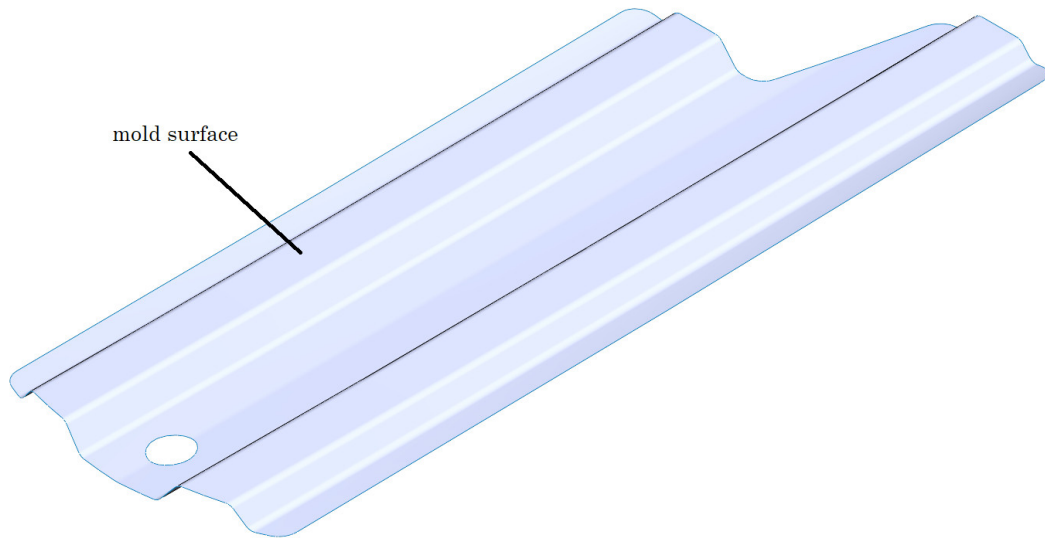


Figure II.2.12: CAD image of the surface used for the bottom longerons's mold generation

(the most internal one) is a glass fibre cloth that tends to isolate the cable from the carbon, which is a semi conductor.

Material	Orientation/deg	Thickness/mm
Carbon, T300	0	0,2
Glass, T300	0	0,2

Table II.2.10: Stratification of Cerberus's upper longeron

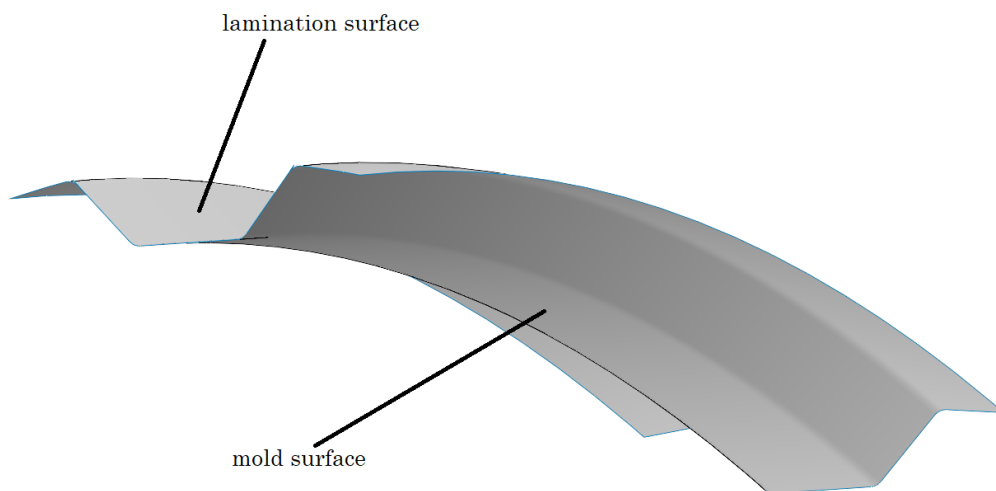


Figure II.2.13: CAD image of the surface used for the upper longeron's mold generation

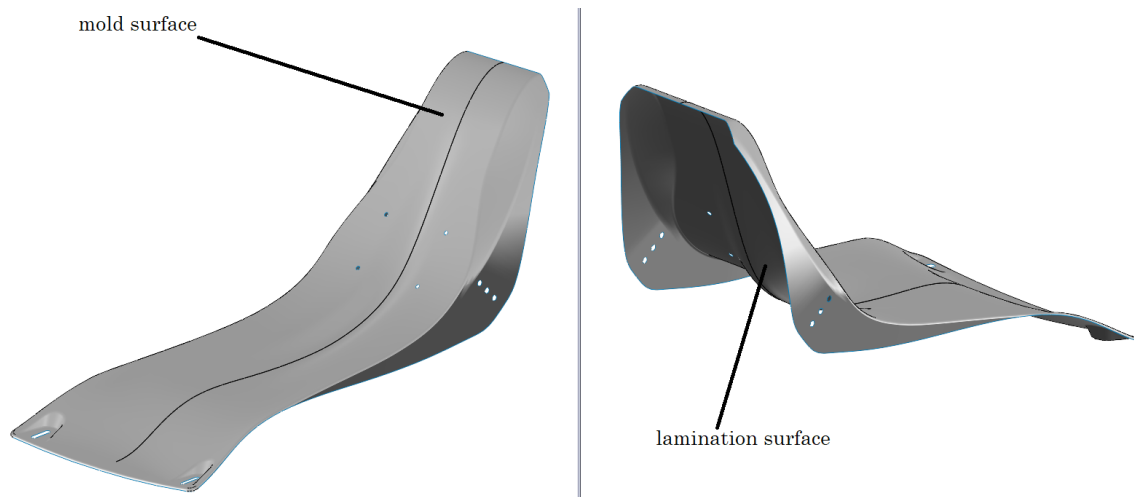


Figure II.2.14: CAD image of the surface used for the upper seat's mold generation

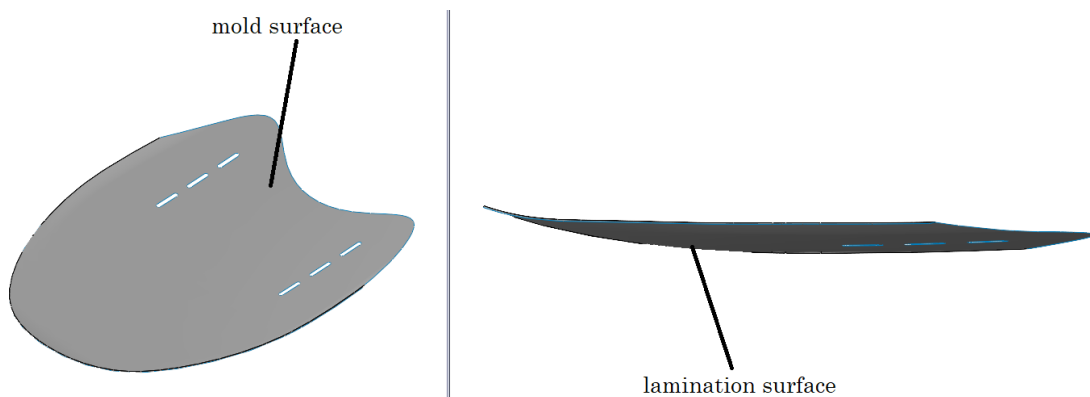


Figure II.2.15: CAD image of the surface used for the lower seat's mold generation

II.2.9 Seat

Material	Orientation/deg	Thickness/mm
Carbon, T300	0	0,2
Carbon, T300	0	0,2
PVC	-	3
Carbon, T300	0	0,2
Carbon, T300	0	0,2

Table II.2.11: Stratification of Cerberus's upper longeron

The seat was modeled after observing Simone Chiarolla's¹ *Carbide handcycle* by *Maddiline*, which is divided in 2 parts (see figures II.2.14 and II.2.15) since there wasn't any time to study an ergonomic geometry. Moreover, this seat is compatible with a dedicated cushion developed for paraplegic athletes by Palintech®.

¹Simone Chiarolla is one of Team Policumbent's riders

Chapter II.3

Additional structural components

II.3.1 Components in AlSi10Mg

Many metal additive components were included in this prototype. They were all designed by Marco Mininni, who made use of the Altair Inspire optimizer in order to reach the maximum stiffness with the minimum weight. The parts were drawn in Solidworks, then Inspire was used to define an optimized design space. After the analysis, the polynurbs command was used. The parts were then redrawn with Solidworks and analyzed with Inspire (figure II.3.1).

Figure II.3.2 shows the 3D printed interfaces that connect the carbon tubes and other components (basin plates, transmission plates and slide) to constrain the transmission's supports.

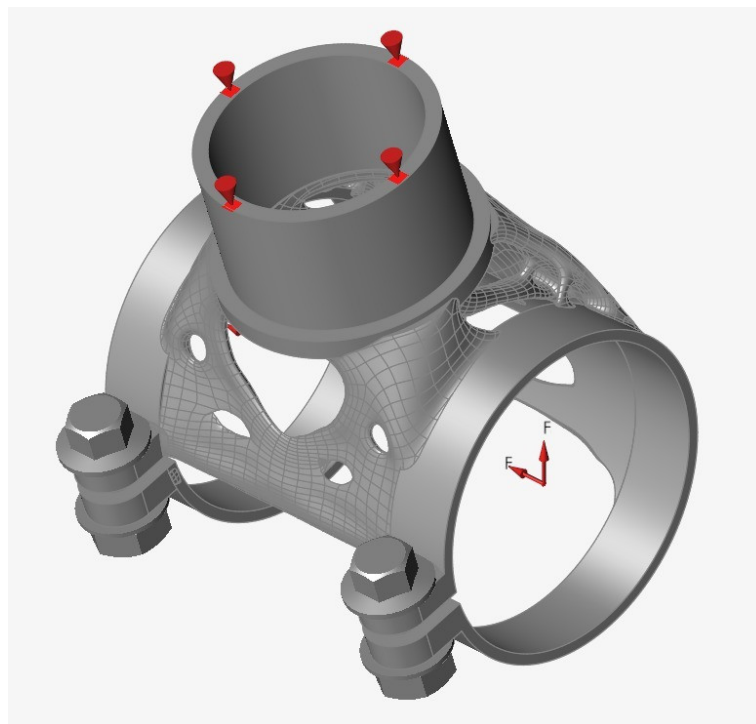


Figure II.3.1: Screenshot of an analysis conducted with Inspire on the clamp that connects the steering column to the crankset



Figure II.3.2: Optimized 3D printed parts used for the transmission’s supports structure

II.3.2 Aluminum plates

Many aluminum slabs were also used as supports or simply as infills in some other cases. Figure II.3.3 shows the 2 supports, designed by Marco Mininni, of the transmission’s main shaft.



Figure II.3.3: Aluminum plates used to support the grooved shaft of the moving cassette system

II.3.3 Carbon fiber tubes

Many commercial carbon tubes were used in this project. They're lightweight, highly resistant and versatile for many applications (figures from II.3.4 to II.3.8).

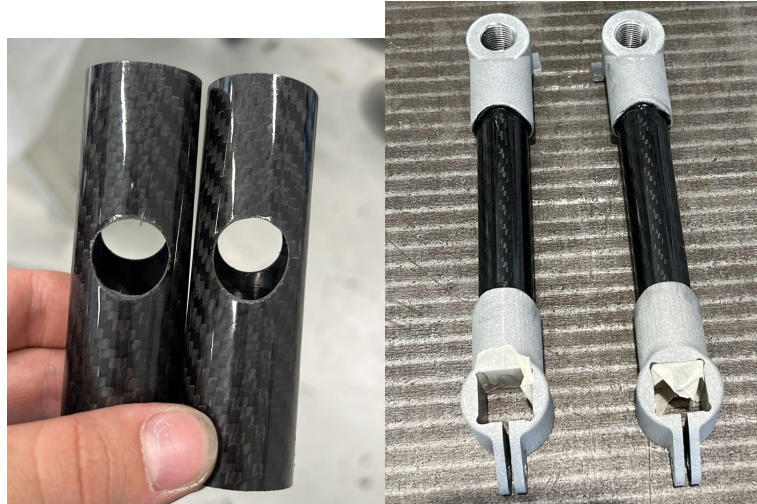


Figure II.3.4: Carbon tube used for the creation of handles (on the left) and cranks (on the right)



Figure II.3.5: Carbon tube used as a support for the brake lever

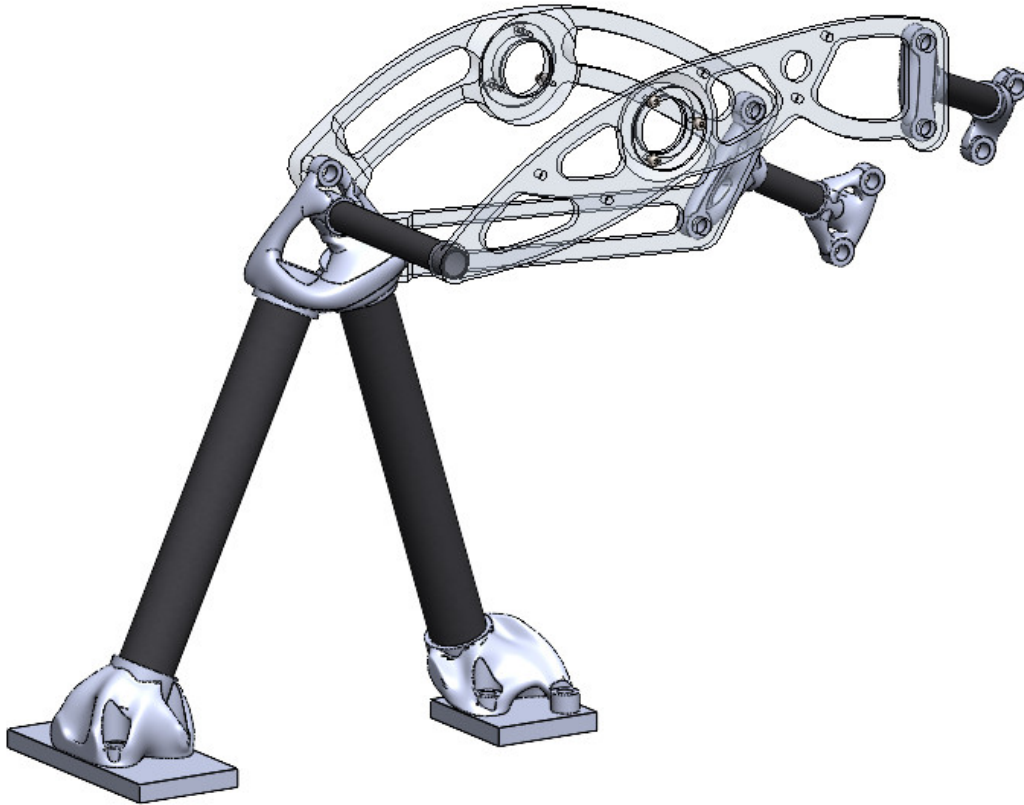


Figure II.3.6: CAD image of the transmission supports

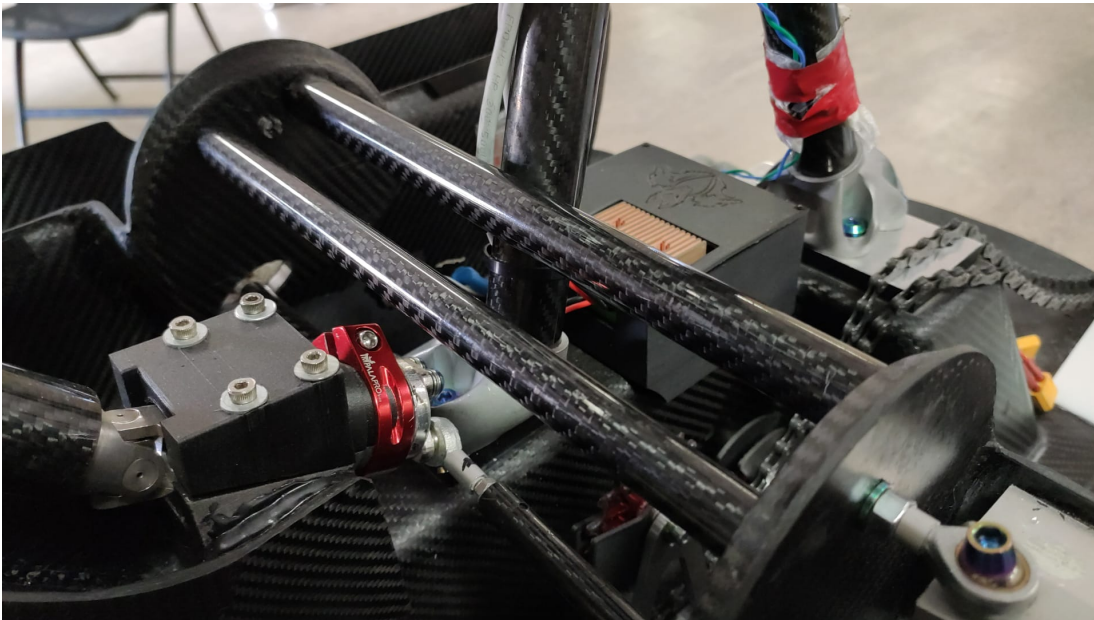


Figure II.3.7: Photo of the 2 carbon tubes used as anti roll bars. They were added to reinforce the plates on which the uprights are linked to through the rod-end bearings



Figure II.3.8: Carbon tubes were used for the steering mechanism too, both for the main column and for the tie-rods

Chapter II.4

Design of the vision system

As mentioned earlier in section I.2.2.3, the pilot sees the road through a double camera system.

Unlike any of the other prototypes of the team, though, Cerberus's entire vision system is placed directly on the front fairing, instead of being set onto the frame. This allows for a better use of space during maintenance and makes the assembly cleaner and more modular, with a full electronic assembly completely detached from the mechanical parts of the vehicle. Because of this, it's possible for the mechanical and electronic divisions to work simultaneously on the trike without disturbing each other. Moreover, once the vision system is fully set, it's less likely that someone bumps into it or moves it slightly while working on something else.

II.4.1 Plexiglass window

This section presents the design of the plexiglass window. Polycarbonate (PC) was also taken into account as a possible material to be used but in the end plexiglass was chosen mainly for its high transparency and low chemical interaction with UV rays (polycarbonate tends to undergo yellowing over time), even though PC has a better formability [24, 25].

II.4.1.1 Requirements

- the window in the front fairing shall be shaped so that the FOV (field of view) of the cameras doesn't intersect the fairing
- the minimum distance from the tip of the vehicle to the nearest point of the road visible on camera, should be reasonably small for safety issues
- the window in the fairing shall have a flange to support the plexiglass during the assembly phase

II.4.1.2 Design

As for the design, the first steps were to create the cameras' FOV and use them as references for the cut of the fairing after being placed in an assembly with it (figures II.4.1 and II.4.2). The shape of the window was then refined in order to add some

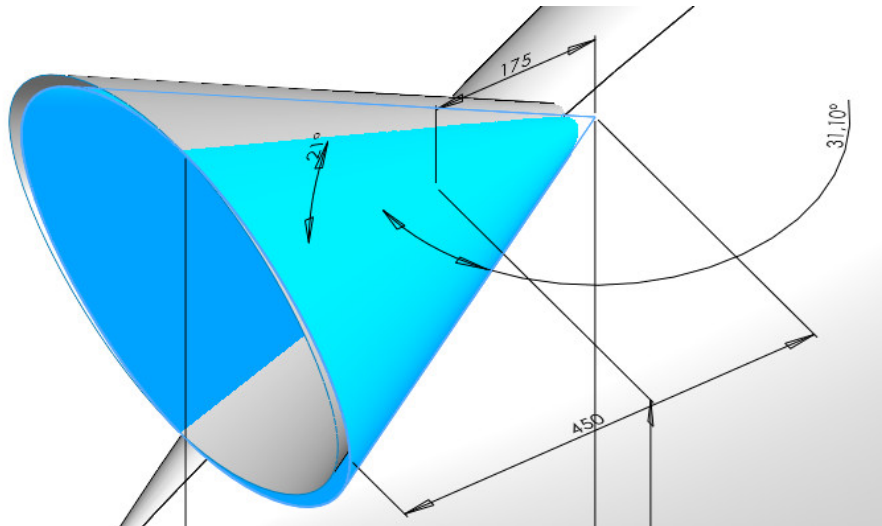


Figure II.4.1: Positioning of the cameras' FOV in the assembly

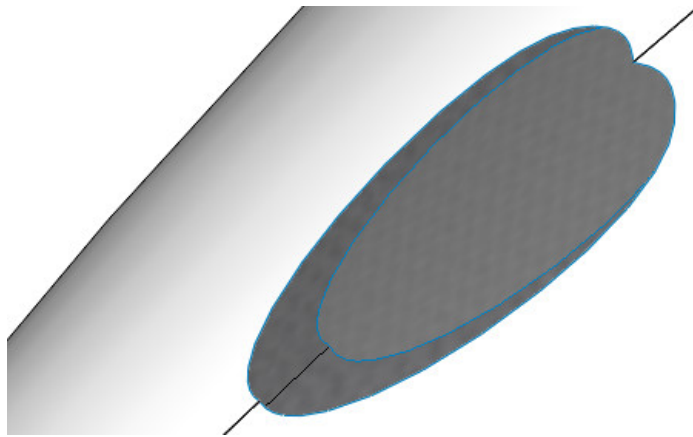


Figure II.4.2: First cut of the fairing, with the 2 FOV as references

margin for the cameras adjustments and for the creation of the assembly flange (figure II.4.3).

As reported in figure II.4.4, the final result was very good in terms of the nearest point of the ground visible on camera (less than 1 m from the tip of the fairing).

II.4.2 Design of the cameras' supports

The study of these components took quite some time, since it had been a problematic part on some prototypes. The design of this subassembly was mostly done by the author but the study and design of the closing system of the rear lid and the coupling system with the fairing was teammate Lucrezia Pasi's work.

II.4.2.1 Required functionalities

For an optimal adjustment of the cameras position, it was required that:

- the analog and digital camera have 2 supports for independent adjustment

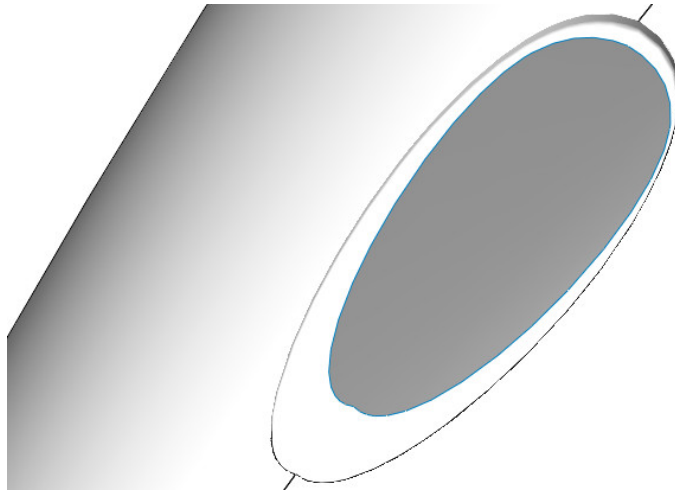


Figure II.4.3: Reshaping of the window

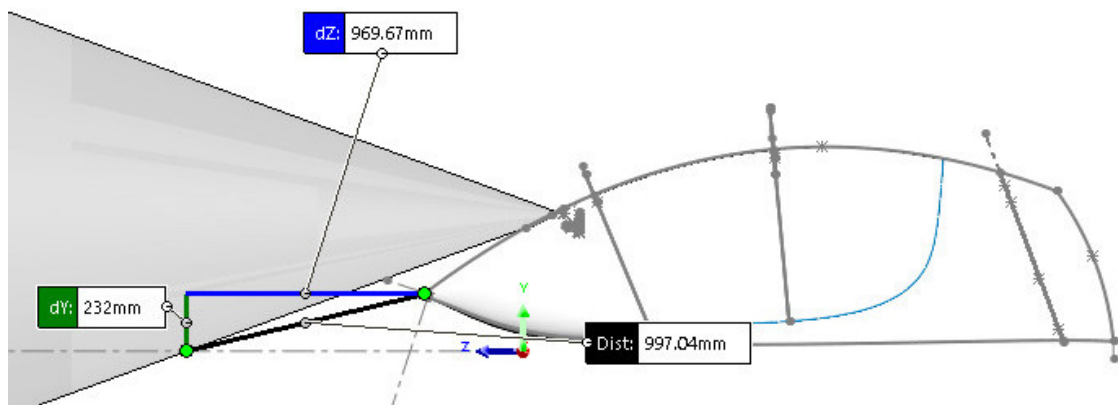


Figure II.4.4: CAD image of the visibility cone of a camera: the intersection with the ground is at about 1 m from the tip of the vehicle, which is definitely reasonably safe

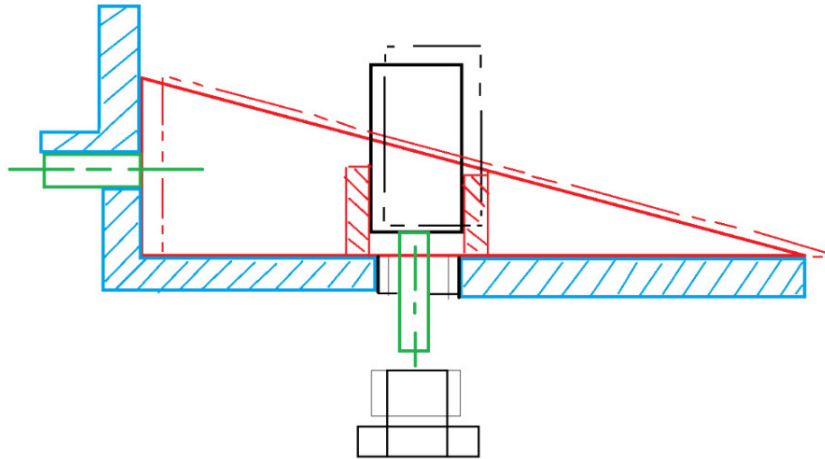


Figure II.4.5: First sketch of the cameras' support in lateral view

- the adjustment be preferably accessible without having to dismount the case from the fairing.

furthermore:

- the case should be sufficiently insulated (preferably fully insulated) from the cockpit so that condensation generated by the pilots heat won't fog up the window
- since it's linked to the fairing, it has to be fairly stiff but lightweight at the same time

The general idea that came from this constraints is represented in figure II.4.5 where are represented:

- in blue: the case, which should be fixed to the fairing and should totally enclose the camera for the insulation matter
- in red: a mobile frame that can translate horizontally thanks to the rear screw (green)
- in black (thick): the cameras, which can translate both horizontally (pushed by the red frame) and vertically (thanks to a screw that can freely slide in a slot in both the case and the frame)
- in black (thin): a cap that comes from beneath to cover the aforementioned slot

II.4.2.2 Components

Figure II.4.6 shows the CAD of the final assembly.

All of the following pieces were produced in Onyx, 3D printed with an FFF¹ professional 3D printer.

¹FFF stands for *fused filament fabrication*. It is a 3D printing technology where the piece is fabricated by laying down multiple layers of hot (temperature above the softening point) material (usually thermoplastics).

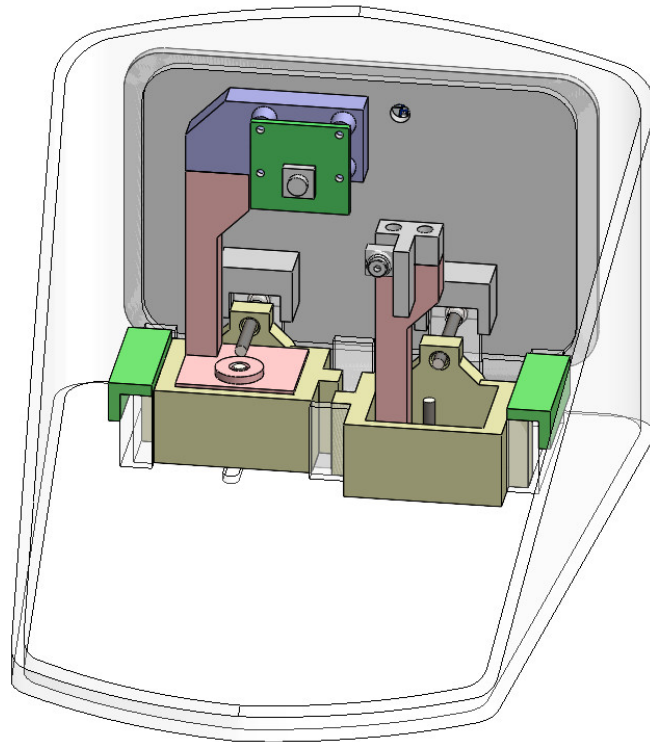


Figure II.4.6: CAD Assembly of the cameras supports

II.4.2.2.1 Case

First of all, there's the case, which was designed to perfectly cover the internal surface of the fairing (as shown in figure II.4.7). It presents some extrusions that function as guides and limiters for the translations of the supports and the 2 slots on the bottom face for the free movement of the bottom screws.

II.4.2.2.2 Back lid

The back lid (figure II.4.8) is a simple plate with 4 extrusions that which house 4 thread inserts that are used to take in place the Raspberry Pi3. The rectangular hole allows the passage of flat cables that link the digital camera to the Raspberry, while the circular one, which was later enlarged, is for the cables of the analog camera.

II.4.2.2.3 Vertical translation support

The same part (figure II.4.9) is adaptable for both the analog and the digital interfaces. It hosts a trough hole on the base for a thread insert and 2 blind holes for centering pins to link the camera interfaces.

II.4.2.2.4 Camera interfaces

Both pieces (figure II.4.10) have the 2 holes for the centering pins but, while the interface for the analog camera doesn't have other holes, the support for the digital one features 4 extrusions in which 4 thread inserts shall be placed for the positioning of the electronic board on which the camera is attached. The analog camera is instead set in place on its support with glue gun.

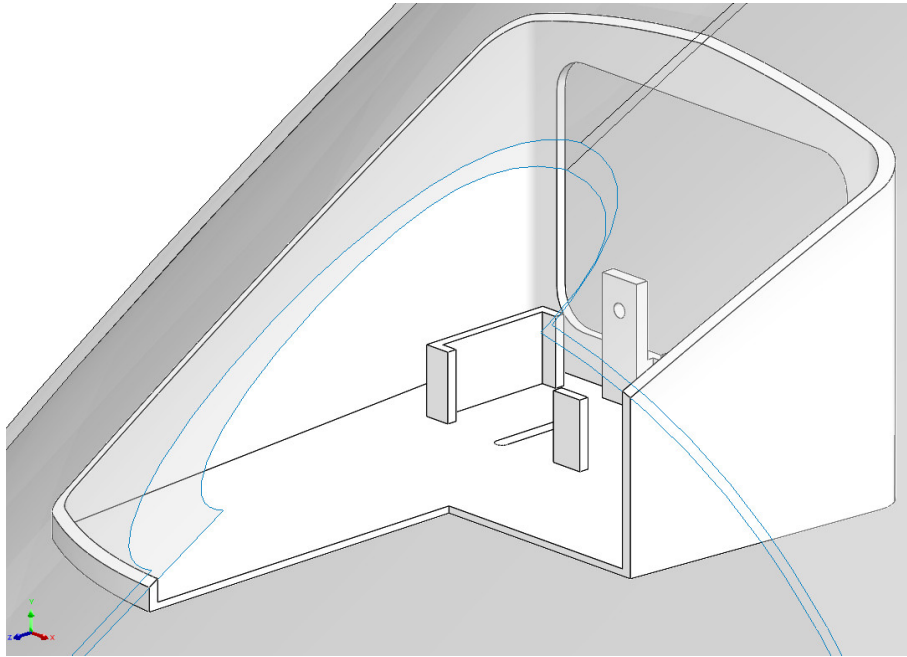


Figure II.4.7: CAD sectioned view of the cameras' case

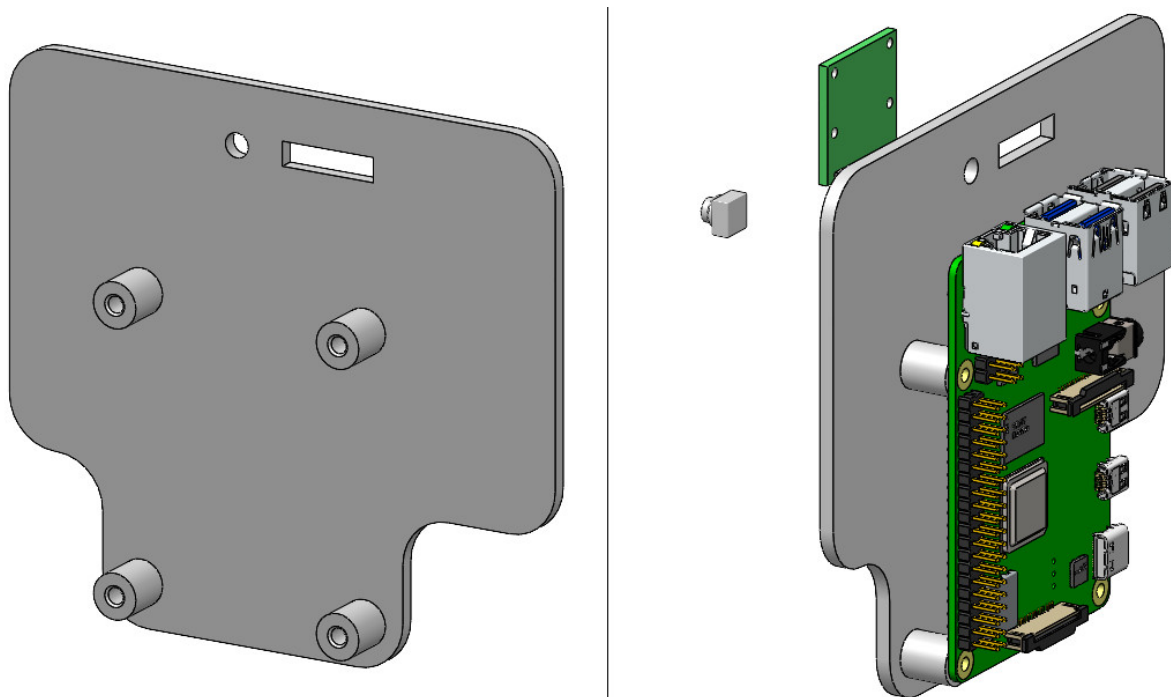


Figure II.4.8: CAD of the back lid without (left) and with (right) the electronic components

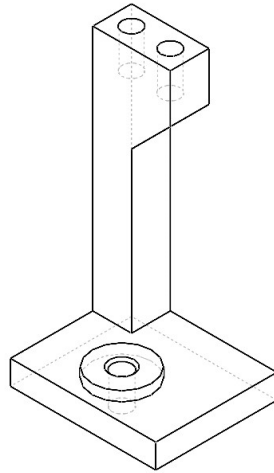


Figure II.4.9: CAD image of 1 of the 2 vertical supports

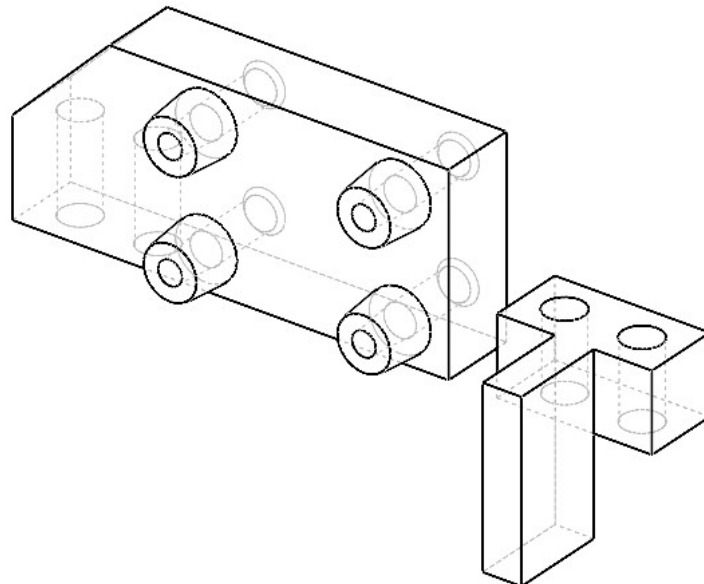


Figure II.4.10: CAD image of the digital (left) and analog (right) camera interfaces

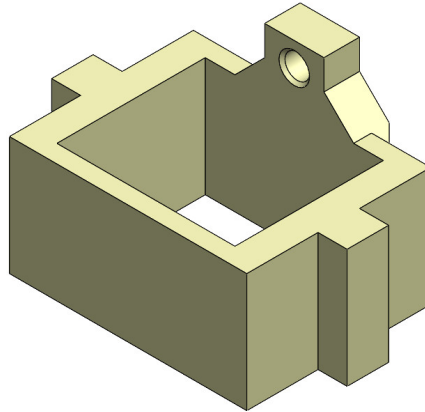


Figure II.4.11: CAD image of the horizontal translation frame

II.4.2.2.5 Horizontal translation frame

This piece (figure II.4.11) acts as the red part in figure II.4.5. The hole on the rear side hosts a thread insert for the forward-backward adjustments. The rectangular hole in the centre serves as a guide for the vertical supports; lastly, the 2 lateral wings operate as limiters of the horizontal movement.

II.4.2.2.6 Anti lift guides

This part (light green in figure II.4.6) ensures that, by pulling up the vertical translation support, the horizontal translation frame doesn't move up as well.

II.4.2.2.7 Rear lid locking mechanism

This work was done by teammate Lucrezia Pasi. The locking system is similar to the frames used for locking some photographs: on the underside there are 2 lamellas that are directly glued to the case. The rear lid is inserted from above and is finally locked on top by the fairing.

II.4.2.2.8 Lateral laths

Once again, this parts were designed by Lucrezia Pasi.

Two laths are glued to the case (one for each side) and support the weight of all the assembly with the use of Dual Lock™, which is a powerful velcro that is also able to damper a bit of vibrations.

II.4.3 Design of the screens' supports

This subassembly is the last of the vision system. It was designed mostly by the author, in collaboration with teammates Stefano Tomassi, Andrea Testera and Pierluigi Scotti in the first phase.

II.4.3.1 Required functionalities

For a correct functioning:



Figure II.4.12: Rear view of the cameras' assembly: the lid is set in place thanks to the 2 lateral lamellas, similarly to a frame for photographs



Figure II.4.13: Picture of one lateral lath glued to the side of the case

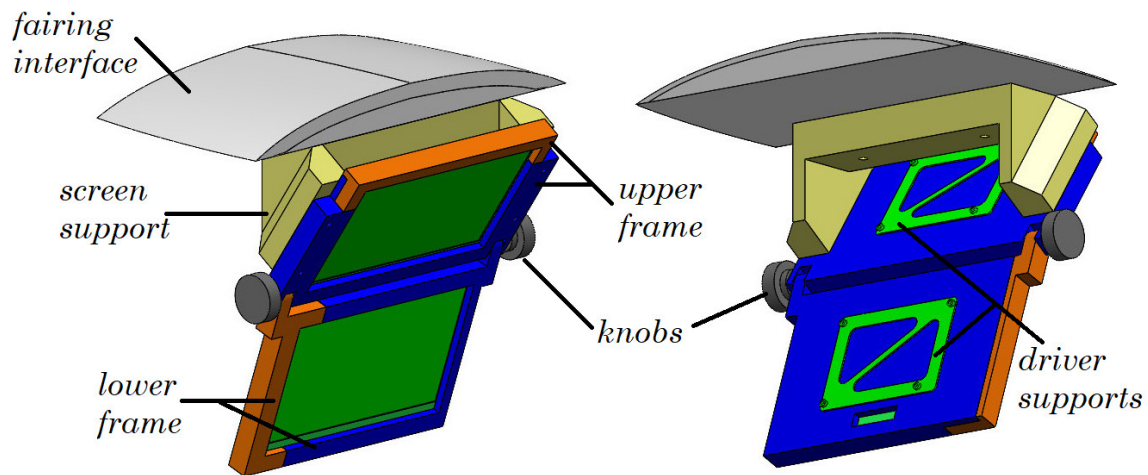


Figure II.4.14: CAD image of the screen assembly

- It should be possible for the athletes to adjust the orientation of the lower screen
- There should be sufficient space to house the batteries
- The screens shall be placed in a position that doesn't interfere with the cranking motion
- The assembly shall have an interface fixed to the fairing but be removable for maintenance reasons

II.4.3.2 Components

Figure II.4.14 shows the full assembly of the screens's supports. Like for the cameras's supports, it was broadly made use of FFF 3D printing.

II.4.3.2.1 Fairing interface

This is the only part of the assembly that was produced in wood, because 3D printing it would have taken too much time (about 1 day and a half). The functions of this piece are:

- to have a fixed part for alignment purposes
- create a planar surface for the batteries to be connected through Dual Lock™

It is glued directly to the fairing and hosts a pair of nuts that are used to bolt the screen support on.

The profile perfectly copies the internal surface of the front fairing.

II.4.3.2.2 Screens support

This part was designed in order to have the less complicated fairing interface and to make the upper screen reclined in the right direction.



Figure II.4.15: Partially mounted frames for the screens

II.4.3.2.3 Screens frames

The 2 screens are put in place thanks to a frame each, both of which are composed by 2 parts. The upper one is supported by the lower part, that is bolted with 4 screws to the screens support. Conversely, since the lower screen is connected with the rest of the structure through 2 hinges, the frame was divided in right and left. Figure II.4.15 shows the frames connected to together.

II.4.3.2.4 Driver support

These parts are glued to the back of the screens frames and are used to support the electronic components that are needed.

Chapter II.5

Design of the moving cassette system

In order to reach high speed, Cerberus is equipped with a 2 branches transmission: the first one connects the crankset to the sprocket pack, while the second is a fixed ratio branch that connects the shaft on which the cassette is placed, with the freewheel. This chapter covers the design of the former.

After the decision to make a tadpole trike, the idea for the transmission was to use a commercial shifting mechanism due to the apparent lack of time for the design of a custom one. In November 2021, though, the author, having concluded the design of the fairing, felt inspired and found some time to try to design a translating sprocket pack. Then, in March 2022, a second mechanism was drawn and put in production later in the year, but, unlike the first one, it had a design problem, so some changes were made in July and August 2022 to solve the issue. This latest part of the design was done in collaboration with teammate Samuel Barbaglia.

The general idea is the following: since the objective of the mechanism is to move the pinions laterally, these have to be linked together on the same sliding element. Translating the shaft isn't an option, since it would require a lot of space and would make the interfaces with the frame more complex; instead, the same idea of a moving sleeve, placed between the shaft and the cassette, already adopted for prototypes Taurus, Taurus-X and Phoenix, seemed way more reasonable. As a matter of fact, since there were 2 spare parts of Taurus-X's sleeve, the whole design revolved around it, though Taurus-X's transmission is very different from Cerberus's.

The advantages of a moving sprocket pack has already been presented in Part I.

II.5.1 First design: external actuation

Figure II.5.1 shows a section of the full assembly, while figure II.5.2 is a simplified version displaying only the kinematic mechanism.

The shifting action starts with an electric signal sent to the motor, which, depending on the sign and modulus of the signal itself, puts into rotation its own pinion. As a result, the *double-sided gear*, bolted to the *rotating spider* that fits on a bearing (which is axially constrained by the *grooved shaft* on one side and by a bushing on the other side), is set in rotation. The kinematic motion continues as the 3 *planets*, each composed by a gear and a partially threaded shaft, start to pivot (note that they're axially fixed thanks to the coupling with the frame shown in figure II.5.3). Consequently, the *translating spider*, by means of its 3 threaded holes, transforms the rotational movement given by the planets into a linear one. Finally, since the spider

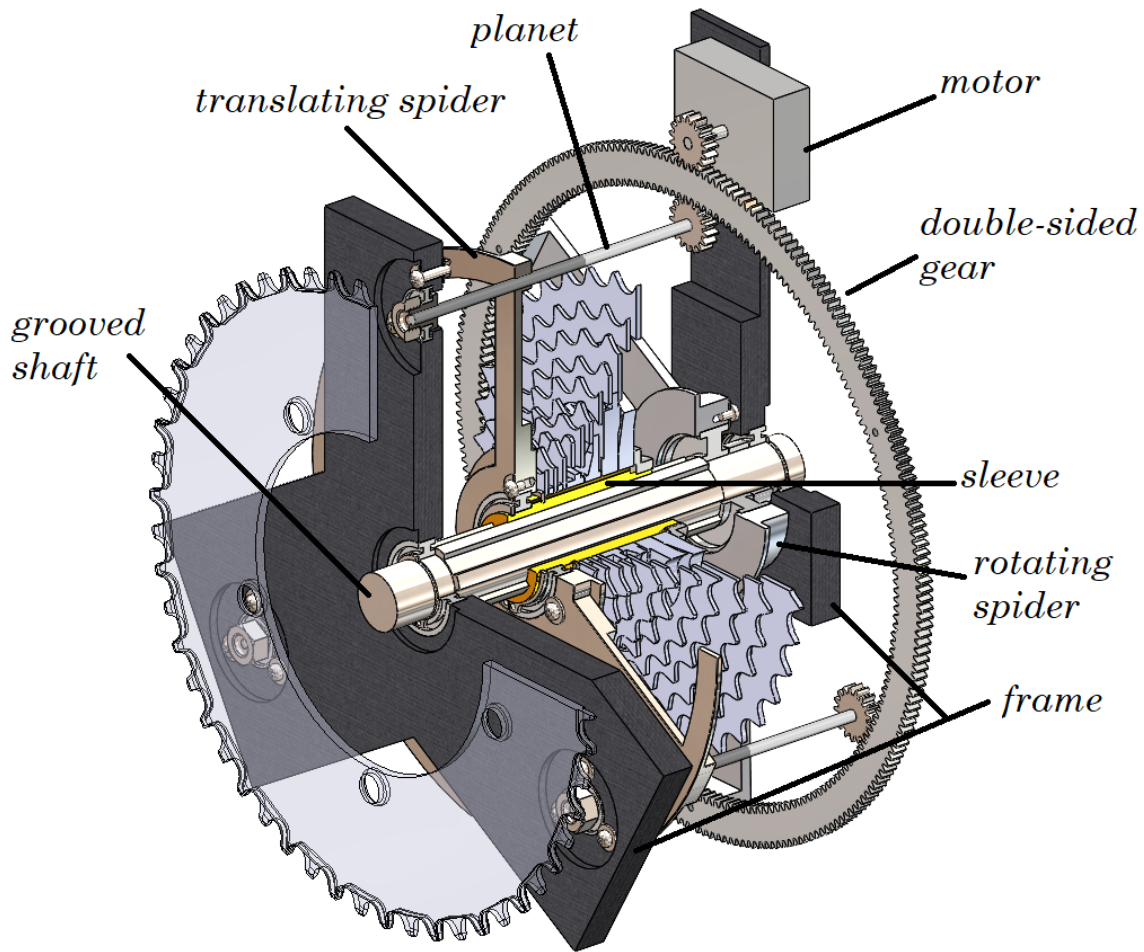


Figure II.5.1: First idea for the moving cassette: complete and sectioned assembly, with names of the most important components

is connected through a bearing to the *sleeve*, the axial movement is transferred to the cassette.

This system might have had some issues that would have had to be verified with a prototype before the final production, if this configuration was chosen. Namely, there was some concern on the possibility that, due to vibrations, one or more of the 3 planets could loose contact with the double-sided gear and jam the mechanism. The fix could have been to redesign the rotating spider by adding 3 shorter arms that would be bolted to an external gear that would mesh with the planets and serve as a guide for them.

Another problem was that 7 bearings (which seemed a bit to many for this application) and a lot of small screws would be needed, making the assembly phase and the maintenance a bit tedious.

Note that in this phase the linking method of the freewheel branch to the cassette branch hadn't been defined yet: that's why figure from II.5.1 shows a floating transparent gear.

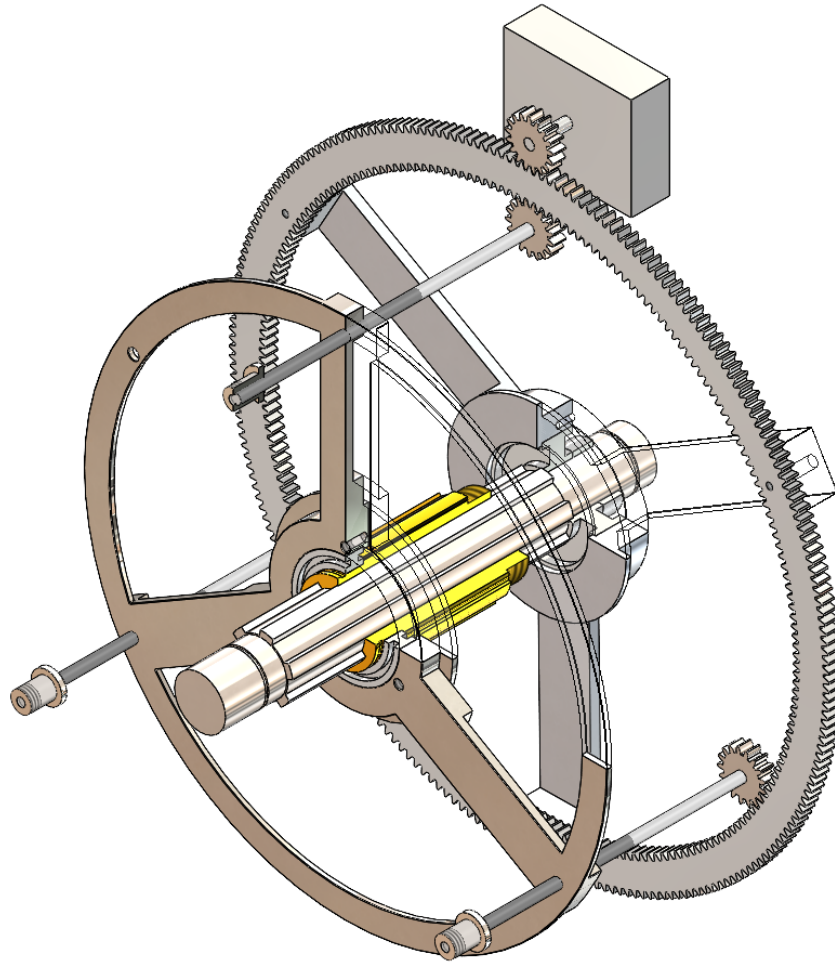


Figure II.5.2: First idea for the moving cassette: sectioned assembly of the kinematic mechanism

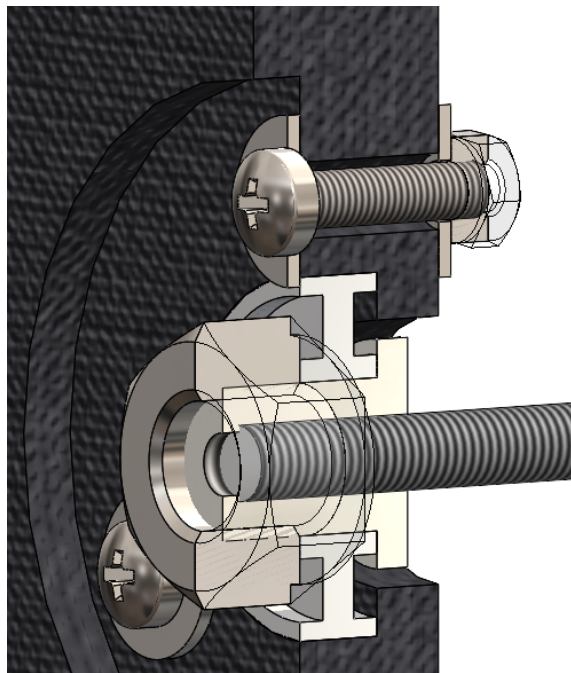


Figure II.5.3: Zoom on the coupling between one planet and the frame

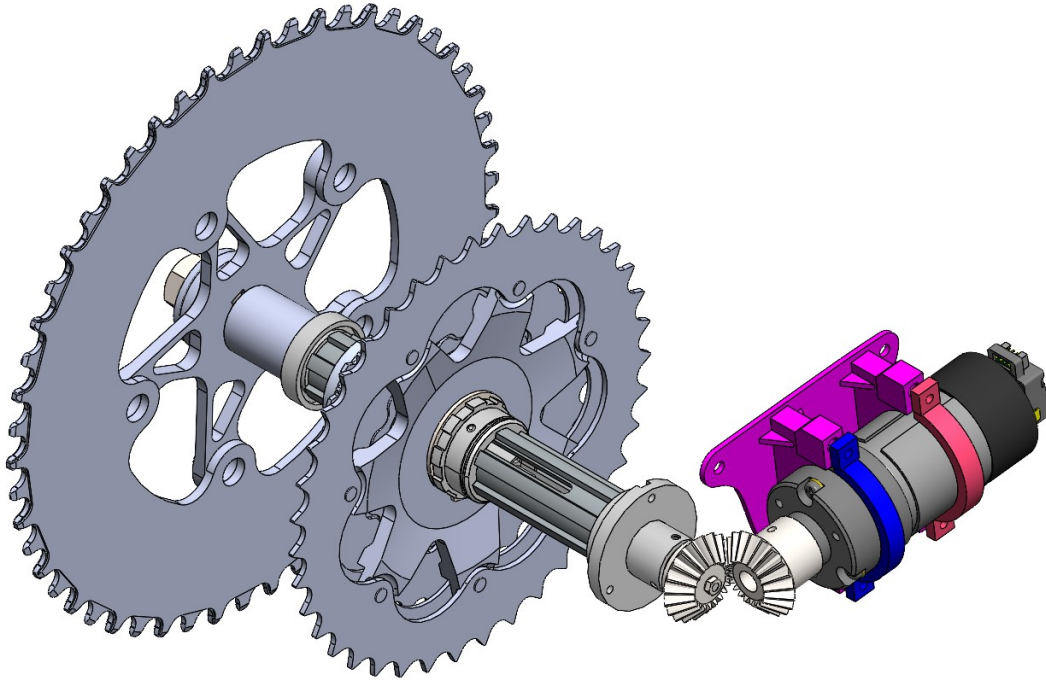


Figure II.5.4: Complete assembly of the system

II.5.2 Second design: actuation internal to the shaft

All the details in terms of dimensioning and tolerancing of the pieces are shown in Appendix B. Hereafter the general behaviour of the mechanism and the mounting procedure are presented.

In this case, for a more compact solution, the motor fits a bevel wheel (figure II.5.4).

The gear coaxial to the grooved shaft is fixed with locknuts on an M3 threaded rod supported by 2 bearings. The first bearing is axially constrained (figure II.5.5) by:

- the shoulders of 2 bushes
- one nut
- one ring pinched by 3 set screws (see the indentations in figure II.5.6)

The second one, instead, is mounted onto the *Leadscrew female element*, to which it's axially fixed with 2 M2 screws (II.5.7), and slides inside the *Guide* (figure II.5.8). Its outer ring is then connected to 2 bushing: the plastic one fits with interference and is reversibly glued on the steel one (acetone can be used to soften and remove the PLA part) which is fixed to the sleeve by means of 3 set screws M3 (see the assembly drawing in Appendix B for more details).

II.5.3 Some important notes

For a smooth motion, the steel bearing and the threaded rod should always be well lubricated with grease. It's important to check the condition of the grease on the rod and to accurately clean the mechanism if dust is found (it could get in by the slots machined on the grooved shaft).

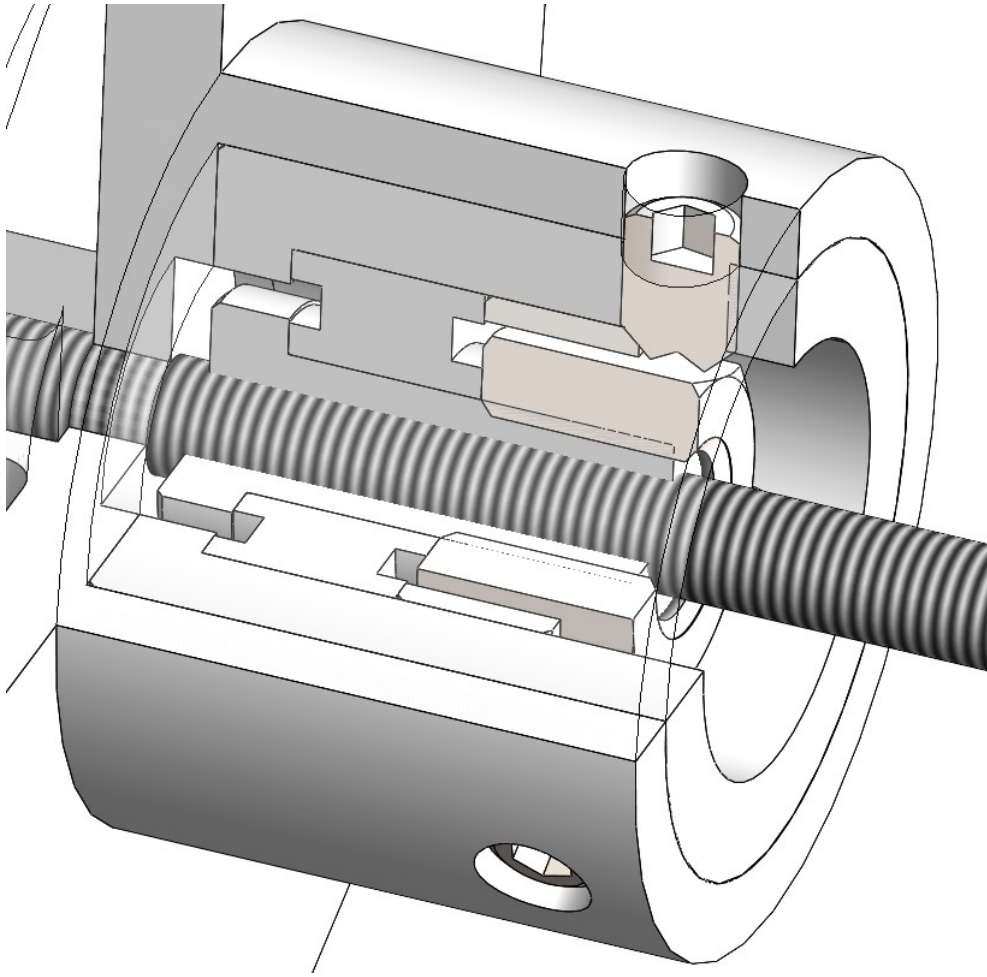


Figure II.5.5: Zoom on the external bearing ($\varnothing 5\text{-}\varnothing 11 \times 5$) locking system

Note also that the tolerances of some pieces were adjusted to $h6$ after seeing that $js6$ was giving too much interference. We understood that ceramic bearings tend to need tighter tolerances due to their minor deformation in comparison to steel ones.



Figure II.5.6: Indented ring



Figure II.5.7: Inner ring of bearing $\varnothing 7\text{-}\varnothing 14 \times 5$ locked in place

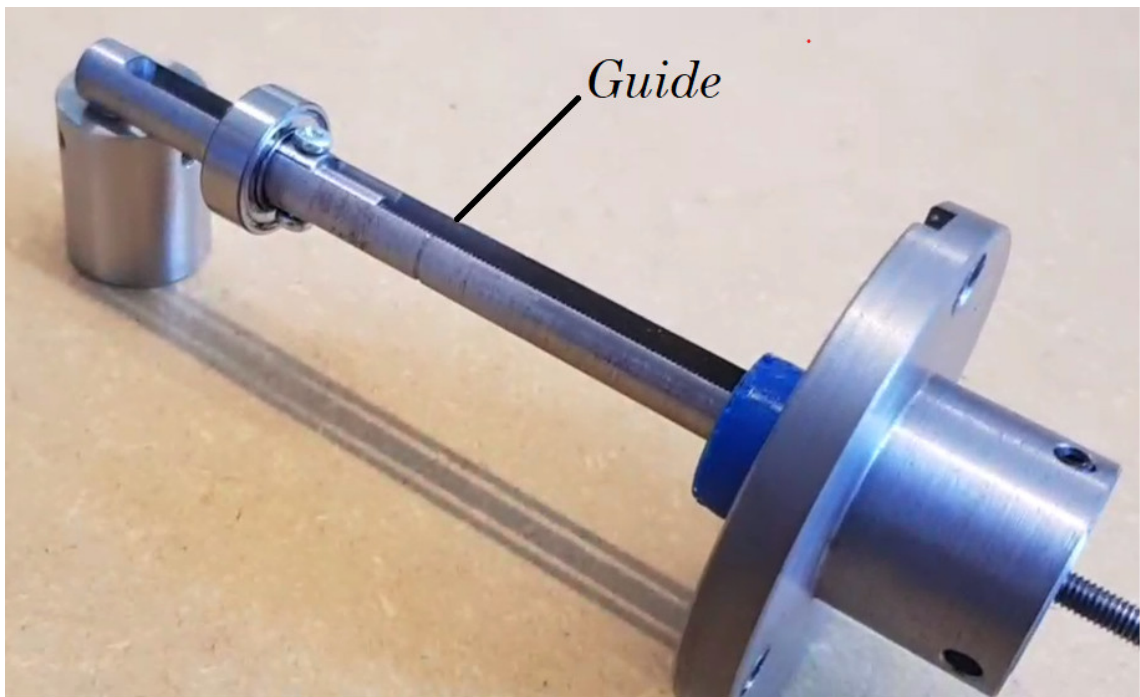


Figure II.5.8: Complete assembly of the system

Chapter II.6

Chain tensioners and carters

Both the chain tensioners and carters' goal is to take the chain in place and not make it fall from the ring, the pinions and the pulleys.

As said earlier in chapter II.5, on Cerberus there are 2 chain branches. In this chapter it's shown how their tensioning is made. This systems were mainly designed in collaboration with some teammates: mainly Giacomo Lussiana (both branches), Samuel Barbaglia (moving branch) and Claudia Barattini (fixed branch).

II.6.1 Fixed branch

On the fixed branch, which connects the second ring to the freewheel, the tensioning is made by means of 6 pulleys connected to 4 supports glued to the structural fairing. The front and rear 2 are connected in pair, while the middle ones are placed under the seat and have each their own structure. All the pulleys are equipped with a carter.

Initially, only 4 pulleys were intended to be used and the 2 concept tensioners were 3D printed in onyx, which were then machined in ergal; the final middle tensioners were made in carbon. Note the slot to change the pulleys height and, therefore, to determine the chain tensioning (figure II.6.1).

Figure II.6.2 shows middle and rear tensioners on the prototype.

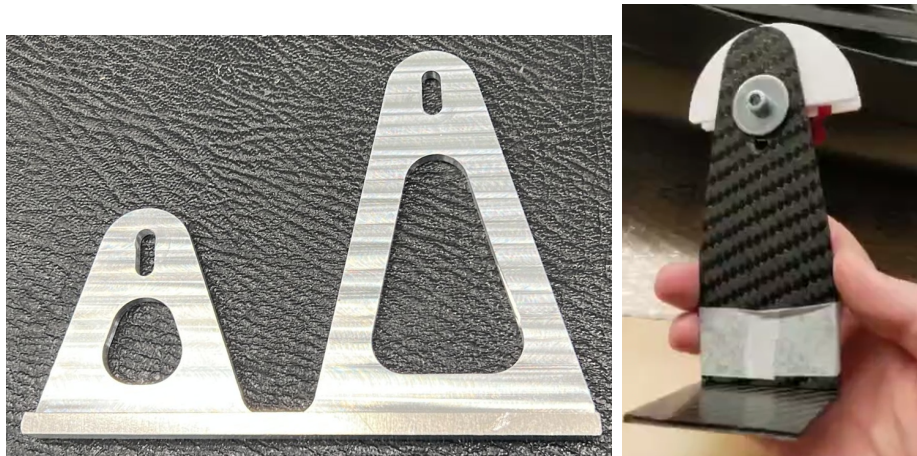


Figure II.6.1: Front tensioner in ergal and one of the 2 middle tensioners in carbon

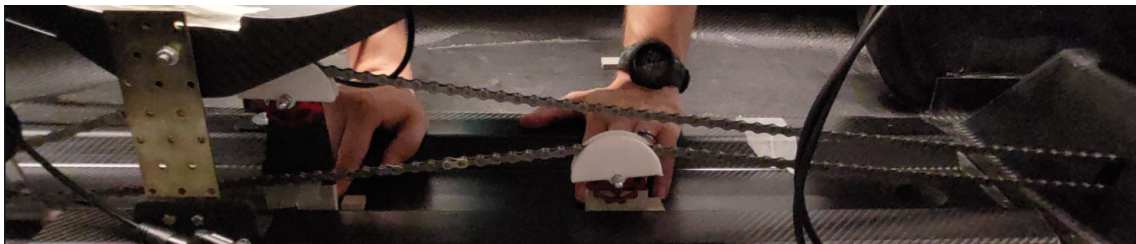
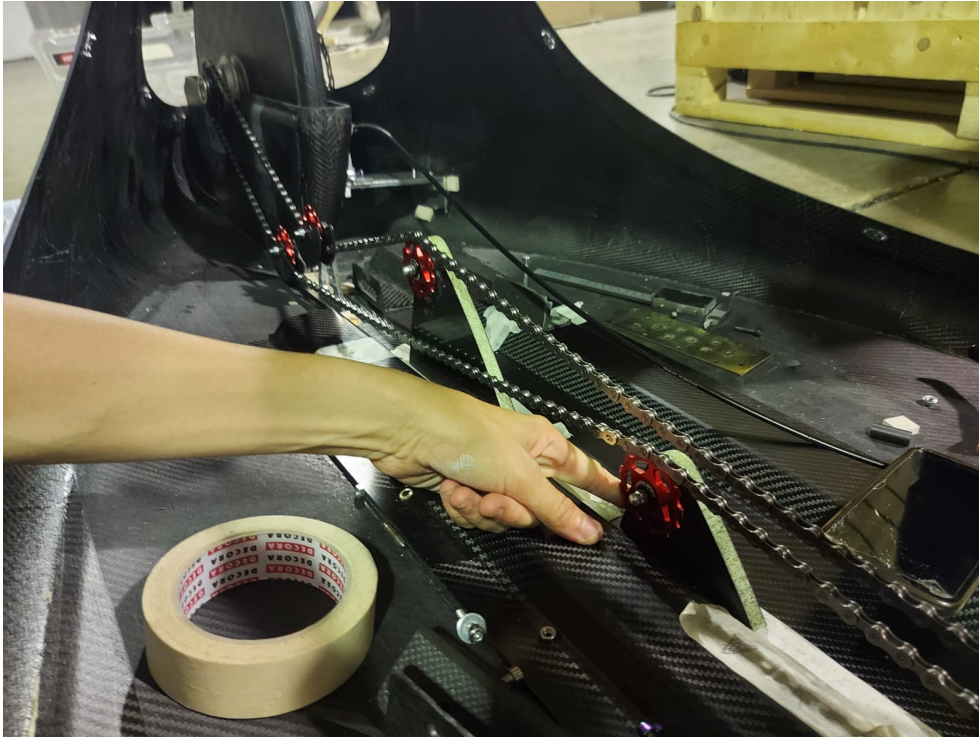


Figure II.6.2: Taking measurements for the middle tensioners with rear tensioner already in position (top). Carbon middle tensioners in place (bottom)

II.6.2 Sprocket pack branch

The moving tensioner is more complex and features a helical spring that's needed to continuously tension the chain, be it in 1st or 11th gear. The two pulleys are connected to each other by a carbon cage which pivots around a fulcrum fixed on 2 onyx supports that are bolted to the frame's aluminum slabs; furthermore, a carter on the main chainring was installed both for safety reasons and as a guide for the chain (figure II.6.3).

Note the 3D printed derailleur: that small piece of plastic is a key feature for a smooth behaviour of the shifting system, as it forces the chain to fall (or rise) on the next pinion for little movements of the sleeve (read chapter II.5 for details on the moving cassette).

In beginning, although the chain was tensioned, it still used to fall way too often; therefore, a carter was added on the upper pulley too (figure II.6.4).

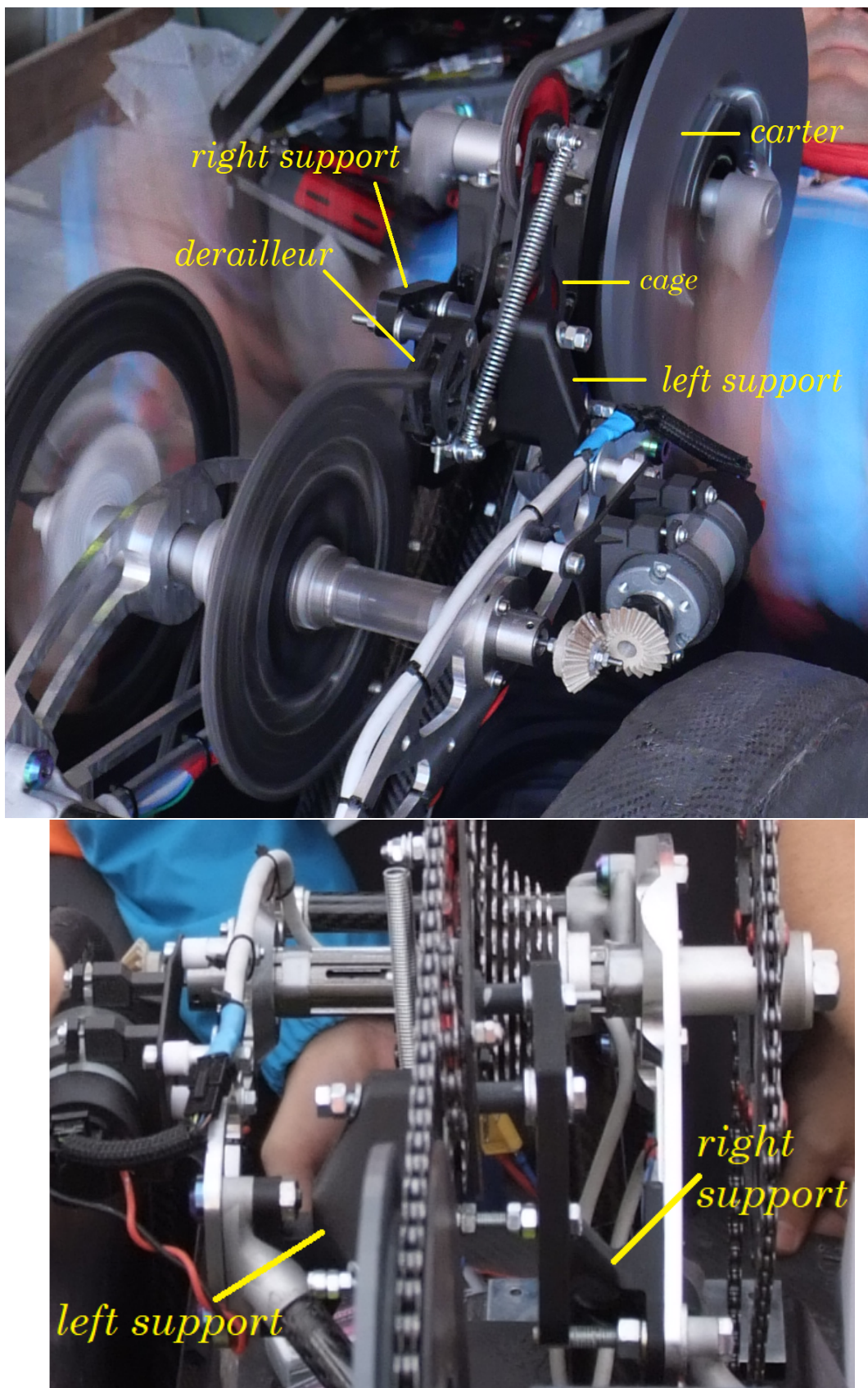


Figure II.6.3: Mobile tensioner

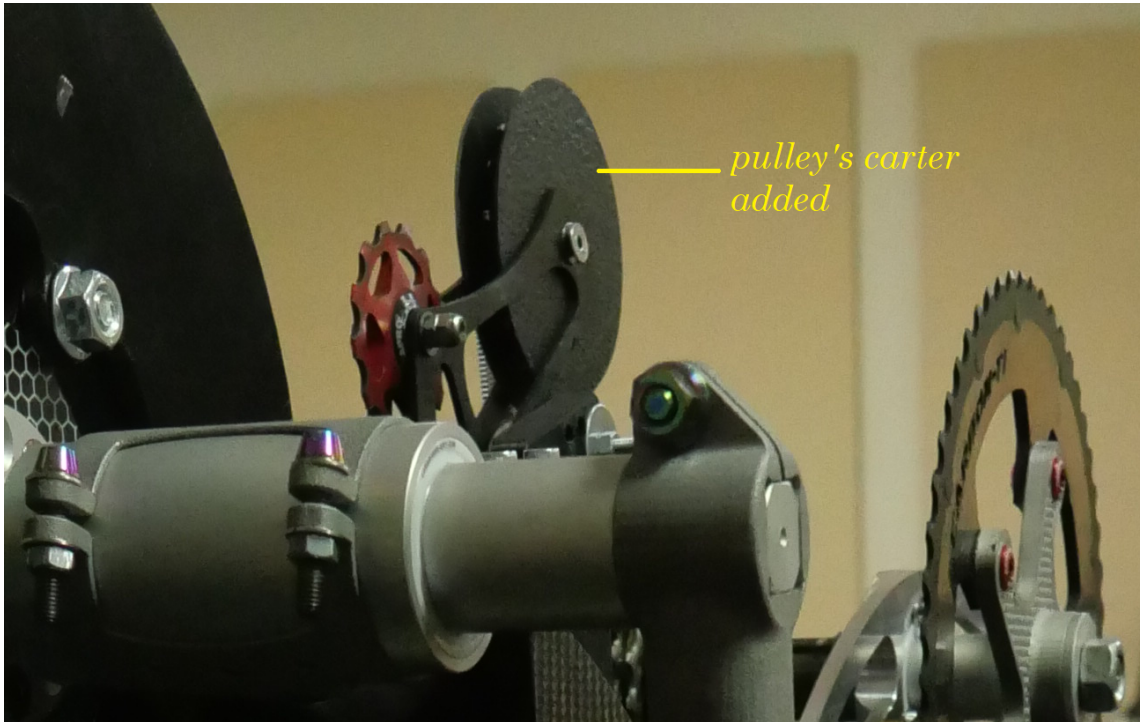


Figure II.6.4: Mobile tensioner

Chapter II.7

Steering mechanism

The steering mechanism is a key element as on it depend both the stability of the vehicle and the rider's safety. Unfortunately, because of lack of time and of human resources, as of September 2022, it had some issues, so, it will have to be updated in the future.

II.7.1 Possible systems

The starting point for the design was the evaluation of 3 main possible mechanisms described below.

- Actuation with 2 levers, connected to the uprights with tie-rods which are linked together with a front beam. It was used in LemonTrike prototype (figure II.7.1) but couldn't be used on an handtrike because the arms not only are used for the vehicle's steering but for its propulsion as well.
- Single rotary actuation on the steering column, with a rack and pinion couple. It was discarded because constraining the rack didn't seem to be simple.
- Single rotary actuation on the steering column, to which a plate is connected at its bottom (figure II.7.2) and is linked to the uprights by means of tie-rods. This is the system typically used on go karts and was the one implemented on Cerberus as well (previously shown in figure II.3.8).

II.7.2 Further description of the system and rod-end bearings' dimensioning

The steering column connection to the frame is performed with some onyx supports (shown in figure II.7.2) which were designed by Samuel Barbaglia with some support from Davide Casotto and from the author (who gave the instructions of which movements those components should constrain).

This system is highly adjustable in terms of levers and angles (caster, camber) but, because of that, it takes some time to fine-tune it. When the lower part of the system is definitive, though, it's possible to act on the clamp that connects the upper part of the steering column with its lower one to adjust a static steering condition.



Figure II.7.1: LemonTrike's steering system

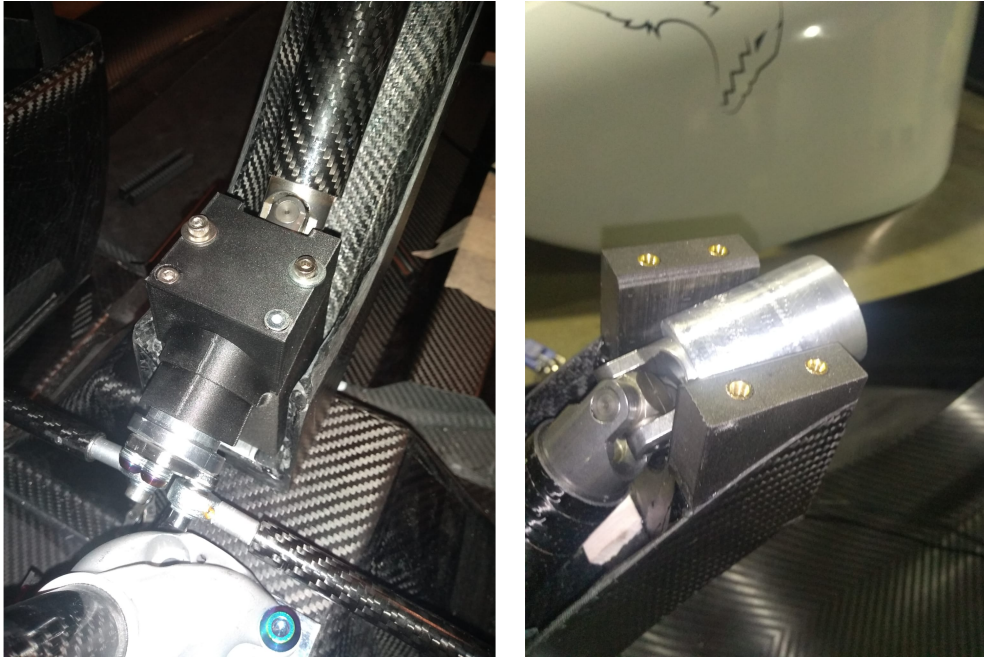


Figure II.7.2: Lower steering column support and connection to the tie-rods (left) and lower half of the upper steering column support

	d/mm	$W/(\text{m}^3)$	F_{max}/N
M5	4,019	6,3731 E-09	203,9
M6	4,773	1,0676 E-08	341,6
M8	6,466	2,6540 E-08	849,3

Table II.7.1: Dimensioning of the rod-end bearings in the steering mechanism

The uprights are connected to the frame with rod-end bearings (figure II.7.3). In the beginning, M5 rod-end bearings were installed, but this resulted in a failure of the lower ones (bent component shown on the right in figure II.7.4); therefore the dimensioning shown in table II.7.1 was conducted, considering the component as a cantilever loaded on the unconstrained tip with a bending force F .

The values used for the dimensioning are the following:

- yield strenght $R_{p0,2} = 640 \text{ MPa}$ as for class 8.8 screws
- lenght of the lever arm $l = 10 \text{ mm}$ (overestimated, since a bushing was inserted between the head of the rod-end bearing and the nut; figure II.7.4 shows the bushing only on the top one which was put at the time)
- safety factor $SF = 2$

therefore, given a diameter d (minor diameter, not the nominal one) of the screw, it's possible to calculate the force necessary to bend the component as follows:

$$F_{max} = \frac{R_{p0,2} \cdot W}{l \cdot SF}$$

where $W = \frac{\pi d^3}{32}$.

The results show that an M8, with a lever arm way higher than the real one and without the stiffening of the added bushing, could sustain about 2,5 times the static weight with a safety factor of 2 in the occurrence that the upper rod-end bearings doesn't support any load.

Satisfied by this result, some adjustments were conducted to install M8 components on the lower part of the uprights.

II.7.3 Final notes

Once the steering system was finally stiff enough and worked fairly well, another major problem became evident: the structure of the lower wheel covers were the aluminum plates are colaminated and support the upper rod-end bearings of the uprights, flexed under impulsive loads and made the vehicle unstable at speeds higher than 55 km/h. Because of that, some reinforcement bars were added later (as formerly shown in figure II.3.7). As that was a last-minute update made on the last day of the September 2022 competition, when in the end Cerberus couldn't run (see part III), as of now (October 2022) the steering system was not tested anymore.

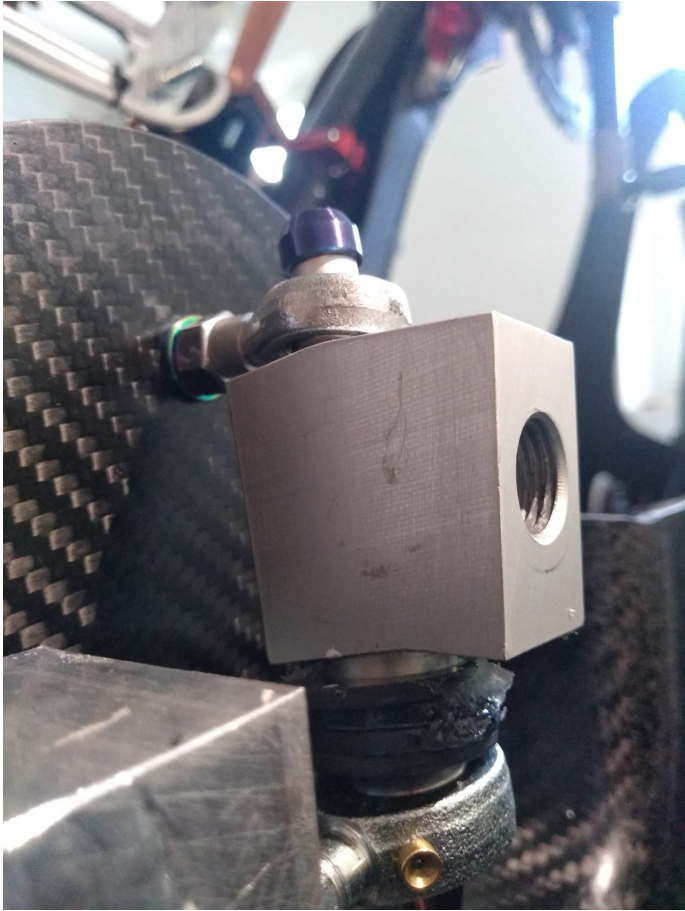


Figure II.7.3: Cerberus's upright connection with the frame



Figure II.7.4: On the right: one of the M5 bent rod-end bearings. On the left: one of the replacement M8 parts used in their stead after a basic dimensioning

Chapter II.8

Breaking system

Prototype Cerberus features an hydraulic disc brake system on the rear wheel. The final design was redone from scratch after the first one was discovered to have an issue during the assembly phase: the rotor couldn't fit very well because the caliper and actuating lever of the brake pads would touch the structural fairing. Therefore, only the coupling system of the disc on the hub was maintained.

II.8.1 Main support

The following system (figure II.8.1) was designed by the author, teammate Riccardo Piani and CEO of Erre Ti Composites Solution (company were the team laminated, partly assembled and machined some parts of the prototype) Raffaele Tucci.

It features:

- 2 interfaces for the structural fairing
- a plate that connects the 2 interfaces with the caliper support
- the caliper support

II.8.1.1 Caliper

First of all, a realistic CAD of the caliper was drawn, after taking measurements of all the necessary dimensions directly from the actual piece that would be used (figure II.8.2), and was put in an assembly with the structural fairing and the disc mounted on the rear hub. Particular attention was given to the location and the piece was finally set in place in an easy to access position for mounting and maintenance reasons.

II.8.1.2 Caliper mount

After that, the support, which features two M6 holes used to take in place the caliper, was drawn (figure II.8.3). With the intent to ease the machining procedure, which would be done with a 5 axis CNC that can be angled at steps of 3 degrees, the upper faces are inclined by 18°. Two slots on the base allow for a forward and backward translation. Since the body itself is structural but doesn't have any other particular functionality, and given that there wasn't time to design something more sophisticated, the 2 columns with the holes were drawn as parallelepipeds with a square base of 10x10

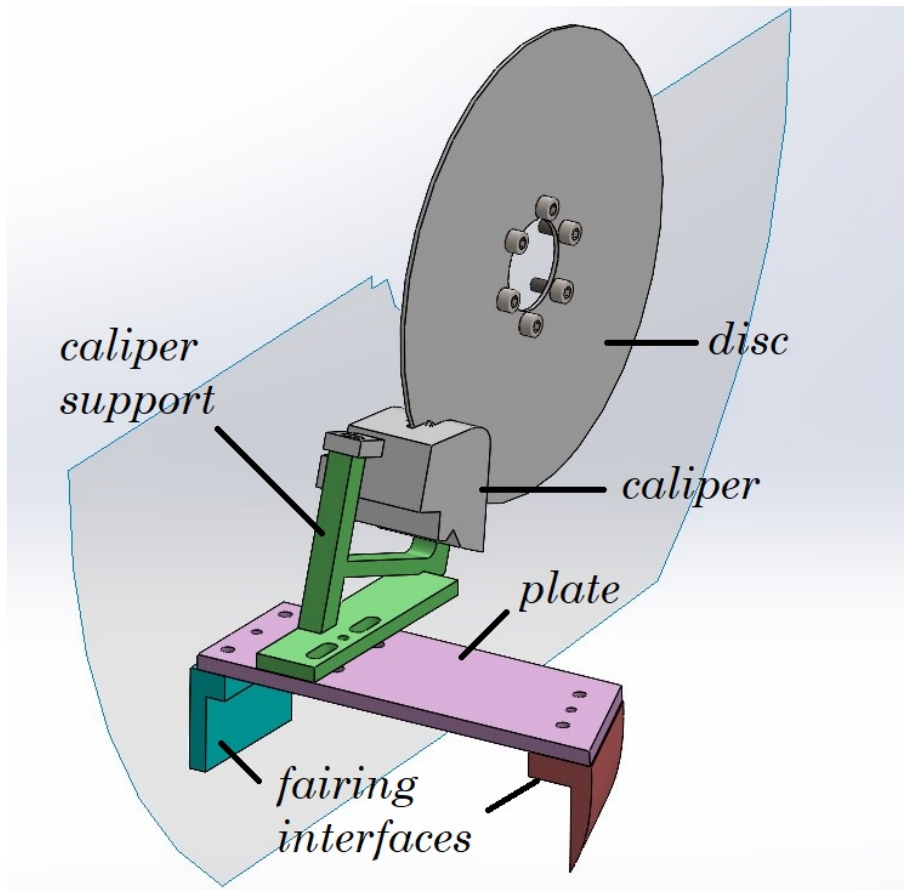


Figure II.8.1: Braking system CAD assembly

mm. No chamfers or fillets were set and it was told to the miller to produce the piece with the minimum cost and time (no restrictions on the tools to be used were given).

II.8.1.3 Plate

The plate (figure II.8.4) serves both as a base for the caliper mount and, thanks to its two slots perpendicular to the support's ones, for the lateral motion of the caliper. Four $\varnothing 5$ through holes are used to bolt the piece to the 2 fairing interfaces; the two $\varnothing 4$ holes are intended to host 2 centering pins once the position is fully defined, in order to avoid the possibility of minimum movements even in worst case of a loosened screw.

II.8.1.4 Fairing interfaces

The 2 interfaces are directly glued to the structural fairing (figure II.8.5). The shape of the surfaces to be glued is a 2,5 mm offset of the fairing's internal surface, since the glue itself occupies some space.

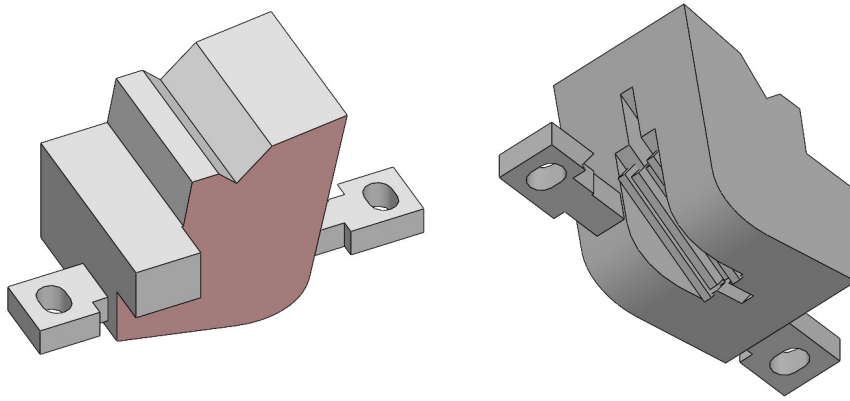


Figure II.8.2: CAD of the caliper

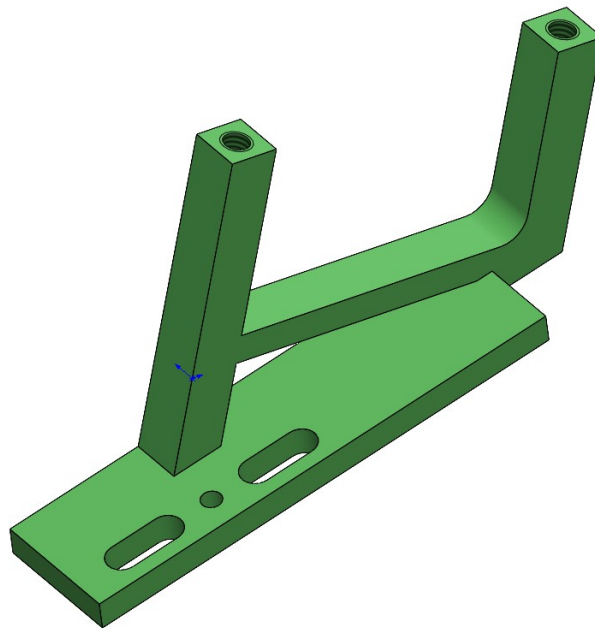


Figure II.8.3: Zoom on the caliper mount

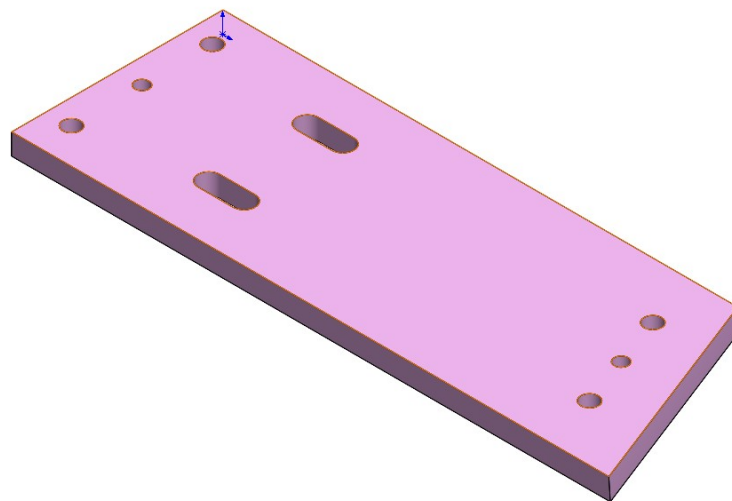


Figure II.8.4: Zoom on the the plate



Figure II.8.5: Braking system in place on Cerberus

II.8.2 Brake lever position

The brake lever position was discussed for months, as it's a very important topic that concerns the safety of both the rider and the vehicle.

Particularly, 3 possible solutions were taken into account but discarded.

- Lever directly integrated in one of the 2 handles: according to rider Simone Chiarolla, who makes use of this solution on his actual handcycle, it's not very comfortable; moreover, this configuration would have the hydraulic tube continuously in movement.
- Lever fixed to the slide: this solution would allow to have a fixed cable but the location didn't seem optimal and it wasn't clear how to connect the two parts since there isn't a lot of room there.
- Lever placed under the seat: it might have been a little too distant from the hands

The final solution was to clamp the lever on a carbon tube (already shown in figure II.3.5), like on the handlebars of normal bikes, and to glue the tube to a 3D printed and holed cube that is likewise glued to the structural fairing.

Chapter II.9

Other components

II.9.1 Hubs

The front hubs were drawn in collaboration with Claudia Barattini, while the rear one was designed with Matteo Ferranti and Giacomo Lussiana. All the drawings of these components can be found in Appendix B.

Since the rear hub is connected to the disc brake, for its dimensioning it was important to take into account the braking torque applied to it. For this purpose, the free body diagram shown in figure II.9.1 represents the contributions considered (the rolling resistance torque wasn't taken into account as its magnitude is neglectable). It's then possible to write the following rotational equilibrium equation:

$$\text{O} \curvearrowright: I\dot{\omega} + T_b + F_x \cdot R = 0 \quad (\text{II.9.1})$$

where T_b is the braking torque and R is the radius of the wheel deformed by the vertical load.

Since F_x is a function of F_y in Coulomb model through the friction coefficient as:

$$F_x = \mu F_y$$

it's possible to rewrite equation II.9.1 as follows:

$$I\dot{\omega} + T_b + \mu F_y \cdot R = 0$$

For conservative calculations, μ was set to 1.

I was calculated considering the wheel as a 1 kg homogeneous disc with radius 250 mm:

$$I = \frac{mR^2}{2} = \frac{1 \text{ kg} \cdot 0,25^2 \text{ m}^2}{2} = 0,03125 \text{ kg} \cdot \text{m}^2$$

Note that all these are conservative assumptions, as the final mass of the laminated wheel was about 850 g, the disc is not homogeneous but it's denser in the centre, where the hub is located and the loaded radius is about 235-240 mm, depending on the clincher used.

The emergency break value considered was 5 m/s², therefore the angular acceleration was set to:

$$\dot{\omega} = \frac{-5 \text{ m/s}^2}{R} = \frac{-5 \text{ m/s}^2}{0,25 \text{ m}} = -20 \text{ rad/s}^2$$

Finally, the vertical load was set to 300 N, which is about 1/3 than the weight of the vehicle. Once again, this is a conservative assumption if one takes into account the fact that a deceleration of 5 m/s² shifts the weight distribution to the front.

With these values, the breaking torque used as a reference was:

$$T_b = I\dot{\omega} - \mu F_z \cdot R = 0,03125 \text{ kg} \cdot \text{m}^2 \cdot (-20 \text{ rad/s}^2) - 1 \cdot 300 \text{ N} \cdot 0,25 \text{ m} = 75,625 \text{ N} \cdot \text{m}$$

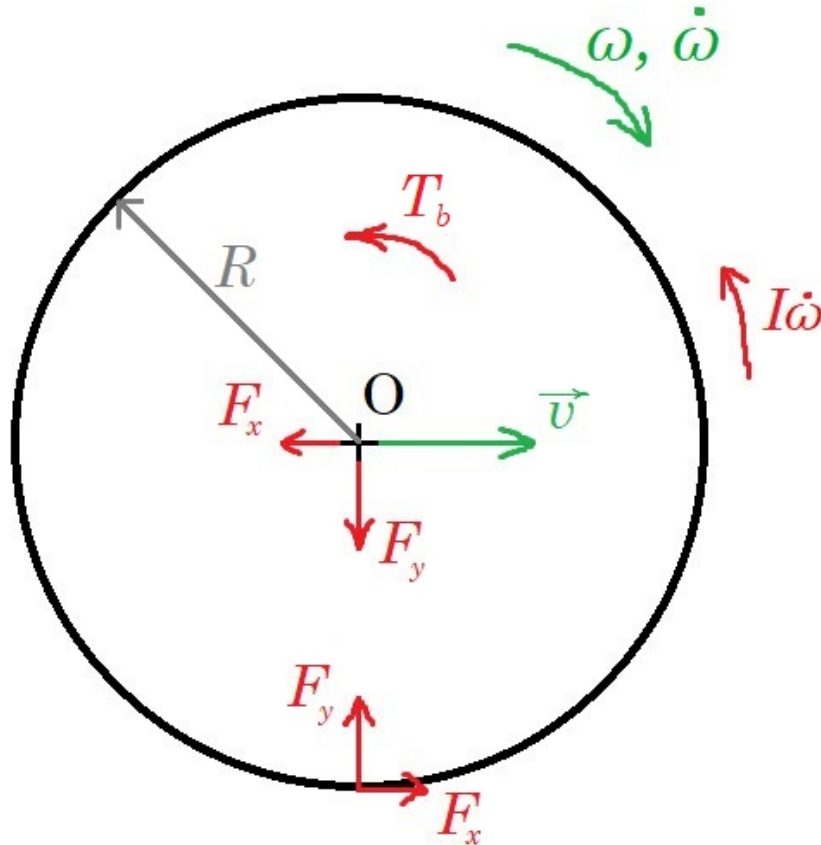


Figure II.9.1: Free body diagram of the rear wheel in acceleration

II.9.2 Crankset and handles

The crankset assembly (see Appendix B for further detail) was drawn in synergy with Nicolò Gallo, who designed the handles too. Figure II.9.2 shows the assembled handles with 3 buttons (gear up, gear down and radio) and wiring installed on the right one. They were then tapered with tennis rackets' overgrip for comfort reasons.

II.9.3 Wheels

The wheels were designed by the FEM division, mainly by Riccardo Grossi and Edoardo Besenval who is writing his bachelor thesis on this topic. Therefore, this matter is not going to be discussed in detail.



Figure II.9.2: Handles, designed by Nicolò Gallo

II.9.4 Adjustable seat

Cerberus's seat is quite adaptable to many riders. Following, is a short explanation on how it works.

The fairing's bottom longerons have been reinforced with wood parts and aluminum (see part III) during the assembly phase. The wood is intended to grant stiffness with a low impact on weight, while the 5 mm thick aluminum slabs in between serve as anchor points for some bolts that connect some carbon L shaped plates to them. To each of the carbon Ls is then fastened a multi-holed steel slab (figure II.9.3)

On the rear, the holed slabs are directly bolted to the seat (figure II.9.4) while on the front a pair of 3D printed onyx pieces serve as interfaces with the lower part of the seat (figure II.9.5).

II.9.5 Seatbelt

The seatbelt locking system was designed by Lucrezia Pasi and Edoardo Besenval. It features 2 rollers that are connected to 2 steel plates each which are glued directly to the fairing (figure II.9.6).



Figure II.9.3: Adjustable seat: plates set in place on the bottom longerons reinforced rear section



Figure II.9.4: Adjustable seat, rear locking system, upper part: depending on the hole used, the seat moves up and down and is reclined

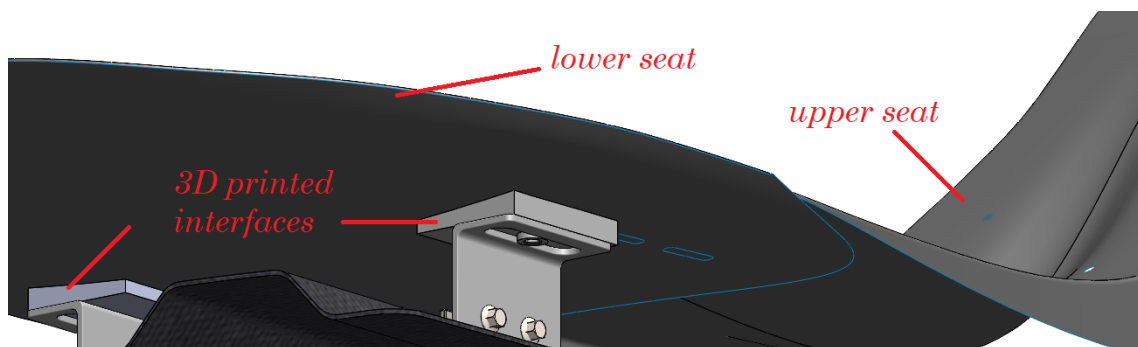


Figure II.9.5: Adjustable seat, front locking system: depending on the position of the plastic parts in the slot, the seat can move longitudinally



Figure II.9.6: Anchoring points for the seatbelt being glued onto the fairing

II.9.6 Air filter

In order to lead clean air in the vehicle, a filter case designed by Matteo Ferranti (figure II.9.7) is located on top of the rear wheel cover (figure II.9.8), as CFD results displayed a high pressure zone there. A filter tissue is set in place into the 3D printed cage and is periodically checked and replaced if need be.

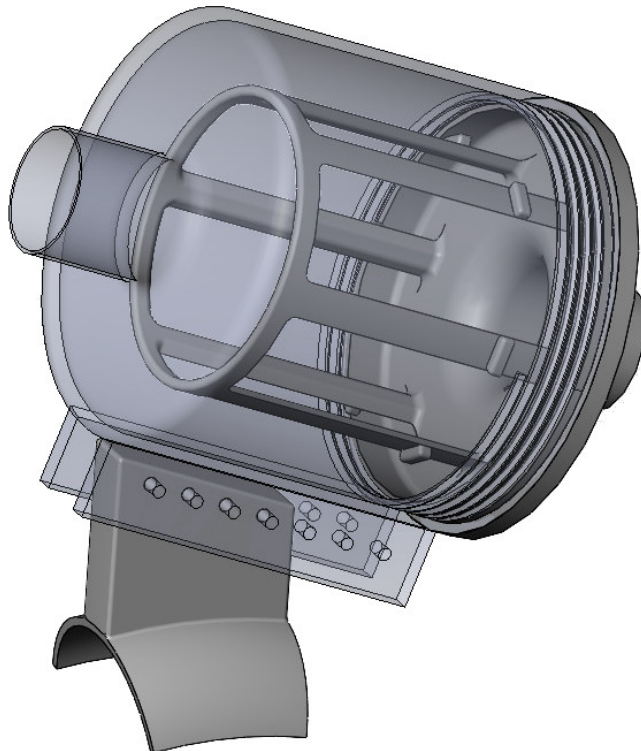


Figure II.9.7: Air filter and its support



Figure II.9.8: Air filter connection on the wheel cover

Part III

Construction and testing

Chapter III.1

Fitting tests

Fitting tests were an important phase as they are the bridge between the design and production phases of the fairing.

III.1.1 June 2021 test

The first test was conducted in June 2021 with rider Simone Chiarolla.

The CAD assembly with the fairing was used as a reference for the creation of some frame of the most important cross sections (i.e. ankles, wheels, hands, elbows and shoulders) which were then crafted by milling some extruded polystyrene panels (figures III.1.1-III.1.2).

Thanks to this meeting with Simone, we discovered that the 3D scan had some issues and we took some measurements to reproduce a more realistic CAD. It has been a very useful check because, had we produced that fairing, we wouldn't have been able to fit the pilots inside and the whole project would have been affected both from an economic point of view and from a long delay in the production, possibly ruining two years of hard work.

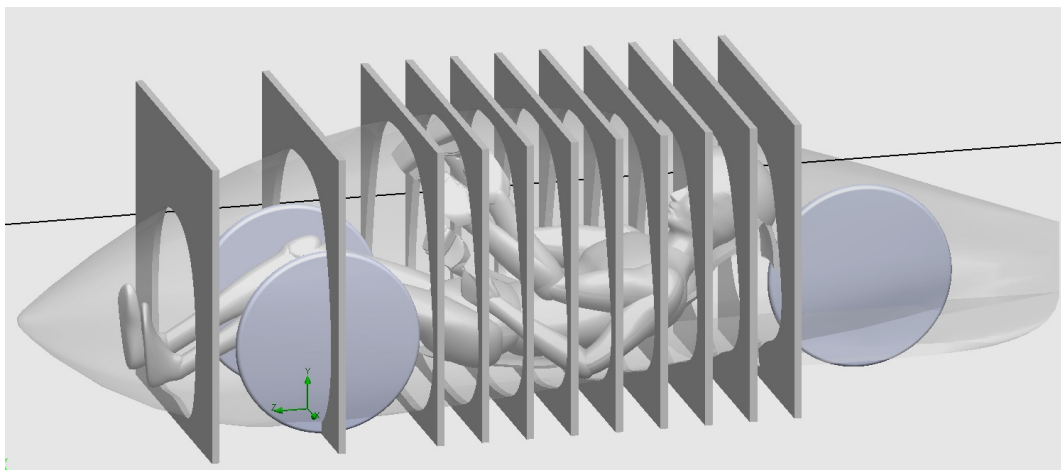


Figure III.1.1: CAD preparation of the panels for the fitting test of June 2021



Figure III.1.2: June 2021 fitting test

III.1.2 October 2021 test

Thanks to the test carried on 4 months prior, with a bigger mannequin and generally more space in the cockpit, the second test went rather smoothly.

This time, a more robust and adjustable structure was designed and tried by the author some days ahead of the test (figure III.1.3). The volume frames, unlike the first time, were 3D printed in PLA for minor costs (figures III.1.4 and III.1.5).

As this was meant to be the final check, we took an appointment on a day in which both the athletes were available and as a final check for the movements of the arms, we also asked Simone Chiarolla to try and fit with his own handcycle in the frames (figure III.1.5).



Figure III.1.3: Structure used for the fitting test in October 2021



Figure III.1.4: Diego Colombari during the fitting test in October 2021



Figure III.1.5: Simone Chiarolla during the fitting test in October 2021

Chapter III.2

Prototype production

III.2.1 Molds and models

In order to produce precise components, each of the laminated parts was manufactured with the use of molds. The materials involved for almost every piece in this processes were MDF (medium-density fibreboard) and resin (figure III.2.1), depending on the dimension of the mold and on the lamination procedure to be used. The structural fairing is the only component which has a non machined mold: it's carbon laminated on an MDF model.

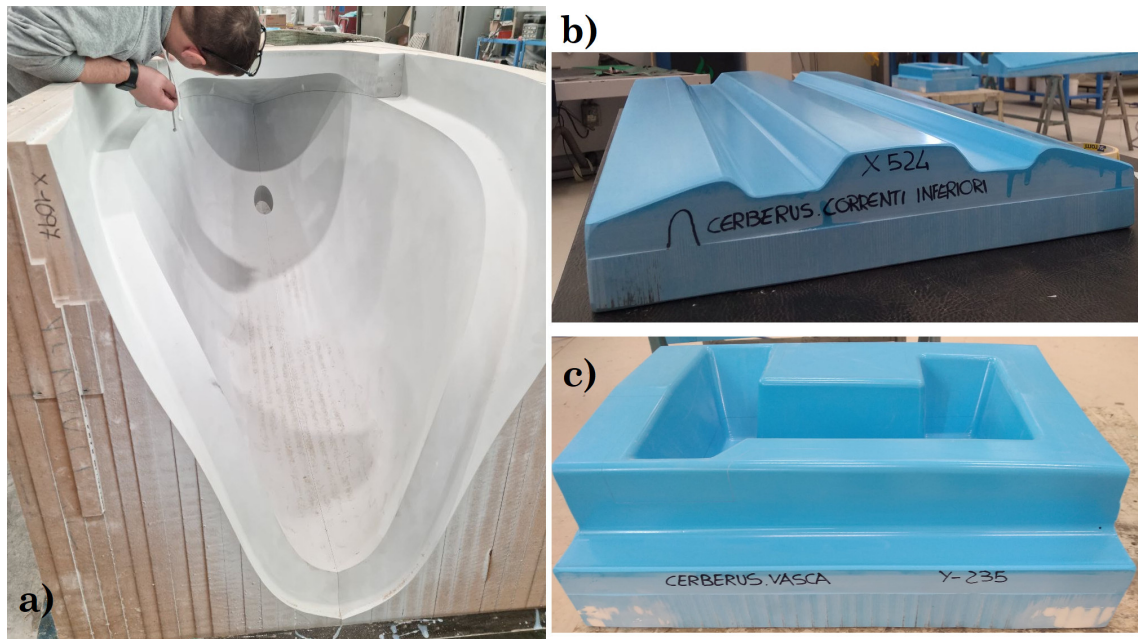


Figure III.2.1: Example of an MDF mold (a, front fairing) and resin molds (b, bottom longerons) (c, basin)

III.2.1.1 From CAD to machining

When creating a mold, it's important to establish which surfaces are going to be in contact with it and which are going to be in contact with the cloth since this affects the



Figure III.2.2: Piece's outlines on the basin's mold

surface finish of the piece. For all the aerodynamic components (i.e. all the parts that are going to be in contact with the air outside the vehicle) the surface in contact with the air is the mold's one. This means that, when generating the CAD, if the components are drawn as surfaces, it's necessary to take into account the actual thickness of the final components in order to define the real volume occupied by the parts.

For manufacturing purposes, every mold is actually bigger than the piece and presents outlines to delimitate the surface of the part and remain impressed on the part itself. Later, by cutting along the lines, the excess material is removed.

Once the CAD is complete, it's possible to use a CAM program and machine the mold with a CNC.

III.2.1.2 Painting

If the material used for the mold is MDF, once the raw machined part comes out from the CNC, it's necessary to spray paint over it in order to cover every imperfection present on it (figure III.2.1.a).

III.2.1.3 Sanding

The next step is then to sand everything until the surfaces are smooth enough. The sanding process should be as uniform as possible. It's mandatory to sand the pieces little by little on the whole surface, in order to avoid changes in the shape of the mold due to the fact that the piece was sanded too much on certain areas.

III.2.1.4 Surface sealer application

On MDF molds, once the sanding is complete, applying a sealer is a good way to get rid of every little surface imperfection. For this prototype Mikon[®] 399 MC was used.

III.2.1.5 Detaching agent application

The final step that precedes the lamination is the application of a detaching agent. Marbocote PK4 was used for this purpose. Generally every mold was wetted 4 times with it and a last application was performed right before the lamination. The application of 1 coat of PK4 consists in:

- slightly impregnating the brush in PK4
- spreading a thin layer of it on the mold
- removing with a cloth PK4 excess (the mold should result just humid)
- waiting for 10 minutes.

For time optimization, it's usual to detach a mold while laminating another component.

III.2.2 Lamination

Lamination is the process of manufacturing a material in multiple layers, so that the composite material achieves improved strength, stability, or other properties from the use of the differing materials [26]. Composites are structures made of reinforcement material immersed in a matrix; for this project the material involved were carbon, glass and kevlar fibres as reinforcements; PVC and aluminum were used as fillers in sandwich structures, while epoxy resin composed the matrix.

III.2.2.1 Cut of the plies

Before starting the lamination process, it's important to prepare the reinforcements; one key and delicate element is the cutting procedure because, since composites are orthotropic (i.e. it's properties depend on the load direction in respect to the fibre direction) it's important to cut the fabrics in the correct direction and without damaging or distorting the fibres.

Thanks to Stefano Tomassi and Riccardo Grossi from the FEM division, who made use of SmartCAE software Laminate Tools (figure III.2.3) for the generation of the developments of many pieces, a lot of plies could be cut with a plotter. This sometimes resulted extremely useful for many reasons:

- there are cases in which cuts by hand can be very difficult to perform
- when the plotter is cutting, it's possible to use that time to prepare the molds, laminate or whatever
- thanks to the *nesting* procedure, material waste are kept to a minimum
- it's possible to accurately design overlaps in the lamination
- cuts with the plotter are not tedious, so it's less likely that one doesn't become tired and the works is rended more efficient

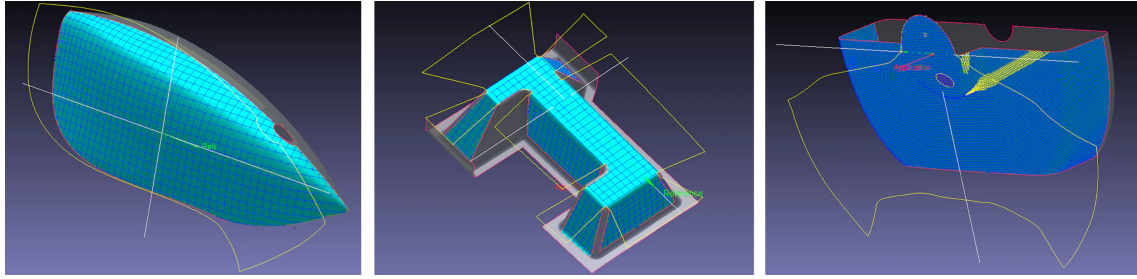


Figure III.2.3: Some views of the developments extractions of some parts in Laminate Tools

III.2.2.2 Techniques used

For the manufacturing of Cerberus, 3 different approaches of lamination were used:

- prepreg
- infusion
- wet-layup (wet-lay) or hand laminating

each of them has pros and cons.

III.2.2.2.1 Prepreg

The name stands for pre-impregnated: it's basically a cloth of fiber (in our case carbon) that is industrially wetted with the resin at a fixed proportion. This makes the material's characteristics very accurate and allows for a precise manufacture. Prepreg cloth is fairly easy to give the desired shape and it's simple to manipulate it without concerns about ruining the weft threads. Moreover, in comparison with the wet-lay, it doesn't stick much on the gloves.

Once the plies are in position, it's necessary to neatly cover the composite with a *breather cloth*, which provides the role of absorbing any excess of resin from the laminate and pressing the piece on the mold. The piece is then insert into a plastic bag, where a valve is installed, and is sealed accurately. Lastly, since prepreg cures under pressure (typically 5-7 relative bar) and with temperature that can reach 150 °C, the whole thing is put into an autoclave (figure III.2.4). If the laminate is thick, every 5 layers, a 15 minutes vacuum treatment should be done in order to compact the sheets together (see next paragraph for vacuum bagging).

It's worth to note that the price of prepreg cloths is higher then dry ones and that, in most cases, the lamination can't be interrupted (it's sometimes possible to put the unfinished component in freezer and ultimate the lamination the day after).

III.2.2.2.2 Wet-layup

In the wet-lay method, dry fibre cloths are added over the mould, one layer at a time, and each layer is wetted out with the matrix, by hand, using a brush, a roller or a silicon spatula. The matrix is made right before starting the lamination by mixing the resin in the right ratio with its catalyst (figure III.2.5).



Figure III.2.4: Structural fairing mold (carbon prepreg) in the autoclave

Once all the reinforcement has been added to the mould and wetted-out, the part can just be allowed to cure at room temperature. However, if it's to be vacuum bagged, then this should be done immediately before the resin starts to cure. In this case, the last ply is covered with a *perforated release film*, which prevents drying the laminate too far, and on top of it is placed the breather cloth, that provides the path for the air to escape to the vacuum and also plays the role of absorbing any excess of resin from the laminate. It's also possible to insert a *peel ply* between the perforated film and the piece: its purpose is to provide a membrane that allows air and resin to pass through into the breather layer but that can later be peeled back from the cured laminate. It also has the benefit of leaving a very neat surface finish that is perfect for bonding too.

As the vacuum is pulling down, the bag should be manipulated into all of the contours and corners to avoid any bridging to ensure that even pressure is applied over the entire part.

III.2.2.2.3 Infusion

Infusion is a technique that, unlike the other two, involves the use of a dry cloth of fiber (we used both carbon, glass and kevlar) all through the modelling process. Every layer is temporarily bonded with the next with the support of an epoxy glue (which is the basis for the epoxy resin).

Once the piece is given its shape, the laminate is covered with peel ply and with a rather rigid net (in black in figure III.2.6) that is needed to let the resin flow uniformly.



Figure III.2.5: Hand lamination: preparing the matrix by combining the resin with its catalyst



Figure III.2.6: Wheel covers during the infusion procedure

The piece and its mold are then bagged and connected in one point to the vacuum pump and on another to a resin tank. These two points should be put as further apart as possible or rather in a way that the matrix covers the whole surface of the piece when flowing to the vacuum valve. The flow is to be interrupted as soon as the resin starts to crawl into the vacuum tube, so that the pump doesn't clog.

III.2.2.3 Visual inspections and final refinements

After the molds are open and the pieces are extracted (figure III.2.7), it's necessary to visually check them and look for possible delaminations, voids or areas in which the weave is tangled.

If, from a structural point of view, all is right, the final refinements, such as cutting the flanges away, opening the holes, covering superficial imperfections (figure III.2.8), coating, painting and polishing are made.



Figure III.2.7: Raw front fairing just extracted from the mold. Window and flange cuts needed



Figure III.2.8: Superficial imperfection created during the infusion



Figure III.2.9: Tolerance checks on the fairing

III.2.3 Assembly

Once all the pieces are refined, it's necessary to bound them all together.

III.2.3.1 Tolerance checks

The first important step to take in the assembly phase is to compare with a CMM (Coordinate-measuring machine) each piece with its CAD geometry. If all is in tolerance, it's possible to use the measuring probe to find some point where the pieces should interface with one another and tracing them with a marker. Later it's possible to temporarily glue some small wood pieces to the bigger piece and use them as stiff guides for the positioning of the part to be structurally glued.



Figure III.2.10: Glue spilling and weight application on the bottom longerons

III.2.3.2 Gluing

The final step consists in spreading the glue on the pieces, and bonding them together by applying the necessary pressure to them and waiting the proper time to have a correct polymerization (figure III.2.10).

III.2.4 Other parts produced autonomously

Amongst these, a lot of rapid prototyping was done (figure III.2.11), making use of the team's students' own 3D printers too. Some other pieces were machined autonomously (like the wooden reinforcements under the seat in figure III.2.12) with a little CNC. In certain cases, some pieces from old prototypes or scraps parts were used or remodeled to try and make some pieces, like for the chain tensioner.

The team made also use of lasercut machines for the production of some wood pieces and for the creation of the plexiglass window for the vision system (figure III.2.13).

Sometimes some pieces, which needed sanding or others modification were also fit onto a screw (figure III.2.14) or remodeled with the help of a dremel or holed under a drill press.

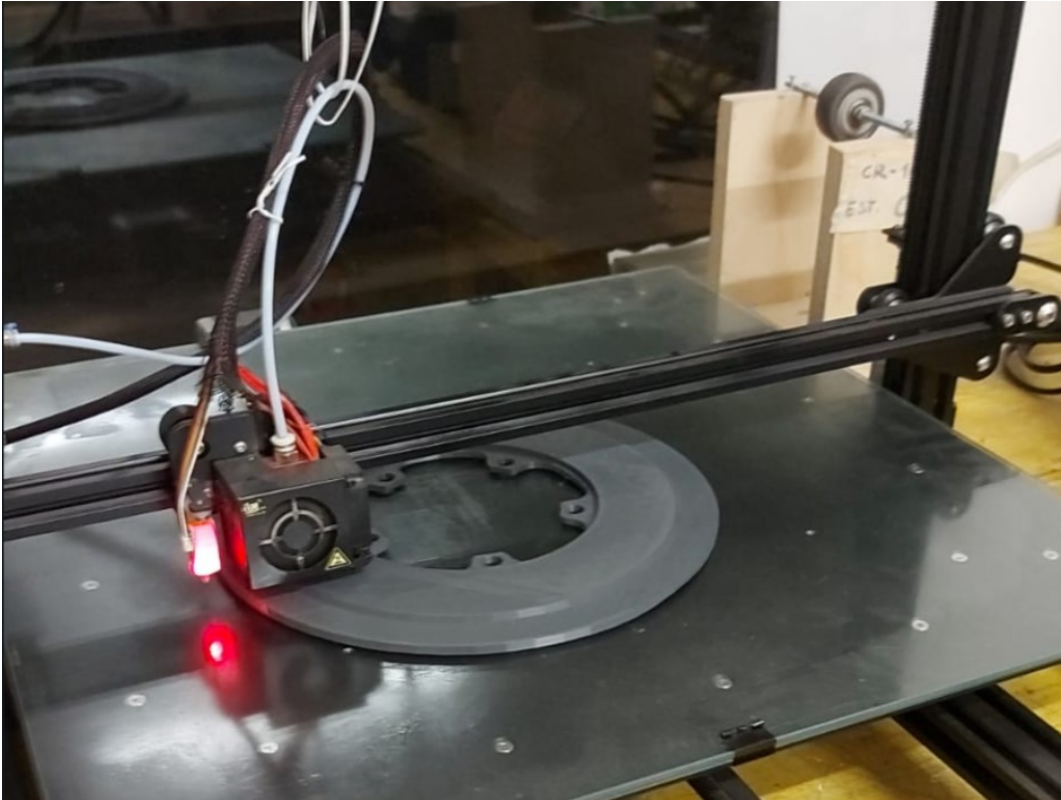


Figure III.2.11: 3D printing the chainring's carter



Figure III.2.12: Wood machined parts: after raw machining on top left, after sanding on top right and set in place for fit check on bottom

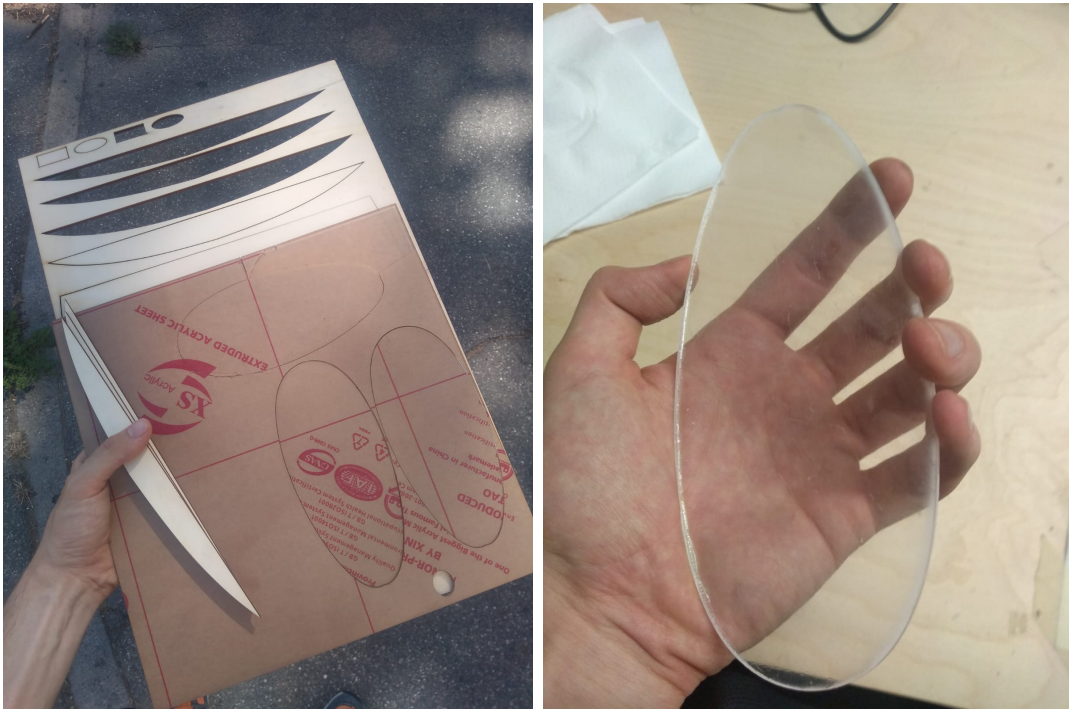


Figure III.2.13: Lasercut wood and plexiglass (left). Plexiglass window after the laser-cut (right)



Figure III.2.14: Sanding a piece fit onto the screw

Chapter III.3

Road testing

III.3.1 Tests

Tests are an important part of the project because they allow for adjustments or redesign of components if need be. The first tests on Cerberus were static ones, such as the connection of the wheels to the steering mechanism (when two rod-end bearings failed by bending, as discussed in chapter II.7). Other tests, like the check of the tensioners, were conducted on the vehicle still in place and with the wheels raised from the ground. Further checks were conducted at low speed indoor, to check the general behaviour of the prototype and try to find solutions to the problems. Luckily, most of the electronic subassemblies could also be tested separately before being mounted on the vehicle, reducing the testing time.

As of October 2022, not many tests have been conducted yet on Cerberus because its construction ended in August 2022 and some modifications were also made in September at the WHPSC competition.

One of the major problems that persisted through all of the test conducted in August 2022 concerned the steering mechanism because during those weeks the team ran out of structural bi-component glue and the suppliers were on vacation; therefore, the prototype ran with some parts of the transmission supports fixed only by interference. This gave a little of movement to the overall structure.

III.3.1.1 Tests in Balocco

On August 2022 Cerberus hit the road for the first time and was taken to Balocco Proving Ground, where Team Policumbent has been leading its most important tests for years now. It's a 3-lane track composed of three straight roads connected by three long curves (figure III.3.1) thanks to which the prototypes can go at their maximum speed. The overall length is about 7,7 km.

The first test took place on the 17th of August but too many problems on the aforementioned steering system forced the team to get back to work just after about two hundred meters on the tarmac.

On the 19th, then, after finally partially solving the problems, Cerberus rode for a few kilometers and reached a speed of about 40 km/h on fixed gear since the electronic shifting system's PID controller had yet to be calibrated.

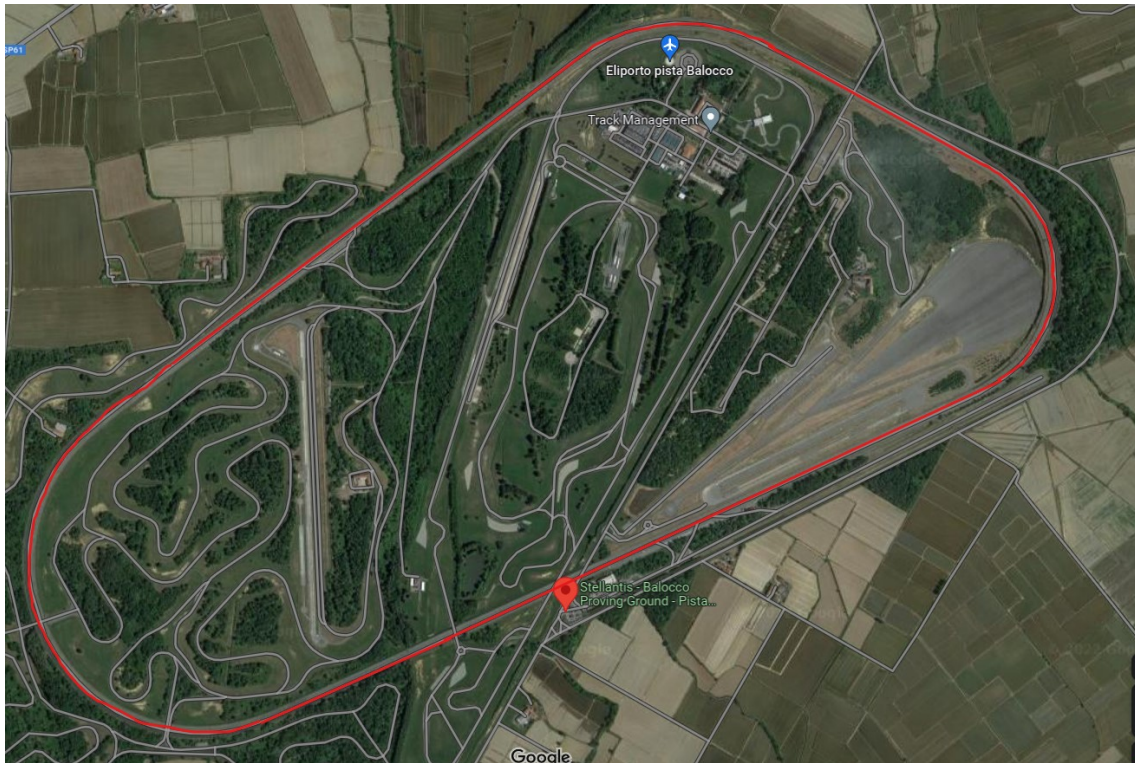


Figure III.3.1: Satellite image of Balocco Proving Ground. In red it's highlighted the track used by Team Policumbent

III.3.1.2 Test in Stupinigi

Another place that Team Policumbent uses for testing is the first part of Stupinigi cycle path's straight road. The asphalt condition though it's not the best and since it's a public road, prototypes usually don't go faster than 40 km/h there for safety reasons.

III.3.2 WHPSC

The World Human Powered Speed Challenge is a 7 days event that takes place on an 8 miles (about 12,8 km) long straight public road which temporarily closes to the traffic in the Battle Mountain, Nevada, at 1450 m of altitude. Participants then run on part of that track depending on the vehicle performance 2,5 miles (about 4 km) or 5 miles (about 8 km) and have 1 mile (about 1,6 km) for decelerating and getting to a complete stop in the catching area. The track has a negative slope of 0.6439% over the 5 miles [28]. The speed is calculated as an average on the 200 m that conclude the 2,5 or 5 miles run (timing zone).

III.3.2.1 September 11th

Morning run: 2,5 miles. Due to a last minute problem with the electronic moving cassette, Cerberus had to race at fixed gear (53-42 on the primary chain and 53-16 on



Figure III.3.2: Team Policumbent testing Cerberus on the 2-lanes straight cycle path in Stupinigi



Figure III.3.3: Team Policumbent testing Cerberus on the 2-lanes straight cycle path in Stupinigi

the secondary chain). Speed at the end of the race: 37,9 mph (50 km/h). The following day, it will be given the possibility to race on the 2,5 or 5 miles track depending on the prototype's completeness.

During the training on the roller, a heavy flexion (probably about 10-15 mm) on the crankset was noticed but couldn't get fixed.

III.3.2.2 September 12th

Morning run: 2,5 miles. Problems with the steering system caused Cerberus to go off the road, without spinning or overturning. No serious damage to the fairing by the prototype and Diego wasn't harm, though the rear tyre was damaged and 4 screws that were taking disc in position were ripped off.

Time was taken to repair everything. The 4 screws, which were strangely just underdimensioned M3, were replaced with M5.

III.3.2.3 September 13th

Due to rainy weather and to further work on the trike, Cerberus didn't run. Some tuning especially on the steering mechanism was made, in an attempt to run the next day. Some loosened screws that should firmly link the basin to the slide were replaced with longer ones and finally the displacement noted 2 days prior on the crankset was rendered null and Diego was able to push at more than 315 W at times.

III.3.2.4 September 14th

First morning run: 2,5 miles. Due to a drop of the chain on the cassette branch, Cerberus had to stop right after the start but the it was allowed to run again later in the morning.

Second morning run: 5 miles. The first attempt to the long run went ok: Diego was able to complete the track and the speed taken in the 200 m was 64 km/h.

Still more tuning on the handling were necessary, as Diego was actually able to crank for just about a third of the time, while trying to keep the trike on the road for the rest of the time (the data analysis showed that the average power of Colombari during the run was of only 103 W). Furthermore, the chain fell right at the end of the run, so Cerberus took too long a time to get to the catching area. The road had to be closed for too long and for this reason, it was not allowed to run in the evening yet.

In the afternoon further adjustments were made and Diego as well as a few of the students tried the trike in on open road of Battle Mountain where there weren't motorized vehicles circulating at that moment. Finally the steering seemed to be very responsive and the hope for a good result the next day, was high.

III.3.2.5 September 15th

Cerberus finally seemed to be tuned pretty well and started to go fairly fast, reaching 65 km/h in less than 1,5 km, where the primary circuit of the cameras malfunctioned and Diego started to look in the backup monitor which though, due to a blunder was mirrored, so Colombari steered on the left to try and correct a trajectory that seemed to take him off road on the right. Therefore, Cerberus went off the track and

overturned twice in the scrub. Luckily no damage was reported on the fairing and more importantly, the rider was extracted unharmed.

All the rest of the day was taken to check thoroughly the prototype and to try to re-fine-tune the steering mechanism, possibly making it even more responsive.

III.3.2.6 September 16th

The morning run was the last one for Cerberus. The steering which seemed stiffer than ever before was very responsive until 55 km/h, when the vehicle became gradually unstable and started to go on the right instead of going straight. Therefore, Colombari had to correct the trajectory and stop cranking at frequent intervals and couldn't raise the speed too much. The data recorded by the team suggest a maximum speed of about 70 km/h and in the 200 m timing trap (in which Cerberus travelled diagonally twice, therefore actually riding for more than 200 m) the calculated speed was 65,79 km/h.

In the afternoon the problem was finally solved with the further stiffening of the structure already presented in figure II.3.7, with two carbon tubes to stabilize the rod-end bearings interfaces that were discovered to bend when steering: they had become the weak link of the mechanism after everything else had been stiffened.

III.3.2.7 September 17th

As already said, in the last day of the competition Cerberus couldn't run. Unfortunately, the M5 thread on the bottom of one of the uprights was damaged. The piece should have been rethreaded and a new, longer screw should have been used. The team was given an extra chance to make a final run under the condition to be reasonably sure that everything would go smoothly. As the prototype was still being tested, though, it was decided to end its competition then.

III.3.3 Final comments

As of October 2022, Cerberus is a prototype that still needs to be tested some more and has to undergo some adjustments, especially on the steering system. Once the trike is finally fine-tuned, though, mainly thanks to its exceptional aerodynamics, it's expected to exceed 100 km/h in Battle Mountain (where the air is more rarefied and there's a slight downslope) and to break the 80 km/h barrier at sea level on a closed circuit (null average slope). For the moment not much more can be said if not that it surely is a very efficient and safe arm-powered recumbent trike.

Part IV
Appendices

Appendix A

Bill of materials

CODE	DESCRIPTION	Manufactured by / bought from	Drawing	Q.TY
TR ¹				
TR_PR ²				
TR_PR_01	Crankset shaft	Gariglio Meccanica	yes	1
TR_PR_02	Flange for power meter	Gariglio Meccanica	yes	1
TR_PR_03	Sleeve	Gariglio Meccanica	yes	1
TR_PR_04	Internal spacer	Gariglio Meccanica	yes	1
TR_PR_05	Right spacer	Gariglio Meccanica	yes	1
TR_PR_06	Shaft-crank interface	Cim 4.0	-	2
TR_PR_07.1	Right handle (with buttons)	Roboze	-	1
TR_PR_07.2	Left handle	Roboze	-	1
TR_PR_08	centering bushing for TR_PR_05	3D Company	-	1
TR_PR_09	Crank-handle interface	Cim4.0	-	2
TR_PR_10	Carter	self produced	-	1
(commercial components)				
	Pedal axle (right)		-	1
	Pedal axle (left)		-	1
	Tube Ø18 x Ø20 x 123,9 mm		-	2

¹Assembly name: Transmission (*Trasmissione* in Italian)

²Subassembly name: Propulsion (*Propulsione* in Italian)

CODE	DESCRIPTION	Manufactured by / bought from	Drawing	Q.TY
	bearing: radial, Ø25-Ø37x7	Lyra Bearing	-	2
	Power Meter 9	SRM	-	1
TR_MO³			yes	
TR_MO_01	Sleeve	Gariglio Meccanica	yes	1
TR_MO_02_v2	Grooved shaft	Gariglio Meccanica	yes	1
TR_MO_03	Ferrule for cassette	Gariglio Meccanica	yes	1
TR_MO_04	Bushing btw spider & bearing	Gariglio Meccanica	yes	1
TR_MO_05	Threaded bushing	Gariglio Meccanica	yes	2
TR_MO_07_v2	Translating bushing	Gariglio Meccanica	yes	1
TR_MO_08	Pinched ring	Gariglio Meccanica	yes	1
TR_MO_09	Bushing with 3 radial M3 holes	Gariglio Meccanica	yes	1
TR_MO_10	Spider	3D Company	yes	1
TR_MO_11	Spacer for spider	Gariglio Meccanica	yes	1
TR_MO_12	Bevel gear for the motor	Roboze	-	1
TR_MO_13	Bevel gear for the shaft	Roboze	-	1
TR_MO_14	Guide	Gariglio Meccanica	yes	1
TR_MO_15	Leadscrew female element	Gariglio Meccanica	yes	1
TR_MO_16	Plastic bushing	self produced	-	1
(commercial components)				
	Cassette		-	1
	Threaded rod, M3 x 100 mm		-	1
	Screw: M3x10		-	3
	Washer: for M3 screws		-	3
	Nut: M3		-	4
	Nut: M5		-	1

³Subassembly name: Mobile Groupset (*Gruppo Mobile* in Italian)

CODE	DESCRIPTION	Manufactured by / bought from	Drawing	Q.TY
	Nut: M12, flanged		-	1
	Set screw: M3x4		-	6
	Seeger: for shaft, Ø32 x 1,5		-	1
	Key: 6x6x14		-	1
	Bearing: radial, Ø7-Ø14x5	SKF	-	1
	Bearing: radial, Ø5-Ø11x5	Lyra Bearing	-	1
	Bearing: radial, Ø20-Ø32x7	Lyra Bearing	-	2
TR_RI⁴				
TR_RI_01	Rear support	Erre Ti Composites Solutions	-	1
TR_RI_02	Carter for pulleys	Erre Ti Composites Solutions	-	8
TR_RI_03	Front support	Erre Ti Composites Solutions	-	1
TR_RI_04	Middle-front support	self produced	-	1
TR_RI_05	Middle-rear support	self produced	-	1
TR_TE⁵				
TR_TE_01	Cage	self produced	-	1
TR_TE_02	Right support	self produced	-	1
TR_TE_03	Left support	self produced	-	1
TR_TE_04	Short bushing	Roboze	-	1
TR_TE_05	Long bushing	Roboze	-	1
(commercial components)				
	Screw, M4 long		-	2
	Screw, M5 long		-	2
	Washer M4		-	7
	Whasher M5		-	8
	Nut M4		-	3
	Nut M5		-	4
	Helical spring		-	1

⁴Subassembly name: Second branch (*Gruppo di Rinvio* in Italian)

⁵Subassembly name: Chain Tensioner (*Tendicatena* in Italian)

CODE	DESCRIPTION	Manufactured by / bought from	Drawing	Q.TY
	Chain, mobile branch (112 interpin) (minimum 1430 mm)	Decathlon (Shimano)	-	1
	Chain, fixed branch (355 interpin) (minimum 4500 mm)	Decathlon (Shimano)	-	3
	Quick link	Shimano		4
	Chain pin	Lordgunbicycles (Shimano)		-
	Chainring (53 teeth)	CarbonTi	-	2
	Chainring (60 teeth)	Garbaruk	-	1
	Pulley, 16 teeth (ceramic bearing)	Aliexpress	-	3
	Pulley, 136 teeth (ceramic bearing)	Amazon (Impalapro)	-	2
	Freewheel	Miche	-	1
FR⁶				
FR_01_v2	Caliper mount	Erre Ti Composites Solutions	-	1
FR_02_v2	Plate with slots	Erre Ti Composites Solutions	-	1
FR_03_v2	Fairing interface 1	Erre Ti Composites Solutions	-	1
FR_04	Fairing interface 2	Erre Ti Composites Solutions	-	1
FR_05	Lever support	self produced	-	1
(commercial components)				
	Caliper	Shimano	-	1
	Break pad	Shimano	-	2
	Disc		-	1
	Lever	Shimano	-	1
	Cable	Shimano	-	1

⁶Assembly name: Brake (*Freno* in Italian)

CODE	DESCRIPTION	Manufactured by / bought from	Drawing	Q.TY
	Screw M5		-	4
	Screw M6		-	4
POS⁷				
POS_01	Top "C"	Gariglio Meccanica	yes	2
POS_02	Bottom "C"	Gariglio Meccanica	yes	2
POS_03	Shaft	Gariglio Meccanica	yes	1
POS_04	Flange	Gariglio Meccanica	yes	2
POS_07	Bushing for freewheel	Gariglio Meccanica	yes	1
POS_08	Bushing for interface	Gariglio Meccanica	yes	1
POS_09	Interface shaft-disc	Gariglio Meccanica	yes	1
POS_10	Bushing for bearing	Gariglio Meccanica	yes	2
(commercial components)				
	Centering pin $\varnothing 3$		-	2
	Whasher for M3 screws		-	8
	Scew M3		-	12
	Scew M5		-	10
	Bearing: radial, $\varnothing 35\text{-}\varnothing 47 \times 7$	Lyra Bearing	-	4
FIL⁸				
FIL_01	Support	3D Company	-	1
FIL_02	Case	3D Company	-	1
FIL_03	Cage	3D Company	-	1
FIL_04	Connection with wheel cover	3D Company	-	1
ST⁹				
ST_01	Clamp for crank shaft	CIM4.0	-	1
ST_02	Steering plate	Gariglio Meccanica	yes	1
ST_03	Insert for tie rods	Gariglio Meccanica	yes	5

⁷Assembly name: Rear Hub (*Mozzo Posteriore* in Italian)

⁸Assembly name: Filter (*Filtro* in Italian)

⁹Assembly name: Steering system (*Sterzo* in Italian)

APPENDIX A. BILL OF MATERIALS

CODE	DESCRIPTION	Manufactured by / bought from	Drawing	Q.TY
ST_04	Bottom plate for upright	self produced	-	2
ST_05	Upright	Gariglio Meccanica	yes	2
ST_06	Interface for M8 rod-end bearing (right)	Erre Ti Composites Solutions	-	1
ST_07	Interface for M8 rod-end bearing (left)	Erre Ti Composites Solutions	-	1
ST_08	Bushing interface for bottom cardano-tube	Gariglio Meccanica	-	1
ST_09	Bushing interface for top cardano-clamp	Gariglio Meccanica	-	1
	Half interface for steering column (upper 1)	3D Company	-	1
	Half interface for steering column (upper 2)	3D Company	-	1
	Half interface for steering column (bottom 1)	3D Company	-	1
	Half interface for steering column (bottom 2)	3D Company	-	2
(commercial components)				
	Cardano joint (top)	SIT S.p.A.	-	1
	Cardano joint (bottom)	SIT S.p.A.	-	1
	Tube for steering column (upper half): Ø30-Ø32x160		-	1
	Tube for steering column (bottom half): Ø27xØ30x240		-	1
	Seat clamp (Ø31,8)	Impalapro	-	1

CODE	DESCRIPTION	Manufactured by / bought from	Drawing	Q.TY
	Seat clamp (Ø34,9)	Impalapro	-	1
	Rod-end bearing M5		-	6
	Rod-end bearing M8		-	2
	Tube for tie rod: Ø10-Ø12x100	Easy Composites	-	2
ANT¹⁰				
ANT_01	Shaft	Gariglio Meccanica	yes	2
ANT_02	Hub	Gariglio Meccanica	yes	2
ANT_03	Flange	Gariglio Meccanica	yes	4
ANT_04	Bushing hub-upright	Gariglio Meccanica	yes	2
ANT_05	Boccola spacer between bearings	Gariglio Meccanica	yes	4
ANT_06	Ferrule	Gariglio Meccanica	yes	2
(commercial components)				
	Bearing: radial, Ø15-Ø28x7	Lyra Bearing	-	4
SPO¹¹				
SPO_SC¹²				
	Composite structure		-	
	Aluminum colaminated plates		-	
(commercial components)				
	Screws		-	
SPO_TR¹³				
	Right aluminum slab supporting the grooved shaft	Erre Ti Composites Solutions	-	1

¹⁰Assembly name: Front Hub (*Mozzo anteriore* in Italian)

¹¹Assembly name: Support (*Supporto* in Italian)

¹²Subassembly name: Slide (*Scivolo* in Italian)

¹³Subassembly name: Transmission (*Trasmissione* in Italian)

APPENDIX A. BILL OF MATERIALS

CODE	DESCRIPTION	Manufactured by / bought from	Drawing	Q.TY
	Left aluminum slab supporting the grooved shaft	Erre Ti Composites Solutions	-	1
	Various additive pieces	Ellena_SPEM	-	6
	Front aluminum plated (on top of the basin)	Erre Ti Composites Solutions	-	1
	Rear aluminum plated (on top of the basin)	Erre Ti Composites Solutions	-	1
(commercial components)				
	Carbon tubes		-	
	screw M6		-	
	screw M8		-	
SPO_MO¹⁴				
SPO_MO_01	Support base	3D Company	-	1
SPO_MO_02	C1	3D Company	-	1
SPO_MO_03	C2	3D Company	-	1
(commercial components)				
	screws		-	7
SPO_EL¹⁵				
SPO_EL_01	Base of the case	3D Company	-	1
SPO_EL_02	Lid's case	3D Company	-	1
SPO_EL_03	Heat sink	3D Company	-	1
(commercial components)				
	screws M2 and M3		-	
SPO_GA¹⁶			-	
	Wedge: foot support	self produced	-	1
VI¹⁷				
VI_TE¹⁸				
VI_TE_01	Case	3D company	-	1
VI_TE_02	Back lid	3D company	-	1
VI_TE_03	Vertical support	3D company	-	2

¹⁴Subassembly name: Motor (*Motore* in Italian)

¹⁵Subassembly name: Motor's Electronic components (*Elettronica motore* in Italian)

¹⁶Subassembly name: Legs (*Gambe* in Italian)

¹⁷Assembly name: Vision System (*Sistema di Visione* in Italian)

¹⁸Subassembly name: Cameras (*Telecamere* in Italian)

CODE	DESCRIPTION	Manufactured by / bought from	Drawing	Q.TY
VI_TE_04	Horizontal translation frame	3D company	-	2
VI_TE_05	Anti lift guide	3D company	-	2
VI_TE_06	Small analog camera interface	3D company	-	1
VI_TE_08	Interfaccia camera digitale	3D company	-	1
VI_TE_09	Lateral laths	self produced	-	2
(commercial components)				
	Screws		-	
	Glue gun		-	
	Dual Lock™	3M	-	
VI_SC¹⁹				
VI_SC_01	Fairing interface	self produced	-	1
VI_SC_02	Screens support	3D company	-	1
VI_SC_03	Top screen's half bottom frame	3D company	-	1
VI_SC_04	Top screen's half top frame	3D company	-	1
VI_SC_05	Bottom screen - right frame	3D company	-	1
VI_SC_06	Bottom screen - left frame	3D company	-	1
VI_SC_07	Driver support	3D company	-	2
	Knob for M5 screw	3D company	-	2
(commercial components)				
	screws		-	
	nuts			
	Dual Lock™	3M	-	
SED²⁰				
SED_01	Interface L-front seat (left)	3D company	-	1
SED_02	Interface L-front seat (right)	3D company	-	1
	Bottom front L	self produced	-	2
	Top front L	self produced	-	2
	Rear L	self produced	-	2
	Multi-holed steel slab	self produced	-	2

¹⁹Subassembly name: Screens (*Schermi* in Italian)

²⁰Assembly name: Seat (*Sedile* in Italian)

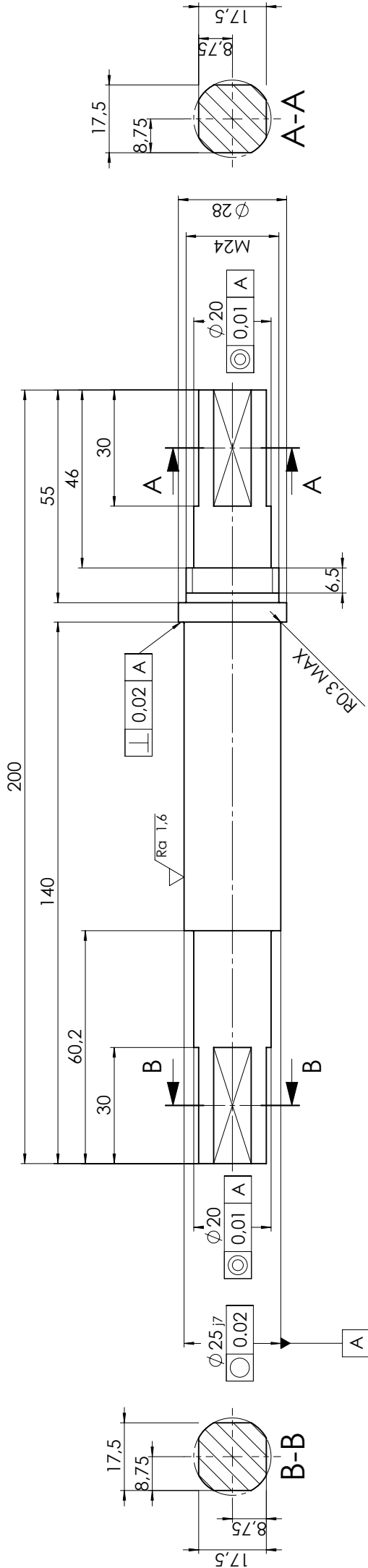
APPENDIX A. BILL OF MATERIALS

CODE	DESCRIPTION	Manufactured by / bought from	Drawing	Q.TY
	Aluminum slabs for threaded holes	Erre Ti Composites Solutions	-	4
	Wood reinforcement interfaces	self produced	-	4
(commercial components)				
	washer		-	26
	screw M5		-	18
	Cushion	LAB5	-	2
CIN ²¹				
	Interface fairing-belt	self produced	-	2
(commercial components)				
	Washer		-	
	Screw M4		-	2
	Nut M4		-	2
	Belt		-	1

²¹Assembly name: Belt (*Cintura* in Italian)

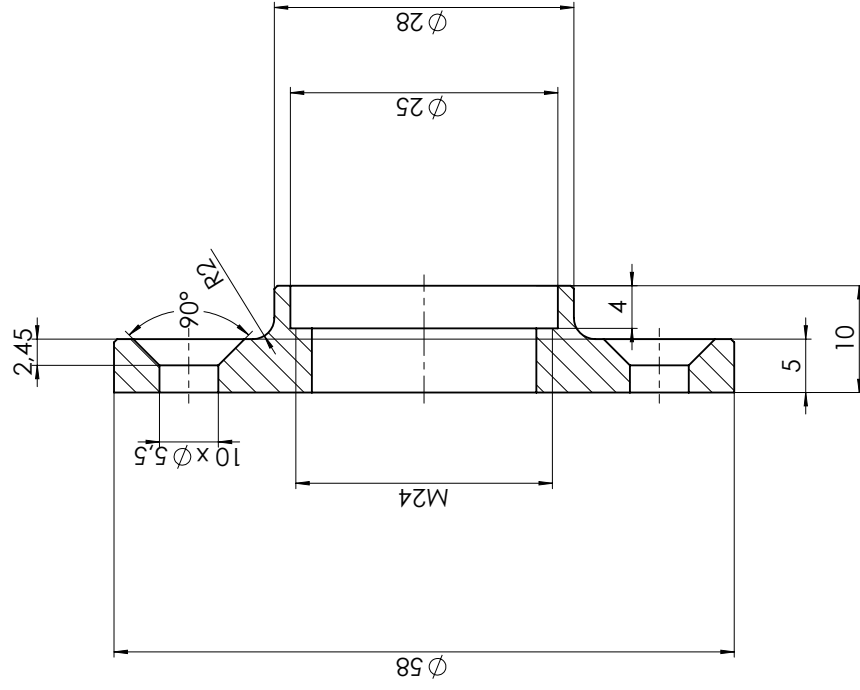
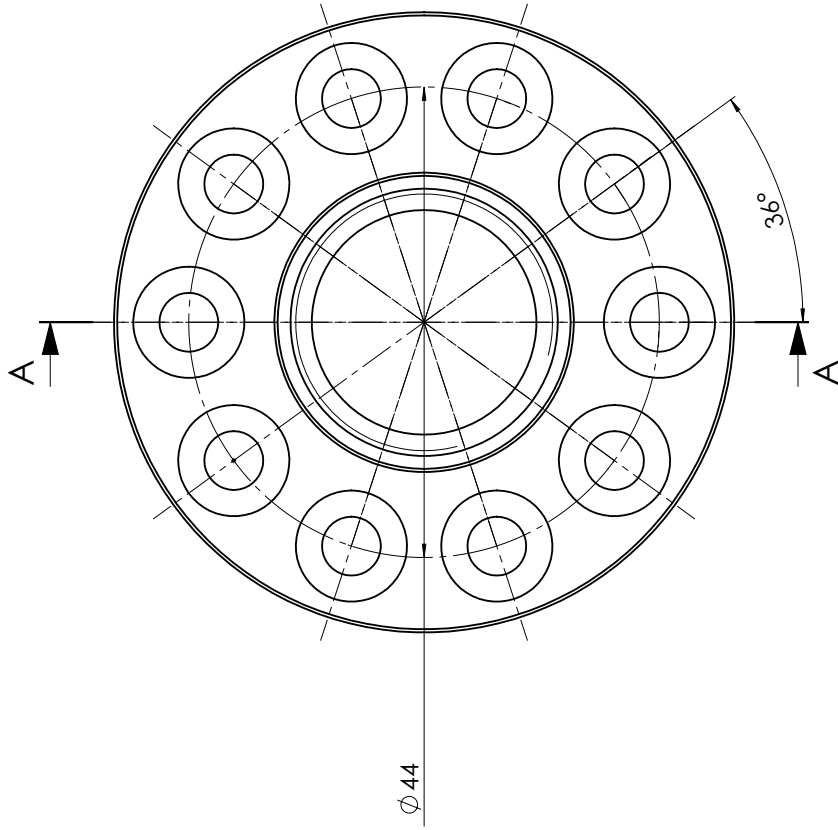
Appendix B

Drawings



Q.TA'	MATERIALE	DISEGNATO DA:	CREATO
1	Alluminio 6082 anodizzazione bianca	Team Policumbent	05/01/2022 20:09:55
OGGETTO	TR_PR_01	GRADO DI FINITURA	SCALA 1:1
DESCRIZIONE	Asse pedalata	▽ (▽)	DATA 29/05/2022
		PESO (g)	
		FOGLIO	
		A3 1/1	Disegno N.
 <p>Politecnico di Torino Corso Duca degli Abruzzi 24 - 10129 Torino</p>			

Raccordi non quotati R0,5 MAX
 Size ISO 14405(E)
 Tolleranze generali ISO 22081
 Dimensioni lineari: ±0,2
 Dimensioni angolari: ±0,5°



A-A

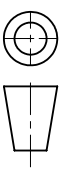
Smussi non quotati 0,5x45°

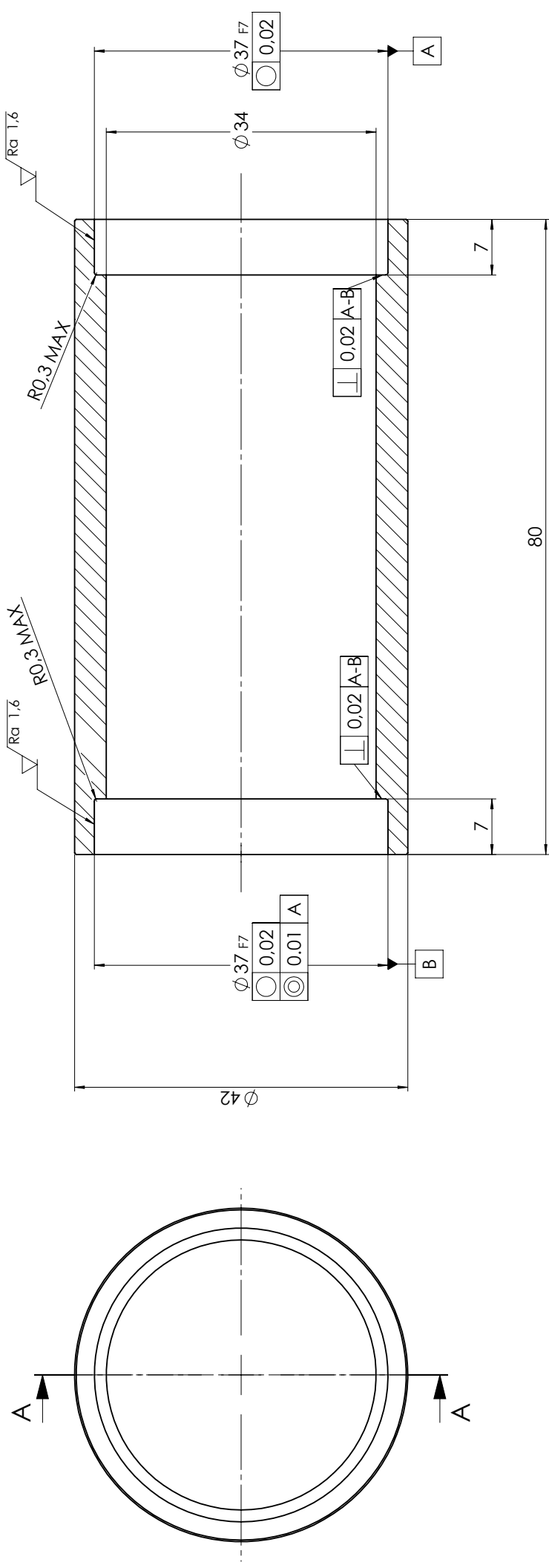
Size ISO 14405(E)

Tolleranze generali ISO 22081

Dimensioni lineari: $\pm 0,2$

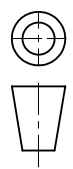
Dimensioni angolari: $\pm 0,5^\circ$

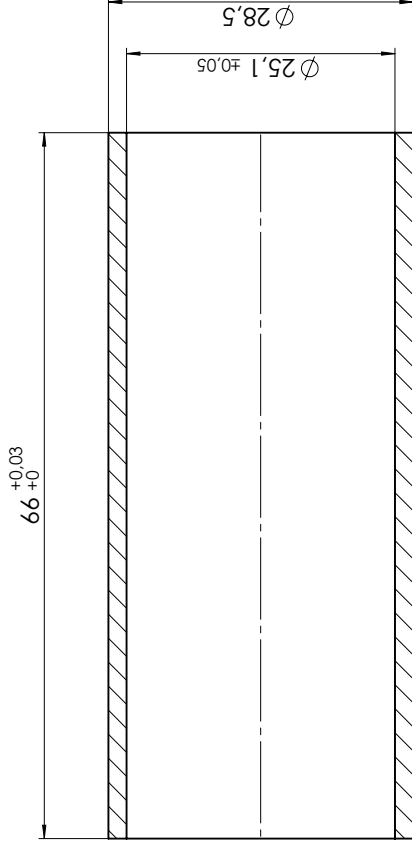
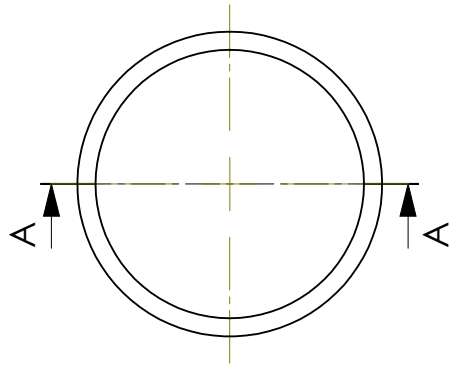
Q.TA' 1	MATERIALE Alluminio 6082 anodizzazione bianca	Disegnato DA: Team Policumbent	Creato 18/05/2022 11:01:23
OGGETTO DESCRIZIONE	TR_PR_02 Flangia smontabile M24	GRADO DI FINITURA $\nabla (\nabla)$	SCALA 2:1
Politecnico di Torino Corso Duca degli Abruzzi 24 - 10129 Torino		PESO (g)	DATA 24/05/2022
		FOGLIO A3 1/1	
		Disegno N.	



A-A

Smussi non quotati 0,2x45°
 Size ISO 14405(E)
 Tolleranze generali ISO 22081
 Dimensioni lineari: ±0,2
 Dimensioni angolari: ±0,5°

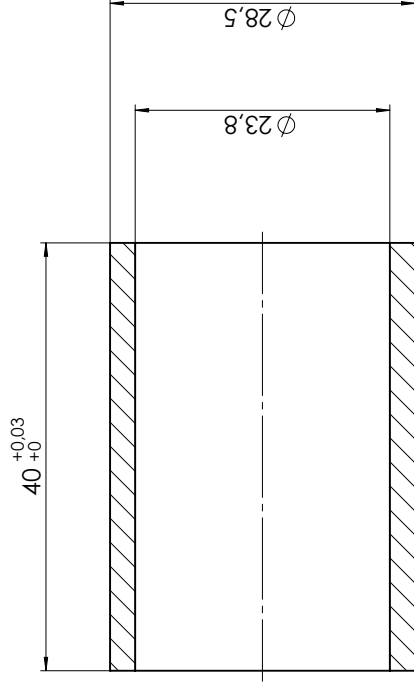
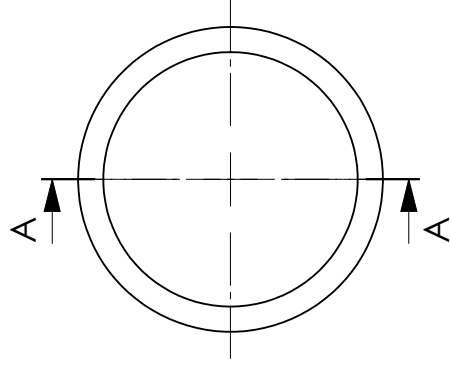
Q.TA' 1	MATERIALE Alluminio 6xxx anodizzazione bianca	Disegnato DA: Team Policumbent	Creato 05/01/2022 12:06:52
OGGETTO TR_PR_03		DESCRIZIONE Corpetto	SCALA 2:1
			DATA 29/05/2022
			GRADO DI FINITURA PESO (g)
			FOGLIO A3 1/1
			Disegno N.
 <p>Politecnico di Torino Corso Duca degli Abruzzi 24 - 10129 Torino</p>			



A-A

Size ISO 14405(E)
 Tolleranze generali ISO 22081
 Dimensioni lineari: $\pm 0,2$
 Dimensioni angolari: $\pm 0,5^\circ$

Q.TA' 1	MATERIALE Alluminio 6xxx anodizzazione bianca	CREATO 06/01/2022 22.54.38
OGGETTO DESCRIZIONE	TR_PR_04 Distanziale interno	SCALA 2:1
 <p>Politecnico di Torino Corso Duca degli Abruzzi 24 - 10129 Torino</p>		DATA 22/05/2022
DISEGNATO DA: Team Policumbent		
GRADO DI FINITURA $\nabla (\nabla)$		PESO (g)
FOGLIO A3 1/1		Disegno N.



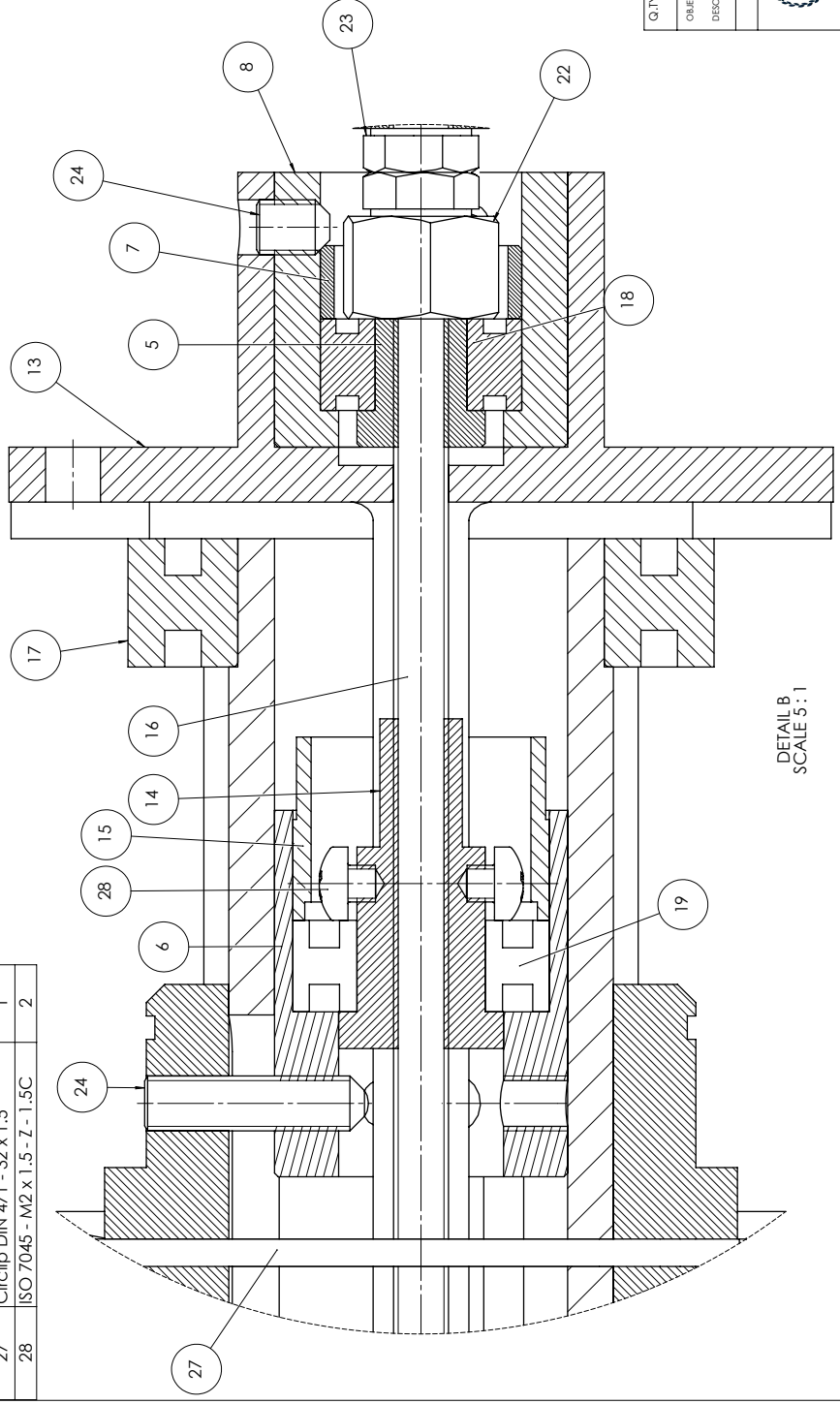
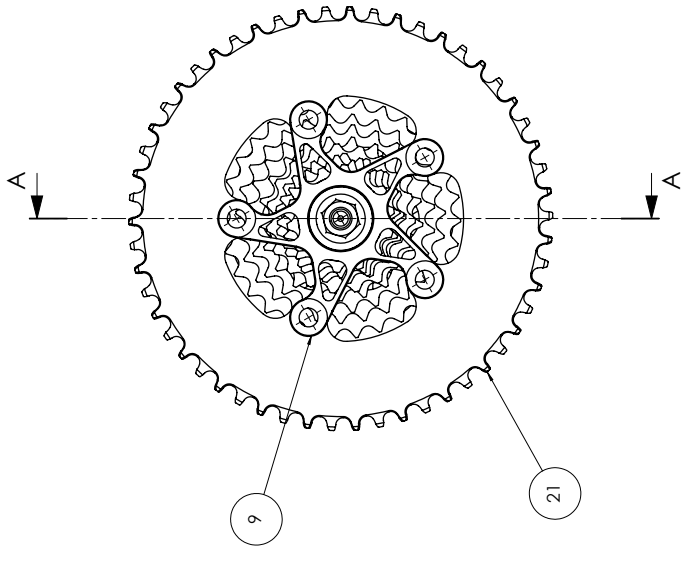
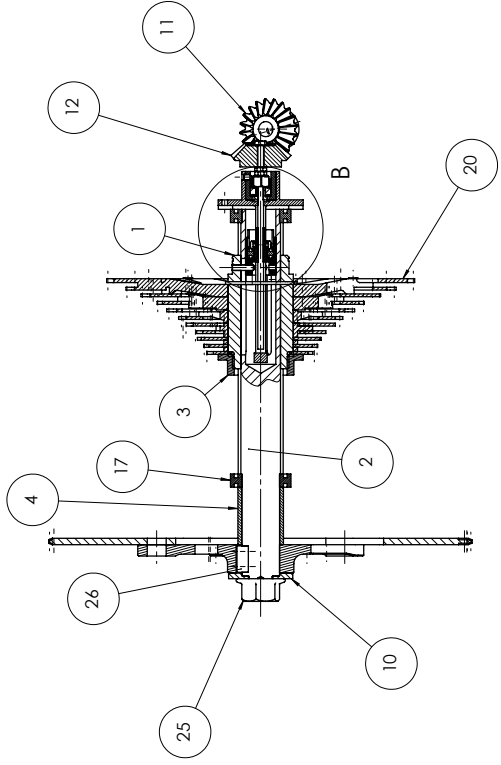
A-A

Size ISO 14405(E)
 Tolleranze generali ISO 22081
 Dimensioni lineari: $\pm 0,2$
 Dimensioni angolari: $\pm 0,5^\circ$

Q.TA' 1	MATERIALE Alluminio 6xxx anodizzazione bianca	Disegnato DA: Team Policumbent	Creato 06/01/2022 23:10:25
OGGETTO DESCRIZIONE	TR_PR_05 Distanziale esterno	GRADO DI FINITURA $\surd (\surd)$	SCALA 2:1
 <p>Politecnico di Torino Corso Duca degli Abruzzi 24 - 10129 Torino</p>		PESO (g)	DATA 22/05/2022
		FOGLIO A3 1/1	
		Disegno N.	

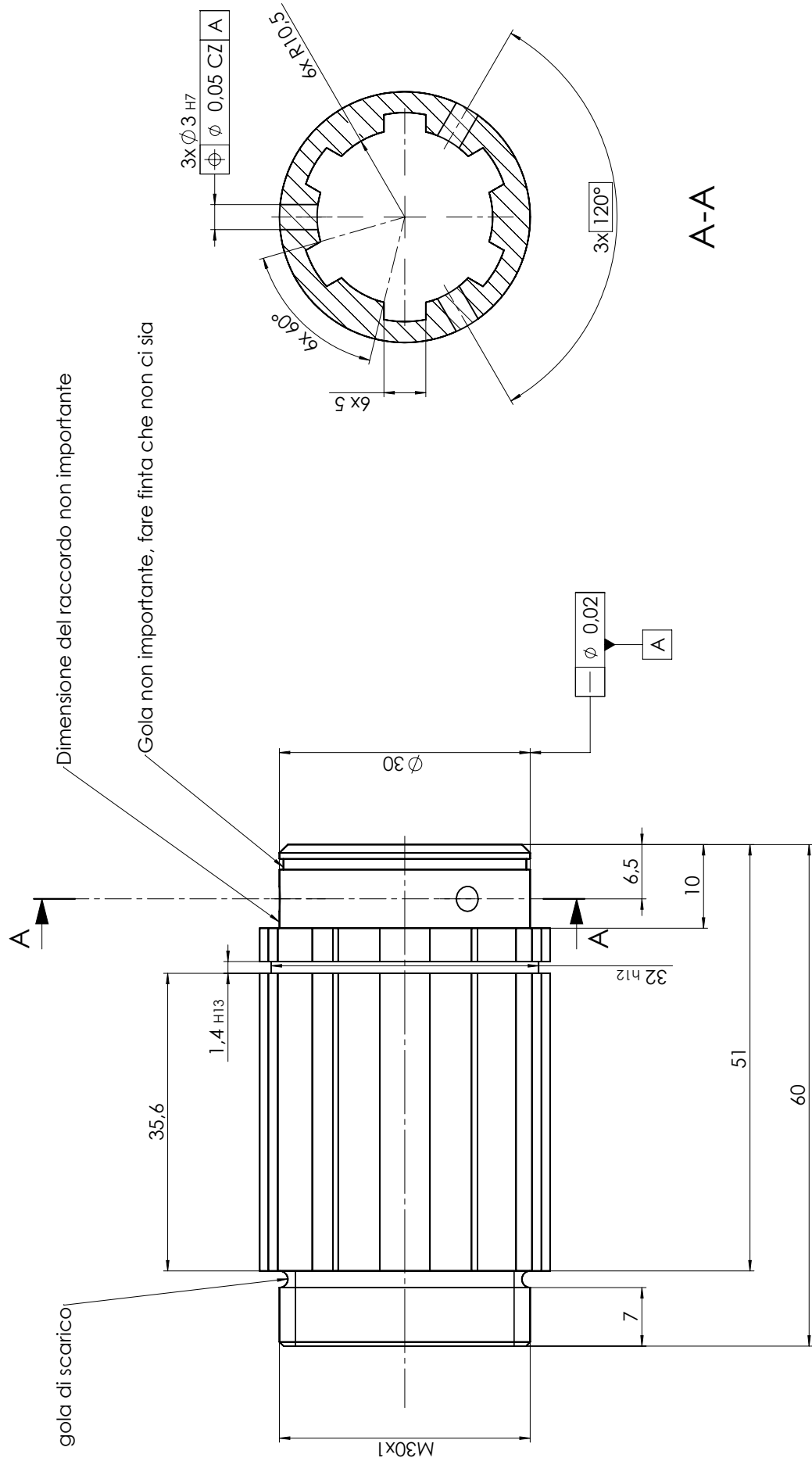
ITEM NO.	PART NUMBER	QTY.
1	TR_MO_01	1
2	TR_MO_02_v2	1
3	TR_MO_03	1
4	TR_MO_04	1
5	TR_MO_05	1
6	TR_MO_07_v2	1
7	TR_MO_08	1
8	TR_MO_09	1
9	TR_MO_10	1
10	TR_MO_11	1
11	TR_MO_12	1
12	TR_MO_13	1
13	TR_MO_14	1
14	TR_MO_15	1
15	TR_MO_16	1
16	Threaded rod M3x110	1
17	Radial Bearing $\varnothing 20-\varnothing 32 \times 7$	2
18	Radial Bearing $\varnothing 5-\varnothing 11 \times 5$	1
19	Radial Bearing $\varnothing 7-\varnothing 14 \times 5$	1
20	Cassette	1
21	Second branch gear	1
22	ISO - 4034 - M5 - C	1
23	ISO - 4032 - M3 - W - C	3
24	ISO 4029 - M3 x 4-C	6
25	ISO - 4161 - M12 - C	1
26	Parallel key A6 x 6 x 14 DIN 6885	1
27	Circlip DIN 471 - 32 x 1.5	1
28	ISO 7045 - M2 x 1.5 - Z - 1.5C	2

A-A



DETAIL B
SCALE 5 : 1

Q.TY	1	MATERIAL		DRAWN BY:	ALESSANDRO DI GESU	Created	05/03/2022 19:47:10
OBJECT	TR_MO_V2			SCALE	1:2		
DESCRIPTION	Transmission - Mobile group			DATE	09/10/2022		
		GRADO DI FINITURA	(V)	Mass (kg)			
		Foglio	A2 1/1	Drawing N.			
Politecnico di Torino Corso Duca degli Abruzzi 24 - 10129 Torino							



Dimensione del raccordo non importante

Gola non importante, fare finta che non ci sia

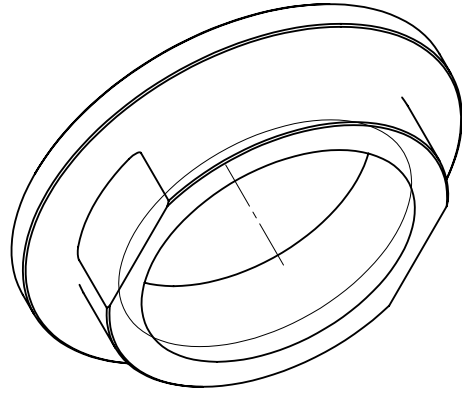
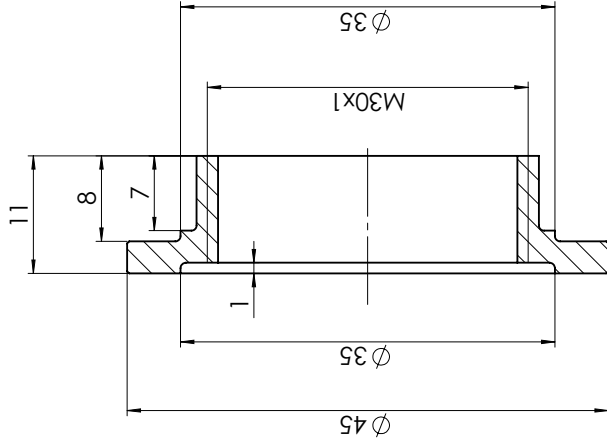
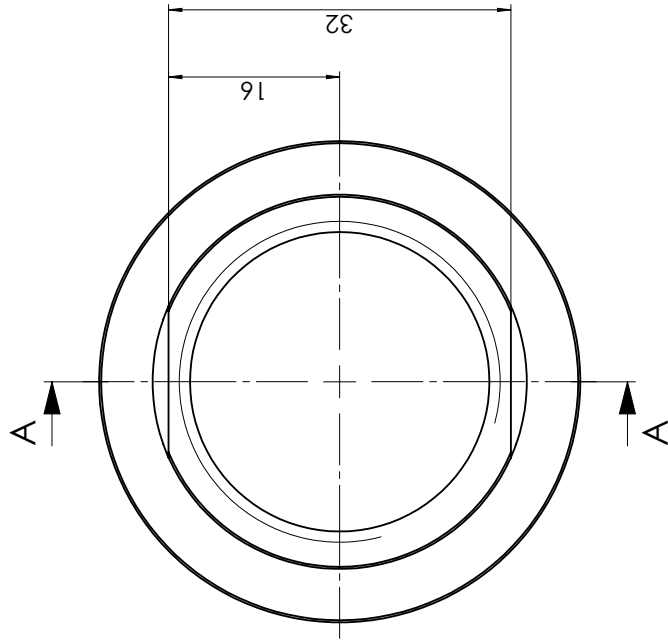
gola di scarico

Smussi non quotati 0,5x45°
 Size ISO 14405(E)
 Tolleranze generali ISO 22081
 Dimensioni lineari: ±0,2
 Dimensioni angolari: ±0,5°

Q.TA' -	MATERIALE Materiali <not specified>	CREATO 02/04/2022 22:20:54
OGGETTO TR_MO_01	DESCRIZIONE Cerberus - Manicotto Traslante	SCALA 2:1
		DATA 29/09/2022
		GRADO DI FINITURA √ (√)
		PESO (g) -
		FOGLIO A3 1/1
		Disegno N.
		Tav. N.



Politecnico di Torino
 Corso Duca degli Abruzzi 24 - 10129 Torino



A-A

Raccordi non quotati R0,5
Smussi non quotati 0,5x45°

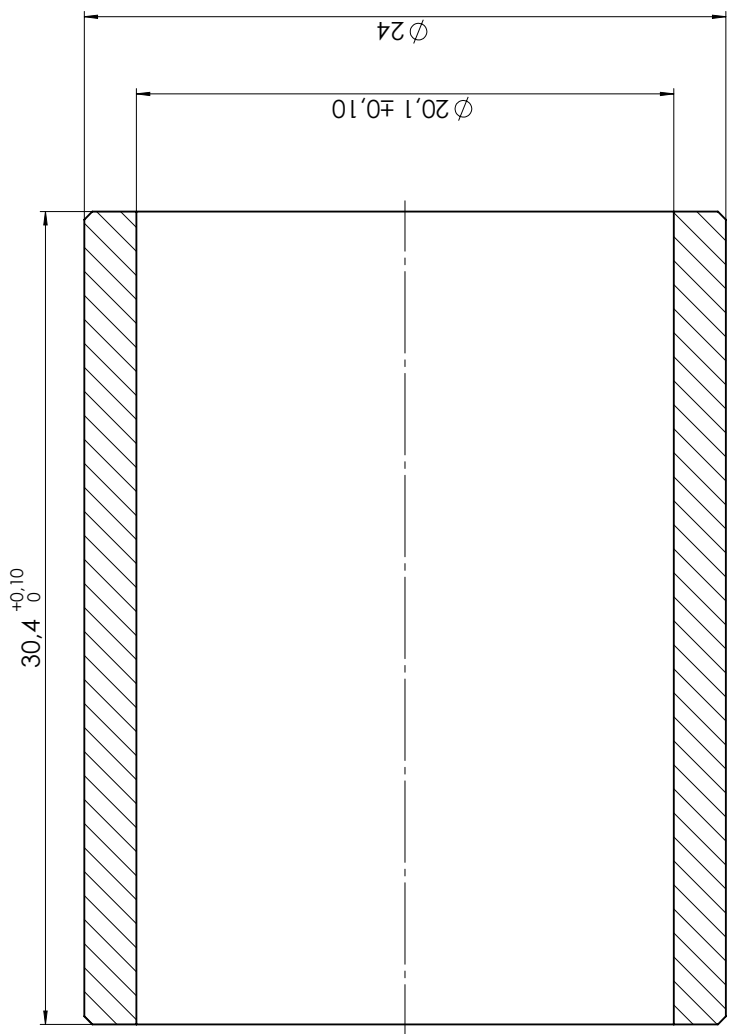
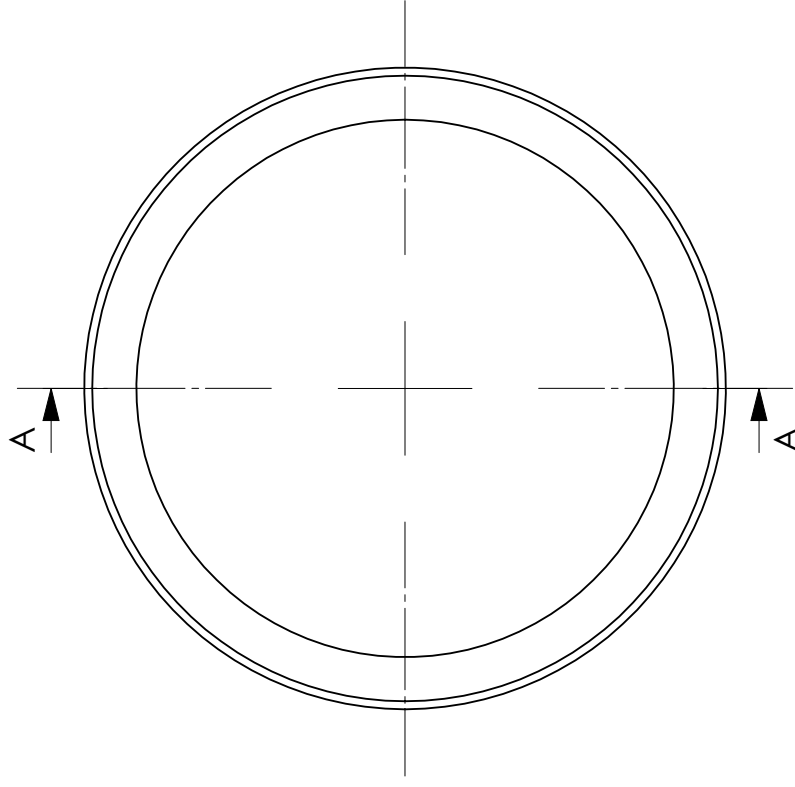
Size ISO 14405 (E)

Tolleranze generali ISO 22081

Dimensioni lineari: ±0,2

Dimensioni angolari: ±0,5°

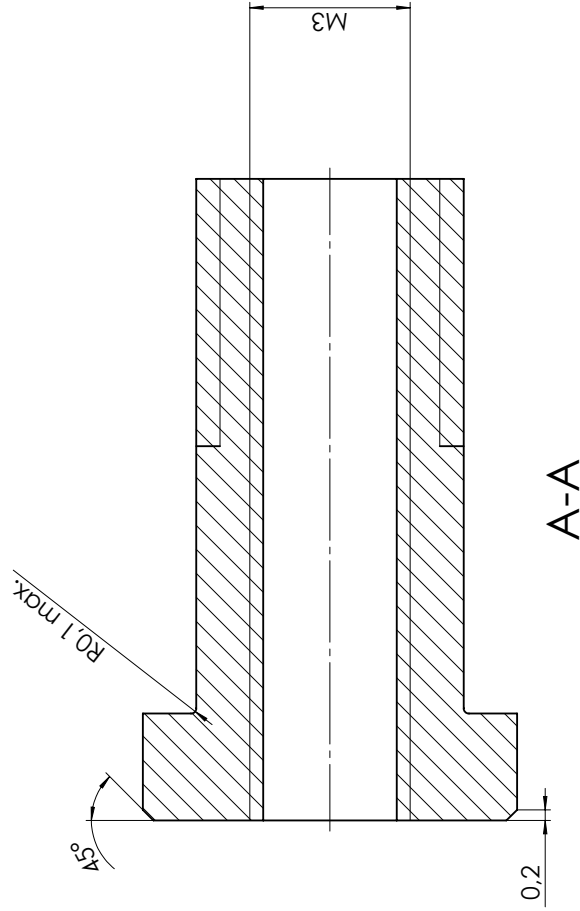
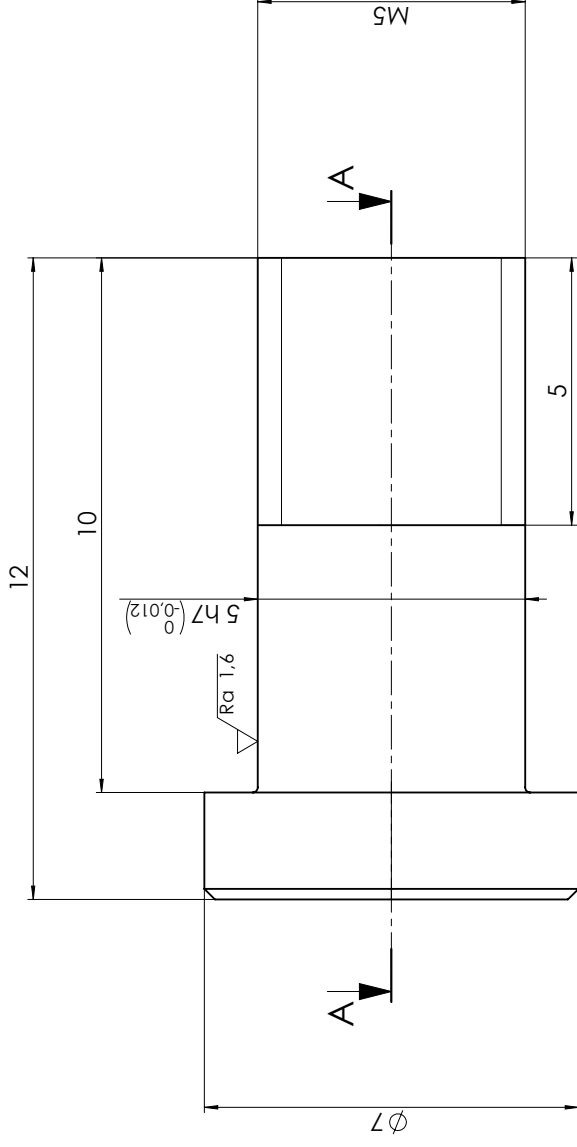
Q.TA' 1	MATERIALE Alluminio 6xxx, anodizzazione bianca	DISEGNATO DA: Team studentesco Policumbent	Creato 26/11/2021 19:22:02
OGGETTO DESCRIZIONE	TR_MO_03 Ghiera per pignone piccolo	GRADO DI FINITURA √ (√)	SCALA 2:1 DATA 29/09/2022
 <p>Politecnico di Torino Corso Duca degli Abruzzi 24 - 10129 Torino</p>		PESO (Kg) FOGLIO A3 1/1	 
		Disegno N.	Tav. N.



A-A

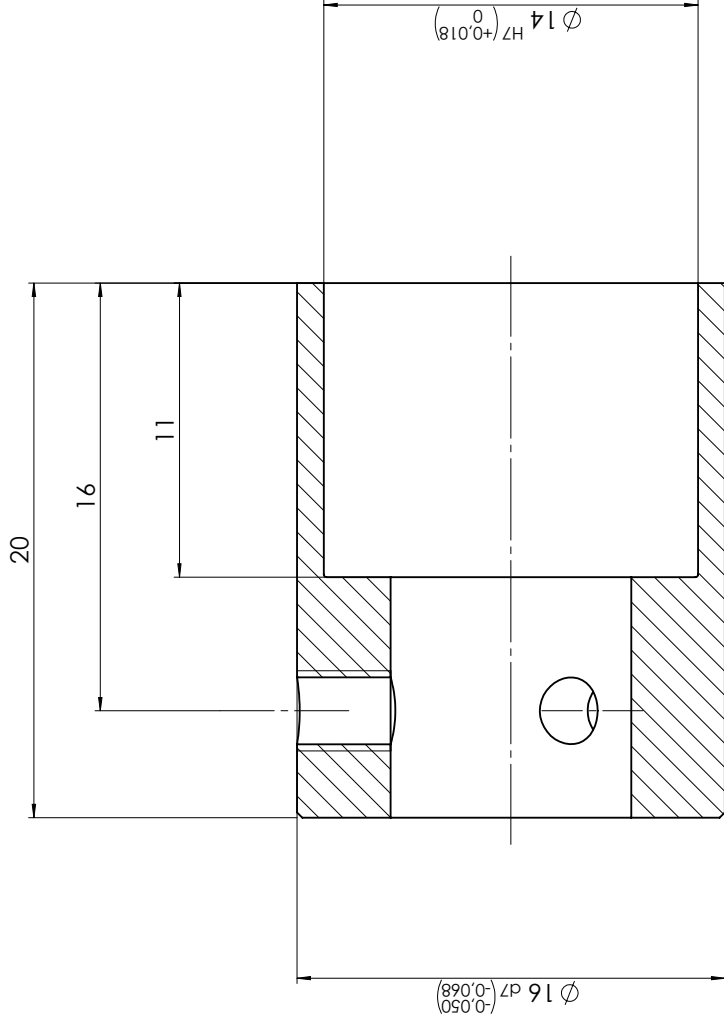
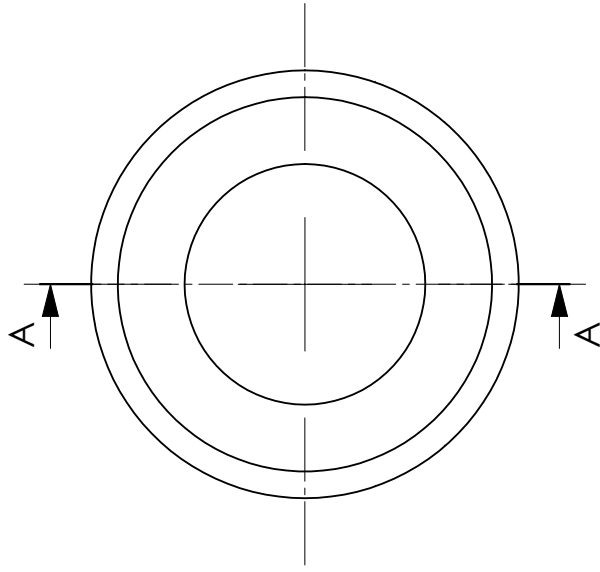
Smussi non quotati 0,3x45°
 Size ISO 14405 (E)
 Tolleranze generali ISO 22081
 Dimensioni lineari: ±0,2
 Dimensioni angolari: ±0,5°

Q.TA' 1	MATERIALE Alluminio 6xxx, anodizzazione bianca	CREATO 26/11/2021 00:51:53
OGGETTO TR_MO_04	DISEGNATO DA: Team Policumbent	SCALA 5:1
DESCRIZIONE Boccola battuta cuscinetto dx	GRADO DI FINITURA ▽ (▽)	DATA 29/09/2022
 Politecnico di Torino Corso Duca degli Abruzzi 24 - 10129 Torino	PESO (Kg) -	 Tav. N.
	FOLIO A3 1/1	



Size ISO 14405 (E)
 Tolleranze generali ISO 22081
 Dimensioni lineari: $\pm 0,2$
 Dimensioni angolari: $\pm 0,5^\circ$

Q.TA' 2	MATERIALE Acciaio AISI 303 (o 304 o 316 a discrezione)	DISEGNATO DA: Team Policumbent	Creato 06/02/2022 21:51:09
OGGETTO DESCRIZIONE	TR_MO_05 Madrevite - boccola interna	GRADO DI FINITURA $\nabla (\nabla)$	SCALA 10:1
 <p>Politecnico di Torino Corso Duca degli Abruzzi 24 - 10129 Torino</p>		PESO (Kg) -	DATA 30/09/2022
		FOLGIO A3 1/1	 
		Disegno N.	Tav. N.



A-A

Raccordi non quotati R0,5
Smussi non quotati 0,5x45°

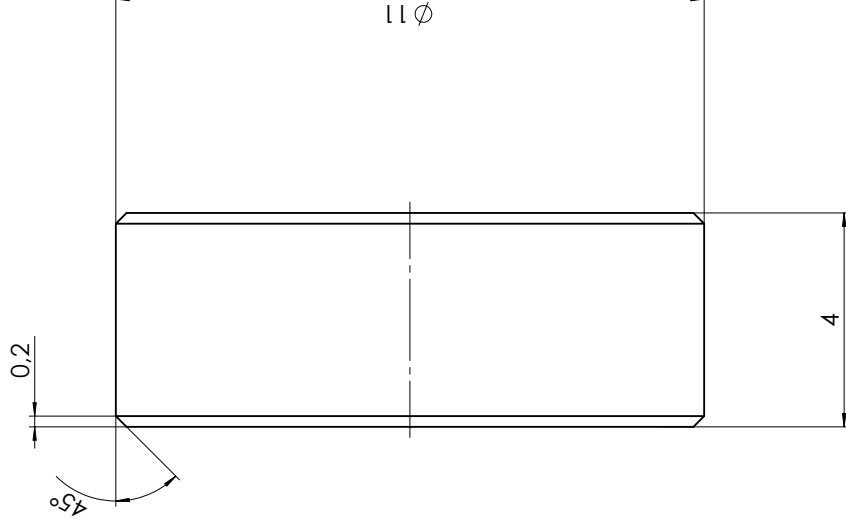
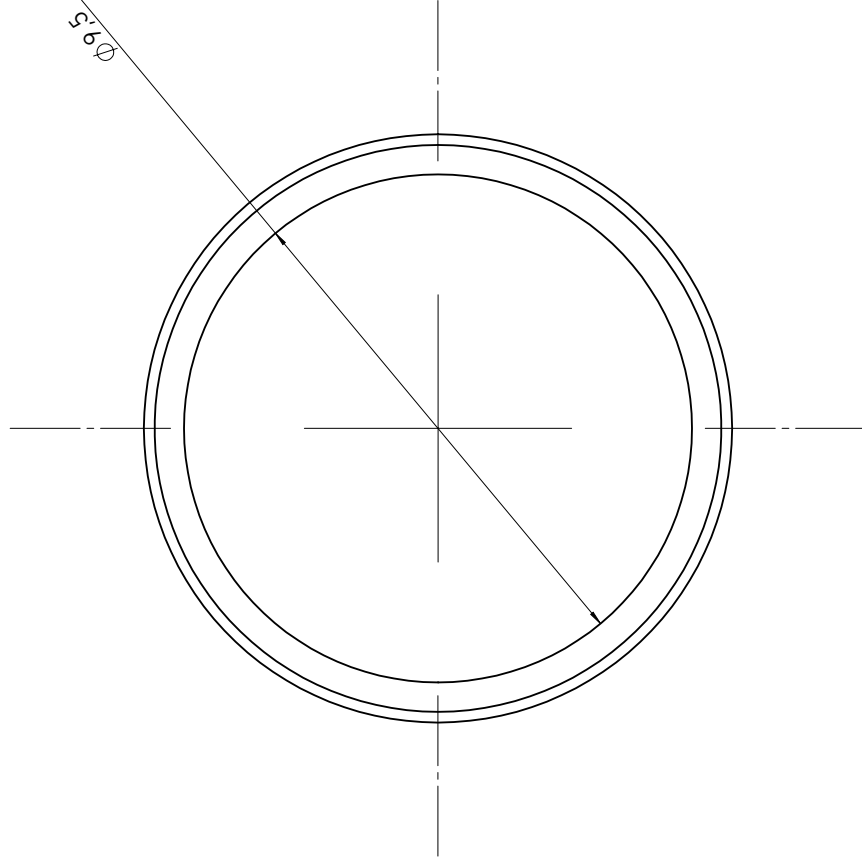
Size ISO 14405(E)

Tolleranze generali ISO 22081

Dimensioni lineari: $\pm 0,2$

Dimensioni angolari: $\pm 0,5^\circ$

Q.T.A	MATERIALE Se ripassiamo quella che ho già era AISI 303 o simile	CREATO 06/02/2022 23.07.24
OGGETTO	TR_MO_07_v2	SCALA 5:1
DESCRIZIONE	Madrevite - boccia esterna, revisionata	DATA 30/09/2022
Politecnico di Torino Corso Duca degli Abruzzi 24 - 10129 Torino		DESIGNATO DA: Team Policumbent
		GRADO DI FINITURA $\nabla (\nabla)$
		PESO (g) 0.00
		Disegno N.
		FOGLIO A3 1/1
		Tav. N.



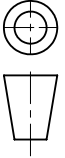
Smussi non quotati 0,2x45°

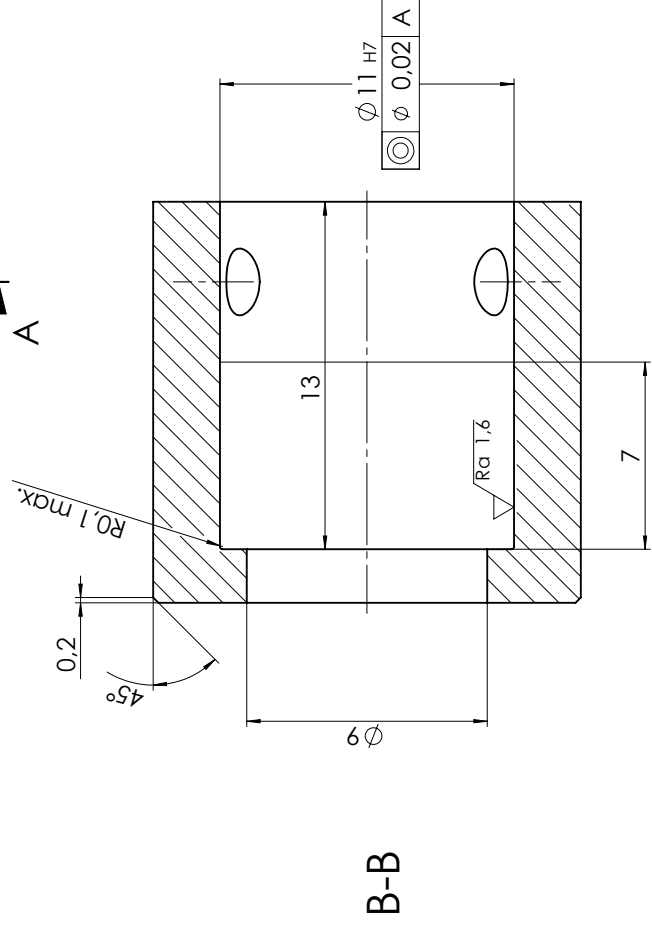
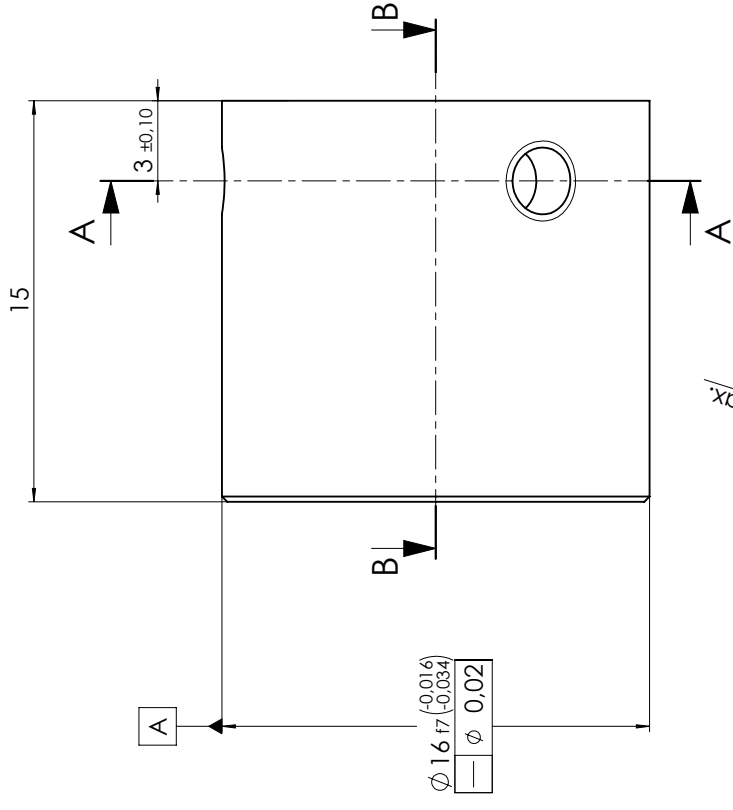
Size ISO 14405 (E)

Tolleranze generali ISO 22081

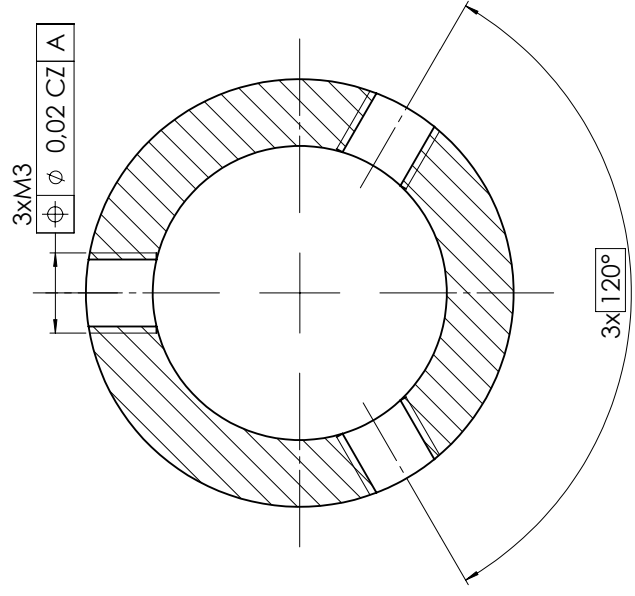
Dimensioni lineari: $\pm 0,2$

Dimensioni angolari: $\pm 0,5^\circ$

Q.TA' 1	MATERIALE Alluminio 6xxx, anodizzazione bianca	CREATO 06/02/2022 23:42:00
OGGETTO TR_MO_08	DESCRIZIONE Distanziale interno sx	DESCRITTORE Team Policumbent
 <p>Politecnico di Torino Corso Duca degli Abruzzi 24 - 10129 Torino</p>		<p>GRADO DI FINITURA $\nabla (\nabla)$</p> <p>FOLIO A3 1/1</p>
<p>DISEGNATO DA: Team Policumbent</p>		<p>DATA 29/09/2022</p> 
<p>PESO (Kg) -</p>		<p>Disegno N. Tav. N.</p>



controllare Ra solo sui 7 mm dallo spallamento



A-A

Smussi non quotati 0,2x45°

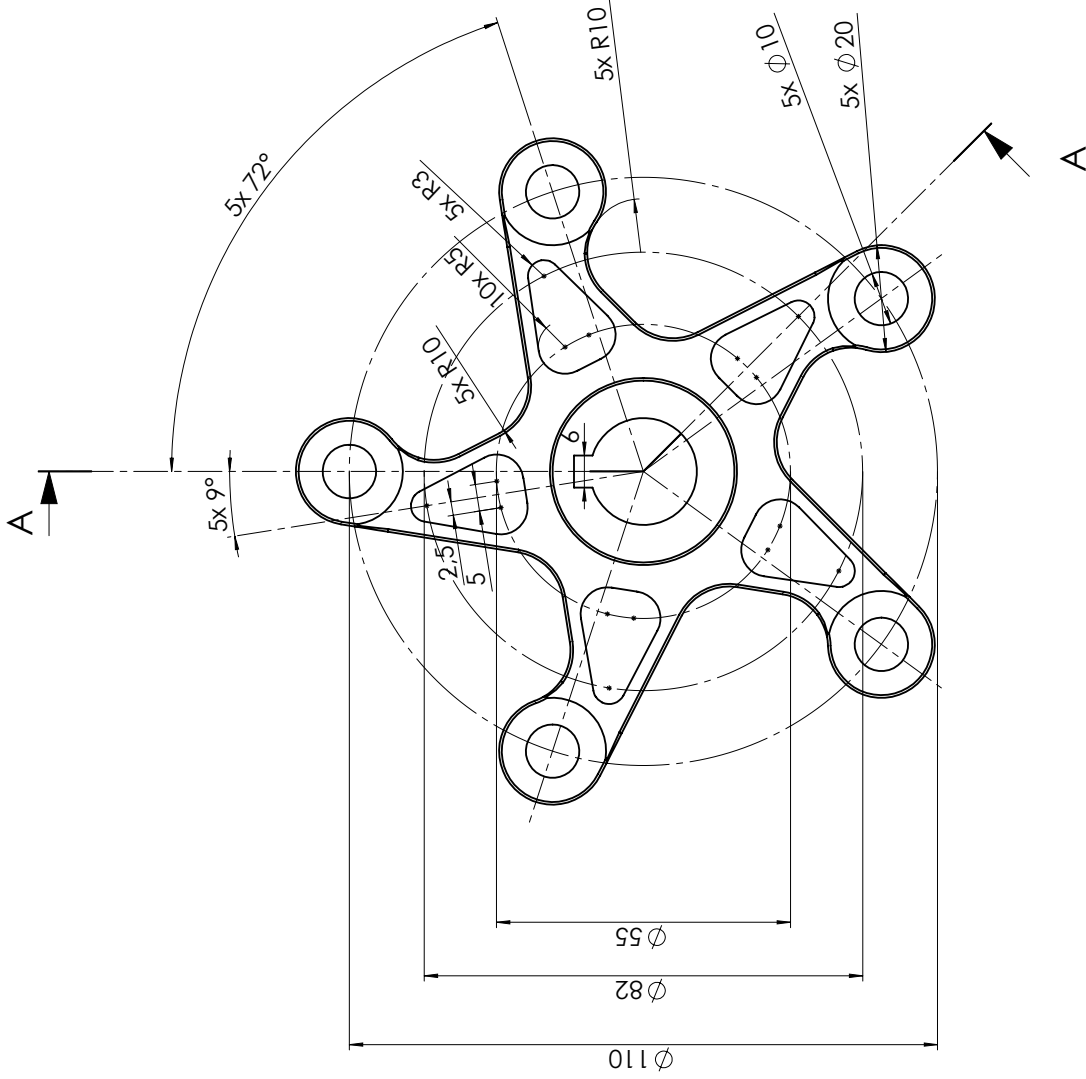
Size ISO 14405(E)

Tolleranze generali ISO 22081

Dimensioni lineari: ±0,2

Dimensioni angolari: ±0,5°

Q.TA' 1	MATERIALE Acciaio AIST 303 (o 304 o 316 a discrezione)	CREATO 06/02/2022 23:07:24
OGGETTO TR_MO_09	DESCRIZIONE Boccola fissaggio 3 grani	SCALA 5:1
DISEGNATO DA: Team Policumbent		DATA 29/09/2022
GRADO DI FINITURA ▽ (▽)		PESO (Kg) -
FOGLIO A3 1/1		Disegno N.
 Politecnico di Torino Corso Duca degli Abruzzi 24 - 10129 Torino		Tav. N.



Smussi non quotati 0,5x45°

Size ISO 14405 (E)

Tolleranze generali ISO 22081

Dimensioni lineari: ±0,2

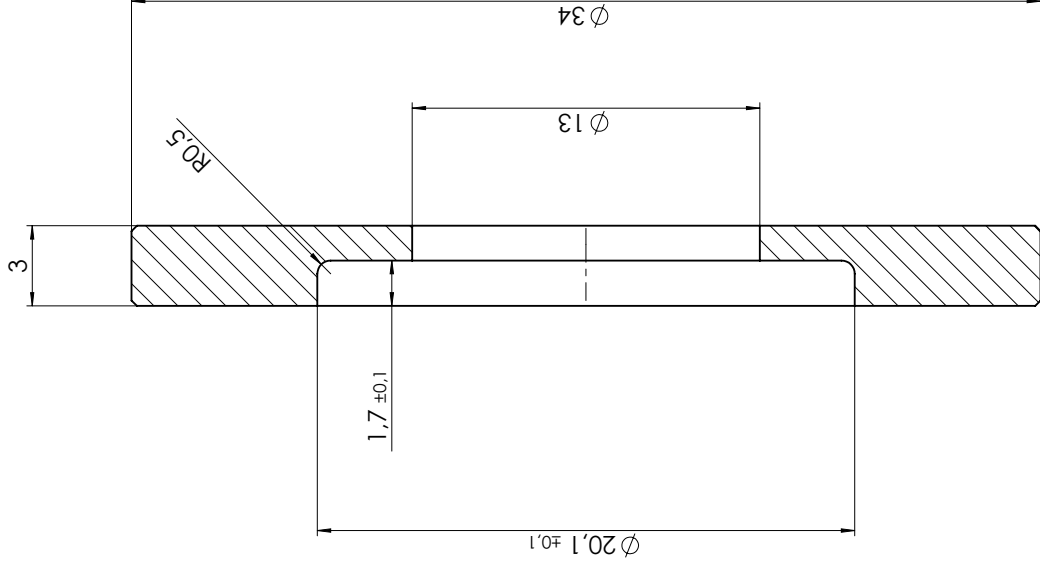
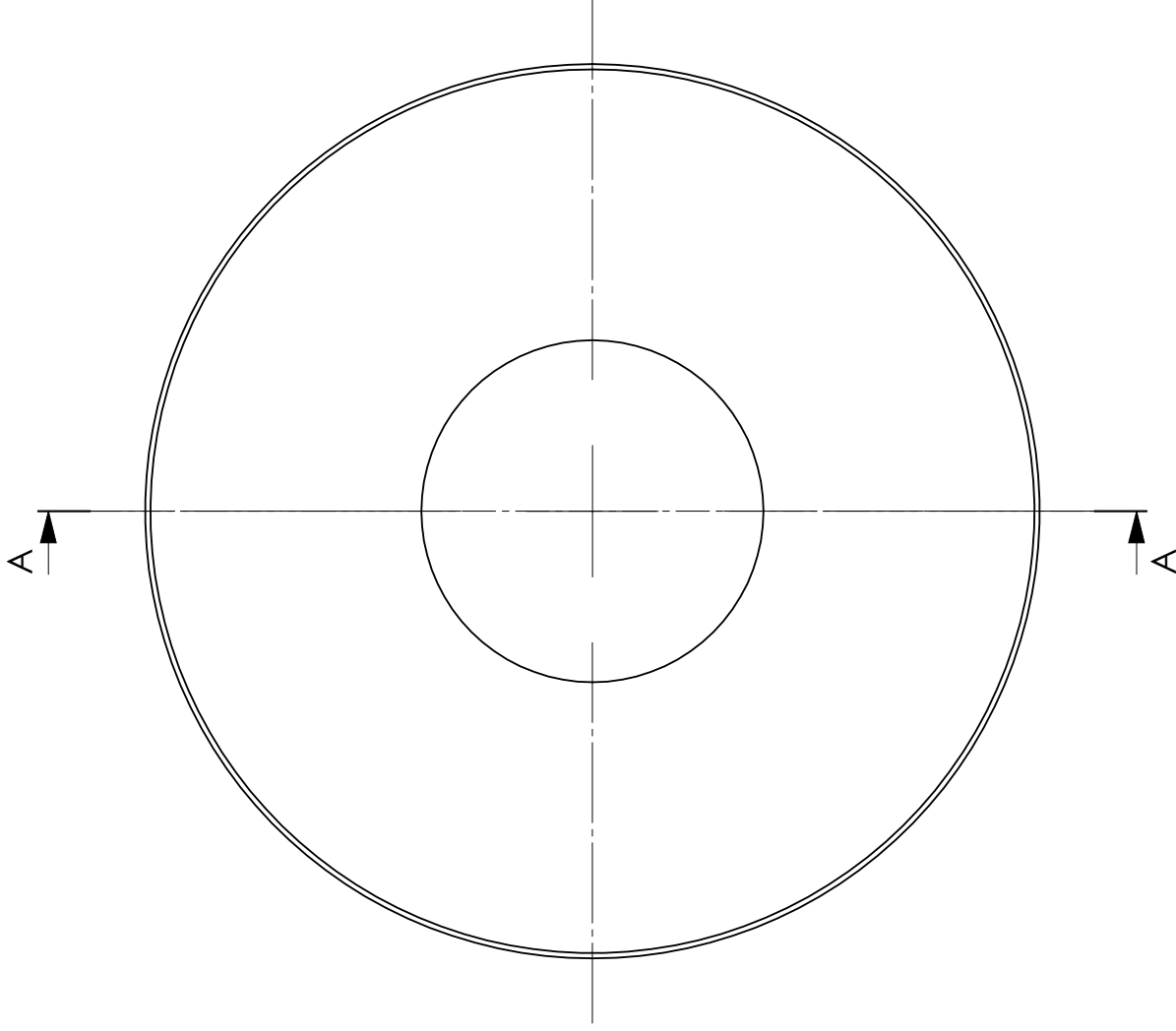
Dimensioni angolari: ±0,5°

Q.TA' 1	MATERIALE Alluminio 6xxx, anodizzazione bianca	CREATO 20/04/2022 09:48:10
OGGETTO TR_MO_10	DESCRIZIONE Spider corona di rinvio	DISEGNATO DA: Team Policumbent
		SCALA 1:1
		DATA 29/09/2022
		GRADO DI FINITURA ▽ (▽)
		PESO (g)
		FOGLIO A3 1/1
		Disegno N.



Politecnico di Torino

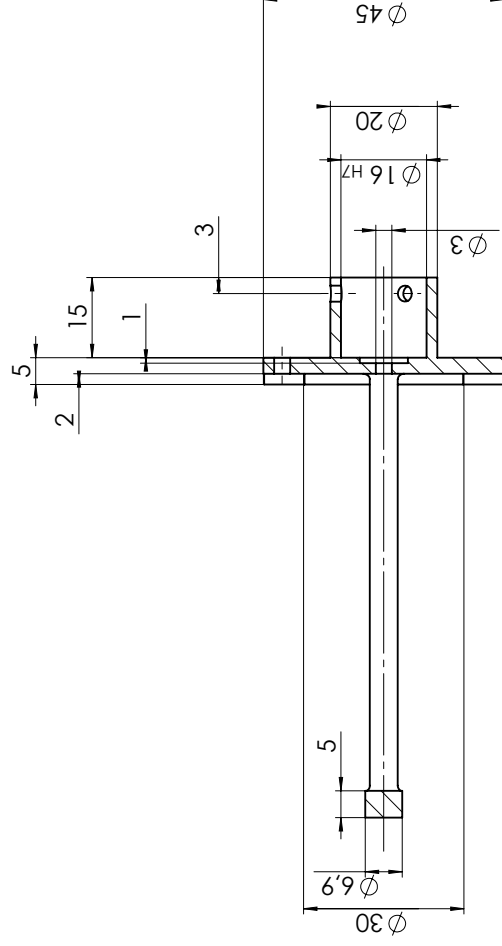
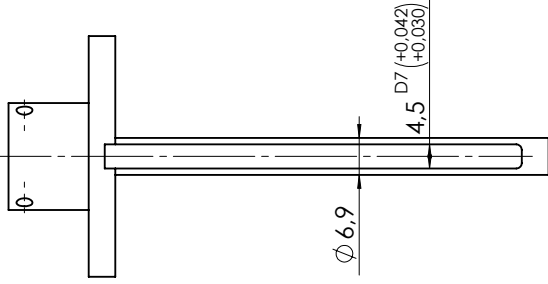
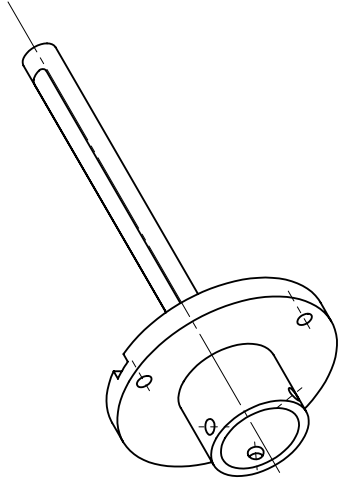
Corso Duca degli Abruzzi 24 - 10129 Torino



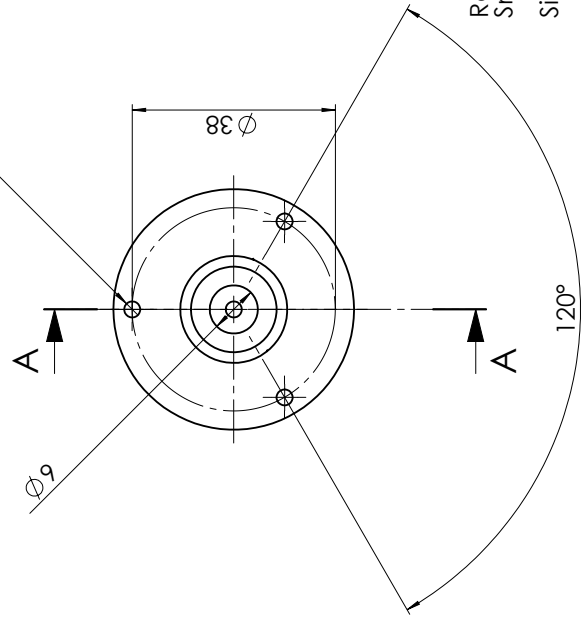
A-A

Smussi non quotati 0,2x45°
 Size ISO 14405 (E)
 Tolleranze generali ISO 22081
 Dimensioni lineari: $\pm 0,2$
 Dimensioni angolari: $\pm 0,5^\circ$

Q.TA' 1	MATERIALE Alluminio 6xxx, anodizzazione bianca	CREATO 20/04/2022 14:43:13
OGGETTO TR_MO_11	DESCRIZIONE Distanziale serraggio spider	SCALA 5:1
 <p>Politecnico di Torino Corso Duca degli Abruzzi 24 - 10129 Torino</p>		DATA 29/09/2022
<p>Disegnato DA: Team Policumbent</p>		<p>GRADO DI FINITURA $\nabla (\nabla)$</p> <p>PESO (g) -</p>
<p>Foglio A3 1/1</p>		<p>Disegno N. Tav. N.</p>

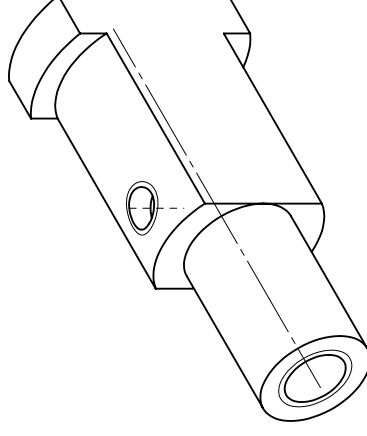
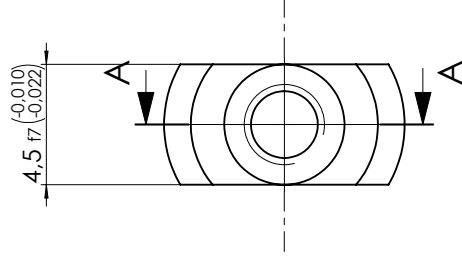
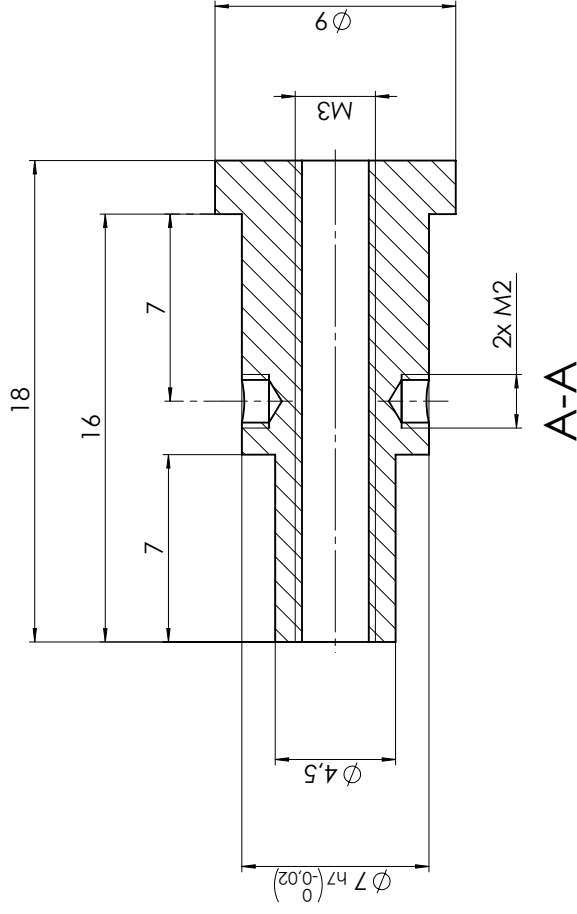


A-A



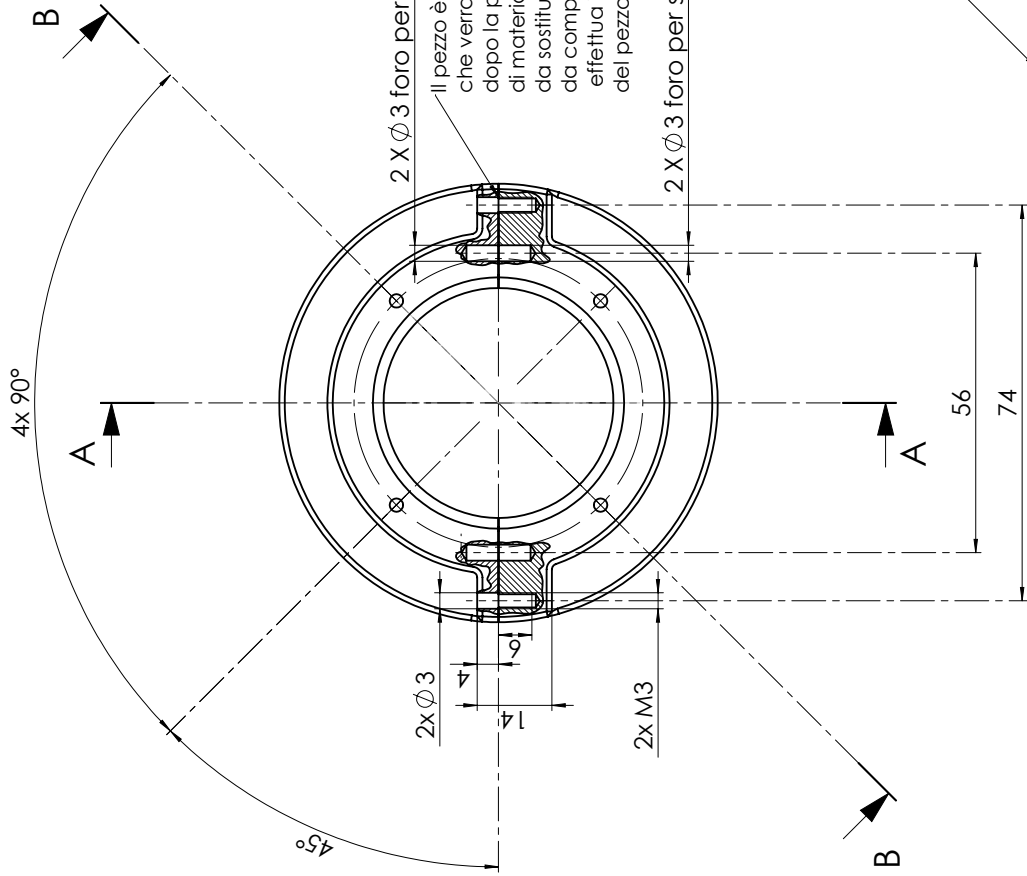
Raccordi non quotati R1
 Smussi non quotati 0,5x45°
 Size ISO 14405 (E)
 Tolleranze generali ISO 22081
 Dimensioni lineari: $\pm 0,2$
 Dimensioni angolari: $\pm 0,5^\circ$

Q.TA' 1	MATERIALE Acciaio a vostra disposizione	DISEGNATO DA: Team Policumbent	Creato 04/08/2022 02:00:49
OGGETTO TR_MO_14	DESCRIZIONE Guida da elettroerosione	GRADO DI FINITURA $\nabla (\nabla)$	SCALA 1:1
		PESO (g) -	DATA 29/09/2022
 <p>Politecnico di Torino Corso Duca degli Abruzzi 24 - 10129 Torino</p>		FOGLIO A3 1/1	 
			Tav. N.



Size ISO 14405(E)
 Tolleranze generali ISO 22081
 Dimensioni lineari: $\pm 0,1$
 Dimensioni angolari: $\pm 0,5^\circ$

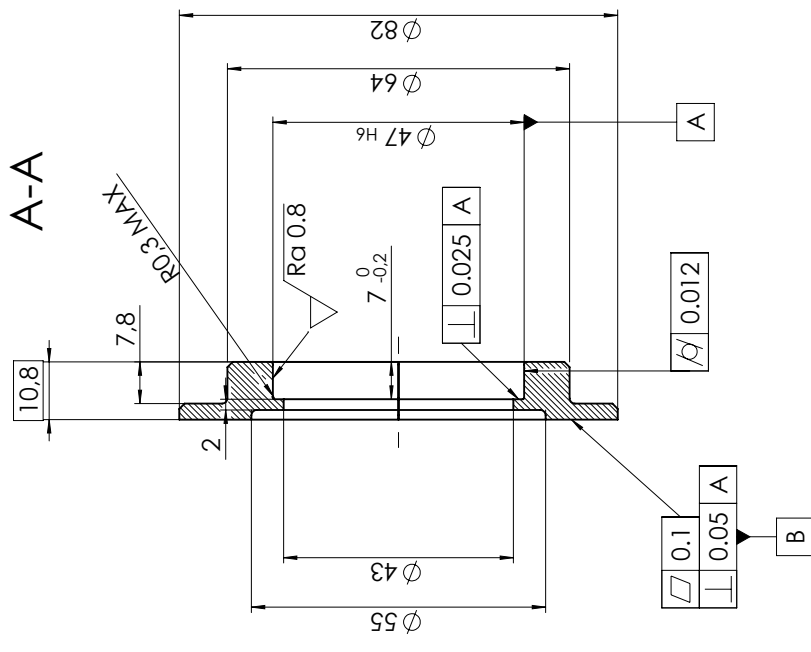
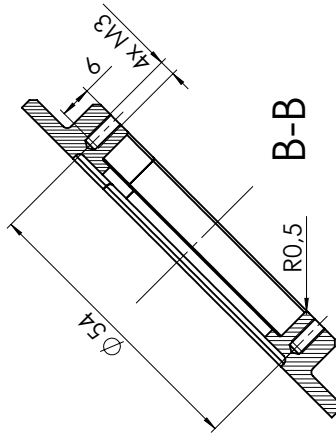
Q.TA' 1	MATERIALE Acciaio a vostra disposizione	CREATO 04/08/2022 01:57:09
OGGETTO TR_MO_15-v2	DISEGNATO DA: Team Policumbent	SCALA 5:1
DESCRIZIONE Boccola madre vite	GRADO DI FINITURA $\nabla (\nabla)$	DATA 29/09/2022
 Politecnico di Torino Corso Duca degli Abruzzi 24 - 10129 Torino	PESO (g) -	  FOLIO A3 1/1
	Disegno N.	



2 X ϕ 3 foro per spina lato mobile

Il pezzo è formato da due componenti che verranno separati lungo la linea evidenziata dopo la prima lavorazione al tornio, lo spessore di materiale rimasto durante la separazione è da sostituire con uno spessore calibrato in modo da compensare il diametro della punta che effettua il taglio per mantenere la circolarità del pezzo

2 X ϕ 3 foro per spina lato fisso



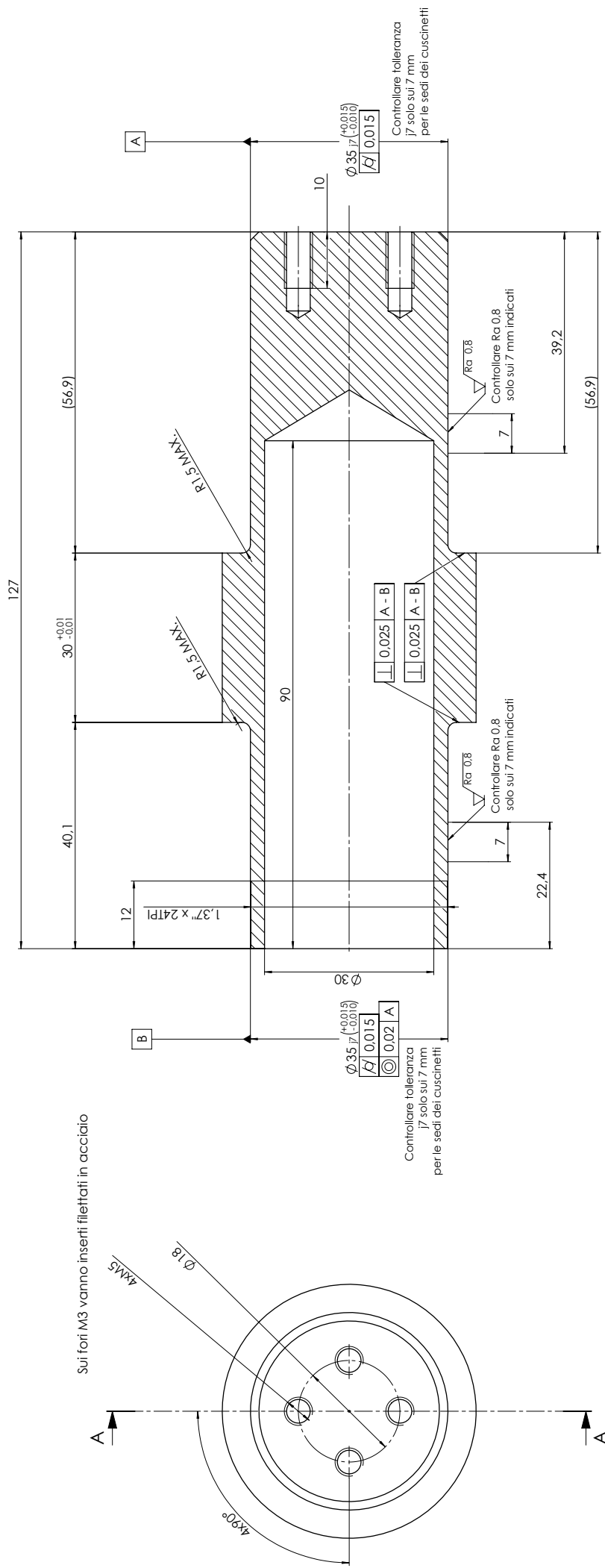
I fori M3 sono tutti da realizzarsi con inserti filettati in acciaio

Smussi non quotati 1X45°
Raccordi non quotati R1

Size ISO 14405 (E)

Tolleranze generali ISO 22081
Dimensioni lineari: ± 0.2
Dimensioni angolari: $\pm 0.5^\circ$

Q.TA' 2	MATERIALE Alluminio 6082-T6 anodizzato bianco	Disegnato da: Team Policumbent	Creato 01/03/2022 23:32:54
OGGETTO POS_01_e_POS_02		Team Policumbent	SCALA 1:1
DESCRIZIONE C - Sedi per cuscinetti			DATA 30/05/2022
<p>Politecnico di Torino</p> <p>Corso Duca degli Abruzzi 24 - 10129 Torino</p>		GRADO DI FINITURA	
		FOGLIO A3 1/1	Disegno N. 1

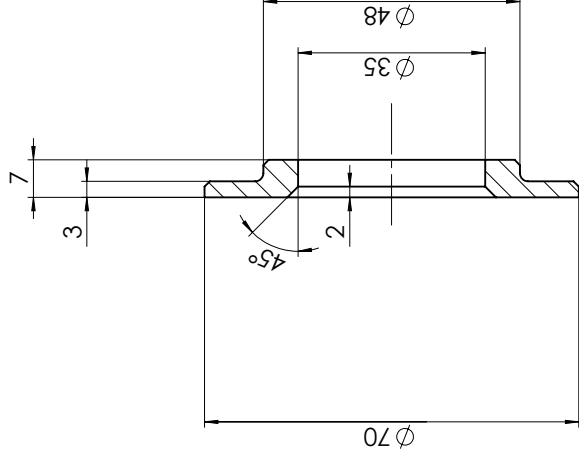
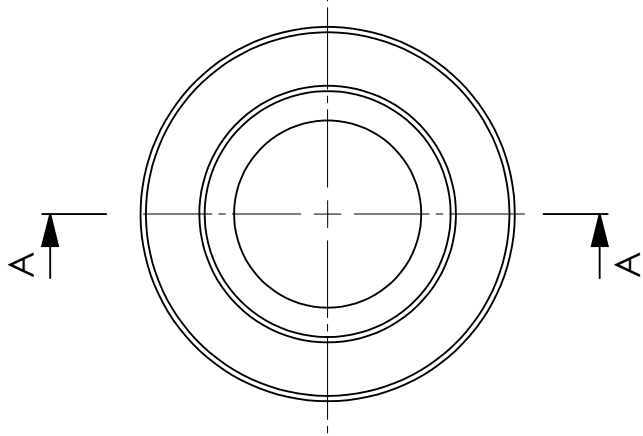


Sui fori M3 vanno inseriti filettati in acciaio

A-A

Smussi non quotati 1,5X45°
 Raccordi non quotati R1,5
 Size ISO 14405(E)
 Tolleranze generali ISO 22081
 Dimensioni lineari: ±0,2
 Dimensioni angolari: ±0,5°

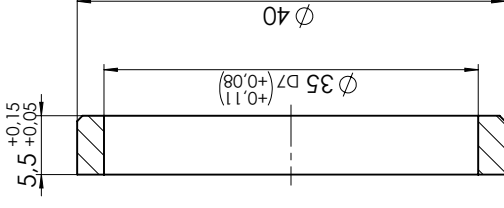
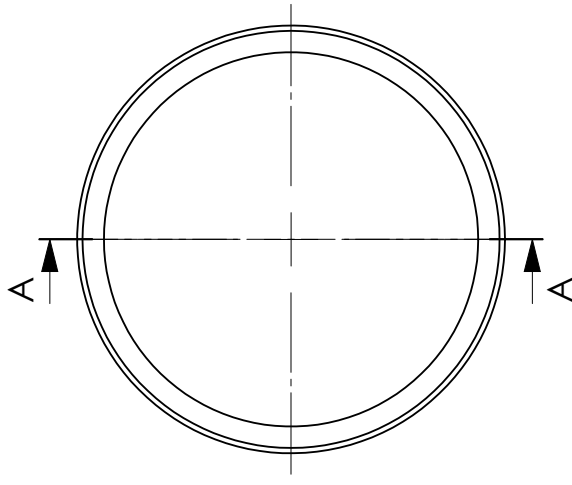
Q.TA 1	MATERIALE Alluminio 6082, anodizzazione bianca	DISGNATO DA: Team Policumbent	Creato 05/03/2022 19:33:23
OGGETTO POS_03	DESCRIZIONE Completto, mozzo posteriore - rev. aggiornata. filettatura ruota libera e mod. filettature per freno da M3 a M5	SCALA 2:1	DATA 29/09/2022
 Politecnico di Torino <small>Corso Duca degli Abruzzi 24 - 10129 Torino</small>		GRADO DI FINITURA √ (✓)	PESO (kg)
		FOGLIO A2 1/1	Disegno N.



A-A

Smussi non quotati 1X45°
 Size ISO 14405(E)
 Tolleranze generali ISO 22081
 Dimensioni lineari: ±0.2
 Dimensioni angolari: ±0.5°

Q.TA' 2	MATERIALE Alluminio 6082-T6 anodizzato bianco	Disegnato da: Team Policumbent	Creato 05/03/2022 20:08:06
OGGETTO POS_04	DESCRIZIONE Flangia	GRADO DI FINITURA Ra 6.4	SCALA 1:1
 <p>Politecnico di Torino Corso Duca degli Abruzzi 24 - 10129 Torino</p>		FOGLIO A3 1/1	DATA 19/05/2022
		Disegno N. 1	



A-A

Smussi non quotati 0,5X45°

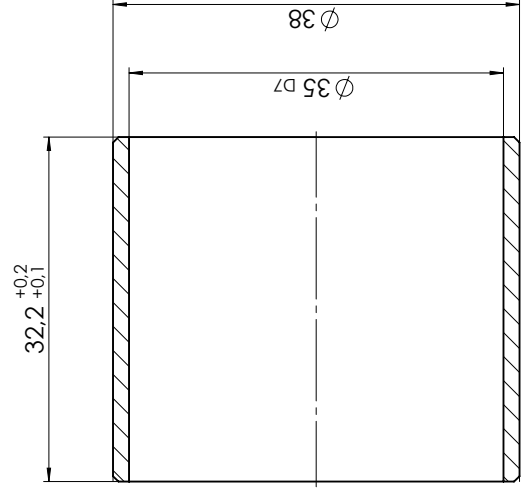
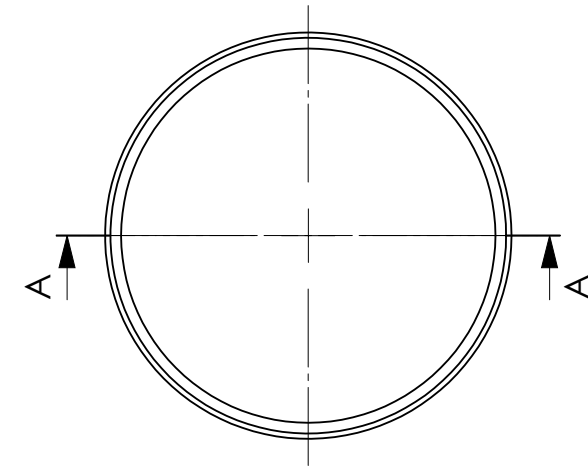
Size ISO 14405(E)

Tolleranze generali ISO 22081

Dimensioni lineari: $\pm 0,2$

Dimensioni angolari: $\pm 0,5^\circ$

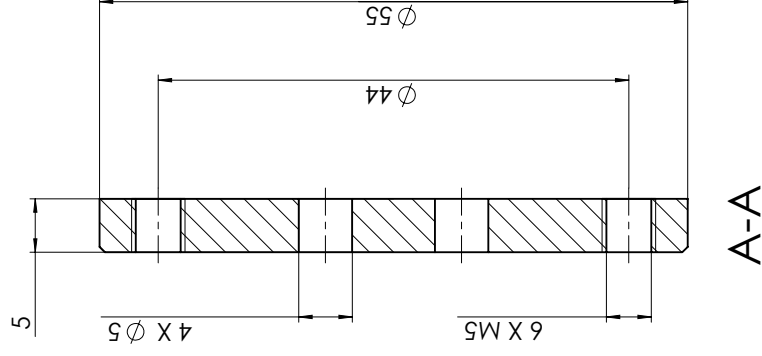
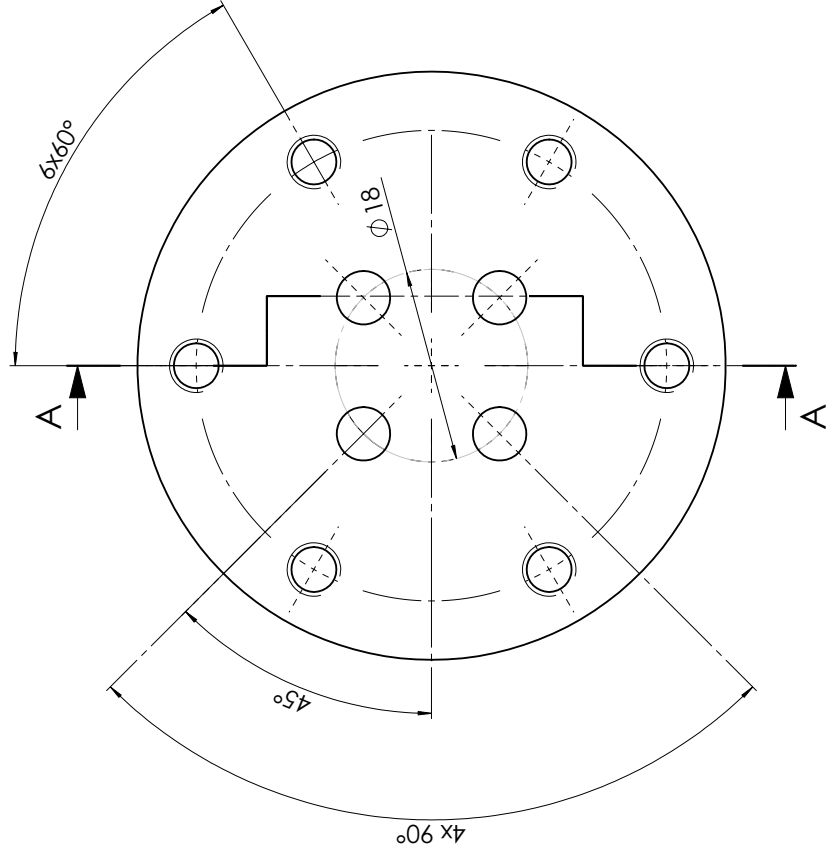
Q.TA' 1	MATERIALE Alluminio 6xxx anodizzato bianco	Disegnato da: Team Policumbent	Creato 11/04/2022 20:13:03
OGGETTO POS_07			SCALA 2:1
DESCRIZIONE Boccola per ruota libera			DATA 17/05/2022
 <p>Politecnico di Torino Corso Duca degli Abruzzi 24 - 10129 Torino</p>		GRADO DI FINITURA  Ra 6,4	
		Foglio A3 1/1	Disegno N. 1



A-A

Smussi non quotati 0.5X45°
 Size ISO 14405 (E)
 Tolleranze generali ISO 22081
 Dimensioni lineari: ±0.2
 Dimensioni angolari: ±0.5°

Q.TA' 1	MATERIALE Alluminio 6xxx anodizzato bianco	Disegnato da : Team Policumbent	Creato 11/04/2022 20:13:03
OGGETTO POS_08			SCALA 2:1
DESCRIZIONE Boccola freno			DATA 17/05/2022
 Politecnico di Torino Corso Duca degli Abruzzi 24 - 10129 Torino		GRADO DI FINITURA 	
		FOLIO A3 1/1	Disegno N. 1



I fori filettati M5 sono da realizzarsi con inserti in acciaio (se possibile usare inserti su fori passanti)

Smussi non quotati 0.5X45°

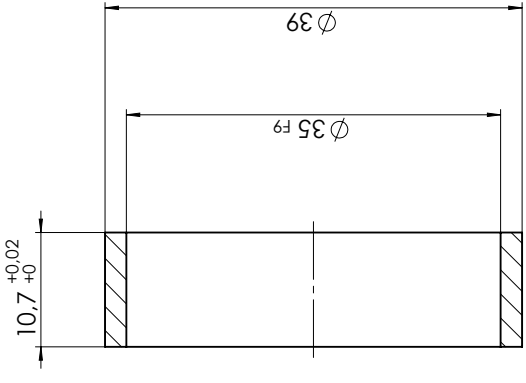
Size ISO 14405 (E)

Tolleranze generali ISO 22081

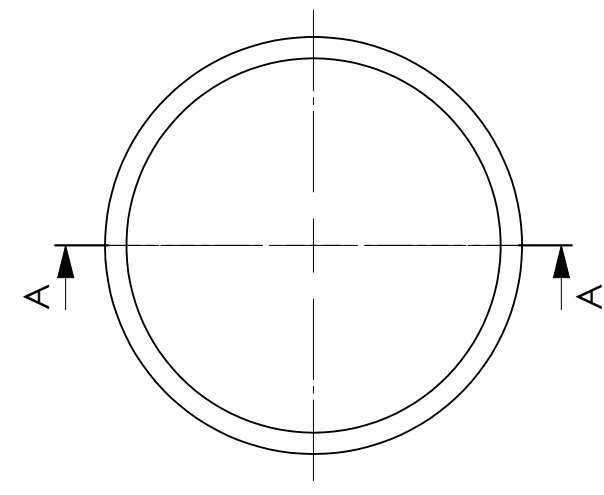
Dimensioni lineari: ± 0.2

Dimensioni angolari: $\pm 0.5^\circ$

Q.TA' 1	MATERIALE Alluminio 6082-T6 anodizzato bianco	Disegnato da: Team Policumbent		Creato 27/01/2022 15:23:21
OGGETTO DESCRIZIONE	Interfaccia disco freno POS_09	Team Policumbent		SCALA 2:1
		GRADO DI FINITURA \sqrt{Ra} 6.4		DATA 29/09/2022
 <p>Politecnico di Torino Corso Duca degli Abruzzi 24 - 10129 Torino</p>		FOGLIO A3 1/1	Disegno N. 1	

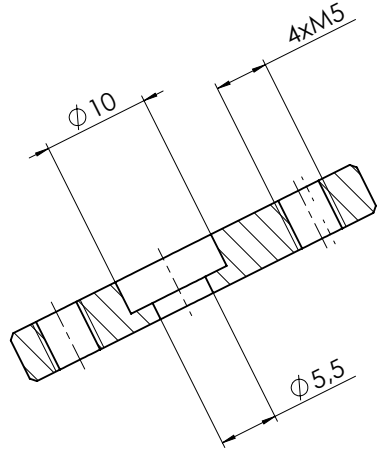
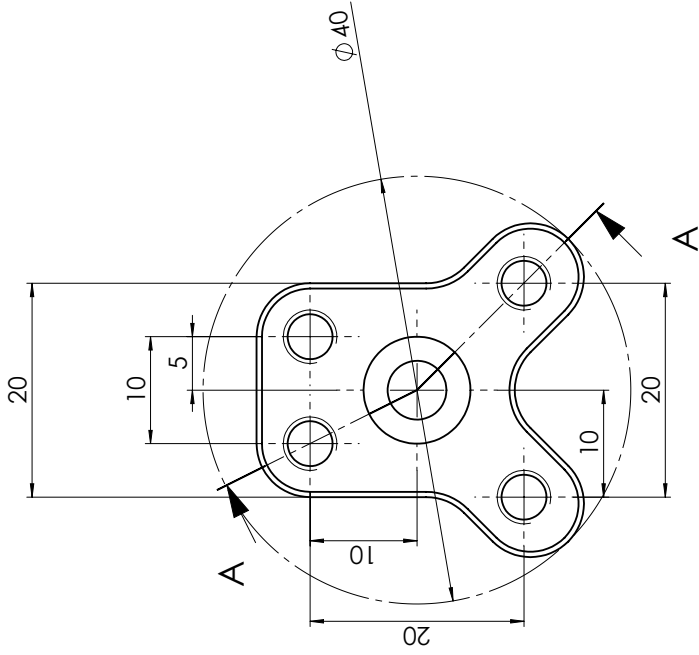


A-A



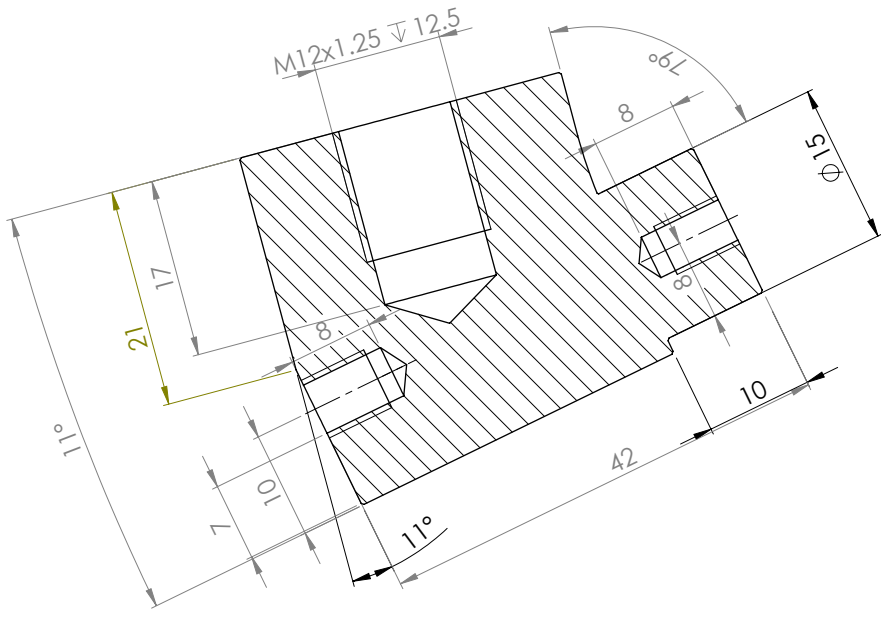
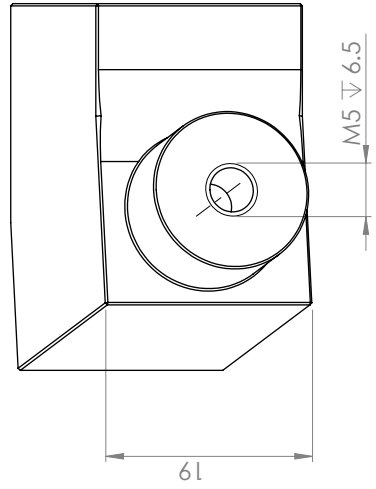
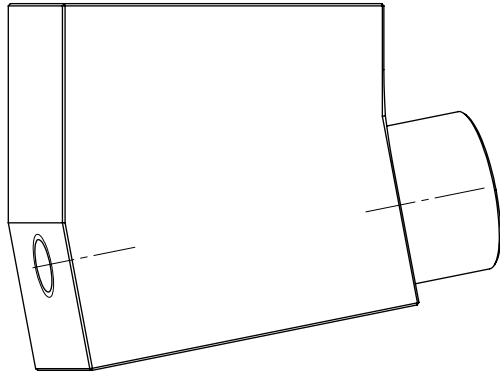
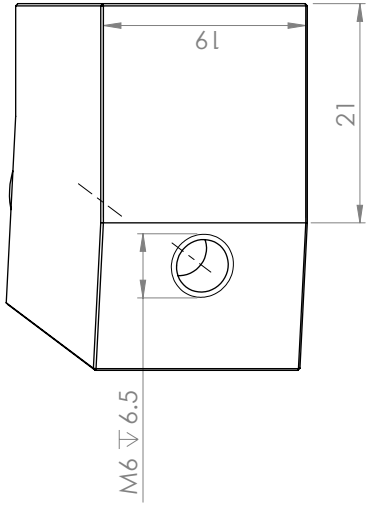
Raccordi non quotati R0,5
 Smussi non quotati 0,5x45°
 Size ISO 14405(E)
 Tolleranze generali ISO 22081
 Dimensioni lineari: ±0,2
 Dimensioni angolari: ±0,5°

Q.TA' 2	MATERIALE Alluminio 6xxx - anodizzazione bianca	CREATO 16/05/2022 19:58:43
OGGETTO Boccola per cuscinetto	DISEGNATO DA: Team Policumbent	SCALA 2:1
DESCRIZIONE POS_10	GRADO DI FINITURA √ (√)	DATA 17/05/2022
 Politecnico di Torino Corso Duca degli Abruzzi 24 - 10129 Torino	PESO (g) -	 Foglio A3 1/1
	Disegno N.	



Raccordi non quotati R5
 Smussi non quotati 0,5x45°
 Size ISO 14405(E)
 Tolleranze generali ISO 22081
 Dimensioni lineari: ±0,2
 Dimensioni angolari: ±0,5°

Q.TA' 1	MATERIALE AISI 303 (o 304 o 316 a discrezione)	CREATO 26/08/2021 23:37:45
OGGETTO ST_02	DESCRIZIONE Placchetta di sterzo	SCALA 2:1
Politecnico di Torino Corso Duca degli Abruzzi 24 - 10129 Torino		DATA 27/04/2022
		
DISEGNATO DA: Team Policumbent		PESO (g) -
GRADO DI FINITURA √ (√)		FOGLIO A3 1/1
Disegno N.		Tav. N.



Raccordi non quotati R0,5
Smussi non quotati 0,5x45°

Size ISO 14405 (E)

Tolleranze generali ISO 22081

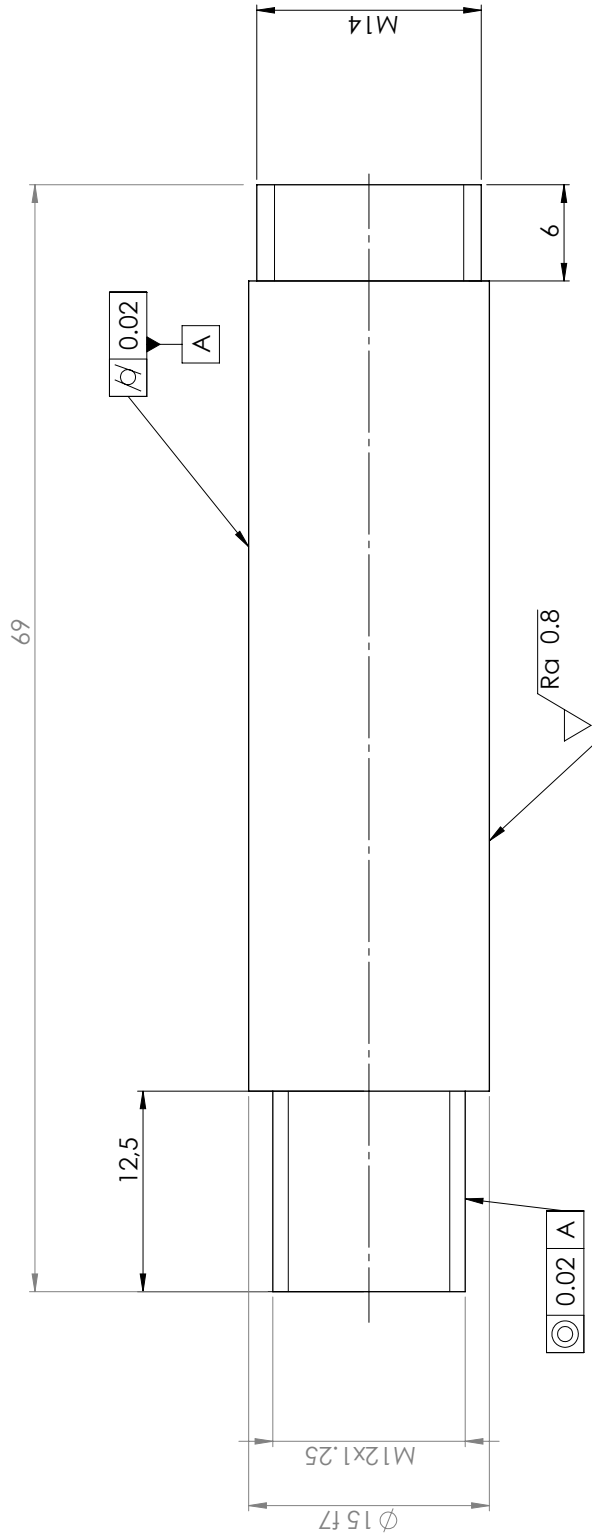
Dimensioni lineari: ±0,2

Dimensioni angolari: ±0,5°

SEZIONE A-A

Utilizzare inserti in acciaio

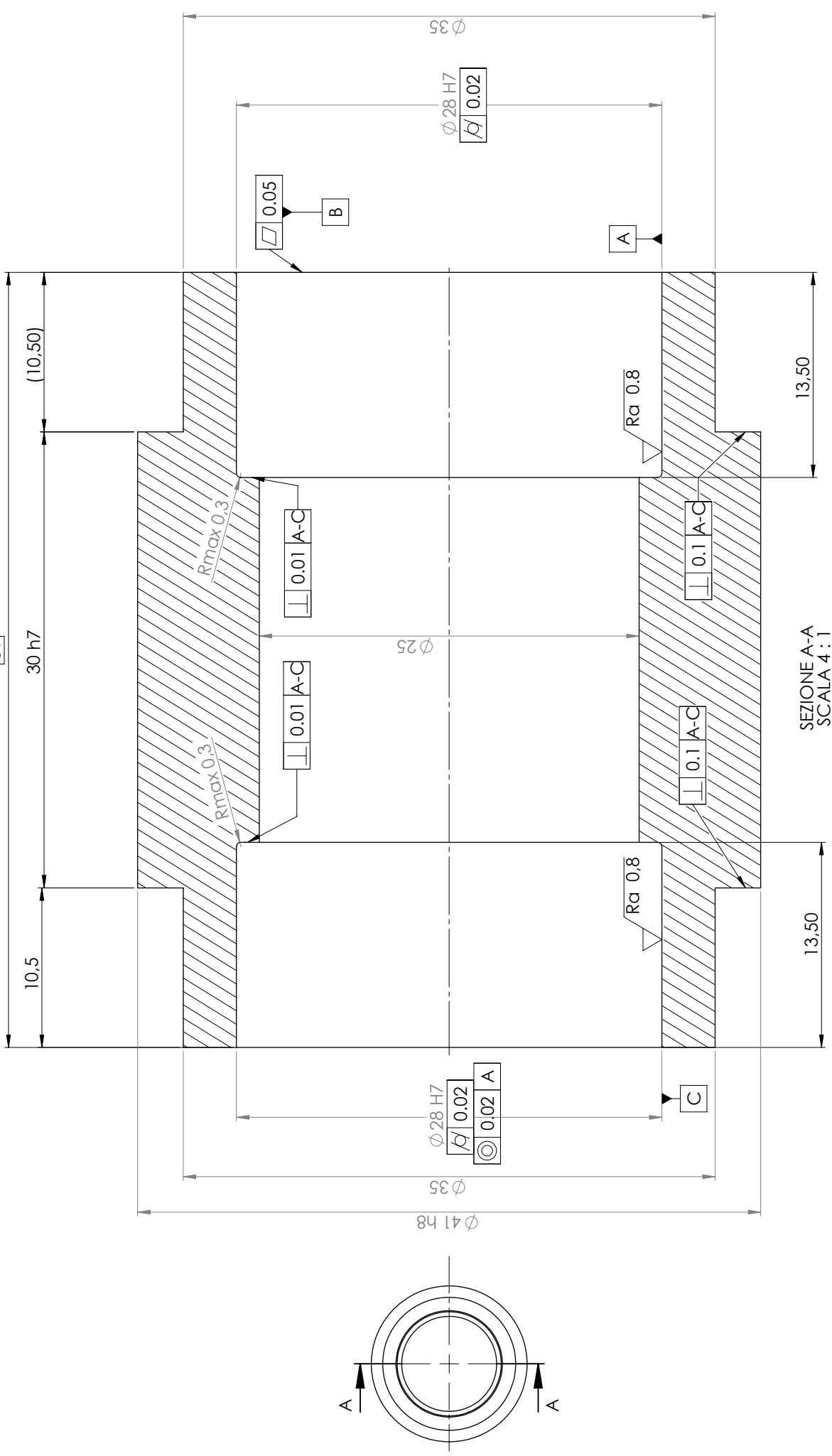
Q.TA' 2	MATERIALE Alluminio 6082 Anodizzazione bianca	CREATO 27/08/2021 22:20:58	Disegnato DA: Team Policumbent	SCALA 2:1	DATA 16/05/2022	
OGGETTO DESCRIZIONE	ST_05 Portarmozzo	Disegnato DA: Team Policumbent	PESO (Kg)			
Politecnico di Torino		GRADO DI FINITURA 	Foglio A3 1/1	Disegno N.		



Size ISO 14405(E)
 Tolleranze generali ISO 22081
 Dimensioni lineari: $\pm 0,2$
 Dimensioni angolari: $\pm 0,5^\circ$

Q.TA' 2	MATERIALE Acciaio AISI 303 (o304 o 316 a discrezione)	DISEGNATO DA: Team Policumbent	Creato 04/04/2022 10:00:12
OGGETTO DESCRIZIONE	ANT_01 Perno	GRADO DI FINITURA $\sqrt{0.02}$ A	SCALA 3:1
Politecnico di Torino		PESO (g)	DATA 16/05/2022
		FOGLIO A3 1/1	
		Disegno N.	

51

SEZIONE A-A
SCALA 4 : 1Raccordi non quotati R0,5
Smussi non quotati 0,5x45°

Size ISO 14405 (E)

Tolleranze generali ISO 22081

Dimensioni lineari: ±0,2

Dimensioni angolari: ±0,5°

Q.TA' 2 MATERIALE Alluminio 6082 Anodizzazione bianca

OGGETTO ANTI_02

DESCRIZIONE CorpettoMozzo

DISEGNATO DA:

Team Policumbent

GRADO DI FINITURA



PESO (g)

Disegno N.

Politecnico di
TorinoFOGLIO
A3 1/1

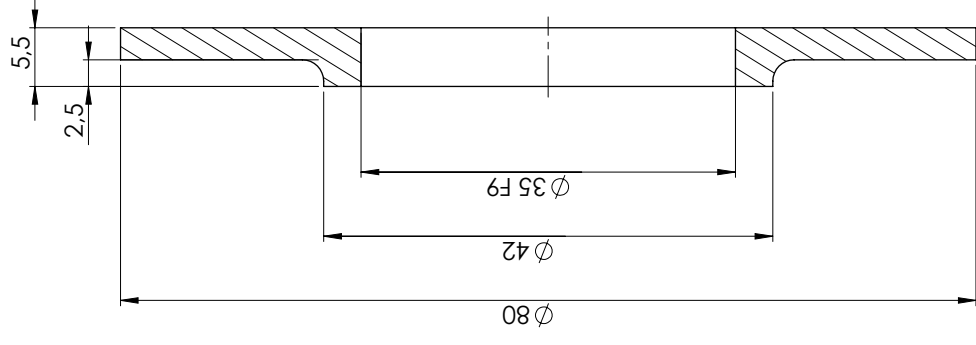
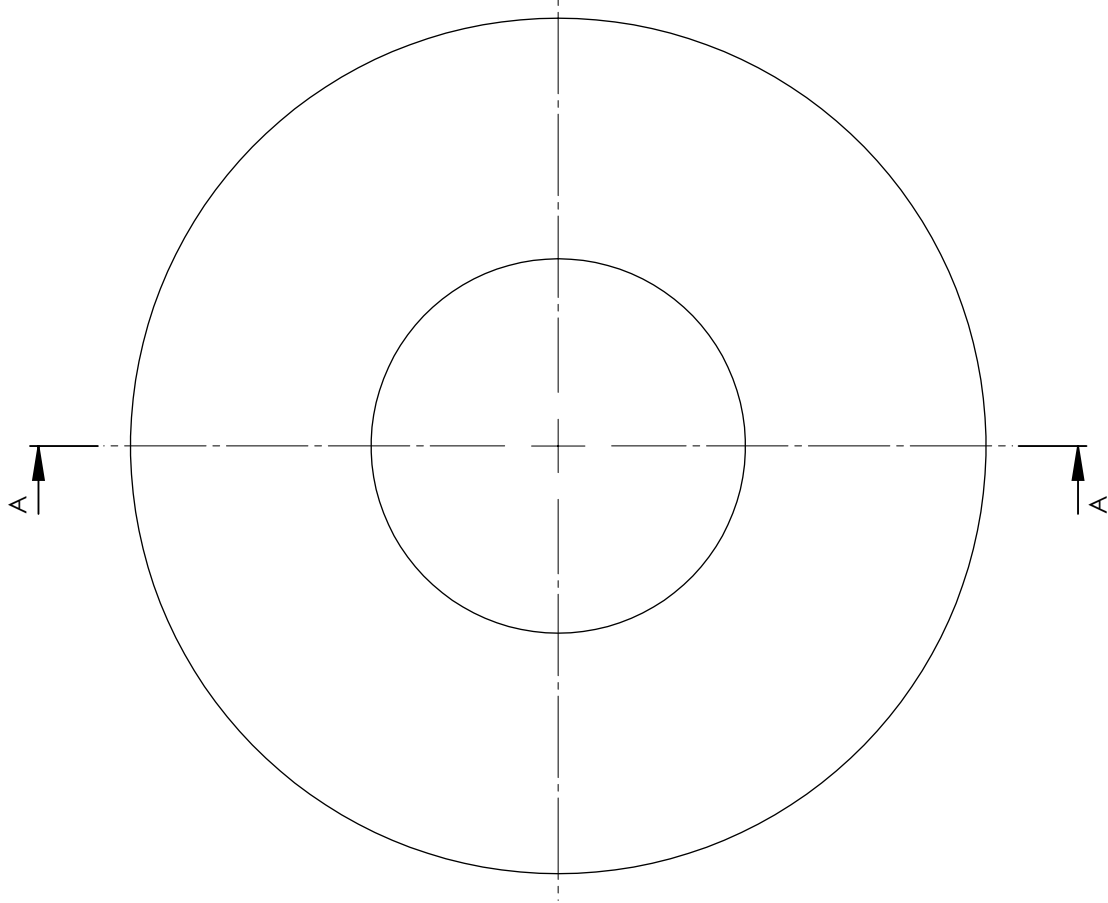
Creato

17/02/2022 22.04.24

SCALA 1:1

DATA 24/05/2022

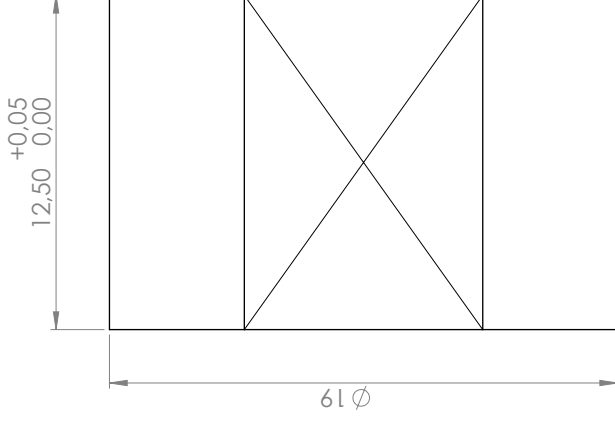
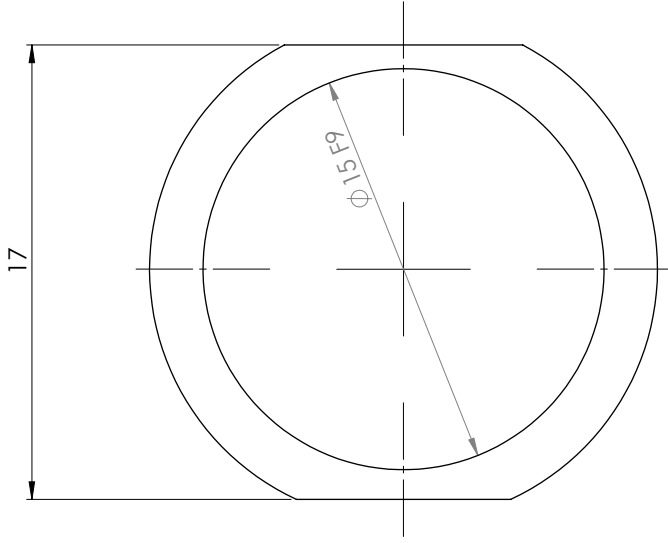




A-A

Raccordi non quotati R2
 Size ISO 14405 (E)
 Tolleranze generali ISO 22081
 Dimensioni lineari: $\pm 0,2$
 Dimensioni angolari: $\pm 0,5^\circ$

Q.TA' 4	MATERIALE Alluminio 6082 Anodizzazione bianca	CREATO 17/02/2022 22:47:07
OGGETTO DESCRIZIONE ANT_03 Flangia	DISEGNATO DA: Team Policumbent	SCALA 2:1
GRADO DI FINITURA $\nabla (\nabla)$		DATA 16/05/2022
Politecnico di Torino		PESO (Kg)
FOGLIO A3 1/1		Disegno N.



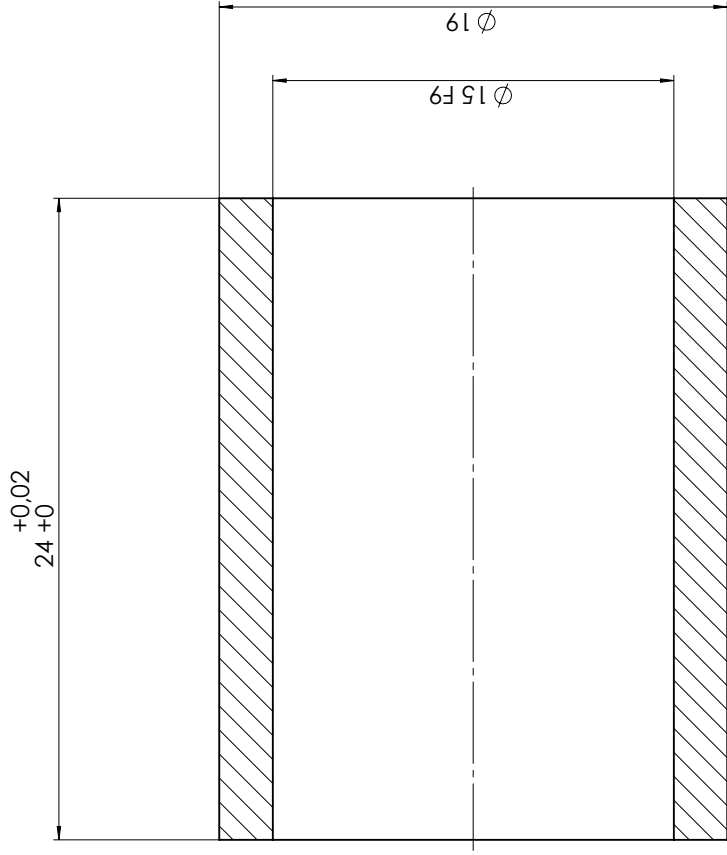
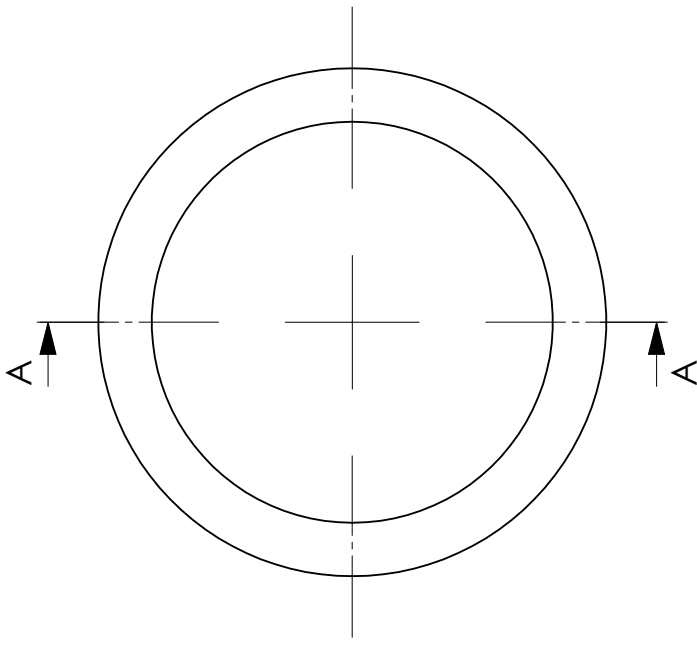
Size ISO 14405 (E)

Tolleranze generali ISO 22081

Dimensioni lineari: $\pm 0,2$

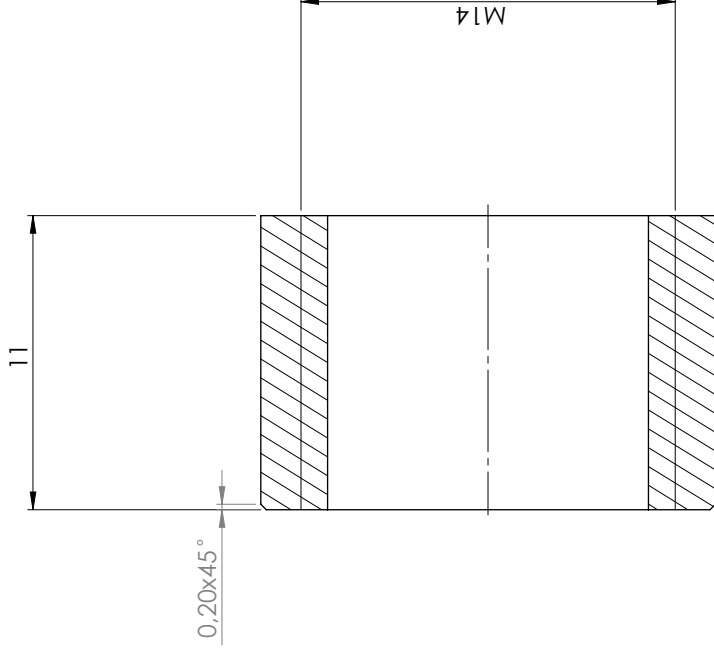
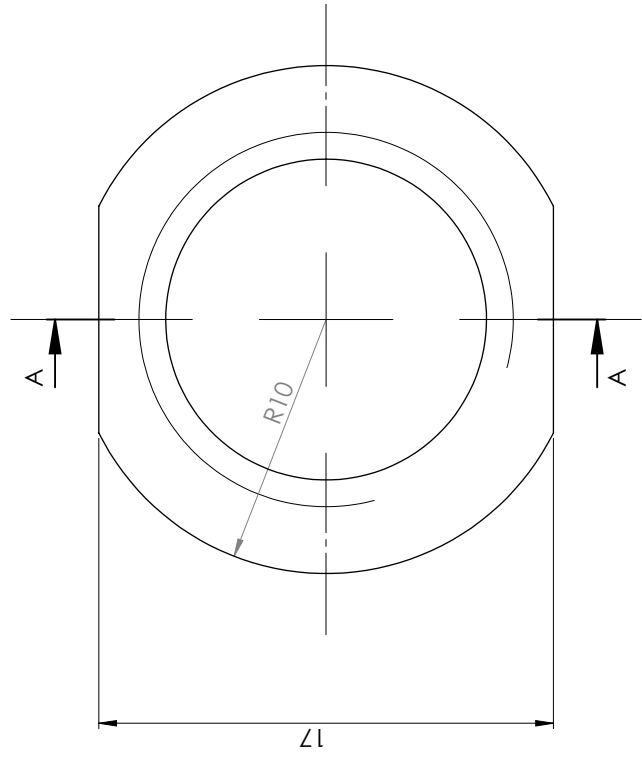
Dimensioni angolari: $\pm 0,5^\circ$

Q.TA' 2	MATERIALE Alluminio 6XXX Anodizzazione bianca	Disegnato DA: Team Policumbent	Creato 28/02/2022 22:03:08
OGGETTO DESCRIZIONE	ANT_04 Boccola interfaccia portamozzo-mozzo anteriore	GRADO DI FINITURA ∇ (∇)	SCALA 5:1 DATA 29/09/2022
 <p>Politecnico di Torino</p>		PESO (Kg)	
		Foglio A3 1/1	Disegno N.



Size ISO 14405(E)
 Tolleranze generali ISO 22081
 Dimensioni lineari: $\pm 0,2$
 Dimensioni angolari: $\pm 0,5^\circ$

Q.TA' 2	MATERIALE Alluminio 6xxx, anodizzazione bianca	Creato 31/05/2022 09:33:58
OGGETTO ANT_05	DISEGNATO DA: Team Policumbent	SCALA 5:1
DESCRIZIONE Distanziale battuta anelli interni cuscinetti	GRADO DI FINITURA $\nabla (\nabla)$	DATA 31/05/2022
 Politecnico di Torino Corso Duca degli Abruzzi 24 - 10129 Torino	PESO (g) -	
	Foglio A3 1/1	



A-A

Size ISO 14405 (E)

Tolleranze generali ISO 22081

Dimensioni lineari: $\pm 0,2$

Dimensioni angolari: $\pm 0,5^\circ$

Q.TA' 2	MATERIALE Alluminio 6xxx Anodizzazione bianca	DISEGNATO DA: Team Policumbent	Creato 28/02/2022 21:59:16
OGGETTO DESCRIZIONE	ANT_06 Ghiera interna	GRADO DI FINITURA ∇ (∇)	SCALA 5:1 DATA 16/05/2022
Politecnico di Torino		PESO (Kg)	
		FOGLIO A3 1/1	
Disegno N.			

Bibliography

- [1] Cox, P. “The Role of Human Powered Vehicles in Sustainable Mobility.” *Built Environment* (1978), vol. 34, no. 2, 2008, pp. 140–60. JSTOR, <http://www.jstor.org/stable/23289803>. Accessed 2 Oct. 2022.
- [2] Gross, Albert C., Chester R. Kyle, and Douglas J. Malewicki. “The Aerodynamics of Human-Powered Land Vehicles.” *Scientific American* 249, no. 6, 1983, pp. 142–53. <http://www.jstor.org/stable/24969056>. Accessed 2 Oct. 2022.
- [3] <https://bentupcyclingjournal.blogspot.com/p/history-of-recumbent-bicycle.html>, accessed on October 2, 2022.
- [4] https://en.wikipedia.org/wiki/Francis_Faure, last edited on 18 June 2022, at 21:59 (UTC); accessed on October 04, 2022.
- [5] <https://www.flickr.com/photos/letterlust/5099661062/>; accessed on October 04, 2022.
- [6] https://en.wikipedia.org/wiki/Piet_Dickentman; accessed on October 04, 2022.
- [7] <http://www.whpva.org/history.html>; accessed on October 04, 2022.
- [8] <https://paraciclismo.feder ciclismo.it/it/infopage/le-classificazioni-nel-ciclismo-paralimpico/88e6be86-4cb0-41e5-8fee-ef177cc1a8bd/>, accessed on September 22, 2022.
- [9] <https://italiawiki.com/pages/sport-per-disabili/hand-bike-classificazione-h1-h2-h3-h4-classe-libera-requisiti-per-handbike-da-competizione.html>, accessed on September 22, 2022.
- [10] Belloli, M., Cheli, F., Bayati, I., Giappino, S., Robustelli, F., “Handbike Aerodynamics: Wind Tunnel Versus Track Tests”, *Procedia Engineering*, Vol. 72, 2014, pp. 750-755.
- [11] Maries, N., Delprete, C., Baldissera, P., “Design of speed record handcycle”, Msc. thesis, Torino, 2020. <https://webthesis.biblio.polito.it/16866/1/tesi.pdf>
- [12] <https://www.policumbent.it/it/>
- [13] <https://jnyyz.wordpress.com/2022/09/12/bm-2022-monday-am-results/>; accessed on October 04, 2022.
- [14] <https://jnyyz.wordpress.com/2022/09/11/bm2022-sunday-am-results/>; accessed on October 04, 2022.

-
- [15] Baldissera, P., Delprete, C., Rossi, M., Zahar, A., “Experimental Comparison of Speed-Dependent Rolling Coefficients in Small Cycling Tires”, *Tire Science and Technology*, Vol. 49, n. 3, 2021, pp. 224-241.
- [16] Velardocchia M., *Appunti di fondamentali di Meccanica del Veicolo*, Politecnico di Torino, 2021, p. 42,68-70.
- [17] https://en.wikipedia.org/wiki/Rolling_resistance, last edited on 13 July 2022, at 21:35 (UTC).
- [18] <https://www.bicyclerollingresistance.com/specials/tubeless-latex-butyl-tubes>, accessed on September 21, 2022.
- [19] <https://www.bicyclerollingresistance.com/specials/tpu-inner-tubes>, accessed on September 21, 2022.
- [20] <https://www.bicyclerollingresistance.com/specials/top-3-fastest-tubeless-vs-tubes>, accessed on September 21, 2022.
- [21] Arina R., *Fondamenti di Aerodinamica Parte I. Nozioni introduttive e teoria del fluido inviscido*, Torino, Levrotto&Bella, 2014, pp 18-20.
- [22] https://en.wikipedia.org/wiki/No-slip_condition, last edited on 9 August 2022, at 09:37 (UTC).
- [23] https://en.wikipedia.org/wiki/Drag_coefficient, last edited on 17 August 2022, at 01:23 (UTC).
- [24] <https://www.plasticexpert.com/wp-content/uploads/2019/01/Why-Do-Polycarbonate-Windows-Turn-Yellow.pdf>, accessed on September 14, 2022.
- [25] <https://www.belleliufficio.it/differenza-plexiglas-policarbonato>, accessed on September 14, 2022.
- [26] <https://en.wikipedia.org/wiki/Lamination>; accessed on October 03, 2022.
- [27] <https://www.easycomposites.co.uk/learning/hand-laminate-vacuum-bag-simple-part>, accessed on October 03, 2022.
- [28] http://recumbents.com/wisil/whpsc/whpsc_site.htm; accessed on October 07, 2022.
- [29] Ferraresi, C., Raparelli, T., *Meccanica applicata*, Torino, CLUT, 2017, III edition